FZD-466

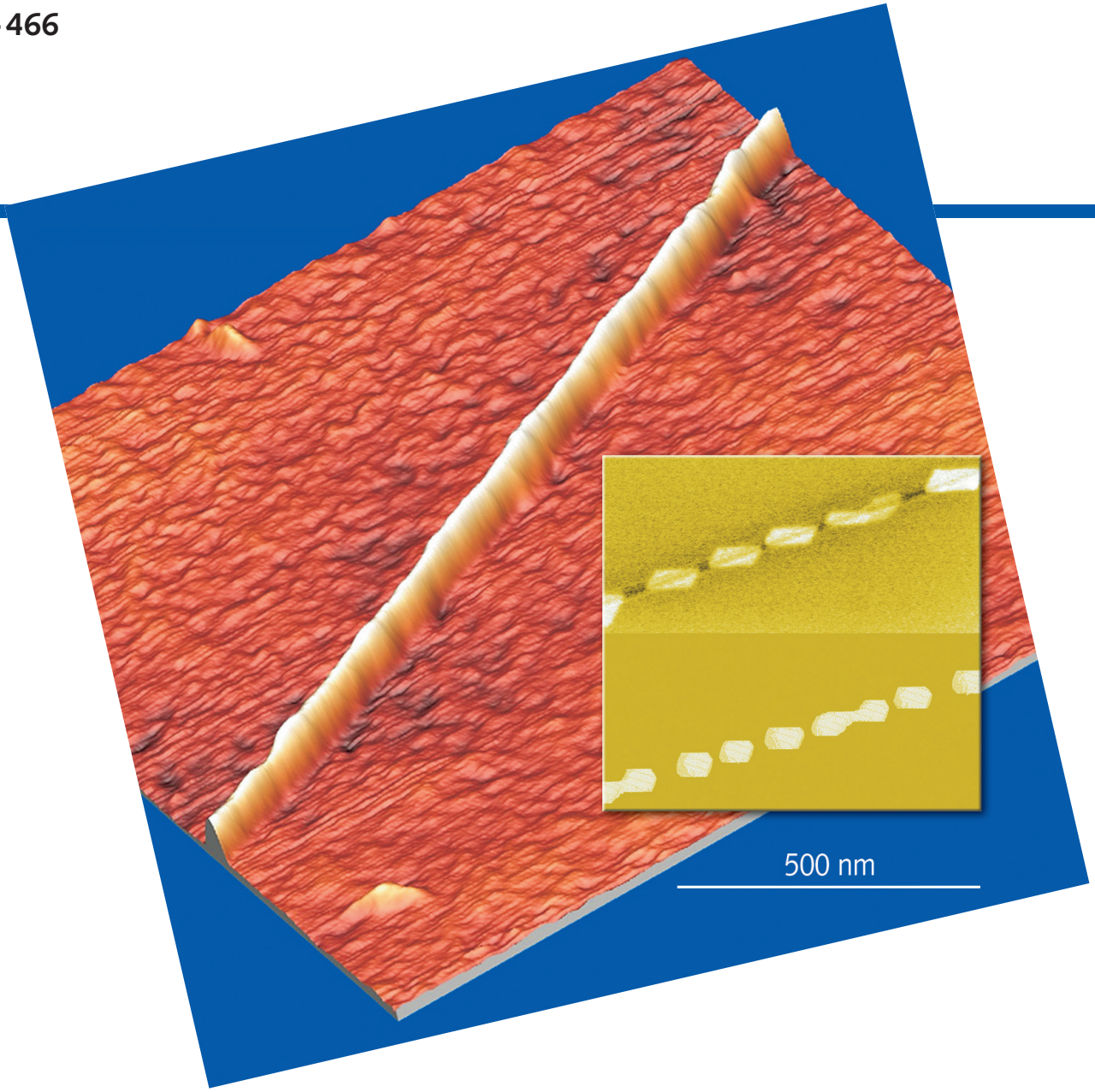

FZD-466 Annual Report 2006 Institute of Ion Beam Physics and Materials Research

Wissenschaftlich-Technische Berichte
FZD-466 2007 · ISSN 1437-322X

ANNUAL REPORT 2006

INSTITUTE OF ION BEAM PHYSICS AND MATERIALS RESEARCH

Forschungszentrum Dresden Rossendorf

Wissenschaftlich-Technische Berichte
FZD – 466
2007

Annual Report 2006

Institute of Ion Beam Physics and Materials Research

Editors:

J. von Borany, V. Heera,
M. Helm, W. Möller

Forschungszentrum
Dresden Rossendorf

Cover Picture:

Background:
AFM image of a self-aligned $CoSi_2$ nanowire in (111)-silicon synthesized by cobalt focused ion beam (FIB) implantation and subsequent annealing. The 30 nm thick nanowire is oriented along the <110>-crystal orientation. The field size is $1.5 \times 1.5\ \mu m^2$. The implantation was done at 450 °C with 60 keV Co^{2+} ions at $2.5 \times 10^{16}\ cm^{-2}$. Subsequently the sample was annealed in two steps 60 min. and 30 min. in dry N_2 at 600 °C and 1000 °C, respectively.

Inset, top:
Scanning electron microscope image of the nanowire decayed into a chain of nanoparticles in (111)-Si due to the 30°-misalignment of the FIB implantation trace relative to the <110>-crystal orientation. The implantation dose is $10^{17}\ cm^{-2}$.

Inset, bottom:
Corresponding result of 3D Kinetic Monte-Carlo simulation.

For details see the contribution of Ch. Akhmadaliev et al., pp. 33-36.

Forschungszentrum Dresden - Rossendorf e.V.
Institut für Ionenstrahlphysik und Materialforschung
Postfach 51 01 19
D-01314 Dresden
Bundesrepublik Deutschland

Direktoren	Prof. Dr. Manfred Helm	Prof. Dr. Wolfhard Möller
Telefon	+ 49 (351) 260 2260	+ 49 (351) 260 2245
Telefax	+ 49 (351) 260 3285	+ 49 (351) 260 3285
E-mail	m.helm@fzd.de	w.moeller@fzd.de

Homepage http://www.fzd.de/FWI

Preface by the Directors

The Institute of Ion Beam Physics and Materials Research (IIM) is the largest of six institutes of the Forschungszentrum Dresden-Rossendorf (FZD) and contributes to its Research Program "Structure of Matter". It combines basic and applied research in the fields of ion beam applications to materials and semiconductor research, with more than 100 scientists, engineers, technicians, and PhD and diploma students. The institute operates a national and international ion beam center, which, in addition to its own scientific activities, offers services and transfers know-how on ion beam techniques to universities, other research institutes, and industry. Parts of its activities are also dedicated to exploit the infrared/THz free-electron laser at the 40 MeV superconducting electron accelerator ELBE for condensed matter research. For both facilities the institute holds EU grants for funding access of external users. Cooperation with our colleagues from the recently established High Magnetic Field Laboratory Dresden (HLD), another institute of the FZD, is increasing as well.

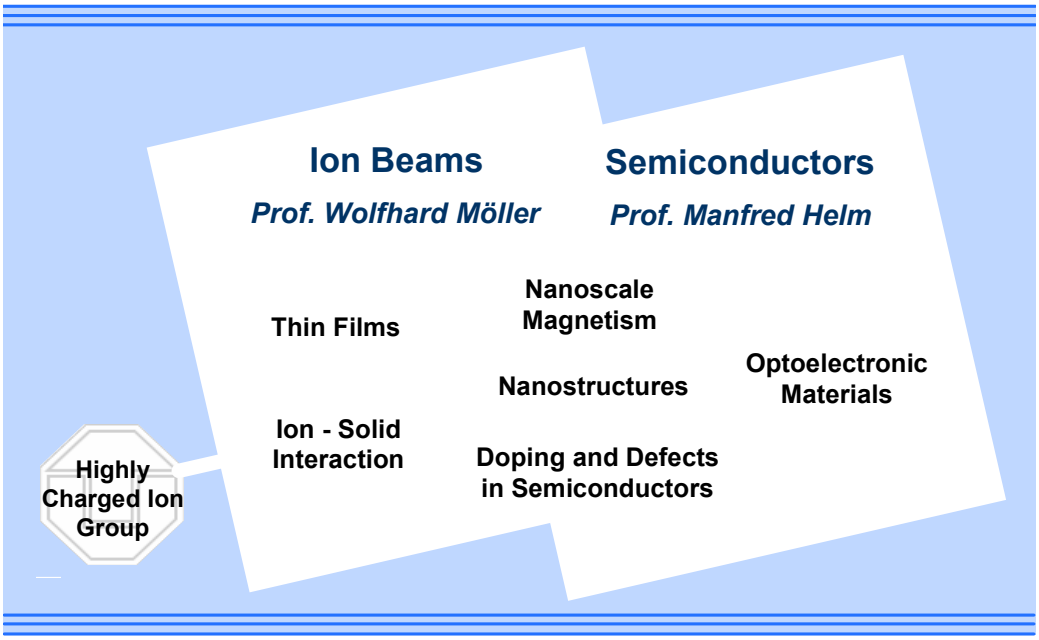

The diagram displays the presently six R&D topics of the institute, together with the associated Highly Charged Ion Group of the TU Dresden. Our research activities span a wide range of topics relevant for future information processing, be it in the realm of nanoelectronics, optoelectronics, magnetoelectronics or spintronics. Highlights of last year's research are presented in this Annual Report through reprints of important papers that were published in *Physical Review Letters* and *Applied Physical Letters*. We feel that this may be a rather effective way of presenting our work, effective both for us and hopefully also for our readers. We are particularly happy that among these we can present the first two publications resulting from work at the free-electron laser FELBE.

For the friends and colleagues who have known our institute for a long time, it may be interesting to observe that our research on optoelectronic materials and nanoscale magnetism, both essentially non-existent a few years back, have now grown into strong and competitive activities, thanks to the excellent young scientists who developed these fields here.

We are also pleased that we can report a quite stable level of third-party funding, in spite of the ever-tougher competition. Here funding from the EU becomes a more and more important fraction, and funding by the German Science Foundation (DFG) is significantly increasing at present. A good part

of funding comes through contracts with industrial companies, in particular also from local micro-electronics and other high-tech industry. Thus also our funding spectrum reflects our scope from more basic to more applied research. Last but not least, the scientific output is what counts most among our peers and for our advisory boards; we believe we have fulfilled our goals and others' expectations, by shifting a growing fraction of publications into high-impact journals.

The institute would like to thank all partners and friends, and the organizations who supported its progress in 2006. Special thanks are due to the Executive Board of the Forschungszentrum Dresden-Rossendorf, the Minister of Science and Arts of the Free State of Saxony, and the Minister of Education and Research of the Federal Government of Germany. Our partners from universities, industry and research institutes all around the world contribute essentially to the success of the institute, and play a crucial role for its further development. Last but not least, the directors would like to thank all staff of the institute for their dedicated efforts and excellent contributions in 2006.

Prof. Manfred Helm Prof. Wolfhard Möller

Contents

Selected Publications

Statistics

Selected Publications

Copyright Remarks

1. G. Abrasonis, W. Möller and X.X. Ma
   Physical Review Letters Vol. **96**, Issue 6, Art.No. 065901, 2006
   Copyright 2006, American Physical Society

2. M. Beckers, N. Schell, R.S.M. Martins, A. Mücklich and W. Möller
   Applied Physics Letters, Vol. **89**, Issue 7, Art.No. 074101, 2006
   Copyright 2006, American Institute of Physics

3. A. Rogozin, N. Shevchenko, M. Vinnichenko, M. Seidel, A. Kolitsch and W. Möller
   Applied Physics Letters, Vol. **89**, Issue 6, Art.No. 061908, 2006
   Copyright 2006, American Institute of Physics

4. T.W.H. Oates
   Applied Physics Letters, Vol. **88**, Issue 21, Art.No. 213115, 2006
   Copyright 2006, American Institute of Physics

5. J. Fassbender and J. McCord
   Applied Physics Letters, Vol. **88**, Issue 25, Art.No. 252501, 2006
   Copyright 2006, American Institute of Physics

6. K. Potzger, Shengqiang Zhou, H. Reuther, A. Mücklich, F. Eichhorn, N. Schell, W. Skorupa, M. Helm, J. Fassbender, T. Herrmannsdörfer and T.P. Papageorgiou
   Applied Physics Letters, Vol. **88**, Issue 5, Art.No. 052508, 2006
   Copyright 2006, American Institute of Physics

7. G. Talut, H. Reuther, A. Mücklich, F. Eichhorn, and K. Potzger
   Applied Physics Letters, Vol. **89**, Issue 16, Art.No. 161909, 2006
   Copyright 2006, American Institute of Physics

8. C. Akhmadaliev, B. Schmidt, and L. Bischoff
   Applied Physics Letters, Vol. **89**, Issue 22, Art.No. 223129, 2006
   Copyright 2006, American Institute of Physics

9. V. Beyer, J. von Borany, and M. Klimenkov
   Applied Physics Letters, Vol. **89**, Issue 19, Art.No. 193505, 2006
   Copyright 2006, American Institute of Physics

10. R. Kögler. A. Peeva, A. Mücklich, F. Eichhorn, and W. Skorupa
    Applied Physics Letters, Vol. **88**, Issue 10, Art.No. 101918, 2006
    Copyright 2006, American Institute of Physics

11. M. Posselt, L. Bischoff, D. Grambole, and F. Herrmann
    Applied Physics Letters, Vol. **89**, Issue 15, Art.No. 151918, 2006
    Copyright 2006, American Institute of Physics

12. J.M. Sun, S. Prucnal, W. Skorupa, M. Helm, L. Rebohle, and T. Gebel
Applied Physics Letters, Vol. **89**, Issue 9, Art.No. 091908, 2006
Copyright 2006, American Institute of Physics

13. H. Schneider, O. Drachenko, S. Winnerl, M. Helm, and M. Walther
Applied Physics Letters, Vol. **89**, Issue 13, Art.No. 133508, 2006
Copyright 2006, American Institute of Physics

14. D. Stehr, S. Winnerl, M. Helm, T. Dekorsy, T. Roch, and G. Strasser
Applied Physics Letters, Vol. **88**, Issue 15, Art.No. 151108, 2006
Copyright 2006, American Institute of Physics

15. C.V.-B. Tribuzy, S. Ohser, S. Winnerl, J. Grenzer, H. Schneider, M. Helm, J. Neuhaus, T. Dekorsy, K. Biermann and H. Künzel
Applied Physics Letters, Vol. **89**, Issue 17, Art.No. 171104, 2006
Copyright 2006, American Institute of Physics

PRL 96, 065901 (2006) PHYSICAL REVIEW LETTERS week ending 17 FEBRUARY 2006

Anomalous Ion Accelerated Bulk Diffusion of Interstitial Nitrogen

Gintautas Abrasonis* and Wolfhard Möller
Institute of Ion Beam Physics and Materials Research, Forschungszentrum Rossendorf, PF-510119, 01314 Dresden, Germany

Xin Xin Ma
School of Materials Science and Engineering, Harbin Institute of Technology, 150001 Harbin, China
(Received 19 August 2005; published 13 February 2006)

Interstitial N diffusion under low energy (~700 eV) Ar^+ bombardment at 673 K in ion beam nitrided austenitic stainless steel is investigated. Ar^+ ion bombardment increases the N mobility in depths far beyond the ion penetration depth, resulting in an increased broadening of the N depth profile as a function of Ar^+ flux. This effect cannot be explained by any established mechanism of radiation-enhanced diffusion. An explanation based on quasiparticle-enhanced mobility is proposed.

DOI: 10.1103/PhysRevLett.96.065901 PACS numbers: 66.30.Jt, 61.80.Jh, 63.20.Ry

Transport phenomena in ion-irradiated solids can be classified into athermal collisional processes such as recoil implantation and cascade mixing, and processes which require thermal activation such as purely thermal diffusion or radiation-enhanced diffusion [1]. The athermal processes act in a depth range which is affected by the slowing down of the ions and relocation of atoms due to single or multiple knock-on events. In contrast, the present Letter reports on the existence of an ion induced athermal process which is effective to a depth being several orders of magnitude larger than the dimensions of the collision cascade. N diffusion in the austenitic stainless steel (ASS) under Ar ion bombardment is studied. Because of the broad application domain of ASS, a large amount of information is available, such as reliable experimental information on point defect diffusion and extensive studies of the modeling of ion nitriding. For the present system of N implanted into ASS, the diffusional formation of a highly metastable supersaturated interstitial N solid solution at temperatures around 673 K is well established [2–6]. However, it was shown that the N diffusivity depends on the N ion flux [7–10] for which no satisfactory explanation could be given. In the present work, an experiment has been designed to clearly establish the effect of ion bombardment on deep diffusion. An interpretation is attempted on the basis of ion irradiation created quasiparticles that can propagate over long distances in the 3D lattice interacting with the interstitial atoms and affecting their mobility.

Three mm thick discs, 10 mm in diameter, were cut from commercial ASS AISI 316L rods (Cr concentration ~18.5 at. %). Mechanical polishing produced a final roughness of 0.01 μm. Ar and N ion bombardment was performed using a Kaufman-type ion source of 3 cm diameter. The ion current density was measured using a Faraday cup. Samples were heated in vacuum up to ~573 K using a boron nitride heater and precleaned for 15 min using a 1 keV Ar^+ beam with a flux of 3.1 ions s^{-1} cm^{-2}. During the precleaning stage the sample temperature T measured by a thermocouple inserted through a hole in the side of the sample reached the steady state at ~673 K. The Ar^+ beam was then gradually changed to a pure N ion beam, resulting in ion beam nitriding for 40 min with 1 keV N ions at 3.1 ions s^{-1} cm^{-2}. The base pressure was 3–4 $\times 10^{-4}$ Pa, rising to 10^{-2} Pa during implantation.

In order to investigate the N diffusion under ion bombardment, after nitriding the samples were immediately (after ~1.5 min) irradiated by Ar^+ at a constant temperature of 673 K. The Ar^+ energy was fixed at 700 eV while the Ar^+ flux was different for each sample: 1.3×10^{15}, 2.5×10^{15}, and 3.8×10^{15} ions s^{-1} cm^{-2} (I_1–I_3, respectively). T decreased by ~20 K while switching the ion beam from N to Ar and reached a steady-state value of 673 K after ~4–5 min. The Ar^+ penetration depth calculated using SRIM 2003 [11] is ~1–2 nm. In view of significant Ar^+ induced sputtering, the ion fluence was held constant at 4.5×10^{18} ions cm^{-2} in order to produce the same amount of sputtered material for all samples. Thus the samples were bombarded during 60, 30, and 20 min for I_1–I_3, respectively. TRIDYN [12] simulations show that Ar^+ bombardment of N containing ASS produces a N depleted near-surface layer, while the sputtering yield of matrix atoms approaches that of the non-nitrided steel. Accordingly, a sputtered depth of ~0.55 μm was measured for the above fluence using surface profilometry on a non-nitrided sample.

X-ray diffraction revealed the modified layer structure to be composed of only "expanded" austenite in both as-nitrided and Ar^+ postirradiated samples, with no evidence of nitride formation. Quantitative N depth profiles were determined by nuclear reaction analysis (for details, see Ref. [10]). Figures 1(a)–1(d) show the N depth profiles without and with Ar^+ irradiation post-treatment. The N profile of the as-nitrided sample can be depicted by an initial quasilinear decrease changing to a sharp leading edge at a depth of ~1 μm. The N concentration at this point is ~15 at. %, which is equal to the Cr concentration taking into account the renormalization of the nominal ASS concentrations due to the N addition. The shape of the N depth profile is consistent with the trapping-

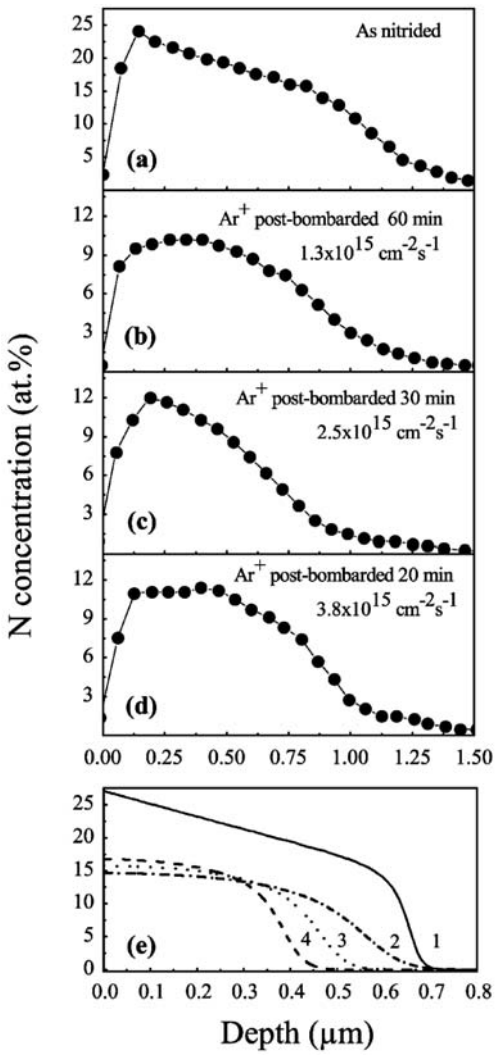

FIG. 1. Experimental (a)–(d) and calculated (e) (using the TD model) N depth profiles in ASS. Experimental profiles correspond to N depth distributions after ion beam nitriding (a) and postnitriding irradiation using an Ar^+ beam with ion fluxes 1.3×10^{15} (b), 2.5×10^{15} (c), and 3.8×10^{15} (d) ions $s^{-1}\,cm^{-2}$. Calculated profiles (e) correspond to N depth distributions after nitriding (curve 1) and subsequent N diffusion under simultaneous sputtering induced surface erosion for different diffusion constants equal to 6.0, 3.0, and 1.5×10^{-12} $cm^2\,s^{-1}$ (curves 2–4, respectively). The as-nitrided profile was calculated for $t = 30$ min assuming an N diffusion coefficient of $D = 3.0 \times 10^{-12}$ $cm^2\,s^{-1}$, a detrapping energy 0.35 eV, a sputtering induced surface recession velocity of $V_S = 1.7 \times 10^{-8}$ $cm\,s^{-1}$, and an incoming N flux of 4.84×10^{15} $cm^{-2}\,s^{-1}$ (according to the distribution of atomic and molecular ions in the beam). The Ar^+ post-treatment was simulated assuming $V_S = 4.4 \times 10^{-8}$ $cm\,s^{-1}$ and $t = 15$ min.

detrapping (TD) model [13], according to which the Cr atoms trap mobile N atoms by forming a chemical bond. This significantly slows down N diffusion in the regions where the N concentration is below the Cr concentration, resulting in the observed profile shape.

In the following, the depth profiles after Ar^+ postirradiation are understood in terms of a sputtering/diffusion balance, where sputtering reduces the integrated N content and the width of the profiles, whereas diffusion broadens the profiles and thereby results in an increased integral N amount. The N distribution profiles exhibit a plateau near the surface followed by a slow decrease in N concentration. The N plateau concentration is slightly dependent on Ar^+ flux and increases from ~10 to ~12 at. % when the Ar^+ flux increases from I_1 to I_3, respectively. Additionally, the N concentration falls below that of Cr, which indicates that N is mainly in the trapped state. It can be seen that after annealing with moderate Ar^+ bombardment, the profile shape changes from the concave characteristic for the leading edge of the as-nitrided sample to a convex characteristics of postnitriding annealed samples [10]. When the Ar^+ flux is doubled (diffusion time t is half), the N penetration depth decrease, which is consistent with conventional diffusion. However, when the Ar^+ flux is tripled in comparison to the lowest one (t is reduced by a factor of 3) the N penetration depth is again higher and similar to that obtained at the longest time, which clearly indicates an additional influence of ion flux on the N transport.

The profile shape after Ar^+ post-treatment is qualitatively consistent with the TD model, as demonstrated in Fig. 1(e) under the assumption of three different diffusion coefficients D (for details of the calculation, see Refs. [10,13]). It is confirmed that sputtering induces a significant N loss, while diffusion results in flattening and broadening of the depth profiles, with higher D yielding higher N penetration depths and lower N near-surface concentrations. Additional simulations show that doubling (or tripling) V_S and D while reducing t by a factor of 2 (or 3) results in identical N depth profiles. In comparison to the above, this indicates that the diffusivity increases by a factor of about 3 when the Ar^+ flux increases from I_1 to I_3 [see Figs. 1(b) and 1(d)]. Thus, although being unable to account for the underlying mechanisms, the TD model provides a quantitative estimate through the assumption of a diffusion coefficient which depends on the ion flux.

This is consistent with previous findings that the N diffusivity during ion nitriding of ASS increases with the N ion flux [7,10]. This also underlines that the observed phenomenon is related to ion irradiation but not to the irradiating species. Also, the observed increase of the nitriding depth with ion energy [7] indicates an irradiation-induced enhancement of diffusion. Further evidence of a yet unidentified transport mechanism has been established for ion nitriding of ASS single crystals, which showed a significant dependence of the nitriding depth on the crystalline orientation [6] (see also Ref. [3]), although the diffusion in a cubic material is expected to be isotropic.

Before tentatively proposing a mechanism of the observed effect, we wish to discuss other processes which would be consistent with present perception. Although unlikely, an influence of the Ar^+ ion flux on the sputtering has been ruled out by demonstrating that identical N depth

profiles are obtained at temperatures between 373 and 473 K at identical fluence but different fluxes. Vacancy or multivacancy mediated diffusion cannot explain the observations as N diffusion has been found to be faster than that of vacancylike defects during ion beam nitriding of ASS [14]. Furthermore, the dynamic vacancy concentration for the present experimental situation has been calculated using simple diffusion theory [15] with the vacancy diffusion constant given by Pokor *et al.* [16] and a vacancy source distribution obtained from SRIM 2003. Assuming a sink at the surface, an almost constant vacancy concentration profile is obtained at the above time of 30 min and the corresponding flux, with a relative concentration close to 10^{-3} which is much smaller than the N concentration. The diffusion of self-interstitials is much faster [16], resulting in an even much lower concentration. Furthermore, a significant self-diffusion would result in the precipitation of CrN [2], which is not observed. Thus, any influence of radiation-induced diffusion can be ruled out with a high level of confidence. Stress-mediated or concentration dependent [17] diffusion would be in contradiction with the similar N depth distributions obtained at different diffusion times for different N ion fluxes [10]. Any thermal acceleration of diffusion by the ion irradiation can also be excluded. An assumed temperature increase of 10 K, which is far above the precision of the experimental control, would increase the diffusion coefficient by a factor of 1.4, which is significantly below the variation shown in Fig. 1. Further, the calculation of the hemispherical thermal spike induced by each ion shows a dissipation to a transient heating of less than 1 mK already at a depth of 0.1 μm, so that any resulting effects can be excluded. Diffusion of lower dimensionality (grain boundaries, dislocations) does not explain the present results either because the N distribution and defect concentration after nitriding is similar for all samples. Thus, from conventional pictures no diffusion acceleration can be expected. Nevertheless, the process appears to be diffusionlike because of the good agreement between experimental and calculated N depth profiles [10,13].

It is well known that if the energy transferred from the ion/recoiled atom to the target atoms is not sufficient to create a Frenkel pair (~30 eV), this energy is dissipated into lattice vibrational excitations. If the transferred energy is of the order of thermal energies (~0.01 eV), the atomic displacement is in the range of linear restoring interatomic forces, and the energy will be dissipated at short distances. This type of lattice excitation cannot influence the atomic diffusion far beyond the ion penetration depth. When the transferred energy is in an intermediate region, atoms will experience large displacements from their equilibrium positions, while remaining at their original lattice sites. Propagation of the corresponding lattice vibrations may be governed by nonlinear forces. As described in the literature, this may result in the formation of a vibrational particlelike soliton which can propagate distances well beyond the dimensions of the collision cascade [18,19].

It was shown theoretically that the presence of the surrounding lattice prevents the propagation of Toda-like solitons [18] but allows breatherlike solitons [or so-called discrete breathers (DB)] to propagate along atomic chains [20]. According to molecular dynamic (MD) simulations, DBs are highly anharmonic longitudinal vibrations, being sharply localized on just a few sites in the longitudional direction and practically across one atomic distance in the transverse direction. Within this oscillation envelope the particles execute antiphase or optical type oscillations [20]. The highly localized excitations on the atomic scale were observed in a quasi-one-dimensional antiferromagnet [21] and atomic lattices [22,23]. Additionally, MD simulations show that giving an impulse, as when an atomic collision takes place, to just one atom is enough to create the moving DB [20]. Following this we speculate that DB's might be created by N or Ar ions during ion nitriding and in the present experiment, leave the collision cascade region, and move away from the surface and enhance diffusion at large depths. It has been shown that vacancy migration can be induced by a DB [24]. In analogy, we expect that a DB can also accelerate the diffusion of interstitial atoms, in particular, as the activation energy of interstitial migration is generally smaller than that of vacancy migration. Because of the high amplitude antiphase vibration, diffusional jumps of N atoms might be assisted by DB's in their close vicinity. In this picture, thermal vibrations and DB's would act synergistically. An independent athermal DB mechanism would result in a constant additional profile broadening at constant ion fluence, and, consequently, in a continuous decrease of the profile width at increasing flux which is in contrast to the findings of Fig. 1. Therefore, one might tentatively write the diffusion coefficient as

$$D = D_0 \exp\left(-\frac{E}{kT}\right)\exp\left(\frac{\alpha I}{kT}\right) = D_{\text{th}} \exp\left(\frac{\alpha I}{kT}\right), \quad (1)$$

with the conventional thermal diffusion coefficient D_{th} given by the preexponential factor D_0 and the activation energy E, and an enhancement term which depends exponentially on the ion flux I, α being a positive constant.

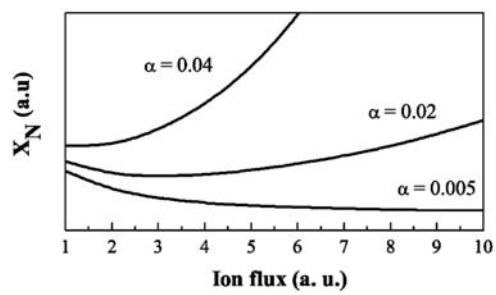

FIG. 2. N penetration depth $X_N \sim \sqrt{Dt}$ as a function of surface irradiating ion flux I for fixed ion fluence and different flux susceptibility factors α (see text). Diffusion preexponential factor D_0, thermal activation energy E, and T were 10^{-3} cm^2 s^{-1}, 1.1 eV, and 673 K, respectively.

Equation (1) can also be interpreted as an effective coefficient of thermal diffusion, the activation energy of which decreases linearly with the ion flux due to the lattice distortions induced by DB's. From Eq. (1), Fig. 2 presents the mean diffusional depth X_N as a function of I for fixed ion fluence (identical sputtered depth) and different α values, assuming the simplest model of "free" N diffusion (i.e., $X_N \sim \sqrt{Dt}$). Three regimes can be identified: (1) low α values—X_N decreases when I increases (ion enhancement is too small as to compensate for shorter diffusion times); (2) high α values—X_N increases when I increases (ion enhancement produces thicker layers despite lower t); (3) intermediate values—X_N decreases, reaching a minimum before increasing. According to this simplified picture, the above results should be related to the intermediate regime.

It can presently only be speculated which implantation conditions may favor the DB generation. They may result from knock-on events which generate recoils with a direction close to low-indexed crystallographic directions, and a transferred energy which is large compared to thermal energies but smaller than the lattice binding energy of a few eV. During the energy dissipation of the collision cascade, such collisions will occur more frequently as the nuclear stopping increases. For Ar^+ bombardment of ASS, nuclear stopping peaks at around 35 keV, so one may anticipate an increase of the effect at higher energies, in qualitative agreement with the increased nitriding depth at increased ion energy [7] as mentioned above. On the other hand, higher energies promote dynamic disorder in the cascade, which may impede the launching of DBs. These questions will be addressed in future experimental and MD computer simulation studies.

In summary, it was observed that low energy (700 eV) Ar^+ irradiation significantly increases the interstitial N mobility in ASS at depths well beyond the ion penetration depth. It manifests itself as the increased broadening of the N depth profile as a function of Ar^+ flux. The observed effect cannot be explained by any established mechanisms of radiation-enhanced diffusion. Therefore, a possible mechanism is proposed involving nonlinear vibrational excitations such as discrete breathers, which might explain the dependence of the diffusional depth on the ion flux and on the crystalline direction in cubic crystals, which were hitherto obscure. This mechanism may be more general and applicable to other processes involving atomic mobility in ion-irradiated materials. The degree to which these processes are influenced by ion bombardment may depend on the type and energy of impinging energetic particles, the composition and microstructure of irradiated material, and the stability of the quasiparticles.

We are grateful for financial support of the Saxonian government and Harbin Institute of Technology Internationalizing Foundation, China. In addition we would like to thank Professor Claude Templier and Professor Jean Paul Rivière from Laboratoire de Métallurgie Physique, Poitiers, France, for providing the austenitic stainless steel samples.

*Electronic address: g.abrasonis@fz-rossendorf.de

[1] P. Sigmund and N. Q. Lam, K. Dan. Vidensk. Selsk. Mat. Fys. Medd. **43**, 255 (1993), and references therein.
[2] D. L. Williamson, O. Ozturk, R. Wei, and P. J. Wilbur, Surf. Coat. Technol. **65**, 15 (1994).
[3] O. Öztürk and D. L. Williamson, J. Appl. Phys. **77**, 3839 (1995).
[4] S. Grigull and S. Parascandola, J. Appl. Phys. **88**, 6925 (2000).
[5] C. Blawert, H. Kalvelage, B. L. Mordike, G. A. Collins, K. T. Short, Y. Jirásková, and O. Schneeweiss, Surf. Coat. Technol. **136**, 181 (2001).
[6] G. Abrasonis, J. P. Rivière, C. Templier, A. Declémy, L. Pranevicius, and X. Milhet, J. Appl. Phys. **97**, 083531 (2005).
[7] D. L. Williamson, J. A. Davis, P. J. Wilbur, J. J. Vajo, R. Wei, and J. N. Matossian, Nucl. Instrum. Methods Phys. Res., Sect. B **127–128**, 930 (1997).
[8] C. Blawert, B. L. Mordike, G. A. Collins, K. T. Short, and J. Tendys, Surf. Coat. Technol. **103–104**, 240 (1998).
[9] N. Tsubouchi, Y. Mokuno, A. Chayahara, and Y. Horino, Surf. Coat. Technol. **196**, 271 (2005).
[10] G. Abrasonis, J. P. Rivière, C. Templier, L. Pranevičius, and N. P. Barradas, J. Appl. Phys. **97**, 124906 (2005).
[11] J. F. Ziegler and J. P. Biersack, Computer code SRIM 2003 program package, http://www.srim.org
[12] W. Möller, W. Eckstein, and J. P. Biersack, Comput. Phys. Commun. **51**, 355 (1988).
[13] S. Parascandola, W. Möller, and D. L. Williamson, Appl. Phys. Lett. **76**, 2194 (2000).
[14] W. Anwand, S. Parascandola, E. Richter, G. Brauer, P. G. Coleman, and W. Möller, Nucl. Instrum. Methods Phys. Res., Sect. B **136–138**, 768 (1998).
[15] J. Crank, *The Mathematics of Diffusion* (Clarendon, Oxford, 1985).
[16] C. Pokor, Y. Brechet, P. Dubuisson, J.-P. Massoud, and A. Barbu, J. Nucl. Mater. **326**, 19 (2004).
[17] S. Mändl and B. Rauschenbach, J. Appl. Phys. **91**, 9737 (2002).
[18] Y. V. Martynenko and P. G. Moscovkin, Radiat. Eff. Defects Solids **117**, 321 (1991).
[19] F. M. Russell and D. R. Collins, Nucl. Instrum. Methods Phys. Res., Sect. B **105**, 30 (1995).
[20] J. L. Marín, J. C. Eilbeck, and F. M. Russell, in *Nonlinear Science at the Dawn of the 21st Century*, edited by P. L. Christiansen, M. P. Sorensen, and A. C. Scott (Springer, Berlin, 2000), p. 293.
[21] M. Sato and A. J. Sievers, Nature (London) **432**, 486 (2004).
[22] B. I. Swanson, J. A. Brozik, S. P. Love, G. F. Strouse, A. P. Shreve, A. R. Bishop, W.-Z. Wang, and M. I. Salkola, Phys. Rev. Lett. **82**, 3288 (1999).
[23] T. Markovich, E. Polturak, J. Bossy, and E. Farhi, Phys. Rev. Lett. **88**, 195301 (2002).
[24] J. Cuevas, C. Katerji, J. F. R. Archilla, J. C. Eilbeck, and F. M. Russell, Phys. Lett. A **315**, 364 (2003).

APPLIED PHYSICS LETTERS **89**, 074101 (2006)

Phase stability of epitaxially grown Ti_2AlN thin films

M. Beckers,[a] N. Schell, R. M. S. Martins, A. Mücklich, and W. Möller
Institute of Ion Beam Physics and Materials Research, Forschungszentrum Rossendorf, P.O. Box 510119, 01314 Dresden, Germany

(Received 6 April 2006; accepted 26 June 2006; published online 14 August 2006)

The phase stability of $M_{n+1}AX_n$ phase (M: early transition metal, A: A-group element, and X: C and/or N) Ti_2AlN thin films reactively sputtered onto MgO(111) and Al_2O_3(0001) substrates has been investigated by *in situ* x-ray diffraction and Rutherford backscattering. High substrate temperature deposition results in epitaxial Ti_2AlN growth with basal planes parallel to the substrate surface. In contrast to reported high thermal stability for bulk Ti–Al–N $M_{n+1}AX_n$ phases in air, Ti_2AlN thin films in vacuum decompose already at ~800 °C. The decomposition proceeds by outward Al diffusion and evaporation, followed by detwinning of the as-formed Ti_2N atomic layers into cubic TiN_x and intermediate phases. © *2006 American Institute of Physics*.
[DOI: 10.1063/1.2335681]

The $M_{n+1}AX_n$ ($n=1-3$) phases are a family of nanolaminated compounds, where M is a transition metal, A an A-group element, and X is nitrogen or carbon.[1] Their hexagonal crystal structure is constructed by repeatedly twinned Ti_nN_{n-1} slabs, interleaved by A-group element layers. For the Ti–Al–N system, Ti_2AlN and Ti_4AlN_3 have been reported.[2,3] Here, the Ti_2N slabs are isostructural with the rocksalt structure of TiN. Since the $M-X$ bonds are of strong covalent-ionic nature, bulk $M_{n+1}AX_n$ phases exhibit typical ceramic properties such as high melting points and good thermal stabilities.[4] On the other hand, the $M-A$ bonds are of metallic weak nature. Therefore, $M_{n+1}AX_n$ phases also exhibit metallic properties such as good electrical and thermal conductivity.[5] Under mechanical force effect, they deform by kink band formation yielding high ductility and machinability. Due to this unique combination of properties, potential applications for $M_{n+1}AX_n$ phases are numerous. $M_{n+1}AX_n$ thin film synthesis has earliest been reported in the Ti–Si–C system using dc magnetron sputtering by Seppänen *et al.* and Palmquist *et al.*[6,7] Results on deposition of other Ti–A–C phase thin films followed.[8,9] Nitride $M_{n+1}AN_n$ phases are more difficult to obtain by sputter deposition, since the nitrogen has to be introduced via the gas phase within a narrow process window. Hence, only recently the deposition of Ti_2AlN thin films by reactive sputtering was demonstrated, using either a compound 2Ti:Al target or elemental Ti and Al targets in a dual magnetron reactive process.[10,11]

In the present study, we used two 1 in. diameter Ti and Al magnetrons to grow Ti_2AlN onto polished MgO(111) and Al_2O_3(0001) substrates of $10\times10\times0.5$ mm^3 size, which were thermally cleaned at ~675 °C for 1 h prior to deposition. The temperature was measured by a K-type thermocouple clamped onto the substrate surface and confirmed by pyrometry above 400 °C within ±25 °C, which is regarded as the experimental error of the temperature measurement. The base pressure at the deposition temperature of 675 °C was $\sim8\times10^{-5}$ Pa. An initial cubic $(Ti_{0.63}Al_{0.37})N$ seed layer was deposited at 0.35 Pa, with Ar and N_2 flow rates of 2.76 and 1.38 SCCM (SCCM denotes cubic centimeter per minute at STP), and Ti and Al magnetron powers set to 60 and 20 W, respectively.[12] For subsequent Ti_2AlN growth, the pressure was increased to 0.8 Pa at Ar and N_2 flow rates of 7.94 and 0.48 SCCM and the Ti and Al magnetron powers changed to 80 and 26 W, respectively, as established in previous work.[11] The entire deposition chamber is mounted into the goniometer of the ROBL beamline (BM20) at the European Synchrotron Radiation Facility (ESRF) and equipped with beryllium x-ray windows.[13] This setup was employed for *in situ* x-ray diffraction during growth and postdeposition annealing using monochromatic synchrotron radiation set to 0.961 Å. The film composition as well as diffusion profiles after annealing were obtained by *ex situ* Rutherford backscattering spectroscopy (RBS) using a 1.7 MeV He^+ beam.

Figure 1 shows *in situ* large angle x-ray diffraction (XRD) data taken in Bragg-Brentano geometry after deposition of Ti_2AlN at 675 °C onto MgO(111) and Al_2O_3(0001), recorded as offset coupled scans locked to Ti_2AlN(0002). $(Ti_{1-x}Al_x)N$ and MgO exhibit perfect cube-on-cube epitaxial relationship, hence the seed layer $(Ti_{0.63}Al_{0.37})N(111)$ peak overlaps with the substrate. For Al_2O_3, this peak is detectable, with distinct Laue oscillations indicating very smooth epitaxial $(Ti_{0.63}Al_{0.37})N$ growth up to its final thickness of ~80 Å as derived from x-ray reflectometry. The asymmetric intensity distribution can be attributed to small residual compressive stress. After a subsequent deposition of 500 Å Ti_2AlN these oscillations diminish, indicating interfacial reactions between Ti_2AlN and $(Ti_{0.63}Al_{0.37})N$ as recently reported.[11] For both substrate materials, predominantly $Ti_2AlN(000\ell)$ plane peaks were observed, as expected from the typical parallel basal plane epitaxial $M_{n+1}AX_n$ phase growth at high temperatures.[6–10]

Figure 2 shows *in situ* XRD data of the Ti_2AlN films taken directly after deposition and after annealing at 800 °C. Here, minor traces of $Ti_2AlN(10\bar{1}4)$ are discernible, since the scans were done offset locked to this peak. Time-dependent data in a narrower angular range were acquired for intermediate temperatures, with approximately 5 min scanning time for each temperature. For the MgO(111) substrate, as displayed in Fig. 2(a), the offset coupled scans locked to $Ti_2AlN(10\bar{1}4)$ reveal a Ti_2AlN decomposition starting at around 750 °C, while 1 h annealing at 800 °C

[a]Present address: Thin Film Division of Physics Department (IFM), Linköping University, 58183 Linköping, Sweden; FAX: +46(13)13-75-68; electronic mail: manbe@ifm.liu.se

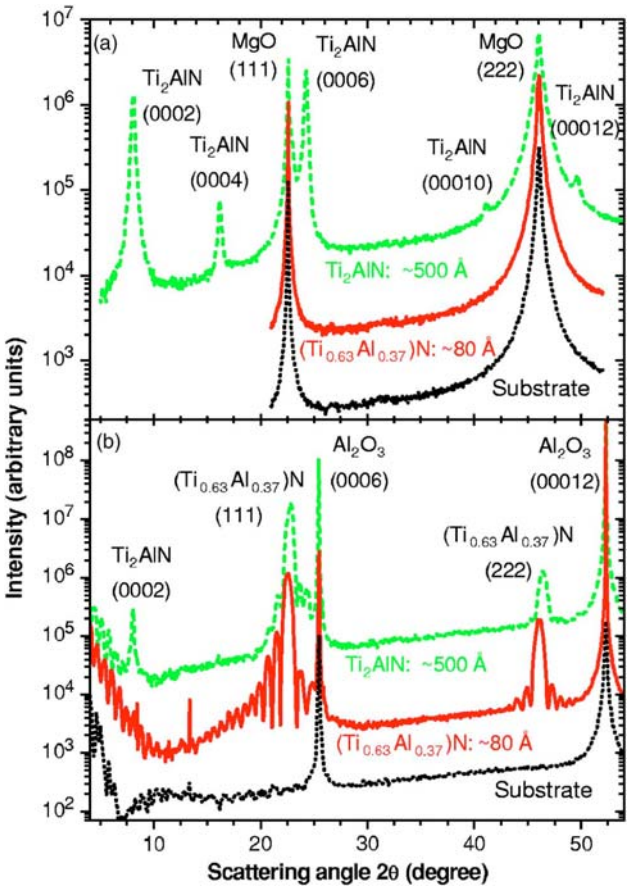

FIG. 1. (Color online) *In situ* XRD patterns recorded after deposition of an 80 Å $(Ti_{0.63}Al_{0.37})N$ seed layer and a subsequent 500 Å thick Ti_2AlN layer at a sample surface temperature of approximately 675 °C, (a) on a MgO(111) substrate and (b) on an $Al_2O_3(0001)$ substrate.

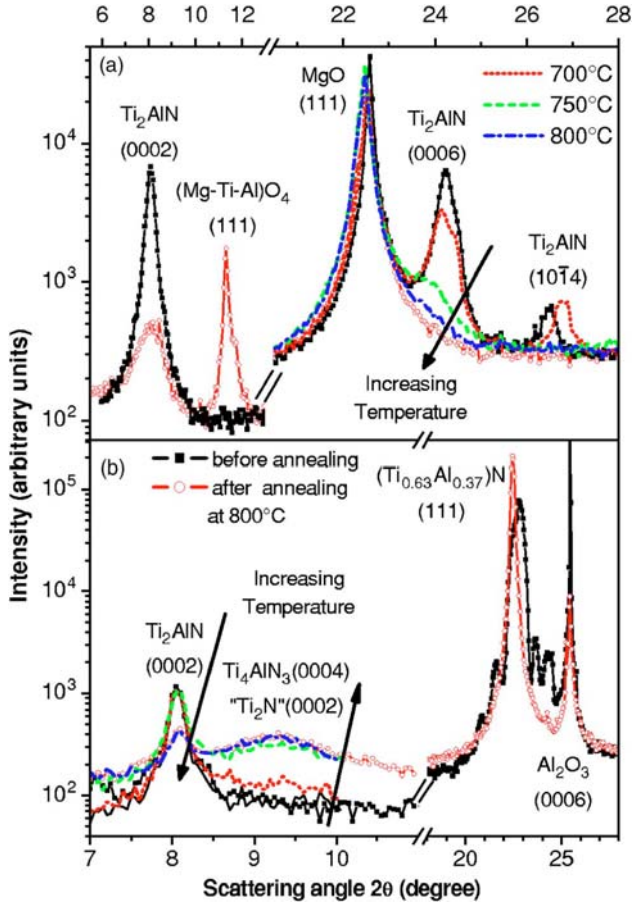

FIG. 2. (Color online) *In situ* XRD patterns recorded during annealing of a 500 Å Ti_2AlN film deposited onto MgO(111) (a) and $Al_2O_3(0001)$ (b). Data were taken after deposition at 675 °C (■) and after annealing at 800 °C for about 1 h (○). Additionally, intermediate time-dependent data were recorded in a reduced angular range (lines) with rising temperature indicated by the arrows.

results in an almost complete decomposition of Ti_2AlN. This is depicted by a factor of 20 intensity loss of $Ti_2AlN(0002)$ and the drowning of the $Ti_2AlN(0006)$ signal in the background. Concurrently, a peak with $d=4.80$ Å lattice spacing arises, which can be attributed to $(Mg-Al-Ti)O_4(111)$, assuming a ternary $(Mg-Al-Ti)O_4$ spinel formation by topotaxial solid-state reaction.[14] The corresponding lattice constant of $a_0=8.31$ Å is close to the literature value of Mg_2TiO_4 ($a_0=8.474$ Å).[14] Figure 3(a) shows the corresponding RBS spectrum of the annealed film. The Al concentration lies considerably below 25%, and the poor single layer fit quality shows that Ti and Al inward as well as Mg outward diffusion have to be considered. Hence, MgO(111) interfacial spinel formation according to

$$4MgO + Ti \rightarrow Mg_2TiO_4 + 2Mg$$

and

$$4MgO + 2Al \rightarrow MgAl_2O_4 + 3Mg \quad (1)$$

takes place. The XRD data of Fig. 2(b) indicate different behaviors for Ti_2AlN deposited onto the Al_2O_3 substrate. After annealing, the Laue oscillations around $(Ti_{0.63}Al_{0.37})N(111)$ vanish completely, again indicating pitting by the Ti_2AlN phase. Simultaneously, the peak shifts to lower angles, i.e., larger lattice constants, and increases in intensity by a factor of 3. Concurrent with the $Ti_2AlN(0002)$ decay, the growth of a nanogranular material is indicated by a broad peak with a lattice spacing around $d=5.93$ Å. The corresponding RBS spectrum is shown in Fig. 3(b). It should be noted that an 800 Å top layer with composition $Ti_{0.51}Al_{0.12}N_{0.37}$ deposited *after* the annealing is included in the spectrum, but of no significance for the present discussion. Assuming bulk Ti_2AlN atomic density, an almost complete depletion of Al for the initial 500 Å thick Ti_2AlN layer is deduced. Since Al inward diffusion in view of the low Al solubility in Al_2O_3 (Ref. 15) is very improbable, we conclude on outward diffusion of the weakly bonded Al out of the Ti_2AlN film with subsequent evaporation according to

$$Ti_2AlN \rightarrow Ti_2N + Al\uparrow. \quad (2)$$

The assumption of Al evaporation is corroborated by a bulk Al vapor pressure of 2.7×10^{-4} Pa at 800 °C, exceeding the base pressure during annealing and likely to occur also for the MgO substrate, concurrent to the spinel formation. A successive detwinning of the as-formed remaining Ti_2N slabs leads to substoichiometric cubic TiN_x,[1] explaining both the increased intensity as well as the shift of the initial seed layer $(Ti_{0.63}Al_{0.37})N(111)$ XRD peak, as seen in Fig. 2(b). An intermediate state consisting of a superstructure built by repeatedly twinned Ti_2N slabs with a shrunk unit cell compared to stoichiometric Ti_2AlN should give rise to a peak at higher scattering angles, in consistence with the peak ob-

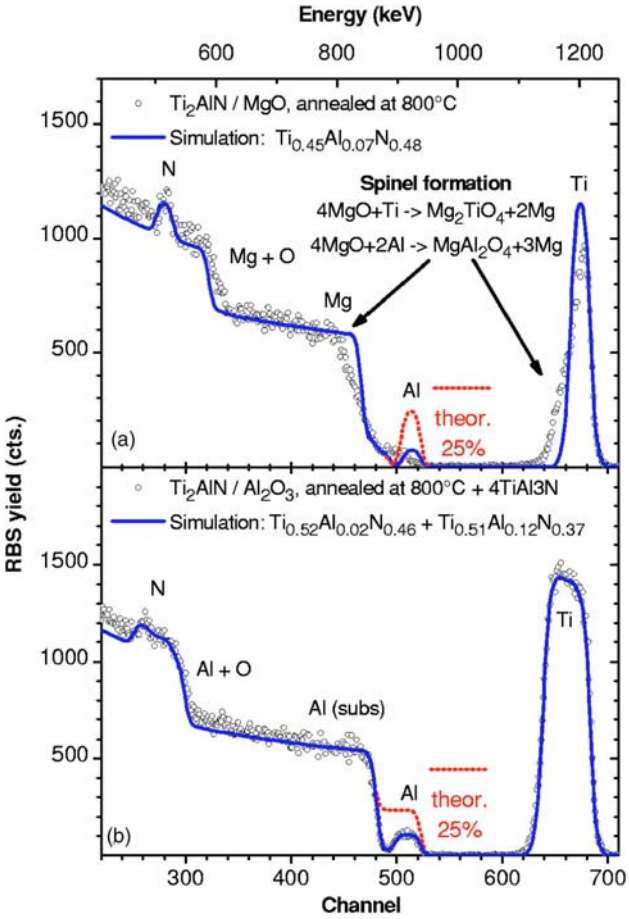

FIG. 3. (Color online) *Ex situ* RBS spectra obtained after annealing. The dashed line indicates the expected Al signal for stoichiometric Ti_2AlN. (a) Ti_2AlN deposited onto MgO(111). The arrows indicate signatures of outward Mg and inward Ti diffusions. (b) Ti_2AlN deposited onto Al_2O_3. The top layer with stoichiometry $Ti_{0.51}Al_{0.12}N_{0.37}$ stems from an additionally deposited layer deposited *after* annealing.

served in Fig. 2(b). Additionally, a fractional loss of every second Al layer according to

$$2Ti_2AlN \rightarrow Ti_4AlN_2 + Al\uparrow \quad (3)$$

with subsequent detwinning, instead would lead to the formation of a vacancy-afflicted Ti_4AlN_3 $M_{n+1}AX_n$ phase with an accompanying observation of the $Ti_4AlN_3(0004)$ peak. However, the large width of the peak indicates the small vertical domain size of both structures proposed above.

In seemingly striking contrast to the present results, bulk T–Al–N $M_{n+1}AX_n$ phases are stable up to 1500 °C in Ar.[16] Recent results on thin film Ti_3SiC_2 in vacuum also showed decomposition at lower temperature values compared to bulk.[17] This can be attributed to the average diffusion distances to the surfaces and, hence, also the characteristic times of outdiffusion being orders of magnitude larger for bulk material. In addition, *A* element atoms would accumulate at grain boundaries, hence for annealing in Ar or air, without the possibility of evaporation, local concentration gradients and thereby diffusion fluxes would be strongly reduced.

In summary, a small temperature rise of only ~125 °C above deposition temperature induces decomposition of epitaxially grown Ti_2AlN thin films by Al depletion. Depending on the reactivity of the surroundings, Al diffusion may result in compound formation through interface reactions and/or evaporation into the vacuum. The decomposition temperature is far below that reported for bulk material. Future studies involving diffusion barrier concepts will be directed towards the suppression of the decomposition which might be essential for potential applications of $M_{n+1}AX_n$ phase thin films.

The authors gratefully acknowledge financial support by the Deutsche Forschungsgemeinschaft under Contract No. SCHE 682.

[1] M. W. Barsoum, Prog. Solid State Chem. **28**, 201 (2000).
[2] W. Jeitschko, H. Novotny, and F. Benesovsky, Monatsch. Chem. **94**, 1198 (1963).
[3] J. C. Schuster and J. Bauer, J. Solid State Chem. **53**, 260 (1984).
[4] F. Adibi, I. Petrov, L. Hultman, U. Wahlström, T. Shimizu, D. McIntyre, and J. E. Greene, J. Appl. Phys. **69**, 6437 (1991).
[5] M. W. Barsoum, H.-I. Yoo, I. K. Polushina, V. Yu. Rud, and T. El-Raghy, Phys. Rev. B **62**, 10194 (2000).
[6] T. Seppänen, J.-P. Palmquist, P. O. Å. Persson, J. Emmerlich, J. Molina, J. Birch, U. Jansson, P. Isberg, and L. Hultman, in *Proceedings of the 53rd Annual Meeting of the Scandinavian Society for Electron Microscopy, Tampere, Finland, 12–15 June 2002*, edited by J. Keränen and K. Sillanpää (University of Tampere Press, Finland, 2002), pp. 142–143.
[7] J.-P. Palmquist, U. Jansson, T. Seppänen, P. O. Å. Persson, L. Hultman, and P. Isberg, Appl. Phys. Lett. **81**, 835 (2002).
[8] O. Wilhelmsson, J.-P. Palmquist, T. Nyberg, and U. Jansson, Appl. Phys. Lett. **85**, 1066 (2004).
[9] H. Högberg, P. Eklund, J. Emmerlich, J. Birch, and L. Hultman, J. Mater. Res. **20**, 779 (2005).
[10] T. Joelsson, A. Hörling, J. Birch, and L. Hultman, Appl. Phys. Lett. **86**, 111913 (2005).
[11] M. Beckers, N. Schell, R. M. S. Martins, A. Mücklich, W. Möller, and L. Hultman, J. Appl. Phys. **99**, 34902 (2006).
[12] M. Beckers, N. Schell, R. M. S. Martins, A. Mücklich, and W. Möller, J. Vac. Sci. Technol. A **23**, 1384 (2005).
[13] W. Matz, N. Schell, W. Neumann, J. Bøttiger, and J. Chevallier, Rev. Sci. Instrum. **72**, 3344 (2001).
[14] L. Hultman, D. Hesse, and W.-A. Chiou, J. Mater. Res. **6**, 1744 (1991).
[15] H. A. Wreidt, *Binary Alloy Phase Diagrams*, 1st ed., edited by T. B. Massalski (ASM International, Metals Park, Ohio, 1986), Vol. 1, pp. 143–145.
[16] A. T. Procopio, M. W. Barsoum, and T. El-Raghy, Metall. Mater. Trans. A **31A**, 333 (2000).
[17] J. Emmerlich, H. Högberg, P. Eklund, L. Hultman, O. Wilhelmson, and U. Jansson, presented at the International Conference on Metallurgical Coatings and Thin Films, San Diego, 2005 (unpublished).

APPLIED PHYSICS LETTERS **89**, 061908 (2006)

Annealing of indium tin oxide films by electric current: Properties and structure evolution

A. Rogozin,[a] N. Shevchenko, M. Vinnichenko,[b] M. Seidel, A. Kolitsch, and W. Möller
Institute of Ion Beam Physics and Materials Research, Forschungszentrum Rossendorf, P.O. Box 510119, 01314 Dresden, Germany

(Received 26 January 2006; accepted 26 June 2006; published online 8 August 2006)

A method of annealing thin films of indium tin oxide in vacuum is proposed using a direct electric current flow through the film. During annealing at a constant electric power, the film resistance, free electron density, and structure evolution were monitored in situ. In comparison with the conventional isothermal annealing, the current annealing is more efficient providing a noticeable reduction in the thermal budget and a decrease in the kinetic exponent of crystallization. Electrical inhomogeneities in the film, which produce locally overheated regions, are discussed as a possible reason for the acceleration of the crystallization process. © *2006 American Institute of Physics*. [DOI: 10.1063/1.2335808]

Thin films of indium tin oxide are widely used in optoelectronic devices due to their transparency in the visible range and low electrical resistivity. The desired properties of films being produced by reactive magnetron sputtering can be achieved by either deposition at elevated substrate temperature[1] or postdeposition annealing of films grown at room temperature (RT).[2,3] Technological applications of indium tin oxide (ITO) often require patterning of the film.[4] For this purpose, postdeposition annealing is preferable because deposition at RT usually results in an amorphous film, which has a considerably higher etching rate compared with crystalline material.[5] Local ordering of the amorphous phase at the beginning of annealing, and subsequent film crystallization are known to result in a decrease of the resistance.[6] Oxygen vacancy generation and tin donor activation are believed to increase the carrier concentration during these processes.[6,7]

Traditionally, thermal heating has only been used for the annealing of transparent conductive oxides (TCO's). As an alternative, treatment by electric current is a relatively well studied process for amorphous metallic alloys[8,9] but has never been experimentally applied to TCO thin films. This method offers a number of technical advantages: (i) no external heater is required and (ii) the Joule heat is released directly in the film, which reduces both the heat load to the surrounding components and the generation of impurities. Therefore, the aim of this letter is to study the annealing of thin ITO films by passing an electric current flow through them.

The films were deposited by reactive middle frequency pulsed magnetron sputtering at a base pressure of 8.6×10^{-4} Pa and process partial pressures of 1.2 and 3×10^{-1} Pa for Ar and O_2, respectively. Two 2 in. magnetrons equipped with high purity (99.99%) In 90%–Sn 10% alloy targets were operated in parallel as described elsewhere.[10] (100)-oriented Si samples ($24 \times 12.5 \times 0.3$ mm^3) having a 1 μm thermal SiO_2 film were used in the experiments. Two aluminum electrodes (12×2 mm^2 and 1 μm thick) were deposited in the form of stripes along the sample edges on top of the SiO_2 layer. During ITO growth, a 12×1.5 mm^2 area of each stripe was shielded from the deposition flow so that the open parts could form electrical contacts with the film. The thickness of the deposited ITO films, as determined by spectroscopic ellipsometry (SE), was in the range of 170–180 nm. As-deposited films were amorphous, as confirmed by x-ray diffraction (XRD) and cross sectional transmission electron microscopy (XTEM).

The sample to be annealed was placed on a ceramic frame and two elastic cylindrical electrodes (1.5 mm in diameter) made of thin (0.05 mm) stainless steel foil were pressed on the uncovered area of the aluminum electrodes so that only the ends of the sample were in thermal contact with the holder. Since the annealing may strongly decrease film resistivity, a special dc power supply was designed to provide constant electric power at variable film resistance. The power was raised from zero to the predetermined constant level within 1 s after the start of annealing. The value of the power and the potential drop measured on the sample was used to determine the real-time behavior of the film resistivity with known film dimensions. During annealing the residual gas pressure was 1×10^{-4} Pa. The temperature was measured with a miniature (0.2 mm in diameter) *K*-type thermocouple and, therefore, the heat conducted away through it was negligibly small compared with the electric power dissipated within the film. Since the sample by its opposite ends was in thermal contact with the ceramic sample holder, one would expect the temperature maximum to occur in the middle of the sample. Accordingly, it was this part of the sample where local measurements of the structure and temperature were performed, thus ruling out the influence of any temperature gradients. The thermocouple was in thermal contact with the sample back being firmly attached to the latter by means of a heat conductive paste. Under this mounting configuration, the temperature difference between the film that was heated by the electric current, and the back of the 0.3 mm thick Si substrate could not exceed a fraction of a degree. Estimates show that the characteristic time taken for heat to diffuse from the front to the back surface of a sample until thermal equilibrium is established is on the or-

[a]Anthor to whom correspondence should be addressed; electronic mail: a.rogozin@fz-rossendorf.de
[b]On leave from Physics Department, Kyiv National Taras Shevchenko University, Kyiv 01033, Ukraine.

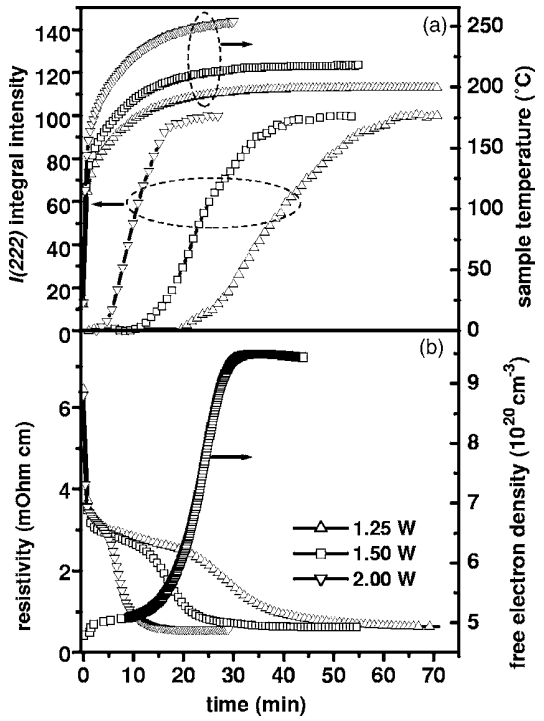

FIG. 1. Evolution of the film properties during annealing by direct electric current at different constant heating powers: (a) film temperature and normalized XRD peak integral intensity; (b) film resistivity and free electron density (the latter at 1.5 W only).

der of 10^{-4} s, whereas the crystallization process lasts for a few up to tens of minutes depending on the power released by the current in the film. Thus, the film temperature and resistivity could be determined simultaneously with a time resolution of 10 s. For comparison, a set of samples was isothermally annealed using a boralectric heater to compare the kinetics of the amorphous-to-crystalline transformation processes.

During isothermal annealing, the sample back was first covered with a heat conductive paste and then firmly pressed onto a ceramic plate, which in turn was placed on a boralectric heater. The thermocouple was inserted through a narrow (1 mm) slit in the ceramic plate and was in proper thermal contact (again using a heat conductive paste) with the middle part of the sample's back surface.

In this case, the film resistivity was measured *in situ* by a four point probe technique. In a separate experiment, a spectroscopic rotating compensator ellipsometer (M-2000, J.A. Woollam Co., Inc.) was used for monitoring *in situ* the ellipsometric film parameters.[10] The data were evaluated using a model[11] which allows for variation of the optical constants with depth. The free electron density, N_{Dr}, was obtained using the Drude-Lorentz parametrization of the film optical constants. Further annealing studies were performed using an *in situ* x-ray diffractometer[12] at the European Synchrotron Radiation Facility. The evolution of the film structure was investigated in real time by XRD in Bragg-Brentano geometry using a multichannel position sensitive detector. Due to the high intensity of the x-ray beam produced by the synchrotron, the acquisition time for a single scan did not exceed 1 min. The integral intensity of the In_2O_3 (222) peak, $I_{(222)}$, was used for further analysis. Denoting the integrated intensity at complete crystallization by $I_{C(222)}$, the time dependence of the normalized intensity, $I_{(222)}/I_{C(222)}$ was taken as a measure of the degree of crystallization, f. This was analyzed using the Kolmogorov-Johnson-Mehl-Avrami equation,[13] $f=1-\exp(Kt^n)$, where K is a temperature dependent constant related to the nucleation and growth rates of the crystalline phase and n is the kinetic exponent.

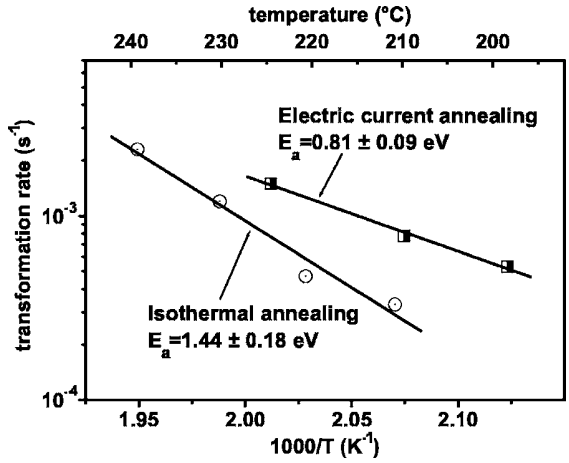

FIG. 2. Arrhenius plots of the amorphous-to-crystalline transformation rate for isothermal and electric current annealing, together with linear fits yielding the corresponding energies of activation, E_a.

The time dependences of the sample temperature, film resistivity, and normalized integral intensity for different values of the annealing power and free electron density for a power of 1.5 W are shown in Fig. 1. After an initial rapid ramp-up, the sample temperature reaches saturation as a result of thermal equilibrium being established between the sample and the holder. The resistivity decreases in two stages. During the first stage the sample remains amorphous as can be inferred from the comparison of Figs. 1(a) and 1(b). The outset of the second stage coincides with the outset of film crystallization for different electric powers. The final resistivity remains approximately the same irrespective of the power. Increasing the power leads to an increase in the sample temperature, accelerates the outset of film crystallization, and reduces the total time of the amorphous-to-crystalline transition. The time dependence of the normalized integral intensity exhibits an s-like shape, which is typical of the crystallization process.

During the first stage, the film resistivity drops significantly, while spectroscopic ellipsometry shows only a slight increase in the free electron density. This may be explained by an increase in the free electron mobility as a result of amorphous film relaxation. After the crystallization outset, which coincides with the beginning of the second stage of resistivity decrease, N_{Dr} grows much faster. However, even in this case the resistivity decreases faster (by a factor of 4.8) than N_{Dr} increases (by a factor of 2). Therefore, one may assume that the free electron mobility is increased by a factor of about 2.4 due to crystallization.

Conventional thermal annealing also reveals a two-stage behavior. However, at a similar film temperature the crystallization starts later and progresses slower than for electric current annealing. In the latter case, the same rate of crystallization is obtained at a lower sample temperature. Figure 2 shows Arrhenius plots of the amorphous-to-crystalline transition rate for both annealing modes. The deduced activation energy of crystallization during isothermal annealing

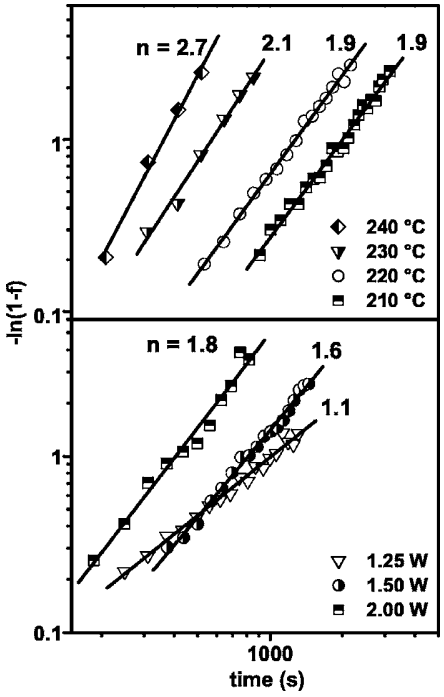

FIG. 3. Kolmogorov-Johnson-Mehl-Avrami plots of the degree of crystallization, f, vs annealing time: (a) during isothermal annealing at different temperatures and (b) annealing by electric current at different electric powers. The linear fits result in the indicated kinetic exponents, n.

amounts to 1.44 ± 0.18 eV, which agrees within the accuracy limits with the value of 1.3 ± 0.2 eV reported by Paine *et al.*[6] In the case of annealing by electric current, the activation energy is significantly reduced being 0.81 ± 0.09 eV.

Since any ballistic atomic transport due to the electron flow can be ruled out given the low electric fields being involved, an explanation of the observed phenomenon is not readily available. However, we speculate that it is associated with inhomogeneous physical properties across the film depth. In spite of the fact that the initial film is amorphous, XTEM results show that the morphology varies with film thickness. A thin ($\sim$20–25 nm) homogeneous zone at the film-substrate interface turns gradually into a pronounced columnar structure with sharp intercolumnar boundaries through the film, which is typical of reactive magnetron deposition.[10,14] Complementary analyses by elastic recoil detection reveal that the films also exhibit a thickness-dependent stoichiometry with the oxygen content decreasing from 5.4×10^{22} cm^{-3} at the substrate region to 4.2×10^{22} cm^{-3} at the film surface. Additionally, SE data show a noticeable increase in the film refractive index from 1.88 at the ITO/substrate interface to 2.04 at the film surface.[15] Consequently, it may be assumed that the electrical resistivity is also graded across the film thickness. Then, the region of the film with the lowest resistivity may be selectively overheated so that the crystallization may start there and proceed toward the still colder regions of the film. The crystallization is accompanied by Sn donor activation[7,16] which would further promote the local overheating. Thus, compared with the thermal annealing, the outset of crystallization may occur at a lower average temperature of the film bringing about an effectively lower activation energy, as shown in Fig. 2.

Figure 3 shows selected crystallization data sets plotted on a log-log scale according to the Kolmogorov-Johnson-Mehl-Avrami equation (see above), with corresponding linear fit functions $-\ln(1-f)$ versus time. For isothermal annealing at different temperatures ranging from 210 to 240 °C, a kinetic exponent $1.9<n<2.7$ is obtained. In contrast, the exponent is in the range of $1.1<n<1.8$ for annealing by electric current at heating powers between 1.25 and 2 W. The kinetic exponent n is indicative of the mechanisms of the amorphous-to-crystalline transition and/or its dimensionality.[13] Two well-defined modes of the crystallization process are described in the literature: (i) site saturated mode when all nuclei are present and begin to grow with the outset of transition and (ii) continuous nucleation when new nuclei appear during transition. The range of n obtained from thermal annealing points toward two-dimensional growth in the site saturated mode.[13] Assuming the same growth mode also for electric current annealing, the lowered kinetic exponent suggests a reduced dimensionality.

In summary, an annealing method using direct electric current at constant power has been developed for the purpose of increasing the conductivity of ITO films. Similarly to the case of thermal annealing, a two-stage decrease in the film resistivity is observed, with the crystallization starting at a significantly lower temperature and proceeding at a faster rate. As an explanation, electrical inhomogeneity of the films is believed to result in a locally overheated depth region. Due to the lowered activation energy, annealing by electric current is expected to be advantageous, in particular, for ITO films grown on thermally sensitive substrates such as polymers.

The authors acknowledge B. Schmidt, U. Strauch, V. Cantelli, A. Mücklich, U. Kreissig, and R. Yankov for invaluable assistance.

[1] R. B. H. Tahar, T. Ban, Y. Ohya, and Y. Takahashi, J. Appl. Phys. **83**, 2631 (1998).
[2] A. J. Steckl and G. Mohammed, J. Appl. Phys. **51**, 3890 (1980).
[3] S. Chaudhuri, J. Bhattacharya, and A. K. Pal, Thin Solid Films **148**, 279 (1987).
[4] B. G. Lewis and D. C. Paine, MRS Bull. **25**, 22 (2000).
[5] M. Ando, E. Nishimura, K. Onisawa, and T. Minemura, J. Appl. Phys. **93**, 1032 (2003).
[6] D. C. Paine, T. Whitson, D. Janiac, R. Beresford, C. Ow Yang, and B. Lewis, J. Appl. Phys. **85**, 8445 (1999).
[7] G. Frank and H. Köstlin, Appl. Phys. A: Solids Surf. **27**, 197 (1982).
[8] H. Mizubayashi and S. Okuda, Phys. Rev. B **40**, 8057 (1989).
[9] P. Allia, M. Barrico, P. Tiberto, and F. Vinai, Phys. Rev. B **47**, 3118 (1993).
[10] A. I. Rogozin, M. V. Vinnichenko, A. Kolitsch, and W. Möller, J. Vac. Sci. Technol. A **22**, 349 (2004).
[11] A. Rogozin, N. Shevchenko, M. Vinnichenko, F. Prokert, V. Cantelli, A. Kolitsch, and W. Möller, Appl. Phys. Lett. **85**, 212 (2004).
[12] W. Matz, N. Schell, G. Bernhard, R. Schlenk, D. Pröhl, H. Funke, M. Betzl, V. Brendler, J. Claußner, S. Dienel, F. Eichhorn, G. Hüttig, H. Krug, W. Neumann, H. Nitsche, W. Oehme, F. Prokert, T. Reich, P. Reichel, U. Strauch, and M. A. Denecke, J. Synchrotron Radiat. **6**, 1076 (1999).
[13] A. E. Kolmogorov, Izv. Akad. Nauk SSSR, Ser. Fiz. **1**, 355 (1937); W. Johnson and R. Mehl, Trans. Am. Inst. Min., Metall. Pet. Eng. **135**, 416 (1939); M. Avrami, J. Chem. Phys. **7**, 103 (1939).
[14] I. Petrov, P. B. Barna, L. Hultman, and J. E. Greene, J. Vac. Sci. Technol. A **21**, 1 (2003).
[15] A. Rogozin, M. Vinnichenko, N. Shevchenko, A. Kolitsch, and W. Möller, Thin Solid Films **496**, 197 (2006).
[16] J. R. Bellingham, W. A. Phillips, and C. J. Adkins, J. Phys.: Condens. Matter **2**, 6207 (1990).

APPLIED PHYSICS LETTERS **88**, 213115 (2006)

Real time spectroscopic ellipsometry of nanoparticle growth

T. W. H. Oates[a)]
Forschungszentrum Rossendorf, Institute of Ion Beam Physics and Materials Research, P.O. Box 510119, Dresden D-01314, Germany

(Received 15 February 2006; accepted 11 April 2006; published online 25 May 2006)

The use of real time spectroscopic ellipsometry to study silver nanoparticle formation in a polystyrene matrix by temperature induced reduction of silver hexafluoroacetylacetonate is reported. The optical properties of the composite are modeled using Mie theory with a modified electron relaxation frequency in silver to account for particle size effects. By measuring the final particle sizes from electron microscopy, the size of the particles during growth can be inferred above a radius of 2.3 nm. Below this radius the model is limited by quantum effects. © *2006 American Institute of Physics*. [DOI: 10.1063/1.2206870]

Noble metal nanoparticles exhibit strong plasmon polariton resonances, a feature that is increasingly utilized in biosensor and optoelectronic applications.[1] It has been shown that it is experimentally possible to relate the broadening of the plasmon resonance with the average size of the nanoparticles by assuming that the dominant contribution to the broadening arises from electron scattering at the particle boundary.[2] By determining the particle diameters from electron micrographs the broadening can be scaled to provide a method of determining the size of the nanoparticle from the optical absorption. Recent advances in spectroscopic ellipsometry (SE) hardware and software make it possible to record in real time changes in optical properties of thin films and overlayers, making it ideal for the study of ultrathin polymer metal nanoparticle composites. SE has been used to determine the size and concentration of embedded copper and gold nanoparticles.[3,4] We recently reported the use of real time *in situ* spectroscopic ellipsometry to study the growth of silver nanoparticles on SiO_2 by magnetron sputtering of silver.[5] The present work examines in real time the growth of silver nanoparticles in a polymer matrix using spectroscopic ellipsometry.

For this study, 0.12 ml of 1,1,1,5,5,5-hexafluoroacetylacetonate (hfac) (Sigma Aldrich) was mixed with a suspension of 0.15 g of Ag_2O (Sigma Aldrich) in 15 ml of toluene (Sigma Aldrich), producing a complex of $Ag(hfac)(toluene)_2$.[6] 0.3 ml of this solution was then mixed with 1 ml of 1% polystyrene (BASF) in toluene. Polystyrene films (ca. 50 nm thick) containing 3% (w/w) of silver in the form of Ag(hfac) were formed on silicon wafers by spin coating at 3000 rpm for 1 min. After drying the samples were placed on a boralectric heater with an attached thermocouple. This arrangement was aligned in the beam of a J.A.Woollam M2000 rotating-compensator spectroscopic ellipsometer[7] at 75° incident angle with a spectral range from 1.3 to 3.3 eV. Spectroscopic data (399 wavelengths) were collected every 5.4 s as the sample was heated to 250 °C.

In the first 3 min of heating the Ag(hfac) decomposed around 120 °C with a concomitant formation of silver nanoparticles. Further heating began to melt the polymer around 180° followed by evaporation above 220°. After 30 min there was an abrupt change in the ellipsometric parameters indicating the complete evaporation of the polymer, leaving exposed silver nanoparticles on the silicon surface. While the literature values for the glass transition temperature and melting point of polystyrene are 100° and 240°, respectively, in ultrathin films these values are dependent on the film thickness and substrate surface energy.[8] The exposed particles were imaged with scanning electron microscopy (SEM) to determine the particle size distribution. For transmission electron microscopy (TEM) analysis a second sample was prepared with a TEM grid on the silicon surface. The heating was stopped at 140 °C, leaving the particles embedded in the polymer.

Figure 1(a) shows a TEM image of a typical nanoparticle in the polymer film. Approximately spherical and 15 nm in diameter, the particle consists of a single fcc crystallite with a lattice constant of 0.409 nm. The majority of particles were observed to consist of a single crystallite. For the ellipsometric analysis presented below we assume that the particles are single crystals and that electron scattering is dominated by collisions with the particle boundaries. Figure 1(b) shows a SEM image of the nanoparticles on the silicon surface, while 1(c) is a size histogram of 501 particles, showing an average particle diameter of 14.8 (±0.1) nm with a standard deviation

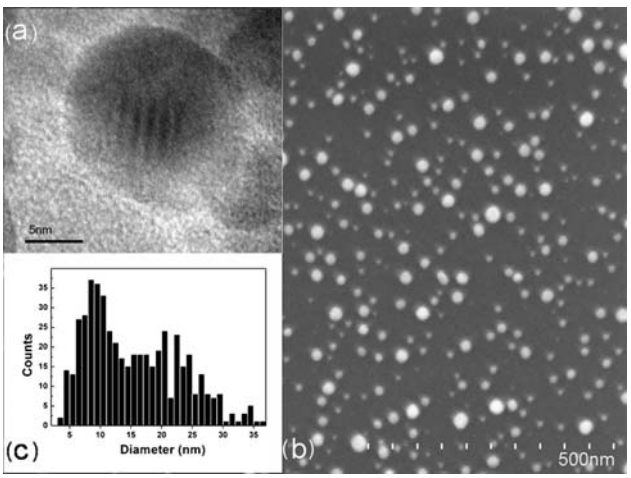

FIG. 1. (a) TEM image of a silver nanoparticle embedded in polystyrene matrix. The particle is an approximately spherical single crystal of radius 7.5 nm; (b) SEM image of exposed nanoparticles following the complete evaporation of the polymer matrix. (c) Particle sizes measured from the SEM image.

[a)]Electronic mail: t.oates@fz-rossendorf.de

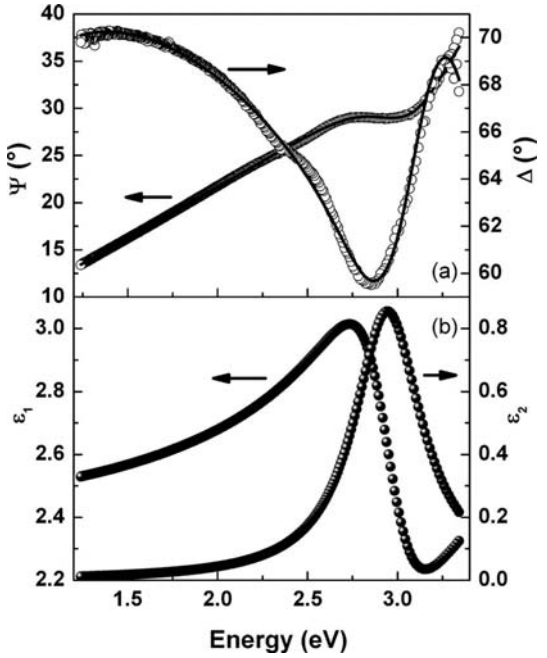

FIG. 2. (a) Measured ellipsometric parameters Ψ and Δ (open circles) at time=5 min and generated fits (solid lines) from the Maxwell-Garnett EMA using a Drude model for silver with modified electron relaxation frequency: (b) Generated dielectric constants for the composite film showing the plasmon polariton absorption at 3.0 eV.

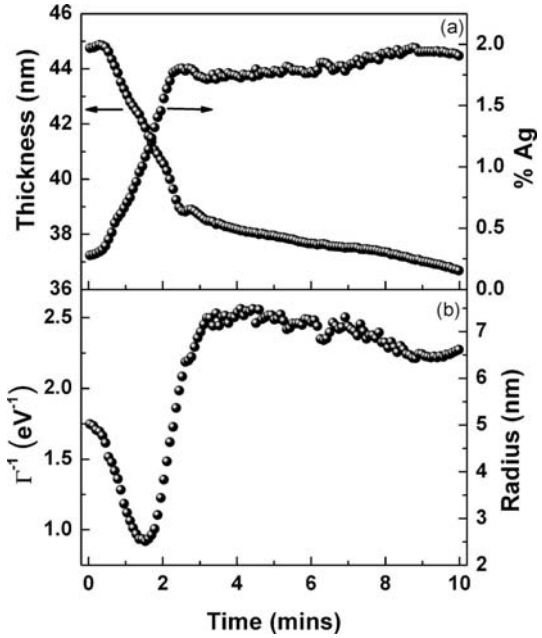

FIG. 3. (a) Film thickness and silver content of the composite film during heating: (b) Inverse of the relaxation frequency and nanoparticle radius calculated by scaling the relaxation frequency with the final value of particle radius determined from microscopy. For particles smaller than 2.3 nm the model is unable to predict the radius due to quantum size effects.

of 7.5 nm. The histogram shows a Gaussian distribution around 10 nm with an extended tail which suggests that some of the particle may have combined during the polymer evaporation phase, forming larger particles and increasing the average size. X-ray diffraction (XRD) was employed using the Scherrer equation on the Ag⟨111⟩ peak, supporting the SEM data with an average crystal size of 14.1 nm.

The ellipsometric data are fitted using the Maxwell-Garnett effective medium approximation[9] (MG-EMA) which is the limiting case for Mie resonances when the particles are small compared to the wavelength of light (ca. $R<10$ nm) (i.e., only the dipolar plasmon resonance is considered).[2] A parametric nonabsorbing two-parameter Cauchy model was used for the polymer matrix. For the first 10 min the Cauchy parameters remained within the range of a pure polymer film subjected to the same heat treatment ($2.35<\varepsilon_1<2.9$) until the polymer began to melt and finally evaporate. Silver optical constants were modeled using the Drude free-electron equation[10]

$$\tilde{\varepsilon}(\omega)=\varepsilon_\infty-\frac{\omega_p^2}{\omega^2-i\Gamma\omega}, \tag{1}$$

where ω_p is the bulk plasma frequency, Γ is the free-electron relaxation frequency, and ε_∞ is the contribution from interband transitions. For particles smaller than the mean free path of electrons in the bulk, Γ is inversely proportional to R and can be described by[11]

$$\Gamma=\Gamma_B+\frac{A\nu_f}{R}, \tag{2}$$

where Γ_B is the bulk free-electron relaxation frequency, ν_f is the Fermi velocity for silver (1.39×10^8 cm/s), and A is a constant of proportionality which must be determined by comparison with microstructural analysis. The parameters ε_∞, ω_p, and Γ_B for silver were determined by fitting Eq. (1) to the data from Johnson and Christy[12] (4.124, 9.22, and 0.022 eV, respectively).

To determine the value of A, the ellipsometric data at the 5 min point were fitted with the above model using five fitting parameters: film thickness, percentage content of silver, Γ, and the two Cauchy parameters. A film thickness of 38 nm and a silver content of 1.8% were obtained with $\Gamma=0.39$ eV. Figure 2(a) shows the agreement between the experimental and generated data (including the silicon substrate). Figure 2(b) shows the dielectric constants of the composite film from the fitted data with the prominent plasmon polariton absorption at 3.0 eV. Γ and R (from the SEM image) are now used in Eq. (2) to give $A=0.47$. Since A is a matrix dependent parameter it can only be compared qualitatively with literature values. Reviews can be found in Refs. 13 and 14, giving theoretical values from 0.29 to 1, while experimental values from 0.15 to 3.6 have been reported.[3,13,15]

Real time data were fitted using the above model for the first 10 min of heating. After this, large variations in the polymer optical properties due to evaporation complicated the modeling. The thickness and silver fraction of the film up to 10 min are shown in Fig. 3(a). Initially the film thickness increases marginally due to thermal expansion before a reduction in film thickness during the nanoparticle formation, explained by the outgassing of volatile components of the organometallic precursor. Figure 3(b) shows Γ^{-1} and the particle radius determined using the predetermined value for A. The main point of interest is that the particle size is observed to increase after 1.5 min from a radius of 2.3 nm to a value of 7.4 nm before reducing slightly due to heating effects to 6.4 nm. Heating effects manifest as an increase in electron-phonon scattering in the particles, thus increasing Γ_B in (2), with the effect of reducing the calculated value of R. Heating

effects are expected to influence the values of particle radius by only a few percent during the particle formation. The change in Γ as the composite film was cooled from 140° to room temperature was 0.01 eV or 2%.

The inability of the model to provide a reasonable estimate for the particle size below 2 nm is primarily due to particle size effects influencing the conduction band in the particle. Doremus and Rao have shown that for gold particles of $R<2$ nm the plasmon band begins to spread out and is completely invisible in particles of 0.5 nm in radius (ca. 31 atoms).[16] The influence of a shift in the interband transitions, considered for a similar system by See *et al.*,[17] is also expected to play a minor role. It has been shown that for gold particles smaller than ca. 2 nm the interband transitions deviate from those in the bulk.[18] Although the model requires further complexity to follow the growth of smaller particles, it is interesting to note that the values of film thickness and silver content remain reasonable in the early stages.

To conclude, a method is introduced to determine the size of nanoparticles in real time for particles in the size range of 2.3–10 nm in radius. The method opens possibilities to study the kinetics of particle formation. Refinement of the particle size determination from electron micrographs and XRD would be advantageous to further define the value of A. This would also be aided by a narrower particle size distribution.

This work was supported by a Marie Curie International Incoming Fellowship under the European Commission's FP6 framework. Thanks to M. Ozerov, A. Mücklich, E. Christalle, and A. Scholz for assistance.

[1]E. Hutter and J. H. Fendler, Adv. Mater. (Weinheim, Ger.) **16**, 1685 (2004).
[2]U. Kreibig and M. Vollmer, *Optical Properties of Metal Clusters* (Springer, Berlin, 1995).
[3]S. Kuerbitz, J. Porstendorfer, K.-J. Berg, and G. Berg, Appl. Phys. B: Lasers Opt. **73**, 333 (2001).
[4]D. Dalacu and L. Martinu, J. Opt. Soc. Am. B **18**, 85 (2001).
[5]T. W. H. Oates and A. Mücklich, Nanotechnology **16**, 2606 (2005).
[6]W. J. Evans, D. G. Giarikos, D. Josell, and J. W. Ziller, Inorg. Chem. **42**, 8255 (2003).
[7]http://www.jawoollam.com/
[8]D. S. Fryer, R. D. Peters, E. J. Kim, J. E. Tomaszewski, J. J. de Pablo, and P. F. Nealey, Macromolecules **34**, 5627 (2001).
[9]J. C. Maxwell-Garnett, Philos. Trans. R. Soc. London **203**, 385 (1904).
[10]P. Drude, Ann. Phys. (Leipzig) **1**, 566 (1900).
[11]U. Kreibig and C. von Fragstein, Z. Phys. **224**, 307 (1969).
[12]P. B. Johnson and R. W. Christy, Phys. Rev. B **6**, 4370 (1972).
[13]D. Dalacu and L. Martinu, J. Vac. Sci. Technol. A **17**, 877 (1999).
[14]U. Kreibig and L. Genzel, Surf. Sci. **156**, 678 (1985).
[15]A. Hilger, M. Tenefelde, and U. Kreibig, Appl. Phys. B: Lasers Opt. **73**, 361 (2001).
[16]R. H. Doremus and P. Rao, J. Mater. Res. **11**, 2384 (1998).
[17]K. C. See, J. B. Spicer, J. Brupbacher, D. Zhang, and T. G. Vargo, J. Phys. Chem. B **109**, 2693 (2005).
[18]U. Kreibig, Solid State Commun. **28**, 767 (1978).

APPLIED PHYSICS LETTERS **88**, 252501 (2006)

Control of saturation magnetization, anisotropy, and damping due to Ni implantation in thin $Ni_{81}Fe_{19}$ layers

J. Fassbender[a)]
Institute of Ion Beam Physics and Materials Research, Forschungszentrum Rossendorf, P.O. Box 51 01 19, 01314 Dresden, Germany

J. McCord
IFW Dresden, Institute for Metallic Materials, P.O. Box 270116, D-01171 Dresden, Germany

(Received 7 December 2005; accepted 2 May 2006; published online 19 June 2006)

The layer magnetization, the saturation magnetization as well as the magnetic anisotropy, and damping behavior of 20 nm thick $Ni_{81}Fe_{19}$ films have been modified by 30 keV Ni ion implantation with fluences up to 1×10^{16} Ni/cm^2 ($\approx$5 at. %). With increasing ion fluence a magnetic dead layer of increasing thickness is formed which leads to a reduction of the total magnetization. In addition, the saturation magnetization of the residual ferromagnetic film decreases due to, both, a shift in stoichiometry and radiation damage. Accordingly a reduction of the magnetic anisotropy and a strong enhancement of the magnetic damping parameter are observed. Moreover, ion implantation in an applied magnetic field allows the setting of the uniaxial anisotropy direction irrespective of its original orientation. Static and dynamic magnetic properties of $Ni_{81}Fe_{19}$ films can be tailored over a wide range after film deposition. © *2006 American Institute of Physics*.
[DOI: 10.1063/1.2213948]

The magnetic anisotropy and the magnetization damping behavior of thin magnetic films and elements are of great importance due to their application in magnetic storage media, memory cells, and read/write heads.[1] In order to achieve ultrafast data rates the magnetization reversal process has to be controlled to a maximum degree.[2,3] This technological demand has also led to a revival in the research of fundamental aspects of magnetic properties as anisotropy and saturation magnetization, which are related to the ferromagnetic precessional frequency and, even more important, the modification of the effective damping parameter.[4]

The high speed magnetization reversal is governed by the saturation magnetization M_s, the effective magnetic anisotropy K_{eff}, and the damping parameter α of the structures. All these material parameters enter the Landau-Lifshitz equation,

$$\frac{1}{\gamma}\frac{\partial \mathbf{M}}{\partial t} = -[\mathbf{M}\times\mathbf{H}_{\mathrm{eff}}] - \frac{\lambda_{LL}}{\gamma M_S^2}[\mathbf{M}\times(\mathbf{M}\times\mathbf{H}_{\mathrm{eff}})],$$

which is commonly used for the simulation of high speed switching processes.[2,3] Here, γ is the gyromagnetic ratio, $\mathbf{H}_{\mathrm{eff}}=\mathbf{H}_{\mathrm{appl}}+\mathbf{H}_k$ is the effective field (consisting of the applied field $\mathbf{H}_{\mathrm{appl}}$ and the anisotropy field $\mathbf{H}_k$), and $\lambda_{LL}=\alpha\gamma(4\pi M_s)$ is the magnetic relaxation rate. Various doping elements have been demonstrated to affect the magnetic properties of thin ferromagnetic films; i.e., Cr (Ref. 5) and Ta (Ref. 6) lead to a reduction of saturation magnetization, rare earth transition metal doping either enhances the magnetic damping[7–9] or modifies the ferromagnetic resonance frequency.[8] In general doping has been performed by cosputtering of the doping element. Only in the case of Cr (Ref. 5) ion implantation doping has been used. The large benefit of ion implantation relies on the fact that a focused ion beam (FIB) implantation can be used for a doping in laterally confined areas and thus a pure magnetic patterning.[10–12] However, in most FIB systems only Ga sources are available.[13] The observed effects can be explained by a combination of Ga ion incorporation and their energy impact. Only one publication reports on the modification of magnetic properties by means of focused ion beams circumventing Ga by the use of Co.[14] Making use of the energy impact only, noble gas ion irradiation in an applied field has been demonstrated to be capable of setting the magnetic anisotropy direction.[15,16]

In this letter we report on the tailoring of the effective magnetic layer thickness, the saturation magnetization, the magnetic anisotropy, and damping parameter by means of Ni implantation in thin $Ni_{81}Fe_{19}$ layers after film deposition. In addition to ion induced changes in film thickness, interfacial mixing with accompanying magnetic dead layer formation and a shift in stoichiometry of the $Ni_{81}Fe_{19}$ film, the observed change in magnetic properties is due to the energy impact associated with the ion implantation.[17]

The initial thin film samples have been prepared by magnetron sputter deposition on a 6 in. SiO_2/Si substrate. 20 nm $Ni_{81}Fe_{19}$ has been deposited on top of a 5 nm Ta buffer layer in an applied magnetic field in order to set the uniaxial magnetic anisotropy direction. In order to reduce the number of interfaces and thus avoid additional intermixing, no cap layer has been used. After deposition the structure was protected from corrosion by a thin photoresist layer. The samples have been implanted at room temperature with 30 keV Ni ions in the fluence regime up to 1×10^{16} Ni/cm^2 in an applied magnetic field of 1500 Oe, which is sufficient to saturate the magnetization, oriented either along the initially easy or hard-axis direction. According to TRIDYN simulations[18] the mean projected range of the Ni ions is r_p=8.5 nm, i.e., the Ni ions are implanted in the center of the $Ni_{81}Fe_{19}$ film.

In Figs. 1(a) and 1(b) the in-plane easy- and hard-axis magnetization reversal curves are shown for a set of different implantation fluences. With increasing ion fluence the magnitude of the Kerr rotation decreases. Comparing these results with *B-H*-looper (inductive) measurements, this drop is mainly attributed to magnetic rather than magneto-optic ef-

[a)]Electronic mail: j.fassbender@fz-rossendorf.de

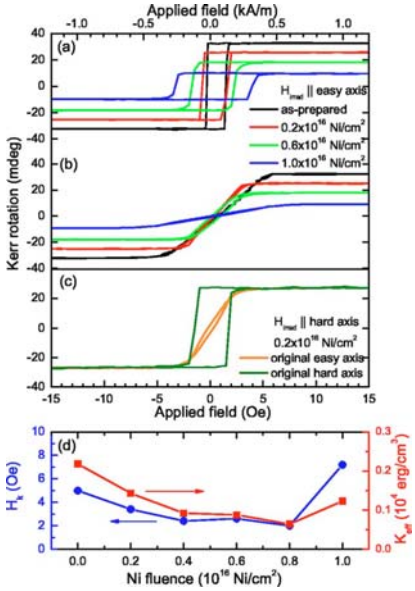

FIG. 1. (Color online) Easy-axis (a) and hard-axis (b) in-plane magnetization reversal curves of the layer system, as-prepared and implanted (30 keV, H_{irrad}||easy axis) with a Ni fluence of 0.2×10^{16}, 0.6×10^{16}, and 1.0×10^{16} Ni/cm^2, respectively. (c) Magnetization reversal curves along the originally easy- and hard-axis directions after Ni ion implantation (30 keV, 0.2×10^{16} Ni/cm^2) in an applied field parallel to the hard axis. (d) Static anisotropy field H_k (circles) and anisotropy constant K_{eff} (squares) as a function of Ni fluence. For the determination of K_{eff} the saturation magnetization determined by PIMM [cf. Fig. 3(a)] has been used.

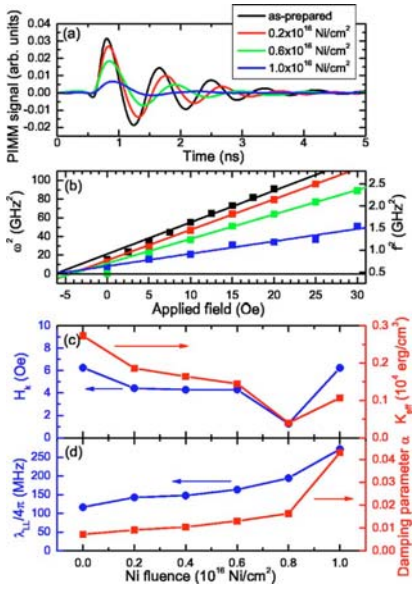

FIG. 2. (Color online) (a) Time dependent inductive signal of the precessing magnetization in response to a 100 ps rise time step pulse for the same samples, as shown in Fig. 1. (b) The square of the precession frequency as determined from (a) as a function of applied field (full symbols). The lines correspond to a linear fit of the data for applied fields $\geqslant$10 Oe. c) Dynamically obtained anisotropy field H_k (circles) and anisotropy constant K_{eff} (squares) as a function of Ni fluence. (d) Magnetic relaxation rate $\lambda_{LL}/4\pi$ (circles) and magnetic damping parameter α (squares) as a function of Ni fluence.

fects and thus due to a reduction in the layer magnetization. The different contributions that account for this reduction will be discussed further below. In addition an increase of coercivity is found [see Fig. 1(a)], which indicates additional pinning sites created by the implantation process and/or a reduction in magnetic thickness, as will be discussed below.[19] The static anisotropy field determined by the magnetization saturation in the hard-axis geometry first decreases as a function of Ni fluence but then increases above the initial value for a fluence of 1×10^{16} Ni/cm^2 [see Fig. 1(d)].

In order to evaluate the potential of ion implantation for the setting of the uniaxial anisotropy direction, the magnetic field during irradiation has been applied along the initially hard magnetization direction. Compared to conventional annealing ($\approx$50 meV) the energy transfer to the phonon system within the magnetic film is much higher ($\approx$20 keV). The magnetization reversal loops shown in Fig. 1(c) clearly indicate that the easy magnetization direction of the uniaxial anisotropy follows the applied magnetic field direction during ion implantation, consistent with investigations making use of 200 keV Ar^+ ion irradiation of $Ni_{81}Fe_{19}$ films.[15] In addition, fluences as low as 5×10^{13} Ni/cm^2 ($\cong$0.2 dpa) have been found to be sufficient to set the uniaxial anisotropy direction without a significant modification of the layer magnetization.

Next we turn to the dynamic magnetic measurements which have been performed by means of pulsed inductive microwave magnetometry (PIMM).[20] These allow the determination of the saturation magnetization (independent of magnetic film thickness), the dynamic anisotropy field H_k, the relaxation rate λ_{LL}, and the magnetic damping constant α. In Fig. 2(a) the dynamic pulse response arising from the time dependent magnetization traces in an easy-axis applied bias field of 10 Oe upon step excitation ($H_{step}\approx2$ Oe) along the hard magnetization axis is shown for the same samples characterized quasistatically in Fig. 1. The precession frequency ω and the magnetic relaxation rate λ_{LL} were determined from fitting an exponentially decaying damped sine function to the data. In the data presented in Fig. 2(a) the drop in overall magnetization can be observed already by the reduction of the first oscillation maximum and the reduction in precession frequency. For a number of different bias fields the dynamic pulse response has been measured and analyzed in detail by using Kittel's formula[21] $\omega^2=\gamma^2H_{eff}(H_{eff}+4\pi M_S)$ in the limit $H_{eff}\ll4\pi M_S$ and thus $\omega^2=\gamma^2 4\pi M_S(H_{appl}+H_k)$. Plotting ω^2 as a function of the applied field H_{appl} [see Fig. 2(b)] then allows the determination of $4\pi M_S$ from the slope and $-H_k$ from the intersection with the abscissa. The extracted values of the anisotropy and of α as a function of Ni ion fluence are shown in Figs. 2(c) and 2(d), respectively. The course of the dynamically obtained anisotropy value is consistent with the static one [cf. Figs. 1(d) and 2(c)]. The slight discrepancy between both values was also observed for other material systems (see, e.g., Ref. 22). The magnetic relaxation rate λ_{LL} and the effective magnetic damping parameter α shown in Fig. 2(d) are strongly affected by the Ni implantation. A continuous increase by a factor of up to 6 (2) is observed for the effective magnetic damping parameter α (relaxation rate λ_{LL}) for an ion fluence of 1×10^{16} Ni/cm^2 compared to the nonimplanted samples. The stronger dependency of the magnetic damping parameter is mainly attributed to the congruent drop in saturation magnetization for implantation fluences above 0.8×10^{16} Ni/cm^2.

In the remaining part of this letter we will focus on the different contributions leading to a drop in the layer magnetization and the saturation magnetization. Therefore we first compare the drop in layer magnetization determined by

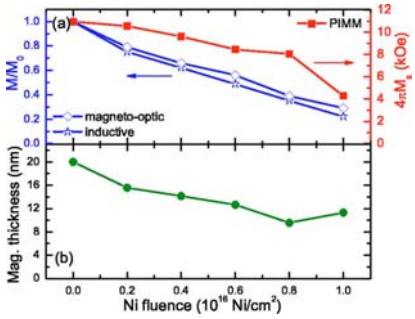

FIG. 3. (Color online) (a) Relative magnetization M/M_0 (open symbols) determined by magneto-optic and inductive techniques, M_0: magnetization of the samples prior to implantation, as a function of Ni fluence. In addition, the saturation magnetization $4\pi M_s$ (full symbols) determined by PIMM is shown. (b) Magnetically active film thickness as a function of Ni fluence. For details of the determination of the film thickness see text.

magneto-optic and inductive techniques with the drop in saturation magnetization determined by PIMM measurements [see Fig. 3(a)]. A large discrepancy between the course of the layer magnetization and the saturation magnetization is found. This can only be explained by a reduction of the magnetic active volume. Knowing both functional dependencies the residual magnetic film thickness can be calculated. In Fig. 3(b) the continuous decrease of the magnetically active film thickness is shown as a function of ion fluence. For implantation fluences above 0.8×10^{16} Ni/cm^2 only half of the initial film thickness is magnetically active. This reduction can be decomposed into two contributions: (i) *Reduction of the physical film thickness*, due to sputter effects the film thickness is reduced by approximately 3 nm at 1×10^{16} Ni/cm^2 according to TRIDYN simulations and cross-sectional transmission electron microscopy (TEM) investigations. (ii) *Magnetic dead layer formation*, due to irradiation induced broadening of the underlying Ta buffer layer profile Ta is mixed into the $Ni_{81}Fe_{19}$ layer. For Ta concentrations above approximately 12 at. % the alloy becomes paramagnetic[23] and above approximately 20 at. % ion induced amorphization takes place.[24] By means of TRIDYN simulations[18] the Ta profile has been determined quantitatively as a function of ion fluence and the predicted location of the crystalline/amorphous transition has been verified by cross-sectional TEM.[25] The location of the ferromagnetic/paramagnetic transition has been determined accordingly leading to a magnetically dead layer of 5 nm thickness at 1×10^{16} Ni/cm^2. In total a reduction of the magnetically active film thickness of 8 nm is expected for an implantation fluence of 1×10^{16} Ni/cm^2, which is in agreement with the experimental result [compare Fig. 3(b)]. However, in order to fully understand the observed modifications also the drop in saturation magnetization has to be addressed. One obvious contribution is the shift in stoichiometry. 5 at. % of Ni is implanted at 1×10^{16} Ni/cm^2 leading to a $Ni_{86}Fe_{14}$ alloy and thus a reduction in saturation magnetization of 10% with respect to $Ni_{81}Fe_{19}$.[26] In addition it is known that neutron irradiation can cause a reduction of the saturation magnetization[17] in the order of 10%. Due to the large difference in mass (Ni ion versus neutron), a more pronounced reduction of M_s for the Ni implantation case is expected. A reduction of $4\pi M_s$ to 8 kOe at an ion fluence of 0.8×10^{16} Ni/cm^2 can thus be explained by a combination of these effects. The reduction of $4\pi M_s$ to 4.3 kOe at a fluence of 1.0×10^{16} Ni/cm^2 cannot be explained completely by these effects. Cross-sectional TEM investigations[25] reveal that at this fluence the continuous $Ni_{81}Fe_{19}$ layer breaks up into crystalline particles at the sample surface which are surrounded by amorphous material due to the proceeding irradiation induced amorphization. In view of these large structural changes, involving a probably low moment or paramagnetic magnetic amorphous phase, the additional reduction in saturation magnetization is not surprising.

In summary, we have shown that by means of Ni ion implantation static and dynamic magnetic properties can be varied over a large range. The reduction in layer magnetization is explained by a combination of sputter effects and magnetically dead layer formation; the reduction in saturation magnetization is explained by a shift in stoichiometry and radiation induced damage formation. A decrease in anisotropy and a large increase in the magnetic damping parameter accompany the above effects. In addition the potential of ion implantation in an applied magnetic field to set the uniaxial anisotropy direction has been demonstrated.

The authors thank R. Mattheis for the thin film preparation, I. Winkler for the ion implantation, and A. Mücklich for performing the cross-section TEM.

[1] R. W. Wood, J. Miles, and T. Olson, IEEE Trans. Magn. **38**, 1711 (2002).
[2] M. Bauer, J. Fassbender, B. Hillebrands, and R. L. Stamps, Phys. Rev. B **61**, 3410 (2000).
[3] J. Miltat, G. Albuquerque, and A. Thiaville, Top. Appl. Phys. **83**, 1 (2002).
[4] B. Heinrich, *Ultrathin Magnetic Structures III*, edited by J. A. C. Bland and B. Heinrich (Springer, Berlin, 2005), p. 143.
[5] L. Folks, R. E. Fontana, B. A. Gurney, J. R. Childress, S. Maat, J. A. Katine, J. E. E. Baglin, and A. J. Kellock, J. Phys. D **36**, 2601 (2003).
[6] G. H. Yu, T. Yang, F. W. Zhu, M. H. Li, and W. Y. Lai, J. Phys. D **36**, 4 (2003).
[7] S. E. Russek, P. Kabos, R. D. McMichael, C. G. Lee, W. E. Bailey, R. Ewasko, and S. C. Sander, J. Appl. Phys. **91**, 8659 (2002).
[8] S. G. Reidy, L. Cheng, and W. E. Bailey, Appl. Phys. Lett. **82**, 1254 (2003).
[9] H. Song, L. Cheng, and W. E. Bailey, J. Appl. Phys. **95**, 6592 (2004).
[10] W. M. Kaminsky, G. A. C. Jones, N. K. Patel, W. E. Booij, M. G. Blamire, S. M. Gardiner, Y. B. Xu, and J. A. C. Bland, Appl. Phys. Lett. **78**, 1589 (2001).
[11] D. Ozkaya, R. M. Langford, W. L. Chan, and A. K. Petford-Long, J. Appl. Phys. **91**, 9937 (2002).
[12] D. McGrouther and J. N. Chapman, Appl. Phys. Lett. **87**, 022507 (2005).
[13] In general, liquid metal ion sources different from Ga are also available: L. Bischoff, Ultramicroscopy **103**, 59 (2005).
[14] J. Fassbender, L. Bischoff, R. Mattheis, and P. Fischer, J. Appl. Phys. **99**, 08G301 (2006).
[15] S. I. Woods, S. Ingvarsson, J. R. Kirtley, H. F. Hamann, and R. H. Koch, Appl. Phys. Lett. **81**, 1267 (2002).
[16] J. McCord, T. Gemming, L. Schultz, J. Fassbender, M. O. Liedke, M. Frommberger, and E. Quandt, Appl. Phys. Lett. **86**, 162502 (2005).
[17] C. W. Chen, *Magnetism and Metallurgy of Soft Magnetic Materials* (North-Holland, Amsterdam, 1977), Chap. 7.
[18] W. Möller, W. Eckstein, and J. P. Biersack, Comput. Phys. Commun. **51**, 355 (1988); the TRIDYN code is available on www.fz-rossendorf.de
[19] S. Middelhoek, *Magnetic Properties of Materials*, edited by J. Smit (McGraw Hill, New York, 1971).
[20] T. J. Silva, C. S. Lee, T. M. Crawford, and C. T. Rogers, J. Appl. Phys. **85**, 7849 (1999).
[21] C. Kittel, *Introduction to Solid State Physics*, 7th ed. (Wiley, New York, 2005).
[22] R. Lopusnik, J. P. Nibarger, T. J. Silva, and Z. Celinski, Appl. Phys. Lett. **83**, 96 (2003).
[23] G. T. Rado and A. R. Kaufmann, Phys. Rev. **60**, 336 (1941).
[24] B. X. Liu, W. S. Lai, and Q. Zhang, Mater. Sci. Eng., R. **29**, 1 (2000).
[25] Due to the limited space the details of this investigation will be published elsewhere: J. Fassbender, A. Mücklich, K. Potzger, and W. Möller, Nucl. Instrum. Methods Phys. Res. B (to be published).
[26] R. M. Bozorth, *Ferromagnetism* (IEEE, Hoboken, NJ, 2003).

APPLIED PHYSICS LETTERS **88**, 052508 (2006)

Fe implanted ferromagnetic ZnO

K. Potzger,[a] Shengqiang Zhou, H. Reuther, A. Mücklich, F. Eichhorn, N. Schell, W. Skorupa, M. Helm, and J. Fassbender
Institute of Ion Beam Physics and Materials Research, Forschungszentrum Rossendorf, P.O. Box 510119, 01314 Dresden, Germany

T. Herrmannsdörfer and T. P. Papageorgiou
Hochfeld-Magnetlabor Dresden, Forschungszentrum Rossendorf, P.O. Box 510119, 01314 Dresden, Germany

(Received 10 September 2005; accepted 9 January 2006; published online 2 February 2006)

Room-temperature ferromagnetism has been induced within ZnO single crystals by implant doping with Fe ions. For an implantation temperature of 623 K and an ion fluence of 4×10^{16} cm^{-2}, very tiny Fe particles, formed inside the host matrix, are responsible for the ferromagnetic properties. They were identified using synchrotron x-ray diffraction and Mössbauer spectroscopy. On the other hand, Fe ions implanted at a temperature of 253 K and an ion fluence of 4×10^{15} cm^{-2} are incorporated into the host matrix and develop a room temperature diluted magnetic semiconductor. © *2006 American Institute of Physics*. [DOI: 10.1063/1.2169912]

In the field of spintronics,[1] diluted magnetic semiconductors (DMS) are worldwide under intense investigation. DMS are "conventional" semiconductors doped with transition metal or rare-earth ions which are diluted within the host matrix and ferromagnetically aligned via an indirect magnetic coupling.[2–7] The existence of DMS based on Mn doped *p*-type ZnO[2] and V, Ti, Fe, Co, or Ni doped *n*-type ZnO (Ref. 7) has been predicted by theory. However, currently only *n*-type conducting ZnO films or single crystals are available. Recent reviews of experimental work in the field are given by Pearton *et al.*[8] and Ü. Özgür *et al.*[9] Among other systems, *n*-type ZnO doped with Fe has been confirmed experimentally[10–12] to exhibit ferromagnetism at room temperature. In some cases, especially at high processing temperatures, unwanted secondary phases are formed inside the ZnO matrix, which are responsible for the ferromagnetic properties.[11] One way to overcome this problem is the use of ion beam doping at low temperatures and thus far from thermal equilibrium.[12–14] In any case, structural analysis methods with high sensitivity are necessary in order to exclude secondary phases. In this letter it will be shown that Fe implantation into ZnO single crystals at a temperature of 623 K can lead to the formation of ferromagnetic α-Fe nanoparticles. On the other hand, Fe ions implanted at a temperature of 253 K are diluted within the ZnO host matrix and develop a ferromagnetic coupling.

For this purpose we used commercially available, hydrothermally grown ZnO single crystals that have been Zn-face epipolished by the supplier. These samples were implanted with ^{57}Fe ions at different temperatures and ion fluences (for a sample register and abbreviations see Table I). The implantation energy of 180 keV yielded a projected range of $R_P = 79\pm33$ nm (TRIM code[15]). Prior to implantation, the virgin samples were characterized by x-ray diffraction (XRD) (Siemens D5005), inductively coupled plasma mass spectrometry, and superconducting quantum interference device (SQUID) (Quantum Design MPMS) magnetometry. It is found that the virgin crystals are perfectly single crystalline showing a contamination below 20 ppm for Cu, Ni, and Fe and below 0.1 ppm for the other transition metals. Most important is the fact that even at low temperatures (5 K) all of the virgin samples behave purely diamagnetic upon magnetization reversal.

After implantation, the four samples (Table I) were analyzed using SQUID magnetometry. It was found that only two of them, i.e., the HFHT and the LFLT samples exhibit a pronounced hysteresis loop upon magnetization reversal at $T=5$ K (Table II). After subtraction of the diamagnetic background, a saturation magnetization of $M_S=0.30\ \mu_B(M_S=1.3\ \mu_B)$ per implanted Fe ion and a coercivity of $H_C=2.4\times10^4$ A m^{-1}($H_C=4.8\times10^3$ A m^{-1}) for the HFHT (LFLT) sample is determined. The hysteretic behavior remains also at $T=300$ K [Figs. 1(a) and 1(b)]. However, for the HFHT sample a more drastic decrease of M_S and H_C as compared to the LFLT sample is observed with increasing temperature (Table II).

In order to analyze the microscopic origin of the measured ferromagnetic properties of the HFHT and LFLT samples, synchrotron x-ray diffraction (SR-XRD) with monochromatic x rays of 0.154 nm wavelength and room-temperature conversion electron Mössbauer spectroscopy (CEMS) were used for all samples. In contrast to conventional XRD, the much higher x-ray intensity in SR-XRD allows one to detect also small amounts of very tiny nanoparticles. Figure 1(c) shows a symmetric $2\theta/\omega$ scan for the

TABLE I. Implantation conditions for ^{57}Fe ions for the investigated samples (T_{imp}=implantation temperature, Φ=ion fluence). The implantation angle was set to 7° in order to avoid channeling effects. The calculated implantation profile thus has a Gaussian shape with a maximum atomic concentration ρ_{max}. The sample identifiers refer to low/high fluence and low/high temperature.

Sample	Φ (cm^{-2})	ρ_{max} (%)	T_{imp} (K)
LFHT	4×10^{15}	0.5	623
HFHT	4×10^{16}	5	623
LFLT	4×10^{15}	0.5	253
HFLT	4×10^{16}	5	253

[a]Electronic mail: k.potzger@fz-rossendorf.de

TABLE II. Saturation magnetization M_S and coercivity H_C determined by SQUID magnetometry. The measurement temperatures are indicated.

	M_S (μ_B implanted Fe)		H_C (A m^{-1})	
Sample	5 K	300 K	5 K	300 K
HFHT	0.30	0.17	2.4×10^4	2.4×10^3
LFLT	1.3	1.0	4.8×10^3	4.0×10^3

HFHT sample. Sharp, high intensity peaks from bulk ZnO are visible at $2\theta\sim34.4°$ and $2\theta\sim72.6°$. At $2\theta\sim44.5°$, a rather broad and low intensity peak originating from α-Fe(110) with a theoretical Bragg angle of $2\theta=44.66°$ occurs. The nanoparticle size is estimated to be around 8 nm using the Scherrer formula.[16] Apart from α-Fe, no other phases are detected. In order to support these findings by real space methods, cross-section transmission electron microscopy (TEM) (Philips CM 300) has been performed. The nanoparticles could be identified indirectly due to a Moiré pattern with a visible diameter of about 6–12 nm (Fig. 2, inset) at a distance of only 30–65 nm from the surface. A broadening of the Fe density profile due to the elevated implantation temperature was observed by means of energy dispersive x-ray microanalysis (EDX). The maximum iron concentration was found at $R_{EDX}=51\pm38$ nm with a broad tail towards the sample bulk. In CEMS, only the HFHT sample exhibits a fraction of ^{57}Fe probe nuclei, that show a clear magnetic hyperfine splitting (sextet) corresponding to a magnetic hyperfine field of $B_{HF}=30.5$ T (Fig. 2) which is—due to size effects—slightly smaller than the known value of metallic α-Fe($B_{HF}=33.0$ T). This fraction covers 12.5% of the ^{57}Fe nuclei absorbing the incident γ radiation. Its isomer shift (IS) of 0.06 mm/s with respect to α-Fe doubtlessly represents metallic Fe^0. The remaining Fe in the HFHT sample exhibits ionic charge states showing no ferromagnetic hyperfine splitting. The interpretation of these fractions is, in part, rather difficult. The best fit has been obtained using one singlet representing a Fe^{3+} state reported already elsewhere[17] and two quadrupole-split lines representing Fe^{2+} states (Fig. 2). The absence of a quadrupole splitting (QS) of Fe^{3+} excludes $ZnFe_2O_4$ precipitates since there is always an electric field gradient present at the octahedral sites.[18,19] Fe_3O_4 usually does not show a quadrupole splitting in the Fe^{2+} states[17] and can thus also be excluded indirectly. These conclusions are consistent with those obtained from SR-XRD.

The interpretation of the origin of the ferromagnetic properties of the HFHT sample is thus straightforward: During implantation metallic Fe nanoparticles are formed. This is due to higher migration of Fe at the elevated temperature as compared to the HFLT and LFLT samples. Moreover, the required diffusion length for nanoparticle formation is much shorter at the higher fluence as compared to the LFHT sample (Table I). The superparamagnetic limit of Fe nanoparticles is described by the relaxation time $\tau=\tau_0\exp[E_AV/k_BT]$, where E_A is the anisotropy energy density (5×10^4 J/m^3 for Fe), V is the particle volume, and k_B is the Boltzmann constant. τ_0 amounts to $\sim10^{-9}$ s (Ref. 20). Thus at $T=5$ K and a measurement time of ~100 s which is typical for SQUID magnetometry the critical nanoparticle diameter for superparamagnetic behavior results to 4 nm. From the earlier discussed structural analysis we know that all nanoparticles diameters are larger than this value and should intrinsically behave like ferromagnetic α-Fe bulk material. Taking into account the fraction of 12.5% of metallic Fe found by CEMS and a magnetic moment of 0.30 μ_B per implanted Fe ion, a value of $M_S=2.4$ μ_B per Fe atom within the metallic nanoparticles is determined in agreement with the known value for bulk Fe of 2.2 μ_B. The slight overestimation probably results from the fact that the CEMS spectrum contains also a small fraction resulting from superparamagnetic Fe nanoparticles which could not be resolved in CEMS. At 300 K, the hysteresis loop obtained by SQUID magnetometry exhibits a distinct decrease of M_S down to 0.17 μ_B per implanted Fe ion, and of H_C down to 2.4×10^3 A m^{-1} compared to the measurement at 5 K (Table II). Both effects result from the size distribution of the Fe nanoparticles, since with increasing temperature also larger nanoparticles become superparamagnetic or approach to the superparamagnetic limit.

In contrast to the other three samples, a long-time CEMS spectrum (500 h) recorded for the LFLT sample ($T_{imp}=253$ K, $\Phi=4\times10^{15}$ cm^{-2}) exhibits only a single line corre-

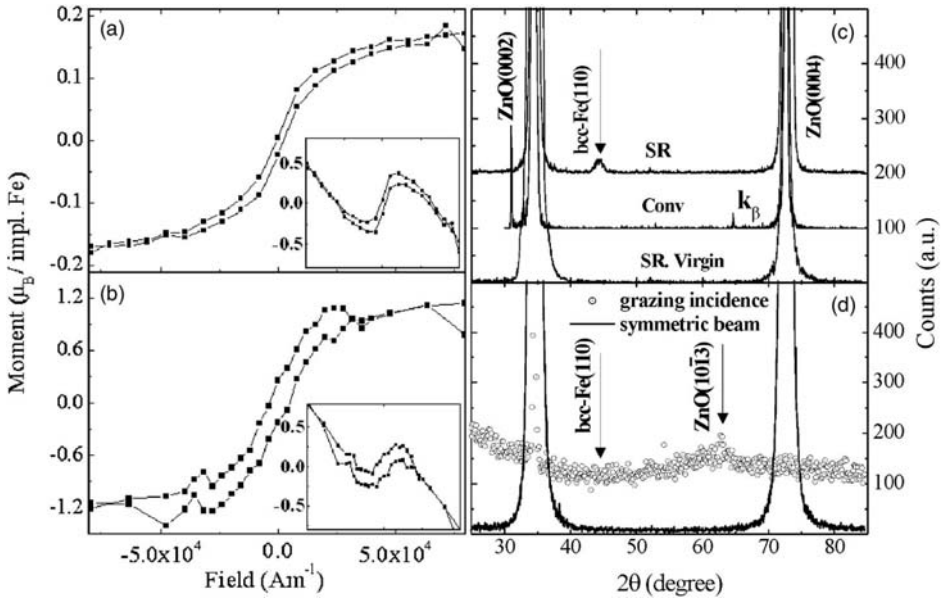

FIG. 1. Magnetization reversal recorded at 300 K using SQUID magnetometry for the HFHT (a) and the LFLT (b) sample. The inset shows the magnetization prior to background subtraction in A m^{-1} with respect to the substrate volume. The horizontal axes have the same scale. (c) Conventional (conv.) and SR-XRD pattern (symmetric $2\theta/\omega$ scan) for the HFHT sample compared to a virgin sample. Small Fe nanoparticles can be detected only by SR-XRD. (d) SR-XRD pattern for the LFLT sample: no secondary phases are found by either a symmetric $2\theta/\omega$ scan or a grazing incidence scan.

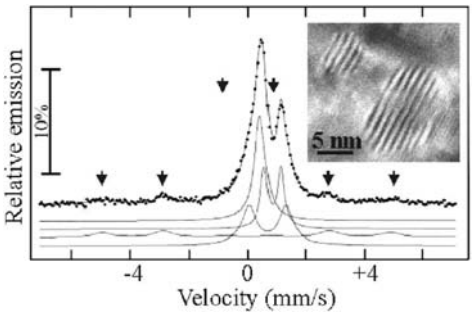

FIG. 2. CEMS of the HFHT sample recorded at 300 K. The fit curves represent (from top to bottom) a single emission line corresponding to a Fe^{3+} state (IS=0.53 mm/s with respect to α-Fe), a quadrupole split emission line (QS=0.6 mm/s) corresponding to a Fe^{2+} state (IS=0.69 mm/s), a sextet line resulting from a magnetic hyperfine splitting of a metallic Fe^0 state (IS=0.06 mm/s) and a strongly quadrupole split line (QS=1.3 mm/s) of a Fe^{2+} state (IS=0.78 mm/s). The inset shows Moiré contrasts measured using TEM that can be associated with small metallic Fe nanoparticles corresponding to the CEMS results. The arrows indicate the sextet.

sponding to a Fe^{3+} state. Thus the majority of the detected ions are ferric but nonmagnetic similar to the results for Fe doped SnO_2.[5] A decision about the existence of a ferromagnetic sextet could not be provided along with CEMS due to the small counting rate resulting from the low fluence implanted and the lower uniformity of the Fe lattice sites as compared to the samples implanted at 623 K. However, for the LFHT, HFLT, and especially the ferromagnetic LFLT sample no secondary phases have been found using SR-XRD [Fig. 1(d)] and no metallic Fe^0 states have been detected using CEMS. *Consequently, the implanted Fe ions are diluted within the ZnO host matrix*. Thus—in sharp contrast to the HFHT sample—the ferromagnetic behavior of the LFLT sample [Fig. 1(b)] results from an indirect exchange interaction between diluted Fe ions similar to the one reported in Ref. 5 for the case of Fe doped SnO_2. Surprisingly the ferromagnetic behavior occurs at much lower Fe concentrations than that reported in Ref. 5 or predicted by theory. In the case of diluted Fe^{3+} (5 μ_B per ion), 28% and in the case of diluted Fe^{2+} (6 μ_B per ion), 23% of the implanted ions would contribute to the ferromagnetic interaction. The minimal Fe–Fe distance for the LFLT sample can be estimated to be 1.3 nm. Considering the different implantation temperatures and fluences affecting the diffusion behavior and the ion induced damage in the four investigated samples, a crude explanation of their behavior with respect to the formation of a DMS can be provided: An implantation temperature of 623 K causes a broadening of the Fe implantation profile. Hence, a ferromagnetic state of the Fe ions that are diluted within the LFHT sample cannot be established due to the low local Fe concentration. Within the LFLT sample, however, the implantation profile is sharper and therefore the local Fe concentration is large enough to form a room-temperature DMS. For the lack of a DMS state within the high fluence implanted samples this argumentation does not hold because the total amount of implanted Fe ions was ten times larger than for the LFHT sample, but with many associated defects. Thus these defects introduced during implantation must play a key role for the DMS formation. Rutherford backscattering (RBS) analysis shows, that the damage level for both high fluence implanted samples are similar, i.e., $\chi_{min} \sim 65\%$,[21] while the damage level for the LFLT sample is much lower ($\chi_{min}=30\%$, χ_{min} of the virgin samples: 3%). Such defects affect the transport properties of ZnO (Ref. 22) and thus the path of ferromagnetic coupling.

In summary, 180 keV Fe implanted ZnO single crystals can develop ferromagnetic properties that are either caused by α-Fe nanoparticles or an indirect coupling of the Fe ions in a DMS system, depending on the details of ion fluence and implantation temperature. Detailed structural analysis is required to rule out secondary phases.

[1] S. A. Wolf, D. D. Awschalom, R. A. Buhrman, J. M. Daughton, S. von Molnár, M. L. Roukes, A. Y. Chtchelkanova, and D. M. Treger, Science **294**, 1488 (2001).
[2] T. Dietl, H. Ohno, F. Matsukura, J. Cibert, and D. Ferrand, Science **287**, 1019 (2000).
[3] V. Barzykin, Phys. Rev. B **71**, 155203 (2005).
[4] D. J. Priour, E. H. Hwang, and S. Das Sarma, Phys. Rev. Lett. **92**, 117201 (2004).
[5] J. M. D. Coey, A. P. Douvalis, C. B. Fitzgerald, and M. Venkatesan, Appl. Phys. Lett. **84**, 1332 (2004).
[6] J. M. D. Coey, M. Venkatesan, and C. B. Fitzgerald, Nat. Mater. **4**,173 (2005).
[7] K. Sato and H. Katayama-Yoshida, Semicond. Sci. Technol. **17**, 367 (2002).
[8] S. J. Pearton, D. P. Norton, K. Ip, Y. W. Heo, and T. Steiner, J. Vac. Sci. Technol. B **22**, 932 (2004).
[9] Ü. Özgür, Ya. I. Alivov, C. Liu, A. Teke, M. A. Reshchikov, S. Doğan, V. Avrutin, S.-J. Cho, and H. Morkoç, J. Appl. Phys. **98**, 041301 (2005).
[10] M. Venkatesan, C. B. Fitzgerald, J. G. Lunney, and J. M. D. Coey, Phys. Rev. Lett. **93**, 177206 (2004).
[11] J. H. Shim, T. Hwang, S. Lee, J. H. Park, S.-J. Han, and Y. H. Jeong, Appl. Phys. Lett. **86**, 082503 (2005).
[12] A. Y. Polyakov, A. V. Govorkov, N. B. Smirnov, N. V. Pashkova, S. J. Pearton, K. Ip, R. M. Frazier, C. R. Abernathy, D. P. Norton, J. M. Zavada, and R. G. Wilson, Mater. Sci. Semicond. Process. **7**, 77 (2004).
[13] E. Rita, U. Wahl, J. G. Correia, E. Alves, and J. C. Soares, Appl. Phys. Lett. **85**, 4899 (2004).
[14] D. P. Norton, M. E. Overberg, S. J. Pearton, K. Pruessner, J. D. Budai, L. A. Boatner, M. F. Chisholm, S. J. Lee, Z. G. Khim, Y. D. Park, and R. G. Wilson, Appl. Phys. Lett. **83**, 5488 (2003).
[15] J. Ziegler, J. Biersack, and U. Littmark, *The Stopping and Range of Ions in Matter* (Pergamon, New York, 1985); SRIM 2000 code, www.srim.org.
[16] B. D. Cullity, *Elements of X-Ray Diffractions* (Addison-Wesley Reading, MA, 1978), p. 102.
[17] E. Murad, Phys. Chem. Miner. **23**, 248 (1996).
[18] H. B. Mathur, A. P. B. Sinha, and C. M. Yagnik, Indian J. Pure Appl. Phys. **5**, 155 (1967).
[19] B. J. Evans, S. S. Hafner, and H. P. Weber, J. Chem. Phys. **55**, 5282 (1971).
[20] R. Waser, *Nanoelectronics and Information Technology* (Wiley-CH, Weinheim, 2003), p. 624.
[21] χ_{min} is the channeling minimum yield in RBS/C, which is the ratio of the backscattering yield when the impinging beam is aligned parallel to a crystallographic axis to that for a random beam incidence. Therefore, an amorphous sample shows a χ_{min} of 100%, while a perfect single crystal corresponds to a χ_{min} of 1%–2%.
[22] S. O. Kucheyev, C. Jagadish, J. S. Williams, P. N. K. Deenapanray, M. Yano, K. Koike, S. Sasa, M. Inoue, and K. Ogata, J. Appl. Phys. **93**, 2972 (2003).

APPLIED PHYSICS LETTERS **89**, 161909 (2006)

Nanocluster formation in Fe implanted GaN

G. Talut,[a] H. Reuther, A. Mücklich, F. Eichhorn, and K. Potzger
Institute of Ion Beam Physics and Materials Research, Forschungszentrum Rossendorf e.V., P.O. Box 510119, 01314 Dresden, Germany

(Received 2 August 2006; accepted 31 August 2006; published online 17 October 2006)

The formation of Fe clusters in wurtzite GaN implanted with 200 keV ^{57}Fe ions at 350 °C was investigated. Cluster sizes from few nanometers up to several 100 nm depending on ion fluence, implantation, and annealing temperature have been observed for ion fluences between 4×10^{16} and 1.6×10^{17} cm^{-2}. A clear epitaxial relation between Fe and GaN was determined. X-ray diffraction, conversion electron Mössbauer spectroscopy, transmission electron microscopy, and Auger electron spectroscopy were used for the characterization of the implanted samples. Mössbauer spectroscopy shows that precipitation of Fe occurs already during implantation. © *2006 American Institute of Physics*. [DOI: 10.1063/1.2363960]

Transition metal doped GaN is expected to be a diluted magnetic semiconductor (DMS) with a Curie temperature (T_C) above room temperature. Generally in a DMS magnetic atoms substitute randomly cation sites. The ferromagnetism is related to the spin coupling between magnetic impurities mediated by the holes. However, the possible presence of metallic precipitates may also play an important role in the discussion of the origin of the ferromagnetism. Though the appearance of those precipitates is not desired in an ideal DMS, it is not clear whether the presence of ferromagnetic nanoclusters excludes the ferromagnetic interaction mediated by charge carriers. Isolated clusters of some nanometer size act as superparamagnets and have negligible dipolar interaction. On the other hand, metallic clusters could be useful regarding their optical, magnetic, and electronic properties as it was suggested in Refs. 1–4. Theodoroupoulou *et al.*[5] and Shon *et al.*[6] reported about ferromagnetism in Fe implanted GaN and T_C up to room temperature and even above 350 K, respectively. In Ref. 5, in most cases, no secondary phases were observed. Shon *et al.* did not report about secondary phases, although the implanted fluence of 5×10^{16} cm^{-2} ($\simeq$5.6 at. % Fe) should inevitably lead to cluster formation. If one considers that the solubility limit for magnetic elements in III-V semiconductors is only few at. %, many nucleation centers which are generated during implantation and the enhanced mobility due to high implantation temperature should promote the cluster formation.

In the present study, ^{57}Fe was used as an atomic sensitive probe to investigate the local environment of Fe by Mössbauer spectroscopy in combination with other techniques to study the precipitation at very early stage. *p*-type (Mg) doped ($\sim10^{17}$ cm^{-3}) single crystalline, wurtzite GaN (001) films of about 3 μm thickness epitaxially grown by metal organic vapor phase epitaxy on sapphire (001) were used. Samples were implanted with 200 keV ^{57}Fe ions with fluences between 1×10^{16} and 1.6×10^{17} cm^{-2} (maximum Fe content of 1–18 at. %) while the temperature was kept at 350 °C in order to avoid amorphization, similar to Ref. 5. In order to reduce the implantation damage and to obtain a redistribution of iron, implanted samples were annealed at temperatures between 700 and 950 °C in N_2 flow (1.1 bars) for 5 min. The Fe implantation profiles were calculated using the TRIDYN-code simulations[7] and compared to concentration depth profiles recorded by Auger electron spectroscopy (AES). The crystallographic phase composition was investigated using a Siemens D 5000 x-ray diffractometer in $\theta-2\theta$ geometry with θ offset of 1° and Cu K_α radiation. The microstructure was studied in cross-sectional specimens by using a Philips CM 300 transmission electron microscope (0.14 nm line resolution). Conversion electron Mössbauer spectroscopy (CEMS) in constant-acceleration mode at room temperature was applied to investigate the Fe lattice sites, electronic configuration, and magnetism. The spectra were fittedwith Lorentzian lines using the least squares computer program NORMOS.[8] The investigations of magnetic properties were performed on a QD MPMS superconducting quantum interference device magnetometer.

AES measurements (not shown here) confirmed the Gaussian shaped implantation profiles for fluences up to 8×10^{16} cm^{-2}. For the sample with the highest implanted fluence (1.6×10^{17} cm^{-2}), a sputter-controlled implantation profile was observed. A contamination with oxygen took place only in the first atomic layers. The outgassing of nitrogen from the sample was successfully prevented by the slight N_2 overpressure (1.1 bars) during annealing, e.g., the nitrogen-concentration profiles remained constant. As a result a change in stoichiometry took place in the implantation profile between Ga and Fe for the benefit of the iron. The X-ray diffraction (XRD) investigation [Fig. 1(a)] of the as-implanted (i) and subsequently at 750 °C (ii) and at 850 °C (iii) annealed samples reveals the generation of Fe crystallites during the annealing procedure for fluences above 4×10^{16} cm^{-2}. A broad peak found around 44.7° is representative for the cluster evolution. This peak is associated with α-Fe (110) or strained γ-Fe (111). The intensity of the Fe peak increases and the full width at half maximum (FWHM) decreases with higher annealing temperature, representing the growth of crystallites. No other secondary phases were detected. However, the presence of very tiny clusters cannot be excluded.

In samples implanted with fluences above 8×10^{16} cm^{-2}, the formation of clusters is observed already in as-implanted state. The XRD pole figure measurement (not shown here) reveals the cluster to be fiber textured with Fe (110) plane oriented parallel to GaN (001), which is in good

[a]Electronic mail: g.talut@fz-rossendorf.de

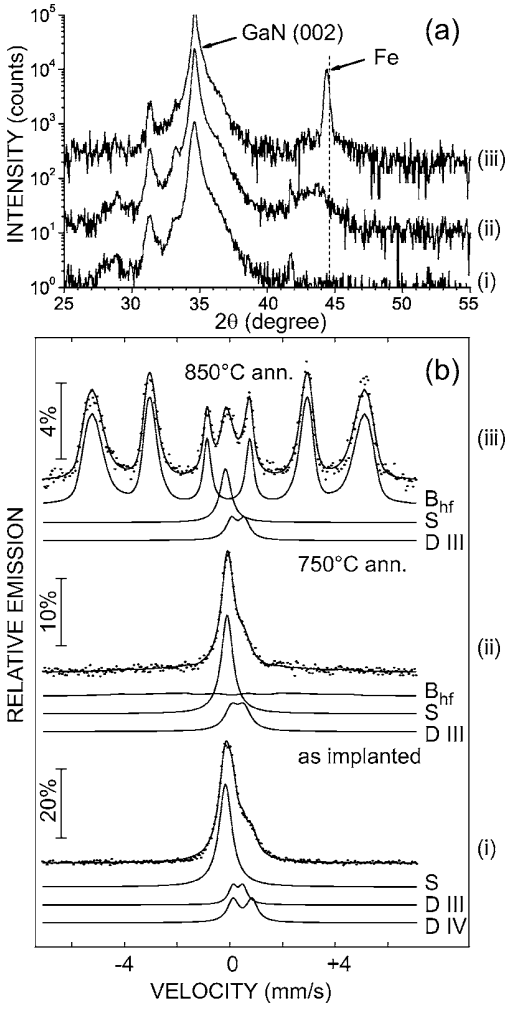

FIG. 1. XRD pattern (a) (spectra are shifted along the ordinate) and room temperature CEM spectra (b) of 4×10^{16} cm^{-2} implanted (i) at 750 °C (ii) and at 850 °C (iii) subsequently annealed samples.

agreement with the orientation of Fe layers deposited on GaN.[9] The clusters are allocated throughout the entire implantation profile as shown exemplarily in a transmission electron microscopy (TEM) micrograph from the sample implanted with 4×10^{16} cm^{-2} and annealed at 800 °C (Fig. 2, left). Epitaxially oriented clusters with sizes up to 8 nm are clearly recognizable by means of Moiré patterns. The number of clusters increases and they coalesce with increasing fluence. Finally, for the highest fluence and highest annealing temperature (1.6×10^{17} cm^{-2}, 950 °C), even Fe islands up to

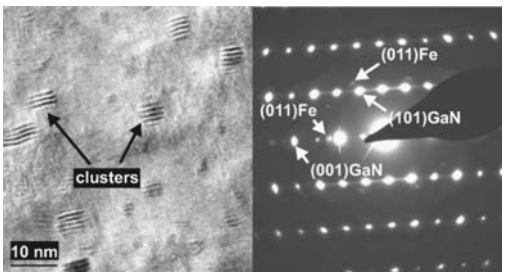

FIG. 2. Fe clusters allocation (moiré pattern) inside the implantation region (the final part) of the 4×10^{16} cm^{-2} implanted and at 800 °C annealed sample (left). Selected area diffraction pattern shows the epitaxial relations of (110)Fe∥(101)GaN and (011)Fe∥(001)GaN (right).

several 100 nm in size are formed on the surface. This island formation is accompanied by a strong roughening of the surface as it was reported by Polyakov *et al.*[10] The islands are also epitaxially aligned to the host as it was proven for clusters. Both for clusters and islands, the interplanar distance of 0.206 nm obtained from selected area diffraction pattern (Fig. 2, right) is very close to the (110) interplanar distance of α-Fe (a=0.203 nm). The following epitaxy relations were determined: (110)Fe∥(101)GaN and (011)Fe∥(001)GaN. CEMS measurements allow one to identify different Fe-site occupations. The hyperfine parameters calculated according to the evaluations of the spectra are given in Table I. Figure 1(b) shows CEM spectra of the sample implanted with 4×10^{16} cm^{-2} and subsequently annealed at 750 and 850 °C. The spectrum of the as-implanted state [Fig. 1(b)(i)] consists of a singlet line and two quadrupole doublets. The singlet can be assigned to either superparamagnetic α-Fe or to paramagnetic γ-Fe with an isomer shift of −0.05 mm/s. This value is similar to the isomer shift (−0.10 mm/s) observed for Fe nanoparticles in Al_2O_3 under high compression.[11] The doublets are fitted with the isomer shifts for Fe in wurtzite AlN given in Ref. 12. The determined values can be assigned to Fe^{3+} with three (D_{III}) and four (D_{IV}) nearest N neighbors with isomer shifts of 0.42 and 0.59 mm/s, respectively. The magnetically isolated Fe^{3+} ions are paramagnetic; thus no ferromagnetic hyperfine splitting is observable. The presence of the Fe^{3+} state is a direct proof of its substitution of Ga sites in the wurtzite structure where Ga is surrounded by four N atoms and vice versa. However, only 23.6% of total Fe amount in as-implanted sample appears to substitute Ga sites. The other part is either on interstitial sites or forming small precipitates (γ- or α-Fe). The formation of ϵ-Fe nitrides cannot be excluded but it is unlikely because they were neither observed by XRD nor by TEM. During annealing at 750 °C, Fe redistributes and only one doublet (D_{III}) can be found. A small amount with a ferromagnetic hyperfine field distribution can be detected [Fig. 1(b)(ii)]. However, this effect is too small for reliable interpretation. Annealing at 850 °C [Fig. 1(b)(iii)] leads to the growth of ferromagnetic α−Fe, represented by a sextet with a mean magnetic hyperfine field of 318 kOe. It differs slightly from bulk α-Fe (B_{hf}=330 kOe) apparently due to size effects, imperfect iron surrounding, and possible strain. The relative area of the α-Fe sextet and thus the α-Fe fraction in clusters increases at the expense of other fractions and covers about 85% of the total Fe content. The relative line intensities of 3:2.6:1:1:2.6:3 of the sextet differ from those of polycrystalline powder material (3:2:1:1:2:3), indicating the presence of a texture. This confirms the crystallographic anisotropy as revealed from XRD and TEM. The quadrupole doublet was fitted with an isomer shift of 0.42 mm/s as before and is attributed to Fe^{3+} with three nearest N neighbors (D_{III}). The increase of the relative area of the magnetic phase observed with increasing annealing temperature is a direct proof for the phase separation. These results show that at elevated implantation temperatures (in this case at 350 °C), the precipitation occurs already during the implantation process.

Finally, magnetization measurements were performed on the 4×10^{16} cm^{-2} implanted and at 750 °C annealed samples containing Fe clusters. The magnetization reversal curves (Fig. 3) show none or just a small hysteresis—an indication of superparamagnetic response of clusters. At room tempera-

TABLE I. Hyperfine parameters obtained from the evaluation of the Mössbauer spectra of the sample implanted with 4×10^{16} cm^{-2} and annealed at 750 and at 850 °C. δ: isomer shift, Δ: quadrupole splitting, B_{hf}: magnetic hyperfine field, Γ: FWHM, A: relative area of each component, S: singlet, D: doublet, and M: sextet.

Sample	Component	δ^a (mm/s)	Δ (mm/s)	B_{hf} (kOe)	Γ (mm/s)	A (%)
As implanted	S	−0.05	⋯	⋯	0.59	62.3
	D_{III}	0.42	0.48	⋯	0.49	14.1
	D_{IV}	0.59	0.71	⋯	0.51	23.6
750 °C annealed	S	−0.01	⋯	⋯	0.53	57.0
	D_{III}	0.42	0.42	⋯	0.64	29.6
	M	0.0	0.0	Distribution	0.30	13.4
850 °C annealed	S	−0.05	⋯	⋯	0.66	8.3
	D_{III}	0.42	0.48	⋯	0.60	6.1
	M	0.05	0.0	Distribution	0.30	85.6

[a]All isomer shifts are given relative to α-Fe.

ture the total magnetic moment is much lower than at 150 K, apparently due to the decrease of the intrinsic cluster magnetization with rising T. At both temperatures, a small paramagnetic contribution from noninteracting ionic Fe^{3+} (Van Vleck paramagnetism) is visible.

In summary, nanocrystalline clusters were produced by Fe implantation into wurtzite GaN at elevated temperatures and a subsequent annealing step. Mössbauer spectroscopy proves the precipitation of Fe already during implantation and their growth during annealing. The clusters are mainly epitaxially oriented to GaN. The fluence plays an important role for the density of cluster allocation and their size. The annealing temperature and time are decisive for the cluster size and crystallinity. As both the recovery of the crystal structure and the formation of nanoparticles are thermally stimulated processes, it will be difficult to enable damage annealing without concurrent cluster formation. The precipitation may be suppressed by implantation at lower temperatures than used here. Also short annealing such as rapid thermal annealing or flash lamp annealing[13] at second or millisecond time scales, respectively, might prevent precipitation.

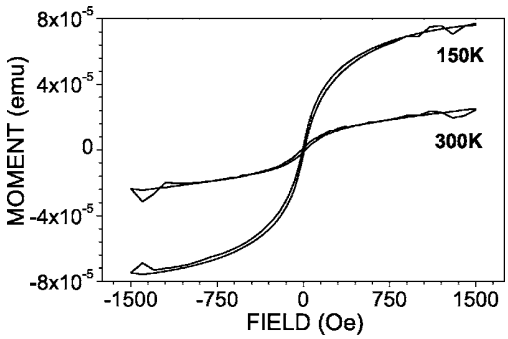

FIG. 3. Magnetization reversal curves of 4×10^{16} cm^{-2} implanted and subsequently at 750 °C annealed samples measured at 150 and 300 K.

This work is supported by the Deutsche Forschungsgemeinschaft (German Research Foundation) under Contract No. Re 868/7-1.

[1]K. Potzger, H. Reuther, S. Zhou, A. Mücklich, R. Grötzschel, F. Eichhorn, M. O. Liedke, J. Fassbender, H. Lichte, and A. Lenk, J. Appl. Phys. **99**, 08N701 (2006).
[2]Y. Xin, J. Lu, P. Stampe, and R. Kennedy, Appl. Phys. Lett. **88**, 112512 (2006).
[3]S. Zhu, L. Wang, X. Zu, and X. Xiang, Appl. Phys. Lett. **88**, 043107 (2006).
[4]D. Kumar, S. Pennycook, A. Lupini, G. Duscher, A. Tiwari, and J. Nrayan, Appl. Phys. Lett. **81**, 4204 (2002).
[5]N. Theodoropoulou, A. Hebard, S. Chu, M. Overberg, C. Abernathy, S. Pearton, R. Wilson, and J. Zavada, J. Appl. Phys. **91**, 7499 (2002).
[6]Y. Shon, Y. H. Kwon, Y. Park, S. Yuldashev, S. J. Lee, C. Park, K. Chung, S. Yoon, H. Kim, W. Lee, D. J. Fu, T. W. Kang, X. J. Fan, Y. J. Park, and H. T. Oh, J. Appl. Phys. **95**, 761 (2004).
[7]W. Möller and W. Eckstein, Nucl. Instrum. Methods Phys. Res. B **2**, 814 (1984).
[8]R. Brand, Nucl. Instrum. Methods Phys. Res. B **28**, 398 (1987).
[9]R. Meijers, R. Calarco, N. Kaluza, H. Hardtdegen, M. Ahe, H. Bay, H. Luth, M. Buchmeier, and D. Burgler, J. Cryst. Growth **283**, 500 (2005).
[10]A. Polyakov, N. Smirnov, A. Govorkov, A. Shlensky, and S. Pearton, J. Appl. Phys. **95**, 5591 (2004).
[11]C. McHargue, P. Sklad, and C. White, Nucl. Instrum. Methods Phys. Res. B **46**, 79 (1990).
[12]M. Borowski, A. Traverse, and J.-P. Eymery, Nucl. Instrum. Methods Phys. Res. B **122**, 247 (1997).
[13]W. Skorupa, Y. Yankov, E. Tyschenko, H. Fröb, T. Böhme, and K. Leo, Appl. Phys. Lett. **68**, 2410 (1996).

APPLIED PHYSICS LETTERS **89**, 223129 (2006)

Defect induced formation of $CoSi_2$ nanowires by focused ion beam synthesis

C. Akhmadaliev,[a] B. Schmidt, and L. Bischoff
Research Center Rossendorf, Institute of Ion Beam Physics and Materials Research, P.O. Box 51 01 19, 01314 Dresden, Germany

(Received 19 September 2006; accepted 21 October 2006; published online 1 December 2006)

Cobalt implantation with a focused ion beam (FIB) was applied to study ion beam synthesis of cobalt disilicide nanowires in silicon. Two mechanisms of $CoSi_2$ nanowire formation were investigated: (a) conventional synthesis by Co^{++} FIB implantation at elevated temperatures into silicon along in-plane ⟨110⟩ Si crystal direction and subsequent annealing and (b) self-aligned $CoSi_2$ nanowire growth in cobalt supersaturated silicon on FIB-induced defects at room temperature during subsequent annealing. The obtained $CoSi_2$ nanowires are 20–100 nm in diameter and several micrometers long. © *2006 American Institute of Physics*. [DOI: 10.1063/1.2400068]

One-dimensional crystalline nanostructures such as semiconducting (Si, Ge, GaN, and InP) and metallic (Au and Ag) nanowires (NWs) have been intensively studied in the past decade.[1,2] It is advantageous for device application if it is possible to produce the desired NWs directly on or under the surface of suitable substrates, e.g., silicon wafers. By means of optical or electron beam lithography submicron silicide structures have been made.[3] These materials are used as low-resistive contacts, gates, and interconnecting lines in very-large-scale integrated circuits. Many efforts have been made to fabricate silicide nanostructures employing the bottom-up approach without elaborate microlithography. For instance, the spontaneous and self-aligned growth of 3–10 nm thick $CoSi_2$ NWs from Co nanoparticles deposited onto the Si surface was described.[4] $CoSi_2$ NWs have been reported utilizing different techniques, such as implantation based ion beam synthesis[5] (IBS) and mesotaxy[6] leading to the formation of wires by growth and coalescence of silicide precipitates during high-temperature annealing.[7] Focused ion beam (FIB) implantation of Co^+ ions[8] and subsequent conventional as well as flash lamp annealing were reported to synthesize nanostructures and NWs with feature dimensions of about 200 nm.[9,10] In this letter the formation of $CoSi_2$ NWs in silicon using FIB IBS and the influence of the defect generation during FIB implantation on the NW growth will be reported.

(100)- and (111)-oriented *n*-type (10–20 Ω cm) silicon substrates were chemically cleaned and thermally oxidized in dry O_2 at 1050 °C in order to grow a 100 nm thick SiO_2 layer. The SiO_2 layer was lithographically patterned to form appropriated oxide windows. The SiO_2 windows were aligned with respect to the ⟨110⟩ crystalline direction to allow a fast preliminary alignment of the sample on the *XY* stage in the FIB chamber relative to the scan direction of the FIB.[11] Subsequently, the samples were locally implanted by a digitally scanned 60 keV Co^{++}-FIB with an ion current in the range of 5–20 pA. The corresponding mean penetration depth of the ions is about 53 nm. The cobalt ions were extracted from a liquid metal ion source operating with a $Co_{36}Nd_{64}$ alloy (melting point of 566 °C).[12] Separation of the Co^{++} from the other ion species coming from the source was done by means of an $E \times B$-type mass filter in the FIB column (Canion 31Mplus, Orsay Physics) which allows the focusing of the Co^{++} ion beam into a spot diameter of 20–50 nm. For the study of the conventional IBS of $CoSi_2$ NWs (phase separation through precipitation and wire ripening during thermal treatment) and their decay into chains of nanoparticles due to NW instabilities, the samples were implanted with high doses (1×10^{16}–2×10^{17} cm^{-2}). To avoid defect accumulation and amorphization of Si during implantation the sample temperature was kept at about 420–450 °C. The implantation was done in a digital mode with a short pixel dwell time (<2 μs) and a long relaxation time of more than 100 μs (time between two exposures of the same pixel). Additionally, the scan direction of the FIB was varied relative to the chosen crystalline direction for the study of the stability of NW growth. Usually, the FIB writing direction was parallel to one of ⟨110⟩ directions on the Si surface which correspond to the energetically favored growth direction of the $CoSi_2$ nanocrystals.[13] In order to investigate the influence of locally FIB induced radiation defects on the $CoSi_2$ NW growth, the samples were implanted at lower ion doses (10^{14}–10^{16} cm^{-2}) at room temperature. Before the FIB implantation the rear side of these samples was covered with a 10 nm Co layer by thermal evaporation to achieve a high concentration of Co in the Si bulk and a supersaturation of Co during cooling down of the samples in the thermal treatment. It was assumed that the amount of Co atoms above the solubility limit will precipitate preferentially on $CoSi_2$ nanoparticles or on defects formed in the FIB trace. After FIB irradiation the samples were annealed by a two step thermal treatment (30 min at 600 °C and 60 min at 1000 °C in dry N_2 atmosphere).[11,14,15] In order to improve the image contrast for scanning electron microscopy investigations of the NWs a short reactive ion etching in CF_4 for 20–40 s was carried out to remove the 15–20 nm thick silicon top layer covering the buried $CoSi_2$ nanostructures. As it is shown in Fig. 1(a) conventionally synthesized NWs have lengths of 10–20 μm and diameters of 100–150 nm in the case of FIB implantation along the chosen ⟨110⟩ direction. A small deviation of the FIB trace from this direction leads to a decay of the NW into shorter ones [Fig. 1(b)]. Larger angles of misalignment result the formation of chains of more or less prolonged $CoSi_2$ nanoparticles [Fig. 1(c)].

[a]Electronic mail: c.akhmadaliev@fz-rossendorf.de

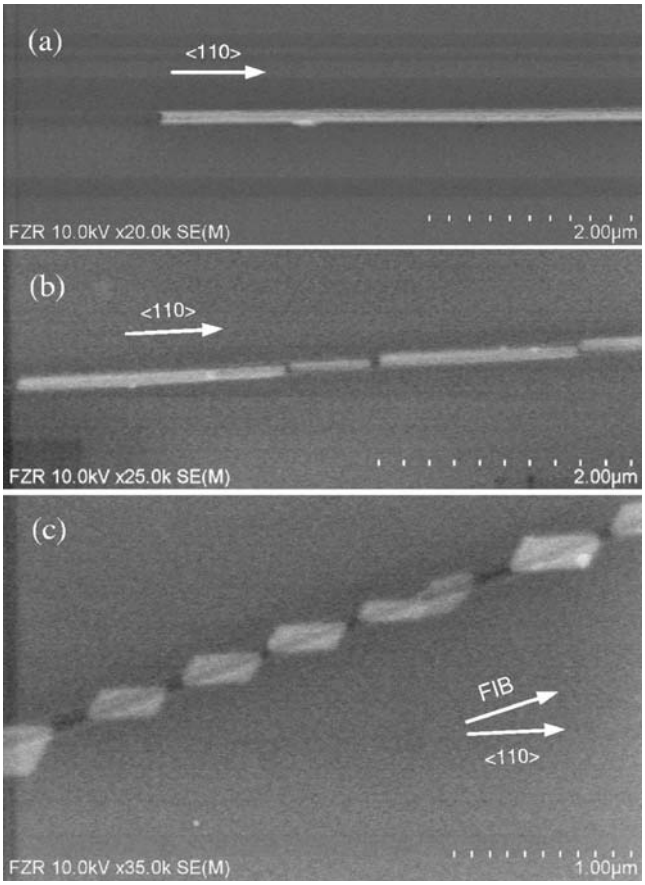

FIG. 1. $CoSi_2$ nanowires in (100)-Si (a), in (111)-Si with a small misalignment (b), and with a misalignment angle of about 15° (c). Co^{++} FIB implantation dose was 1×10^{17} cm^{-2}.

A further reduction of the NW diameter can be expected by decreasing the concentration of cobalt atoms implanted in silicon at the same FIB spot. NWs synthesized at lower doses of 1×10^{16}–3×10^{16} cm^{-2} are not stable and decay into shorter NW fragments with a diameter of about 50 nm [Fig. 2(a)]. Moreover, because of the existence of the other ⟨110⟩ crystalline directions crossing the FIB trace, there is a certain probability of spontaneous and self-aligned NW growth in these directions [Fig. 2(b)]. One of the possible reasons of this effect should be related to the well known {311} defects in silicon induced during FIB implantation.[16] It can be assumed that the generation of {311} defects in the silicon crystal plays a crucial role in the $CoSi_2$ nanowire formation process. {311} defects consist of excess Si interstitials coming from FIB induced point defects which rapidly agglomerate at the beginning of annealing (temperature ramp up).[17] They are relatively stable at temperatures below 600 °C, at 800 °C they grow up to 150 nm in length via nonconservative Oswald ripening[18] and at 850–1000 °C they anneal out in a few minutes forming stable dislocation loops and ejecting silicon interstitials. These defects are closed between two {311} planes and are elongated in the ⟨110⟩ direction.[17] From transmission electron microscopy (TEM) investigations it is known that after annealing at 800 °C the {311} rodlike defects can also transform into similar ones embedded in {111} habit planes and elongated in the ⟨110⟩ direction.[19] During annealing the implanted and solved Co atoms diffuse and can be gettered in the {311} defects. They react with silicon and form silicide precipitates along these defects, i.e., along the

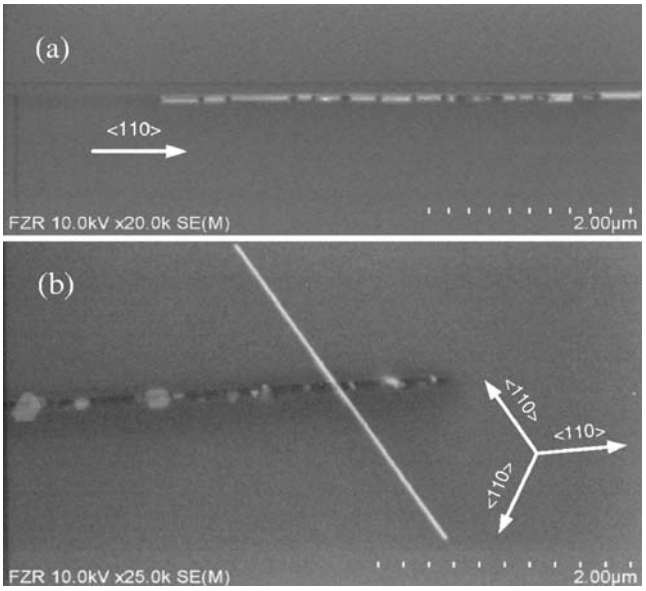

FIG. 2. $CoSi_2$ NW in (100)-Si implanted with a dose of 7×10^{16} cm^{-2} (a) and in (111)-Si, implanted with a dose of 3×10^{16} cm^{-2} (b).

⟨110⟩ direction which is the most preferable direction for the one-dimensional $CoSi_2$ crystalline structure growth. This process stabilizes the defect structure and hinders dissolution of the rodlike defects. Subsequent Oswald ripening of the silicide precipitates along this ⟨110⟩ direction leads to the formation and alignment of oblong initial $CoSi_2$ nanoparticles at the defect position. During further heating the solved cobalt atoms are still available around the nanoparticles and diffuse to them promoting the growth of crystalline $CoSi_2$ NWs. This finally results the formation of some micrometer long NWs.

In order to prove this assumption, a high concentration of defects was introduced by FIB line implantation of Co^+ and Co^{++} as well as of other ions (Nd^{++}, Ga^+, Au^+, and Si^{++}) at doses of 10^{14}–10^{15} cm^{-2} at room temperature. The samples were covered with a 10 nm Co film on the rear side. After the FIB irradiation these samples were annealed at 1000 °C for different times in N_2 ambient. The cobalt layer on the rear side serves as a reservoir of cobalt atoms during annealing. At this temperature the solubility and the diffusivity of Co in Si are 5×10^{14} cm^{-3} and 1×10^{-4} cm^2 s^{-1}, respectively. Already after 10 min of annealing short (200–500 nm) and 10–30 nm thin NWs self-aligned along the ⟨110⟩ directions were observed independent on the kind of implanted ions [Fig. 3(a)]. This effect was also clearly seen in the case of a dotlike FIB implantation (without pixel overlapping). It is essential that at lower doses (10^{14}–10^{15} cm^{-2}) the NW growth occurs more effectively than at higher ones, presumably depending on the defect structure complexity. After 30 min annealing the wires reach several micrometers in length and 20–50 nm in diameter [Fig. 3(b)]. Similar results were obtained using, for example, Ga^+ FIB irradiation [Fig. 3(c)] and irradiation with the other ions (not shown here). It should be mentioned here that these NWs are very stable (e.g., for some hours at 1000 °C), but it is difficult to provide a better controlled growth of such nanowires because of the spontaneous nature of the defect generation.

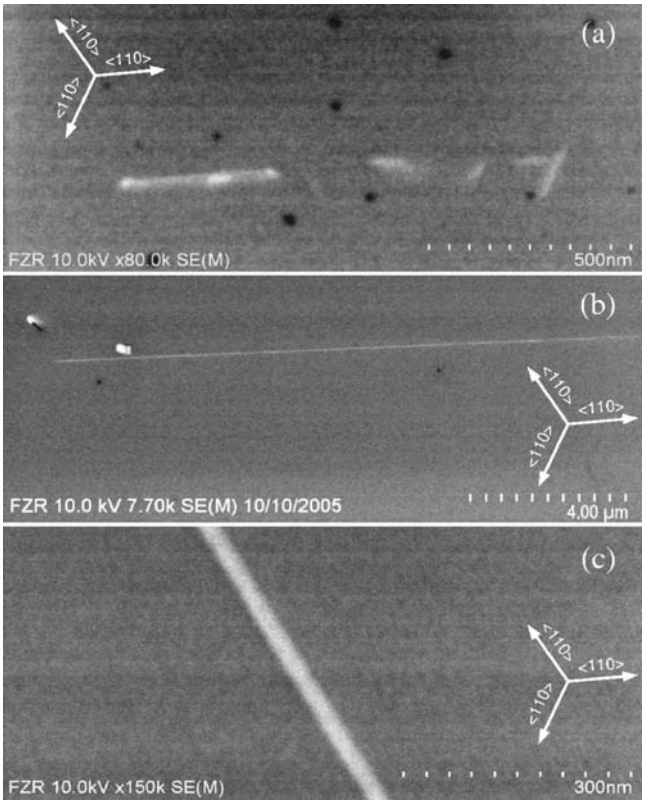

FIG. 3. $CoSi_2$ NWs in (111)-Si after 60 keV Co^{++} FIB implantation and annealing at 1000 °C for 10 min (a), for 30 min (b), and after 30 keV Ga^+ FIB implantation and annealing at 1000 °C for 30 min (c).

In conclusion, conventional ion beam synthesis of $CoSi_2$ NWs using high dose FIB implantation and subsequent annealing was demonstrated. The growth stability of long NWs embedded in Si sensitively depends on the accuracy of FIB trace alignment relative to the preferred growth directions, namely, the in-plane ⟨110⟩ Si crystal directions. A small misalignment of the FIB trace of a few degrees leads to the decay of the $CoSi_2$ NWs into shorter parts and a larger deviation causes a chain of $CoSi_2$ nanoparticles. Furthermore, it was observed that the stability of continuous NW growth is reduced with lowering the implantation dose. The controlled alignment of silicide NW growth is hindered by FIB induced defects initiating a spontaneous $CoSi_2$ NW growth along other in-plane ⟨110⟩ Si crystal directions. In contrast to conventional ion beam synthesis of $CoSi_2$ NWs by high dose FIB implantation along a narrow trace, the defect induced and self-aligned NWs seem to be more stable.

The authors would like to thank K.-H. Heinig and L. Röntzsch for helpful discussions of theoretical aspects. This work was financially supported by Deutsche Forschungs gemeinschaft under Priority Program 1165 Contract No. SCHM1490/6-1.

[1]G. Fasol, Science **280**, 545 (1998).
[2]C. Thelander, P. Agarwal, S. Brongersma, J. Eymery, L. F. Feiner, A. Forchel, M. Scheffler, W. Riess, B. J. Ohlsson, U. Gösele, and L. Samuelson, Mater. Today **9**, 28 (2006).
[3]A. Alberti, F. La Via, V. Raineri, and E. Rimini, J. Appl. Phys. **86**, 3089 (1999).
[4]J. D. Carter, G. Cheng, and T. Guo, J. Phys. Chem. B **108**, 6901 (2004).
[5]A. E. White, K. T. Short, R. C. Dynes, J. P. Garno, and J. M. Gibson, Appl. Phys. Lett. **50**, 95 (1987).
[6]S. Mantl, J. Phys. D **31**, 1 (1998).
[7]S. Mantl, Mater. Sci. Rep. **8**, 1 (1990).
[8]L. Bischoff, Ultramicroscopy **103**, 59 (2005).
[9]S. Hausmann, L. Bischoff, J. Teichert, M. Voelskow, D. Grambole, F. Herrmann, and W. Möller, J. Appl. Phys. **72**, 2719 (1998).
[10]L. Bischoff, K.-H. Heinig, J. Teichert, and W. Skorupa, Nucl. Instrum. Methods Phys. Res. B **112**, 201 (1996).
[11]L. Bischoff, B. Schmidt, Ch. Akhmadaliev, and A. Mücklich, Microelectron. Eng. **83**, 800 (2006).
[12]E. Hesse, L. Bischoff, and J. Teichert, J. Phys. D **27**, 427 (1994).
[13]D. P. Adams, S. M. Yalisove, and D. J. Eaglesham, J. Appl. Phys. **76**, 5190 (1994).
[14]C. Akhmadaliev, L. Bischoff, and B. Schmidt, Mater. Sci. Rep. **C26**, 818 (2006).
[15]S. Mantl, R. Jebasinski, and D. Hartmann, Nucl. Instrum. Methods Phys. Res. B **59/60**, 666 (1991).
[16]D. J. Eaglesham, P. A. Stolk, H.-J. Grossmann, and J. M. Poate, Appl. Phys. Lett. **65**, 2305 (1994).
[17]A. Claverie, B. Colombeau, B. de Mauduit, C. Bonafos, X. Hebras, G. Ben Assayag, and F. Cristiano, Appl. Phys. A: Mater. Sci. Process. **A76**, 1025 (2003).
[18]P. Calvo, A. Claverie, N. Cherkashin, B. Colombeau, Y. Lamrani, B. de Mauduit, and F. Christiano, Nucl. Instrum. Methods Phys. Res. B **216**, 173 (2004).
[19]S. Boninelli, N. Cherkashin, A. Claverie, and F. Cristiano, E-MRS Spring Meeting 2006, Nice, France, 29 May–2 June 2006 (unpublished).

APPLIED PHYSICS LETTERS **89**, 193505 (2006)

Determination and evolution of tunneling distances in Ge nanocrystal based memories

V. Beyer[a)] and J. von Borany
Forschungszentrum Rossendorf, Institute of Ion Beam Physics and Materials Research, P.O. Box 51 01 19, D-01314 Dresden, Germany

M. Klimenkov
Forschungszentrum Karlsruhe, Institute for Materials Research I, P.O. Box 36 40, D-76021 Karlsruhe, Germany

(Received 27 July 2006; accepted 27 September 2006; published online 9 November 2006)

A Ge nanocrystal layer embedded in a thin gate oxide was prepared by ion beam synthesis in direct-tunneling distance to the Si substrate. The write performance was investigated in metal-oxide-semiconductor capacitors by means of capacitance measurements. With the experimental data and calculations using a floating-gate-like approach, the distribution of the tunneling oxide thickness d_{tox} can be determined in high precision confirmed by high-angle annular dark-field scanning transmission electron microscopy imaging. The evolution of d_{tox} during heat treatment is discussed in terms of Ostwald ripening; i.e., d_{tox} increases with annealing time. © *2006 American Institute of Physics*. [DOI: 10.1063/1.2387900]

Multidot memories are expected to replace classical floating-gate-based flash devices in the future.[1] The approach includes the nanocrystal memory[2] where preferably Si or Ge nanocrystals (NC's) embedded in thin gate oxides are used as storage nodes.[2,3] Short write/erase cycles with ultralow power consumption and high endurance have been achieved using a direct-tunneling distance (<3.0 nm) between the NC's and the Si substrate/device channel, but this is connected to a tradeoff of a short data retention (minutes or seconds).[4,5] As a consequence, the performance of such a memory is more "quasi-nonvolatile" or "long refresh dynamic" than really nonvolatile strongly depending on the tunneling distance. In this letter, we consider an ion-beam synthesized layer of Ge NC's in a thin SiO_2 film which is located very close ($\lesssim$2 nm) to the Si/SiO_2 interface. By means of capacitance-voltage (C-V) measurements at metal-oxide-semiconductor (MOS) capacitors, the write performance for charging of the NC's with holes is studied. The experimental data are compared with the write characteristics calculated in a floating-gate-like approach, which enables a prediction of the flatband voltage shift for write times of microseconds or even below. It is shown that the measured write characteristics allow one to evaluate very precisely the distribution of the NC distance to the Si/SiO_2 interface. The evolution of the mean distance during annealing is discussed in terms of Ostwald ripening.

A 20 nm thick gate oxide was thermally grown on ⟨100⟩ p-type Si (10 Ω cm). Ion implantation of 12 keV $^{74}Ge^+$ ions was performed at a dose of 5×10^{15} cm^{-2} at room temperature. After standard cleaning in H_2O_2/H_2SO_4 rapid thermal annealing was carried out at 950 or 1050 °C for 30 s in Ar. MOS capacitors (A=0.1 mm^2) were prepared by Al sputtering, photolithographic patterning, and 400 °C furnace annealing in N_2 for 15 min. The Ge NC distribution in the gate oxide was characterized by scanning transmission electron microscopy (STEM) using a high-angle annular dark-field (HAADF) detector (acceptance angle about 2.8°) in a FEI Tecnai 20 FEG microscope operating at 200 kV. The write characteristic is obtained by two sequenced negative gate voltage pulses applied to the MOS capacitors, a programming ($-3\ \mathrm{V}\geqslant V_{prog}\geqslant -8\ \mathrm{V}$ with duration of $3\ \mathrm{ms}\leqslant t_{prog}\leqslant 30\ \mathrm{s}$) and a smaller read pulse ($|V_{read}|<|V_{prog}|$ with $t_{read}=t_{prog}$), while the C-V data $C(V_{read})$ were recorded to obtain the flatband voltage shift ΔV_{FB}.

Annealing during ion beam synthesis (IBS) of Ge NC's in thin SiO_2 films leads to a significant redistribution of the as-implanted Ge profile towards the Si/SiO_2 interface.[6–8] As confirmed by STEM in Fig. 1, a layer of Ge NC's forms in the oxide close to the interface. The distance between the NC's and the Si substrate, i.e., the tunneling distance d_{tox}, varies between about 0.6 and 2.5 nm.

The transient charging dQ_{NC}/dt of the Ge NC's (Q_{NC} is the effective charge density of the NC layer) is calculated in a floating-gate-like approach[4,9] according to

$$\frac{dQ_{NC}}{dt}=\left(\frac{\pi}{4}d_{NC}^2N_{NC}\right)J_{DT}-J_{FN}. \quad (1)$$

For negative gate voltages and low applied oxide fields ($E_{ox}<7$ MV/cm) the Fowler-Nordheim tunneling current

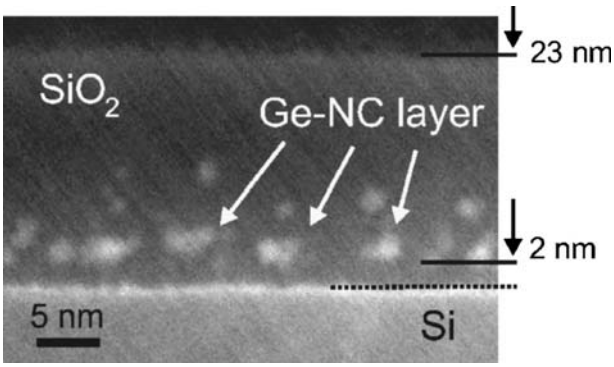

FIG. 1. HAADF STEM image of the NC's containing oxide (950 °C annealing). The Ge NC's are visible as bright spots.

[a)]Electronic mail: v.beyer@fz-rossendorf.de

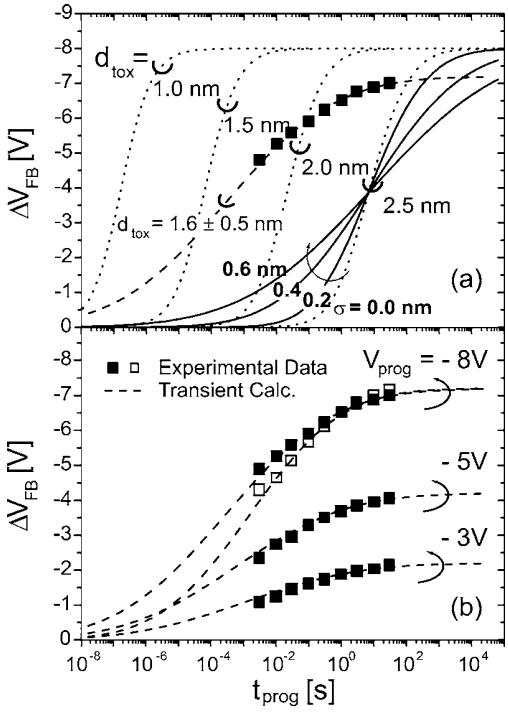

FIG. 2. (a) Comparison of the measured flatband voltage shift ΔV_{FB} ($V_{prog}=-8$ V) obtained for 950 °C annealing (■) with the simulated programming characteristics for different spatial distributions of the Ge NC's, (i) 1.0 nm$\leqslant d_{tox}\leqslant$2.5 nm const, i.e., $\sigma=0$ (dotted lines) and (ii) $d_{tox}=2.5$ nm with 0.2 nm$\leqslant\sigma\leqslant$0.6 nm (straight lines). The dashed line indicates the best fit of the experimental result with $d_{tox}=(1.6\pm0.5)$ nm and $V'_{gate}=-7.2$ V. (b) The calculated distribution of d_{tox} holds for a series of transient programming characteristics with different programming voltages V_{prog}. The experimental data for the sample annealed at 1050 °C are shown (□) together with a best fit for $d_{tox}=(1.75\pm0.4)$ nm ($V_{prog}=-8$ V).

(J_{FN}) of electrons from the gate can be neglected. The NC's close to the Si substrate with size d_{NC} and density N_{NC} are charged by the respective direct-tunneling hole current density J_{DT}

$$J_{DT}=A\frac{E_{tox}^2}{\phi_b}\exp\left(-\frac{B[\phi_b^{3/2}-(\phi_b-|qV_{tox}|)^{3/2}]}{|E_{tox}|}\right), \qquad (2)$$

with $A=q^3m_0/(8\pi hm_{ox})$ and $B=8\pi\sqrt{2m_{ox}}/(3hq)$. The tunneling barrier for holes from the emitting Si valence band is $\phi_b=4.5$ eV with an effective hole mass in the oxide $m_{ox}=0.32m_0$, h is Planck's constant, q the elementary charge, and m_0 the free electron mass. Quantum confinement of the NC's is negligible as enough empty energy states are available for hole charging due to the relative band gap position of Ge to Si and a quenched band gap of the Ge NC's caused by oxygen passivation.[10] The electrical field across the tunneling oxide is given by $E_{tox}=V_{tox}/d_{tox}$, whereas the voltage drop across the tunneling oxide V_{tox} can be easily calculated as usual for classical floating gate memories.[4,9]

The self-organized formation of a Ge NC layer close to the Si/SiO_2 interface by IBS is a statistical process of interface mixing, phase separation, and Ge redistribution, leading to a variable distance of the NC's to the Si substrate. Thus, a normalized Gaussian distribution of d_{tox} with a standard deviation of σ is introduced. NC's far in the oxide bulk are not considered due to their long distance to the Si substrate. The calculated programming characteristics for $\Delta V_{FB}(t,d_{tox},\sigma)\sim Q_{NC}(t)$ (Refs. 4 and 9) are shown in Fig. 2 in comparison

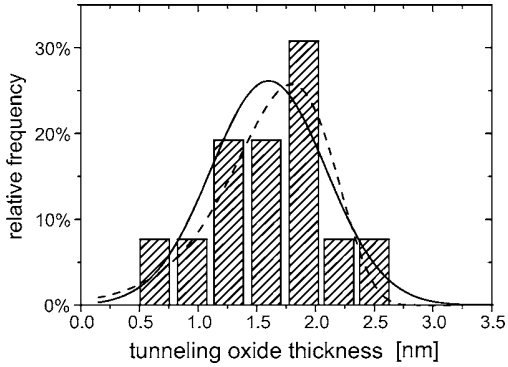

FIG. 3. Stack histogram of d_{tox} from the NC distribution in Fig. 1 with $d_{tox}=1.67$ nm at an average (error±0.13 nm) obtained from 26 Ge NC's over a 120 nm image size. The calculated Gaussian-like best-fit distribution of d_{tox} (1.6±0.5 nm) corresponding to Fig. 2 (950 °C) and, for comparison, a mirrored log-normal distribution (dashed line) are shown.

to experimental data, i.e., $\Delta V_{FB}=f(V_{prog},t_{prog})$. The structural NC parameters are derived from the TEM image in Fig. 1 ($d_{NC}=2$ nm and $N_{NC}=3\times10^{12}$ cm^{-2} for the NC's vicinal to the Si substrate). Thus, a ΔV_{FB} of −7 V corresponds to two to three holes per NC. For a constant d_{tox} ($\sigma=0$) the simulations [see Fig. 2(a)] result in characteristics with a stronger slope (dotted lines) compared to the measured data in a semilog plot. With increasing σ the slope gets weaker. A fit of the measured data leads to values of $d_{tox}=1.6$ nm and $\sigma=0.5$ nm, which holds for all programming voltages [Fig. 2(b)]. The charging saturates for $t_{prog}>10$ s for all characteristics at $\Delta V_{FB,max}=V'_{gate}$ (V'_{gate} is the gate voltage in the simulation). The constant difference to the experimental V_{prog} of $\simeq-0.8$ V corresponds mainly to the work function difference ϕ_{MS} between the Al gate and the p-Si substrate. The assumed Gaussian distribution of d_{tox} in the fitting procedure is a reasonable approximation as confirmed by Fig. 3.

For a higher thermal budget, i.e., during annealing at an enhanced temperature (1050 °C) or for a much longer annealing time at 950 °C, d_{tox} grows and its distribution narrows to $d_{tox}=1.75$ nm with $\sigma=0.40$ nm considering d_{NC} and N_{NC} to be constant [see Fig. 2(b)]. In case d_{tox} grows to the debit of the NC size with stable N_{NC}, one gets $d_{tox}=1.72$ nm for $d_{NC}=1.8$ nm ($\sigma=0.40$ nm is unaffected). Such minor changes of d_{tox} during annealing can hardly be recognized by STEM imaging which underlines the high sensitivity of the electrical characteristics. This is due to the fact that $\Delta V_{FB}(t)$ is much more affected by the exponential dependence in J_{DT} ($1/E_{tox}\sim d_{tox}$) than by a change of d_{NC}.

The evolution of d_{tox} is connected to the evolution of the NC size which follows a diffusion controlled ripening process (Ostwald ripening for $t\rightarrow\infty$) considering the substrate as a crystal with infinite radius [the NC size distribution has a log-normal shape in the early stage of the NC evolution (Fig. 3)]. Solving Poisson's equation for stationary diffusion fields, the solute concentration $c(\mathbf{r})$ leads, in an approximation for a medium consisting of N sources (monopoles) with strengths Ω_i (emitted atoms from the NC surface area per second) and known location $\mathbf{r}_i$, to[11,12]

$$c(\mathbf{r})\simeq c_u+\frac{1}{4\pi D}\sum_{i=1}^{N}\frac{\Omega_i}{|\mathbf{r}-\mathbf{r}_i|}. \qquad (3)$$

The mobility of an emitted monomer in the medium depends on the diffusion coefficient D. Like in electrostatics the dif-

fusion field caused by a single NC with radius R and source strength Ω_1 embedded in SiO_2 close to the Si/SiO_2 interface (z is the distance of the NC center to the Si substrate) can be calculated by an image source Ω_2 at distance $-z$ within the substrate ($\Omega_2=-\Omega_1$). At the NC surface the monomer concentration is $c(\mathbf{r}_1)=c_R$. A mean monomer concentration in the matrix is close to the equilibrium solubility at the substrate surface ($c_u=c_\infty$). These approximations together with the continuity equation (V_a is the atomic volume of the monomer)[12,13] expressed by

$$\Omega_1 = 4\pi D\left(\frac{c_R - c_\infty}{(1/R) - (1/2z)}\right) \quad \text{and} \quad \frac{4\pi}{V_a}R^2\frac{dR}{dt} = -\Omega_1 \tag{4}$$

lead to the nonlinear differential equation

$$\frac{dR}{dt} = -DV_aR_cc_\infty\frac{1}{R^2(1-R/2z)} \approx -\frac{dd_{\text{tox}}}{dt}, \tag{5}$$

with respect to the linearized Gibbs-Thomson relation $c_R=c_\infty(1+R_c/R)$ (R_c is the capillary length).[6] The evolution of the NC size by attachment or detachment of monomers is expressed by dR/dt, which is also proportional to the evolution of the tunneling oxide thickness ($d_{\text{tox}}=z-R$). Typically for Ostwald ripening, this leads to a decrease of the NC radius as

$$R(t) = (R_0^3 - 3\xi DV_aR_cc_\infty t)^{1/3} \approx z_0 - d_{\text{tox}}(t), \tag{6}$$

whereas the NC volume $[(R(t)^3)]$ dissolves in the late stage of ripening proportional to time. R_0 is the initial NC radius at an early stage ($t=0$) after the NC's have formed. With invariant NC center position z_0 the NC's dissolve with time in the same way as the tunneling distance d_{tox} increases. The variable ξ is between $1<\xi<2$ within the limits of $z\approx d_{\text{tox}}\gg R$ and $z\rightarrow R$ ($d_{\text{tox}}\rightarrow 0$); i.e., the closer the NC's are located to the Si/SiO_2 interface, the faster they dissolve. In addition to the interaction with the substrate, the NC's compete with each other in plane and above (Fig. 1). This enhances the dissolution of small, close NC's and stabilizes bigger, more distant ones (both relative to the Si substrate). As a consequence, d_{tox} grows and its distribution narrows with time which clearly confirms the experimental data and the respective model calculations.

The position of the storage nodes (here the Ge NC's) with respect to the Si substrate, i.e., the tunneling distance d_{tox}, was derived from write characteristics with high precision exceeding TEM imaging capability. A close agreement between experimental data and calculations based on a modified floating gate approach confirms direct tunneling as the dominant charge transfer process. Possibly occurring trap-assisted tunneling would be interpreted as a shortened d_{tox}. The general applicability of the model depends on the relevance of, e.g., quantum confinement effects which is connected to the NC material, density, and size. A higher thermal budget during IBS leads to an increase of d_{tox} which is explained, in agreement with the theory of Ostwald ripening, to be due to a dissolution of small NC's close to the Si substrate. This confirms the validity of the model calculations according to experimental data with respect to multidot memory device performance adjustment.

[1] 2003 edition of the ITRS, http://public.itrs.net/

[2] S. Tiwari, F. Rana, H. Hanafi, A. Hartstein, E. F. Crabbé, and K. Chan, Appl. Phys. Lett. **68**, 1377 (1996).

[3] H. I. Hanafi, S. Tiwari, and I. Khan, IEEE Trans. Electron Devices **43**, 1553 (1996).

[4] B. De Salvo, G. Ghibaudo, G. Pananakakis, P. Masson, T. Baron, N. Buffet, A. Fernandes, and B. Guillaumot, IEEE Trans. Electron Devices **48**, 1789 (2001).

[5] S. Tiwari, J. Wahl, H. Silva, and J. Welser, Appl. Phys. A: Mater. Sci. Process. **71**, 403 (2000).

[6] K. H. Heinig, T. Müller, B. Schmidt, M. Strobel, and W. Möller, Appl. Phys. A: Mater. Sci. Process. **77**, 17 (2003).

[7] V. Beyer and J. von Borany, in *Materials for Information Technologies*, edited by Zschech and Mikolajick (Springer, Berlin, 2005), pp. 139–147.

[8] J. von Borany, R. Grötzschel, K.-H. Heinig, A. Markwitz, B. Schmidt, W. Skorupa, and H.-J. Thees, Solid-State Electron. **43**, 1159 (1999).

[9] G. Groeseneken, H. Maes, J. VanHoudt, and J. Witters, in *Nonvolatile Semiconductor Memory Technology*, edited by Brown and Brewer (Wiley-IEEE, Piscataway, NJ, 1997), Chap. 1, pp. 1–88.

[10] A. Puzder, A. J. Williamson, J. C. Grossman, and G. Galli, J. Chem. Phys. **117**, 6721 (2002).

[11] P. W. Voorhees and M. E. Glicksman, Acta Metall. **32**, 2001 (1984).

[12] M. Strobel, S. Reiss, and K.-H. Heinig, Nucl. Instrum. Methods Phys. Res. B **120**, 216 (1996).

[13] T. Müller, Ph.D. thesis, TU Dresden, 2005.

APPLIED PHYSICS LETTERS **88**, 101918 (2006)

Alternating layers of vacancy-type and interstitial-type defects in Ge ion implanted silicon

R. Kögler[a)]
Forschungszentrum Rossendorf, PF 510119, D-01314 Dresden, Germany

A. Peeva
Institute of Solid State Physics, BAS, 72 Tzarigradsko Chaussee, 1784 Sofia, Bulgaria

A. Mücklich, F. Eichhorn, and W. Skorupa
Forschungszentrum Rossendorf, PF 510119, D-01314 Dresden, Germany

(Received 21 September 2005; accepted 30 January 2006; published online 10 March 2006)

The defect structure of Ge-implanted and annealed silicon was investigated. A stacked structure of alternating layers of vacancy-type defects (cavities) and interstitial-type defects (dislocation loops) was detected. These defects form a substructure within the basic dual structure consisting of a near surface vacancy-dominated and a deeper interstitial-dominated region. The appearance of vacancy clusters in the interstitial-dominated region and of dislocation loops in the vacancy-dominated region indicates significant vacancy-vacancy and interstitial-interstitial clustering in addition to the vacancy-interstitial defect recombination. The observed defect structure is in contrast to the widely accepted +1 model which predicts the *complete* local recombination of ion-generated vacancies and interstitials. Limits of the +1 model are discussed. © *2006 American Institute of Physics*.
[DOI: 10.1063/1.2186068]

Numerous studies were performed to investigate the residual damage in ion-implanted and annealed Si. Previous investigations showed, in addition to the damage generation by ion energy deposition, a spatial separation of the ion-induced vacancies and interstitials due to the forward momentum of ions.[1–6] The resulting defect structure can be explained by the so-called +1 model which assumes the complete local recombination of ion-generated vacancies and interstitials.[6,7] According to this model the damage state after annealing is characterized by the implanted atoms (+1), by excess vacancies which remain after the complete vacancy-interstitial recombination in the depth region around half of the mean projected ion range (R_P) and by excess interstitials remaining in the region at R_P. So far, evidence for the +1 model was always based only on the observation of interstitials.[8,9] Vacancy clusters are difficult to observe directly.[4,5] Clusters with a number $10 \leqslant n \leqslant 20$ of vacancies were detected in ion-implanted Si at the depth of $1/2R_P$ by positron annihilation spectroscopy (PAS).[10] Larger vacancy clusters with diameters of $d \geqslant 2$ nm ($n \geqslant 220$) were visualized by cross-sectional transmission electron microscopy (XTEM) applied on cleaved specimens.[11] In addition, Cu or Au atoms, intentionally incorporated into ion-implanted Si, are preferentially trapped by vacancy clusters.[3,4,6] The Cu depth profile measured by secondary ion mass spectrometry (SIMS) closes the gap of vacancy cluster detection for cluster sizes $20 \leqslant n \leqslant 220$ and agrees very well with PAS and XTEM results.[10,12] Cu profiles can be taken as an excellent marker for vacancy defects despite the fact that a fraction of Cu is also trapped at the open volume related to interstitial defects.[10]

In the present study, both interstitial-type and vacancy-type defects are investigated in more detail. Ge ions were implanted with ion energies of 750 and 900 keV to fluences between 2.5×10^{14} and 1×10^{15} cm^{-2} into n-type Cz–Si (100) substrates (1–5 Ω cm). Implants were performed at room temperature with ion current densities of

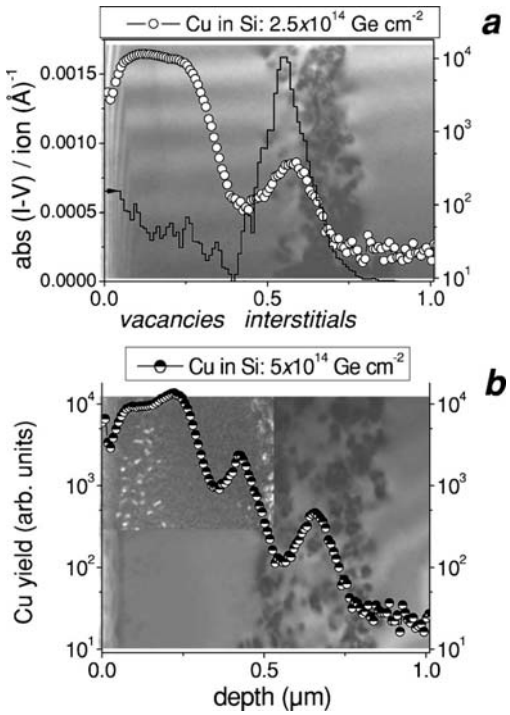

FIG. 1. Overlays of Cu depth distributions (arb. units, right scale) for Si samples implanted with 750 keV Ge ions to 2.5×10^{14} cm^{-2} (a) and 5×10^{14} cm^{-2} (b) after annealing of 900 °C, 30 s and the corresponding bright field XTEM images of cleaved specimen after annealing of 30 min. The weak beam micrograph inset in Fig. 1(b) (top left) shows dislocation loops close to the surface as bright spots. The calculated depth distribution of excess defects, the difference of interstitials and vacancies, is indicated in Fig. 1(a) (black line). The excess defect profile also includes the +1 atom.

[a)]Author to whom correspondence should be addressed; electronic mail: r.koegler@fz-rossendorf.de

7.7×10^{10} cm^{-2} s^{-1} (750 keV) and 1.5×10^{11} cm^{-2} s^{-1} (900 keV). The samples were annealed at 900 °C for 30 s or 30 min in Ar ambient and subsequently contaminated with Cu by implantation of 3×10^{13} cm^{-2} with 20 keV ion energy into the sample rear side. Cu atoms were redistributed throughout the sample by a thermal treatment of 700 °C for 3 min with reproducible cooldown cycle. Analysis of the samples (without Cu) was performed by x-ray diffraction and by XTEM as described elsewhere.[11] The Cu profiles were determined by SIMS.

Figure 1 shows overlays of Cu depth profiles after annealing at 900 °C for 30 s and XTEM micrographs taken after annealing for 30 min to have larger dislocation loops. In this way the depth distributions of interstitial-type defects (dislocation loops) and vacancy-type defects (Cu profile) can be compared. The results for the lower Ge fluence [Fig. 1(a)] correspond with the calculated excess defect distribution (black line) representing the +1 model.[6] The peak ratio of the Cu peaks, the $1/2R_P$ gettering peak and the R_P peak, is opposite to the calculated excess defect concentrations. This reflects the significantly higher gettering efficiency of vacancy defects at $1/2R_P$. In the case of the higher Ge fluence the TEM investigation reveals small amorphous islands in Si after implantation. However, no continuous amorphous layer was formed. There are some more gettering peaks in the Cu profile [Fig. 1(b)], one just at $x=0.4$ μm where the calculation shows no excess of vacancies or interstitials. The XTEM image in Fig. 1(b) demonstrates that the dislocation loops split in two layers. The Cu peaks at $x=0.4$ and 0.65 μm appear just alongside the dislocation loop layers. Some dislocation loops were also observed close to the surface at $x=0.05-0.15$ μm where they are admixed within the

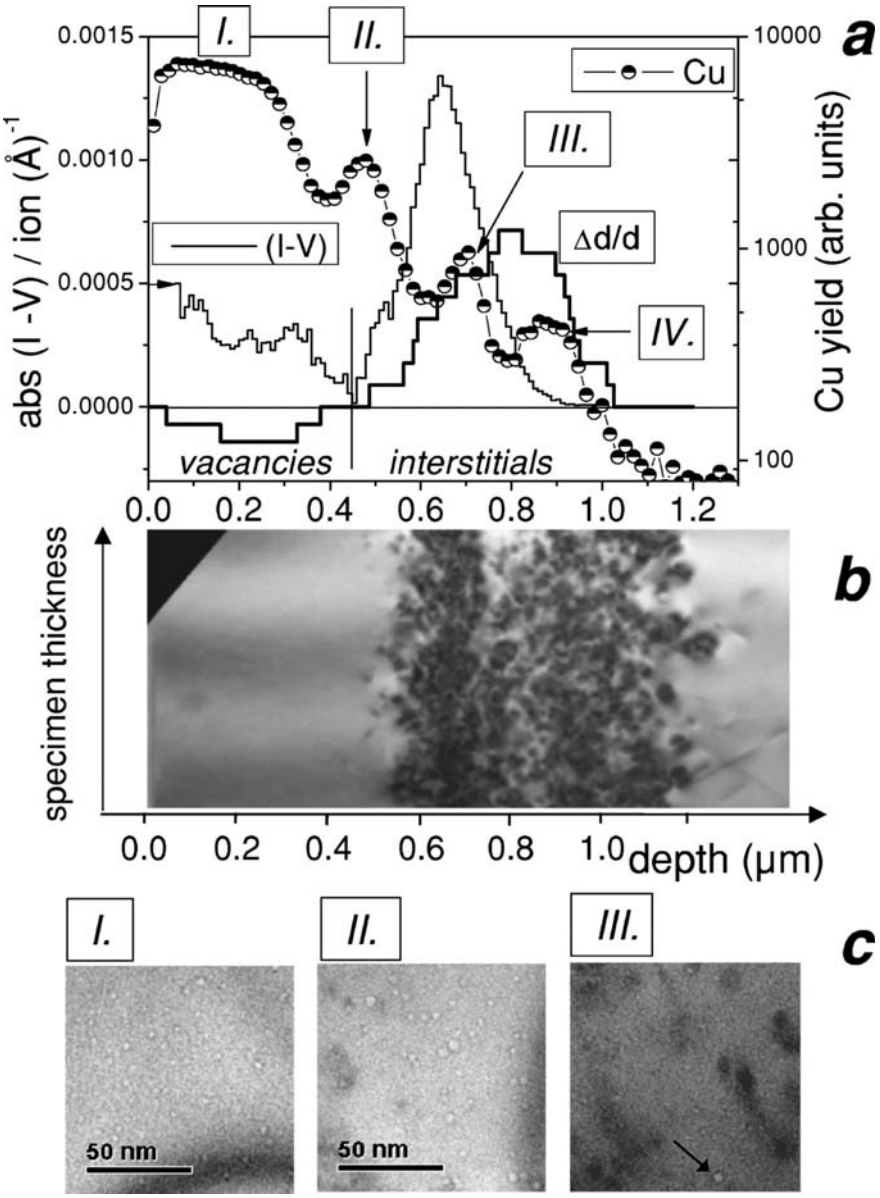

FIG. 2. Comparison between Cu depth distribution (arb. units, right scale) and strain profile ($\Delta d/d$, left scale without axis title) in Si after Ge ion implantation with 900 keV, 1×10^{15} cm^{-2} and annealing at 900 °C for 30 s and the profile of excess defects (*I-V*), calculated according to the +1 model (a). The bright field XTEM micrograph of cleaved specimen taken in (220) two beam case shows an overview of the distribution of interstitial-type dislocation loops (b). Micrographs taken in higher magnification, kinematical conditions, underfocus (c) show cavities as bright spots with dark ring for different depth regions corresponding to the Cu peaks labeled in Fig. 2(a).

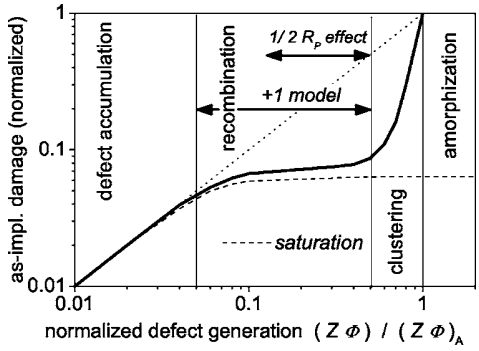

FIG. 3. Scheme of damage evolution during implantation vs the accumulated defect generation normalized by the amorphization level (Z: defect generation per ion, Φ: ion fluence). Defect reactions controlling the defect state after annealing are indicated in the four different sections. In the defect clustering section the $+1$ model is not valid. The defect state is controlled by vacancy and interstitial clustering in addition to vacancy-interstitial recombination. The straight dotted line indicates the path of damage accumulation without *in situ* dynamical annealing. The dashed line represents the path of damage saturation.

vacancy-dominated region. These defects are inhomogeneously distributed in the sample and are better visible as bright spots in the weak beam micrograph inset. The results in Fig. 1(b) do not correspond with the +1 model. Experimental results for another sample are compared in Fig. 2 with the calculated as-implanted excess defect distribution (I-V). The strain profile, $\Delta d/d$, [Fig. 2(a)] agrees with the dual layer structure of the (I-V) distribution. The XTEM image [Fig. 2(b)] shows a layered arrangement of dislocation loops. No loops were observed in the vacancy region. However, four Cu peaks in the Cu profile [labeled *I*.-*IV*. in Fig. 2(a)] indicate a more complicated layering of the defects. Cavities were found in the regions of three Cu peaks by XTEM investigations [Fig. 2(c)]. The diameters of cavities were about 2.5 nm in the depth region *I* and were increased to maximum values of 5 nm in region *II*. The cavity density was reduced by 25% in this case. The concentration of vacancies bound in the cavities at Cu peak *II* is $c_V=3.6(\pm1)\times10^{19}$ cm^{-3}, a value higher than the calculated average of excess vacancy concentration of $c_{VE}=2.4\times10^{19}$ cm^{-3}. Few cavities [Fig. 2(c) arrow] were observed at Cu peak *III* ($x=0.7$ μm) between the dislocation loops. Cavities are supposed to be clusters of the excess vacancies [dislocation loops are "clusters" of interstitials on (111) planes].[5,6] The appearance of such defects in the excess defect "free" region and even more the appearance of cavities in the excess interstitial region or of interstitials in the excess vacancy region [Fig. 1(b)] is in contradiction to the *complete* local defect recombination predicted by the $+1$ model. Vacancy clustering inside the excess interstitial region indicates *incomplete* vacancy-interstitial recombination. Vacancy-type and interstitial-type defects in alternating layers or their mixing can be explained by coupled defect reaction processes. Cavities consume vacancies and dislocation loops consume interstitials. One process reinforces the other. The cavities in the excess defect free region at $x=0.45$ μm in Fig. 2(c) are larger than those in the vacancy-dominated region because of the proximity of interstitial-type defects. Such effects modify the implantation related dual structure of only one vacancy-dominated and one interstitial-dominated layer. The onset of substructure formation proceeds for a sufficiently high defect density, but without the formation of an homogenous amorphous layer. The atomic density of an amorphous island surrounded by solid crystalline bulk Si is different depending on whether it is formed in vacancy-rich or interstitial-rich material. Amorphous island formation conserves excess defects as the recrystallization of such amorphous islands restores the excess of vacancy or interstitial defects. The volume fraction of the amorphous regions could not be related to the excess defect formation.

Another process potentially forming a substructure of the defect profile is Ostwald ripening, but this process proceeds during longer annealing times and does not cause a spread out of defects.[9,13]

A scheme for the increase of damage versus the defect concentration is shown in Fig. 3. The main variable is the *accumulated* defect concentration, $Z\Phi$, where $Z(x)$ is the defect generation rate (vacancies per ion) and Φ is the ion fluence.[14] $Z\Phi$ is normalized to the amorphization level $(Z\Phi)_A$ to eliminate the dependency of other parameters as implantation temperature and ion current density which are held constant. The damage level during implantation either proceeds toward saturation (dashed line) or to progressive damaging and bulk amorphization.[14] For medium defect densities the local vacancy-interstitial recombination as the dominating process is almost completed when dislocation loops and cavities subsequently form. The $+1$ model is valid in this case. The lower limit of the defect recombination region at $(Z\Phi)/(Z\Phi)_A=0.05$ in Fig. 3 is taken according to Ref. 15. The process window in which vacancy and interstitial clustering proceeds simultaneously with defect recombination is estimated to be in therange of $0.5\leqslant(Z\Phi)/(Z\Phi)_A\leqslant1$. After completing the bulk amorphization, annealing proceeds via epitaxial layer recrystallization. The remaining defect structure (end of range defects) is controlled again by the $+1$ model.[9]

[1] M. Tamura, T. Ando, and K. Ohyu, Nucl. Instrum. Methods Phys. Res. B **59**, 572 (1991).
[2] O. W. Holland, L. Xie, C. Nielson, and D. S. Zhou, J. Electron. Mater. **52**, 99 (1996).
[3] V. C. Venezia, D. J. Eaglesham, T. E. Haynes, A. Agarwal, D. C. Jacobson, H.-J. Gossmann, and F. H. Baumann, Appl. Phys. Lett. **73**, 2980 (1998).
[4] R. A. Brown, O. Kononchuk, G. A. Rozgonyi, S. Koveshinikov, A. P. Knights, P. J. Simpson, and F. Gonzalez, J. Appl. Phys. **84**, 2459 (1998).
[5] J. S. Williams, M. J. Conway, B. C. Williams, and J. Wong-Leung, Appl. Phys. Lett. **78**, 2867 (2001).
[6] R. Kögler, A. Peeva, J. Kaschny, W. Skorupa, and H. Hutter, Nucl. Instrum. Methods Phys. Res. B **186**, 298 (2002).
[7] K.-H. Heinig and H.-U. Jäger, Proceedings of First ENDEASD Workshop, Santorini, Greece, 21–22 April 1999, p. 297.
[8] P. A. Stolk, H.-J. Gossmann, D. J. Eaglesham, D. C. Jacobson, C. S. Rafferty, G. H. Gilmer, M. Jaraiz, J. M. Poate, H. S. Luftman, and T. E. Haynes, Appl. Phys. Lett. **81**, 6031 (1997).
[9] C. Bonafos, D. Mathiot, and A. Claverie, J. Appl. Phys. **83**, 3008 (1998).
[10] R. Krause-Rehberg, F. Bórner, F. Redmann, J. Gebauer, R. Kögler, R. Kliemann, W. Skorupa, W. Egger, G. Kögel, and W. Triftshäuser, Physica B **308–310**, 442 (2001).
[11] A. Peeva, R. Kögler, and W. Skorupa, Nucl. Instrum. Methods Phys. Res. B **206**, 71 (2003).
[12] A. Peeva, R. Kögler, W. Skorupa, J. S. Christensen, and A. Y. Kuznetsov, J. Appl. Phys. **95**, 4738 (2004).
[13] V. A. Borodin, K.-H. Heinig, and S. Reiss, Phys. Rev. B **56**, 5332 (1997).
[14] M. Posselt, L. Bischoff, J. Teichert, and A. Ster, J. Appl. Phys. **93**, 1004 (2003).
[15] Y. Zhong, C. Bailat, R. S. Averback, S. K. Ghose, and I. K. Robinson, J. Appl. Phys. **96**, 1328 (2004).

APPLIED PHYSICS LETTERS **89**, 151918 (2006)

Competition between damage buildup and dynamic annealing in ion implantation into Ge

M. Posselt,[a] L. Bischoff, D. Grambole, and F. Herrmann
Institute of Ion Beam Physics and Materials Research, Forschungszentrum Rossendorf, P.O. Box 510119, D-01314 Dresden, Germany

(Received 28 July 2006; accepted 23 August 2006; published online 13 October 2006)

Channeling implantation of Ga into Ge is performed at two very different ion fluxes (10^{12} and 10^{19} cm^{-2} s^{-1}), at two temperatures (room temperature and 250 °C), and at five different fluences. The fluence dependence of the range profiles and of the implantation damage is strongly influenced by defect accumulation and dynamic annealing. At 250 °C, the maximum lifetime of the defects is less than 10 s. On the other hand, at room temperature no significant annealing is found within the first 10 s after ion impact. The measured Ga depth profiles are reproduced very well by atomistic computer simulations. © *2006 American Institute of Physics*. [DOI: 10.1063/1.2360238]

In the past, the lack of a stable oxide on germanium and the inability to epitaxially grow thick germanium layers on silicon were serious obstacles to the integration of germanium into the mainstream Si-based technology. Recent advances, such as high-κ dielectrics[1] and germanium-on-insulator substrates,[2] have made germanium a promising candidate for future high-mobility devices. For these reasons, electrical doping of germanium by ion implantation and subsequent annealing has drawn a renewed interest.[3–5] The understanding of ion-beam-induced defect evolution in germanium is crucial for the application of this method. In this letter, the competing influence of ion flux and implantation temperature on the evolution of implantation damage is investigated. Compared to similar studies in the past,[6,7] the present work contains a number of new aspects: A focused ion beam (FIB) system is employed, which enables the use of ion fluxes that differ by seven orders of magnitude. The ions are implanted into a channeling direction, since in this case both the range and the damage profiles show a significant dependence on the defect evolution. The experimental results are discussed qualitatively, considering the accumulation, the annealing, and the lifetime of defects. The measured range profiles are reproduced by atomistic computer simulations.

The IMSA-Orsay Physics FIB system was used to perform 30 keV Ga^+ implantation into *n*-type (001) Ge. The direction of the ion beam was equal to the [001] axial channel direction of the Ge substrate. The FIB spot had a diameter of about 50 nm, and the beam current was 50±2 pA. Averaged over the intensity distribution within the beam spot, this corresponds to an ion flux of about 10^{19} cm^{-2} s^{-1}. During the FIB implantation, the beam was scanned meanderlike[8] over an area of 300×300 μm^2. The scan was performed step by step with a certain pixel dwell time (PDT) and with a distance between the centers of the pixels of about 70 nm. Here the term pixel denotes the region irradiated by the FIB spot during one step. Because of the small pixel size and the high thermal conductivity of Ge, the heating of the sample due to the FIB implantation can be neglected.[9]

The FIB implantation was performed at room temperature (RT) and at 250 °C using fluences between 5×10^{12} and 5×10^{14} cm^{-2}. Changing the PDT and/or the area over which the beam is scanned allows a wide variation of the ion flux which is effectively employed in the implantation. Two extreme cases were studied: (i) Each pixel was irradiated only once at the nominal flux of 10^{19} cm^{-2} s^{-1}, and the desired fluence was achieved by varying the PDT. (ii) A constant PDT of 1 μs was used, and many repetitions of the beam scan yielded the desired fluence. In this case the effective flux was estimated in the following manner. For a single ion impact, the lateral cross section σ_0 of a region with significant primary defect production was calculated by $\sigma_0 = S_n/E_c$, where S_n and E_c are the nuclear stopping cross section and the critical nuclear energy deposition (per atom) for defect formation, respectively.[10] The value of E_c should be lower than the nominal displacement threshold E_d since most atomic displacements are formed in a region of a collision cascade where the target structure is no longer perfect. Assuming that $E_c=0.25E_d$ (cf. Ref. 10) and a displacement threshold of 15 eV (cf. Refs. 11 and 12), the size of σ_0 is about 10 nm^2. Consequently, at the nominal flux of $\dot{D} = 10^{19}$ cm^{-2} s^{-1}, the average time $\tau_i = 1/\dot{D}\sigma_0$ between consecutive ion impacts into the same region is about 1 μs. That means that during the given PDT the overlap of regions with defects produced by different ions is not very probable. Therefore, the effective ion flux can be estimated by the division of 10^{19} cm^{-2} s^{-1} by the total number of pixels formed during the beam scan, leading to a value of about 10^{12} cm^{-2} s^{-1}.

The Ga range profiles were determined by secondary ion mass spectrometry (SIMS) at Evans Analytical Group employing a PHI Quadrupole instrument. The implantation damage was measured by channeling Rutherford backscattering spectrometry using a 3 MeV He^+ microbeam with a diameter of about 100 μm (micro-RBS/C).[13–15] The continuous lines in Figs. 1(a) and 1(b) show the measured Ga range profiles for the two widely different effective ion fluxes and for an implantation temperature of 250 °C. In the case of the high ion flux, the shape of the Ga depth profiles changes with increasing fluence, i.e., the peak region shows a stronger increase with fluence than the tail. This behavior is caused by the enhanced dechanneling of the incident ions due to the

[a]Author to whom correspondence should be addressed; electronic mail: m.posselt@fz-rossendorf.de

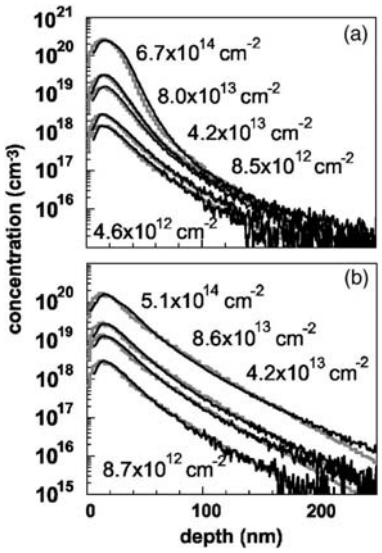

FIG. 1. Depth profiles of Ga obtained by 30 keV implantation into the [001] channeling direction of (001) Ge at 250 °C and at two widely different ion fluxes: 10^{19} cm^{-2} s^{-1} (a) and 10^{12} cm^{-2} s^{-1} (b). The black lines and the gray histograms show the SIMS data and the results of CRYSTAL-TRIM simulations, respectively.

accumulation of radiation damage. On the other hand, at the low ion flux the shape of the Ga range distributions is independent of the fluence, which is a clear indication for a complete dynamic annealing of the most relevant defects. The Ga depth distributions obtained at RT do not depend on the ion flux (Fig. 2). The fluence dependence of the profile shape shows that damage accumulation occurs during the implantation. From the micro-RBS/C spectra the relative disorder was determined by the normalization of the integral over the damage depth profile to the corresponding integral obtained at random incidence.[16] The results shown in Fig. 3 confirm the interpretation of the range distributions given above. Independent of the ion flux, at RT the implantation damage accumulates until the amorphization threshold of about 10^{14} cm^{-2} is reached. At 250 °C and a flux of 10^{19} cm^{-2} s^{-1}, the amorphization occurs at a higher fluence (5×10^{14} cm^{-2}). At a flux of 10^{12} cm^{-2} s^{-1}, dynamic annealing prevails. In this case, the calculation method described above yields 10 s for the average time between consecutive ion impacts into the same target region, whereas this time is equal to 1 μs for the high ion flux. Consequently, at 250 °C

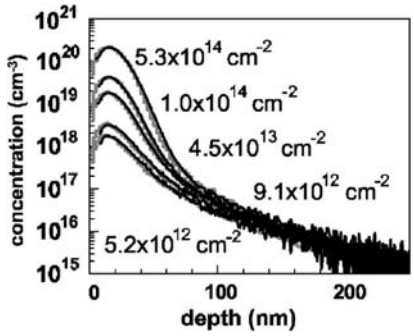

FIG. 2. Ga range distributions for RT implantations at 10^{19} cm^{-2} s^{-1}. The profiles determined for the case of the low ion flux (10^{12} cm^{-2} s^{-1}) are nearly identical. The meaning of lines and histograms is the same as in Fig. 1.

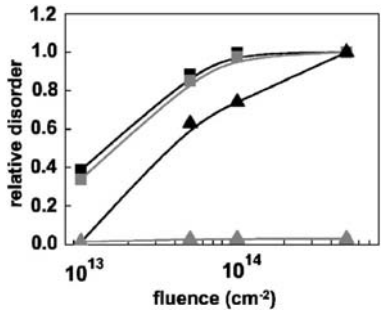

FIG. 3. Dependence of the relative disorder on the implantation fluence. The symbols show the data obtained from micro-RBS/C (squares: RT; triangles: 250 °C; black: 10^{19} cm^{-2} s^{-1}; gray: 10^{12} cm^{-2} s^{-1}). The lines have been drawn to guide the eye.

the lifetime of the most relevant defects is less than 10 s, whereas at RT it is much higher than 10 s. On the other hand, at 250 °C and for an ion flux of 10^{19} cm^{-2} s^{-1} some annealing occurs already within the first microsecond after an ion impact. The dechanneling of the implanted Ga^+ ions and the analyzing He^+ ions is mainly caused by defects that lead to significant lattice distortions, such as defect complexes and amorphous pockets. That means that some point defects may still exist for longer times and at higher temperatures than discussed above. The dynamic annealing observed in this work is mainly related to short-range recombination processes within the region of a collision cascade, such as close Frenkel pair annihilation, rearrangement of defect complexes, and recrystallization of amorphous pockets. The present data and their interpretation are consistent with previous results of Haynes and Holland[6,7] who investigated the temperature and flux dependence of the implantation damage in a similar temperature range and for low fluxes between 10^{11} and 10^{13} cm^{-2} s^{-1}.

The CRYSTAL-TRIM code was used to simulate the measured Ga depth profiles. The details of this program were already described elsewhere.[10,17,18] In the following, only the values of certain parameters are given, and the modeling of the damage buildup is discussed. On top of the (001) Ge substrate an amorphous Ge layer of 2.5 nm thickness was assumed. This layer models the deviation from the bulk atomic order in the vicinity of the surface. The parameters C_λ and C_{el} used in the model for the electronic energy loss of an incident ion[17] had the following values: $C_\lambda=0.9$ and $C_{el}=1$. The first parameter is employed to calculate the electronic energy loss averaged over all impact parameters, using the stopping cross section of Ziegler *et al.*[19] The second parameter describes the impact-parameter dependence of the electronic energy loss in a modified Oen-Robinson model.[17,20] A further parameter is the Debye temperature used in the model for the thermal displacements of the atoms. Similar to the case of Si (Ref. 21), the value of 290 K used for Ge is about 20% lower than the Debye temperature given in textbooks. This difference is related to the simplified description of the lattice vibrations. The case of complete dynamic annealing was simulated with the parameter values given above. The results are shown by the histograms in Fig. 1(b). A very good agreement with the SIMS profiles is obtained. In the CRYSTAL-TRIM code the damage buildup is described by a simple model which relates the nuclear energy deposition per target atom E_n^A and the probability p_d that the implanted ion collides with an atom of a damaged region.[10] The first quan-

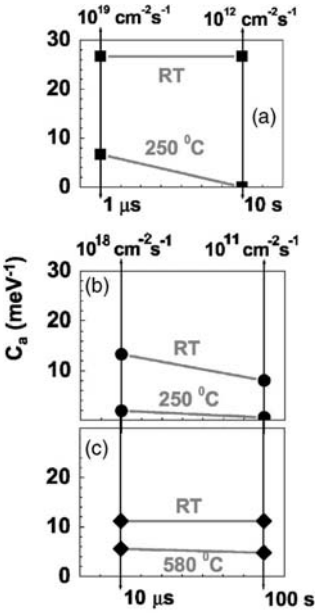

FIG. 4. Schematic representation of the quantity C_a which is as a measure of the normalized damage level (related to the nuclear energy deposition per target atom) formed after a single ion impact, for Ga implantation into Ge (a) as well as for Ge implantation into Si (b) and SiC (c) (Ref. 10). The symbols show the values of C_a. The lines have been drawn to guide the eye. On the abscissa both the ion flux and the time between successive impacts into the same target region are shown.

tity can be calculated exactly considering the ballistic processes. It increases monotonically during the implantation. The quantity p_d characterizes the damage level and depends on E_n^A, the ion species, the target temperature, and the ion flux. E_n^A and p_d are local quantities, i.e., their values vary in dependence on the considered volume element of the target. For low values of E_n^A the damage probability p_d increases linearly with E_n^A ($p_d = C_a E_n^A$). The local region is amorphized ($p_d = 1$) if p_d exceeds the threshold p_t ($p_t \leq 1$). C_a and p_t depend on the ion mass, the temperature, and the flux.[18] Note that the two model parameters are independent of fluence and energy. For the RT implantation of Ga into Ge, $C_a = 26.7$ meV^{-1} and $p_t = 0.2$ are assumed, whereas for 250 °C and 10^{19} cm^{-2} s^{-1}, the values $C_a = 6.67$ meV^{-1} and $p_t = 0.2$ are used. In the latter case, C_a is smaller because of the partial dynamic annealing. Figures 1(a) and 2 illustrate that using the simple damage buildup model, the measured SIMS profiles can be reproduced very well. The experimental values for the amorphization fluences are also reproduced.

The parameter C_a can be considered as a measure of the normalized damage level (related to the nuclear energy deposition per target atom) formed after a single ion impact. Figures 4(a)–4(c) compare the values of C_a used in this work with data for Si and SiC published recently.[10] Note that the comparison is only possible since the mass of the Ge ions used in Ref. 10 is nearly equal to that of the Ga ions and since the ion fluxes are similar. Therefore, the defect behaviors in the time interval between 10 μs and 10 s after an ion impact can be compared. The schematic representation in Fig. 4 shows that at RT the dynamic annealing of Ge and SiC is negligible and that for Ge the value of C_a is higher than that for Si and SiC. On the other hand, at RT the normalized damage level in Si diminishes faster than at 250 °C. In the case of Ge, the value of C_a decreases more rapidly with temperature and within a narrower temperature range than for Si and SiC. The explanation of the difference between the three target materials is related to the kinetics of the different defect types formed by a single ion impact. The understanding of these processes could be essentially improved if not only two widely different but a variety of ion fluxes would be considered at given temperatures. In this manner, the defect level at different times after an ion impact could be determined, and important information about unknown defect recombination and migration barriers could be obtained.

The authors thank C. Magee and M. S. Denker (Evans Analytical Group) for the SIMS analysis and for valuable comments.

[1] C. O. Chui, H. Kim, D. Chi, B. B. Triplett, P. C. McIntyre, and K. C. Saraswat, Tech. Dig. - Int. Electron Devices Meet. **2002**, 437.
[2] C. J. Tracy, P. Fejes, N. D. Theodore, P. Maniar, E. Johnson, A. J. Lamm, A. M. Paler, I. J. Malik, and P. Ong, J. Electron. Mater. **33**, 886 (2004).
[3] C. O. Chui, L. Kulig, J. Moran, W. Tsai, and K. C. Saraswat, Appl. Phys. Lett. **87**, 091909 (2005).
[4] A. Satta, E. Simoen, T. Clarysse, T. Janssens, A. Benedetti, B. De Jaeger, M. Meuris, and W. Vandervorst, Appl. Phys. Lett. **87**, 172109 (2005).
[5] A. Satta, T. Janssens, T. Clarysse, E. Simoen, M. Meuris, A. Benedetti, I. Hoflijk, B. De Jaeger, C. Demeurisse, and W. Vandervorst, J. Vac. Sci. Technol. B **24**, 494 (2006).
[6] T. E. Haynes and O. W. Holland, Appl. Phys. Lett. **59**, 452 (1991).
[7] T. E. Haynes and O. W. Holland, Appl. Phys. Lett. **61**, 61 (1992).
[8] S. Hausmann, L. Bischoff, J. Teichert, M. Voelskow, and W. Möller, J. Appl. Phys. **87**, 57 (2000).
[9] J. Melngailis, J. Vac. Sci. Technol. B **5**, 469 (1987).
[10] M. Posselt, L. Bischoff, J. Teichert, and A. Ster, J. Appl. Phys. **93**, 1004 (2003).
[11] J. J. Loferski and P. Rappaport, J. Appl. Phys. **30**, 1296 (1959).
[12] J. W. Mayer, L. Eriksson, S. T. Picraux, and J. A. Davies, Can. J. Phys. **46**, 663 (1968).
[13] F. Herrmann and D. Grambole, Nucl. Instrum. Methods Phys. Res. B **104**, 26 (1995).
[14] S. Hausmann, L. Bischoff, J. Teichert, D. Grambole, F. Herrmann, and W. Möller, Microelectron. Eng. **41/42**, 233 (1998).
[15] D. Grambole, F. Herrmann, V. Heera, and J. Meijer, Nucl. Instrum. Methods Phys. Res. B (submitted).
[16] *Handbook of Modern Ion Beam Material Analysis*, edited by J. R. Tesmer, M. Nastasi, J. C. Barbour, C. J. Maggiore, and J. W. Mayer (Materials Research Society, Pittsburgh, 1995).
[17] M. Posselt, Radiat. Eff. Defects Solids **130/131**, 87 (1994).
[18] M. Posselt, B. Schmidt, C. S. Murthy, T. Feudel, and K. Suzuki, J. Electrochem. Soc. **144**, 1495 (1997).
[19] J. F. Ziegler, J. P. Biersack, and U. Littmark, *The Stopping and Range of Ions in Solids* (Pergamon, New York, 1985).
[20] O. S. Oen and M. T. Robinson, Nucl. Instrum. Methods **132**, 647 (1976).
[21] M. Posselt, M. Mäder, R. Grötzschel, and M. Behar, Appl. Phys. Lett. **83**, 545 (2003).

APPLIED PHYSICS LETTERS **89**, 091908 (2006)

Increase of blue electroluminescence from Ce-doped SiO_2 layers through sensitization by Gd^{3+} ions

J. M. Sun,[a] S. Prucnal, W. Skorupa, and M. Helm
Institute of Ion Beam Physics and Materials Research, Forschungszentrum Rossendorf, POB 510119, 01314 Dresden, Germany

L. Rebohle and T. Gebel
Nanoparc GmbH, Bautzner Landstrasse 45, D-01454 Radeberg OT Rossendorf, Germany

(Received 27 May 2006; accepted 5 July 2006; published online 29 August 2006)

Efficient blue electroluminescence peak at around 440 nm with a maximum output power density of 34 mW/cm^2 was obtained from Ce and Gd coimplanted metal-oxide-semiconductor light emitting devices. Energy transfer from Gd^{3+} to Ce^{3+} ions was observed during the excitation process, leading to a more than threefold increase of the external quantum efficiency of the blue Ce^{3+} luminescence up to 1.8%. This is evidenced by the increase of the excitation cross section of Ce^{3+} ions from 4.8×10^{-13} to 3.5×10^{-12} cm^2 and the simultaneous reduction of the decay time and the impact cross section of Gd^{3+} ions. © *2006 American Institute of Physics*. [DOI: 10.1063/1.2338892]

Silicon based light emitters in the visible and ultraviolet (UV) are attractive for possible applications in integrated systems of solid-state microlighting, microdisplays, interchip optical coupling, and biological agent detection. Efficient green and UV electroluminescence (EL) at 543 and 316 nm has been demonstrated from metal-oxide-semiconductor light emitting devices (MOSLEDs) incorporating Tb and Gd implanted thermally grown SiO_2 layers.[1,2] Blue EL from $5d$-$4f$ transitions of Ce^{3+} in SiO_2 MOSLEDs has been reported as well.[3] However, the observed quantum efficiency is usually still not so high (~0.5%) due to the susceptibility of the $5d$ states of Ce^{3+} ions (which are more extended than the $4f$ states) to the host lattice environment, which implies a strong phonon coupling and larger linewidths. Ce^{3+} plays an exceptional role among the rare-earth ions, since it has no intra-$4f$ transitions in the visible; it is rather the interconfigurational $5d$-$4f$ transition that occurs in the blue (or UV, depending on the host material). In contrast to the intra-$4f$ transitions which are dipole forbidden and thus exhibit a long (milliseconds) lifetime, the $5d$-$4f$ transition is dipole allowed with a much shorter radiative lifetime, which is an important feature for fast modulation speed in optical devices and in scintillators. In this letter we demonstrate that the blue EL efficiency from Ce^{3+} ions increases from 0.5% to 1.8% after coimplantation of Gd^{3+} ions in SiO_2 layers. The changes of the luminescence decay time and excitation cross sections of Ce^{3+} and Gd^{3+} with energy transfer are investigated in detail.

Samples were prepared by silicon MOS technology on 4 in. (001) oriented n-type silicon wafer with a resistivity of 2–5 Ω cm. The structures were fabricated by local oxidation of silicon with gate oxide and a field oxide thickness of 1 μm. The active layer in the gate oxide is a 100 nm thick thermally grown SiO_2 layer. The whole wafer was implanted with Ce^+ ions at 100 keV, which generates a Ce profile with a maximum concentration of 1% at 46 nm below the surface of the SiO_2 layer, then three quarters of the wafer were implanted with the same energy of Gd^+ ions at different concentrations of 0.5%, 1.5%, and 3.0%, leaving one quarter with Ce^+ implantation only. Reference samples implanted with Gd^+ ions only were also prepared with the same implantation energy and concentrations. The implantation was followed by furnace annealing at 900 °C in flowing N_2 for 30 min, and then a 50 nm SiON layer was deposited on the active layer by plasma-enhanced chemical vapor deposition followed by another annealing step. Finally, the gate electrode consisting of a 100 nm transparent indium tin oxide layer was deposited by rf sputtering.

EL spectra of the MOSLED structures with a circular indium tin oxide electrode of 500 μm diameter were measured at a constant current of 30 μA. Details of the experimental setup were described in Ref. 1. PL and PL excitation spectra were also measured with the same system using a 75 W xenon lamp as an ultraviolet light source. The decay time of the EL was measured with a multichannel scaler (Stanford Research System SR430, minimum time resolution: 5 ns) after the excitation with 2 μs voltage pulses.

Figure 1 shows the EL spectra from the MOSLEDs measured on different areas of one wafer with a Ce concentration of 1% and different concentrations of Gd ions of 0.5%, 1.5%, and 3%. The average electric field in the SiO_2 layers was around 8.5 MV/cm. The spectrum from a reference sample implanted with 1.5% Gd only was also measured for com-

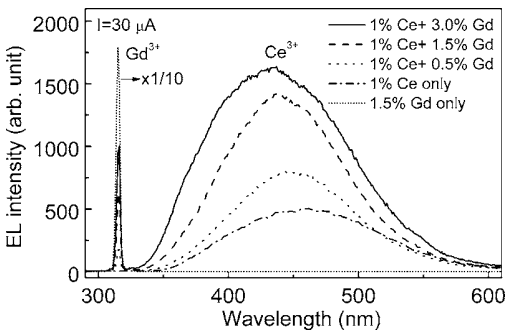

FIG. 1. EL spectra from MOSLEDs with a 100 nm SiO_2 layer implanted with the same Ce concentration of 1% and different concentrations of Gd sensitizers of 0.5%, 1.5%, and 3%, measured on different parts of one wafer. The spectra from a reference sample implanted with 1.5% Gd only were also measured for comparison.

[a]Author to whom correspondence should be addressed; electronic mail: jmsun1968@yahoo.com.cn

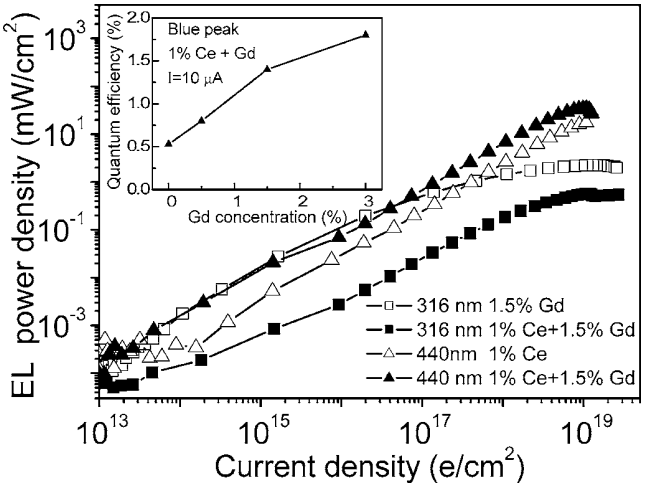

FIG. 2. EL output power density of the UV peak from Gd^{3+} ions at 316 nm (squares) and the blue peak from Ce^{3+} at 440 nm (triangles) vs the injected current density of three samples implanted with 1.5% Gd (hollow squares), 1% Ce+1.5% Gd (solid symbols), and 1% Ce (hollow triangles). The insert is the quantum efficiency of the blue EL peak from Ce^{3+} ions with different concentrations of Gd sensitizers.

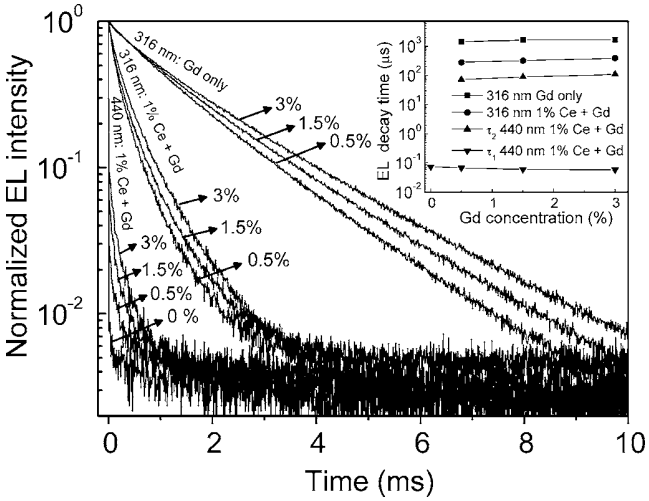

FIG. 3. Normalized EL decay curves of the blue peak at 440 nm from Ce^{3+} ions and the UV peak at 316 nm from Gd^{3+} ions after a 2 μs current-pulse injection. Samples are implanted with a Ce concentration of 1% only and coimplanted with different concentrations of Gd sensitizers of 0.5%, 1.5%, and 3%. The reference samples are implanted with Gd only at concentrations of 0.5%, 1.5%, and 3%. The insert shows the decay time (determined as the time at $1/e$ of the initial intensity) of the Gd^{3+} UV line at 316 nm as well as the decay times of the fast component τ_1 and the slower component τ_2 of the blue peak at 440 nm from Ce^{3+} ions.

parison. All devices implanted with 1% of Ce show a broad peak at 440 nm resulting from the $4f^0 5d^1$ to $^2F_{7/2}$ and $^2F_{5/2}$ transitions of the Ce^{3+} ions in SiO_2, which is similar to the PL spectra of Ce-doped Gd_2SiO_5 crystals.[4,5] The EL spectra from Gd implanted samples show a sharp UV peak from $^6P_{7/2}$ to $^8S_{7/2}$ transitions of Gd^{3+} ions.[2,6] The blue EL peak from the Ce^{3+} ions increases more than three times upon increasing the coimplanted Gd concentration up to 3% compared to the sample implanted with Ce only. At the same time, the UV peak from Gd^{3+} ions is reduced by more than one order of magnitude in the Ce and Gd coimplanted samples compared to the reference sample only implanted with 1.5% Gd. This already indicates an energy transfer from Gd^{3+} to Ce^{3+} ions.

Figure 2 shows the integrated EL output power density of the UV emission from Gd^{3+} and the blue emission from Ce^{3+} versus the injected current density of three samples implanted with 1.5% Gd, 1% Ce +1.5% Gd, and 1% Ce. Over the whole range, the EL power density of the 440 nm blue peak from Ce^{3+} ions (solid triangles) is higher compared to the one without Gd^+ implantation (hollow triangles). The external quantum efficiency of the blue EL increases from 0.5% to 1.8% with increasing the coimplanted Gd concentration up to 3% (as shown in the insert), while the UV peak of Gd^{3+} ions from the sample coimplanted with 1% Ce is quenched by one order of magnitude compared to the sample implanted with 1.5% Gd only. At low current density, the EL power from both blue and UV peaks increases linearly with increasing injection current density, then the UV peak saturates, while the blue peak still increases further. As a result the blue emission shows a much higher maximum EL power density of $\sim 34\ \mathrm{mW/cm^2}$ than the UV emission ($2\ \mathrm{mW/cm^2}$).

The energy transfer process is evidenced by the time resolved measurements. Figure 3 shows the normalized decay curves of the EL from the blue and the UV peaks after a 2 μs current-pulse injection. The inset shows the decay time (determined as the time at 1/e of the initial intensity). For the samples only implanted with Gd at concentrations of 0.5%, 1.5%, and 3%, the decay curve at 316 nm shows a nearly single exponential decay with the decay time slightly increasing from 1.43 to 1.66 ms. This is probably due to a reduction of the nonradiative recombination by filling of the vacancies in SiO_2 with rare-earth atoms. When these samples are coimplanted with 1% additional Ce, the decay time of the Gd^{3+} line drops down to the range of 280–400 μs, but still shows a slight increase with Gd concentration.

For the blue Ce^{3+} peak at 440 nm in the Gd coimplanted samples, the decay process is similar to the behavior of the blue luminescence of Gd_2SiO_5:Ce scintillator excited by UV light or γ rays.[7] It consists of a fast and an unusual, slower component with the decay times τ_1 and τ_2. The fast process with a decay time of $\tau_1 = 75$ ns (not discernible in the main picture; see inset) is determined for the sample implanted with 1% Ce only. This fast decay component can be attributed to $5d$-$4f$ transitions of the directly excited Ce^{3+} ions by hot electrons and is similar to the lifetime of the Ce^{3+} luminescence in other host materials.[4] The decay time τ_1 drops down to 60 ns followed by an increase of a slow component with increasing the coimplanted Gd concentration. This slow component τ_2 increases form 70 to 110 μs for Gd concentrations of 0.5%–3%, following the same tendency as the UV Gd^{3+} line. Therefore the slow decay is probably related to an indirect excitation by energy transfer from the Gd^{3+} to the Ce^{3+} ions.[4] This additional energy transfer mechanism increases the total relaxation rate of the electrons at the excited states of Gd^{3+} ions, and so explain the drop of the decay time of the band at 316 nm (squares and circles in the insert). Due to the still relatively long lifetime of the excited state of Gd^{3+}, the Ce^{3+} ions are populated in a delayed way, thus a long decay component is observed for the 440 nm blue band.

The product of the excitation cross section and the overall lifetime is evaluated by fitting the dependence of EL intensity versus injection current density for the blue and UV peaks from the Ce^{3+} and Gd^{3+} ions,[8] respectively. The excitation cross sections of the EL from Gd^{3+} ions were calcu-

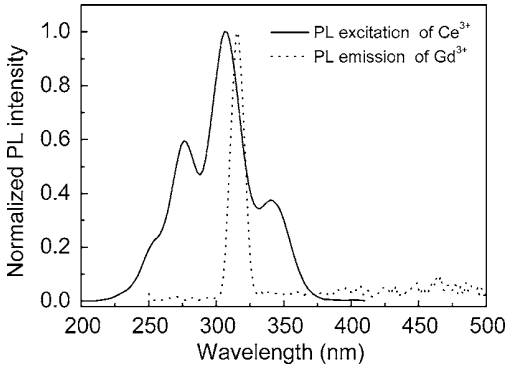

FIG. 4. PL excitation spectrum of Ce^{3+} ions monitored at 440 nm and PL emission spectrum of Gd^{3+} ions, measured on the same sample (coimplanted with 1% Ce and 1.5% Gd).

lated from the measured EL decay times. For the device implanted with Gd only, the excitation cross section of Gd^{3+} slightly increases from 2.8 to 7.4×10^{-15} cm^2 with increasing the Gd concentration from 0.5% to 3%. For the device implanted with 1% Ce only, the excitation cross section of Ce^{3+} calculated using a decay time of 75 ns is as large as 4.8×10^{-13} cm^2. Whereas in the Ce and Gd coimplanted samples the coimplantation of the Gd^{3+} sensitizers causes a strong increase of the excitation cross section of Ce^{3+} up to 3.5×10^{-12} cm^2, while the excitation cross section of the Gd^{3+} emitters reduces to $(1.3-1.6)\times10^{-15}$ cm^2.

The possible energy transfer path from Gd^{3+} to Ce^{3+} ions was studied by the excitation spectra of the Ce^{3+} ions in the SiO_2 layer, as shown in Fig. 4. The excitation spectrum of blue Ce^{3+} peak shows a maximum at around 300–310 nm, which overlaps with the $^6P_{7/2}$ to $^8S_{7/2}$ transition of Gd^{3+} ions. This provides a resonant energy transfer from ^6P_j states of Gd^{3+} to the $5d$ levels of Ce^{3+} ions. In addition, we also investigated the microstructure of the samples containing 1.5% Gd after annealing at different temperatures from 800 to 1000 °C. We found that the implanted rare-earth atoms experienced a preclustering state with small rare-earth-rich clusters of the size of 2–5 nm after annealing at 900 °C for 1 h.[8] This spatial vicinity may increase the possibility of energy transfer from the Gd to the Ce ions. Finally, we propose a transfer mechanism of excitation energy to Ce^{3+} in the Gd coimplanted MOSLEDs. Under high-electric-field injection, hot electrons in the conduction band of SiO_2 gain an average energy above 4–5 eV by electric-field acceleration.[9] The electrons in the ground state $^8S_{7/2}$ of the Gd^{3+} ions are excited to ^6P_J energy levels by the hot electrons. Since the transition energy of the $^6P_J-^8S_{7/2}$ transition overlaps with the $5d$ excitation band of Ce^{3+} ions and due to the relatively long life time of the former, this resonant energy transfer from the $^6P_{7/2}$ Gd^{3+} level to the $5d$ Ce^{3+} level may efficiently increase the excitation of the blue luminescence band.

In summary, an increase of blue EL has been obtained from Ce and Gd coimplanted indium tin oxide/SiO_2:Gd:Ce/Si MOSLEDs. An efficient, resonant energy transfer from Gd^{3+} to Ce^{3+} ions was observed during the EL excitation process in the SiO_2 layers, which leads to an increase of the excitation cross section of the blue Ce^{3+} luminescent ions.

The authors would like to thank J. Winkler and F. Ludewig for the ion implantation, H. Felsmann, C. Neisser, and G. Schnabel for the processing of the MOS structures, and A. Mücklich for the transmission electron microscopy analysis.

[1]J. M. Sun, W. Skorupa, T. Dekorsy, M. Helm, L. Rebohle, and T. Gebel, J. Appl. Phys. **97**, 123513 (2005).
[2]J. M. Sun, W. Skorupa, T. Dekorsy, M. Helm, L. Rebohle, and T. Gebel, Appl. Phys. Lett. **85**, 3387 (2004).
[3]M. E. Castagna, S. Coffa, M. Monaco, A. Muscara, L. Caristia, S. Lorenti, and A. Messina, Mater. Sci. Eng., B **105**, 83 (2003).
[4]K. Mori, M. Nakayama, and H. Nishimura, Phys. Rev. B **67**, 165206 (2003).
[5]M. Sekita, Y. Miyazawa, T. Akahane, and T. Chiba, J. Appl. Phys. **66**, 373 (1989).
[6]U. Vetter, J. Zenneck, and H. Hofsäss, Appl. Phys. Lett. **83**, 2145 (2003).
[7]H. Suzuki, T. A. Tombrello, C. L. Melcher, and J. S. Schweitzer, Nucl. Instrum. Methods Phys. Res. A **320**, 263 (1992).
[8]J. M. Sun, S. Prucnal, W. Skorupa, T. Dekorsy, A. Mücklich, M. Helm, L. Rebohle, and T. Gebel, J. Appl. Phys. **99**, 103102 (2006).
[9]D. J. DiMaria, T. N. Theis, J. R. Kirtley, F. L. Pesavento, D. W. Dong, and S. D. Brorson, J. Appl. Phys. **57**, 1214 (1985).

APPLIED PHYSICS LETTERS **89**, 133508 (2006)

Quadratic autocorrelation of free-electron laser radiation and photocurrent saturation in two-photon quantum well infrared photodetectors

H. Schneider,[a] O. Drachenko, S. Winnerl, and M. Helm
Institute of Ion Beam Physics and Materials Research, Forschungszentrum Rossendorf, P.O. Box 510119, 01314 Dresden, Germany

M. Walther
Fraunhofer-Institut for Applied Solid State Physics, Tullastrasse. 72, D-79108 Freiburg, Germany

(Received 12 July 2006; accepted 17 August 2006; published online 27 September 2006)

Using the free-electron laser facility FELBE, the authors have studied the influence of the intensity on the quadratic autocorrelation measured with two-photon quantum well infrared photodetectors (QWIPs). At high illumination powers, the shape of the autocorrelation trace is affected by photocurrent saturation of the two-photon QWIP. They describe the saturation mechanism by different analytical models taking account of the photocurrent nonlinearity in analogy to linear QWIPs and give conditions where true quadratic behavior can be observed. While these studies were carried out at 77 K, properties of two-photon QWIPs at room temperature will also be addressed. © *2006 American Institute of Physics*. [DOI: 10.1063/1.2357936]

Quantum well infrared photodetectors (QWIPs) have developed into a mature technology for thermal imaging, and extensive theoretical and experimental studies have been performed.[1] Further possible applications of QWIPs rely on their high electrical bandwidth, which makes them useful for heterodyne detection[2] and for monitoring short optical pulses.[3] Even better time resolution in the subpicosecond regime has been achieved by quadratic detection, which exploits two-photon absorption involving a virtual[4] or a real[5,6] intermediate state. For the latter approach, we use n-type quantum wells with three equidistant levels, namely, two bound subbands and one continuum resonance (see inset of Fig. 1). Two infrared photons are thus necessary to excite an electron out of the well, such that the resulting photocurrent depends quadratically on the incident power. We have convinced ourselves previously[5,6] that these three levels are energetically equidistant. Autocorrelation measurements of weak subpicosecond midinfrared pulses have revealed subpicosecond population relaxation ($\sim$0.5 ps) and dephasing ($\sim$0.1 ps) times,[5] which makes two-photon QWIPs very promising for pulse monitoring.

For quadratic detection, a ratio of 8:1 is expected between the measured photocurrent for zero time delay and for temporally separated pulses in the case of interferometric autocorrelation and 3:1 for intensity autocorrelation.[6] Therefore, the observed shape and the interpretation of autocorrelation traces will be influenced by photocurrent saturation. In fact, it is well known from linear QWIPs that screening of the electric field can give rise to photocurrent nonlinearities even at low excitation power.[7,8]

In this letter, we exploit two-photon QWIPs for autocorrelation measurements of midinfrared laser pulses from the free-electron laser (FEL) facility FELBE at the Forschungszentrum Rossendorf,[9] and study the intensity dependence of the measured autocorrelation signals. Our results indicate that the observed saturation behavior is caused by internal space charges rather than capacitive discharging or absorption saturation. In addition, we explore detection properties of two-photon QWIPs at room temperature, where a linear photocurrent is superimposed to the quadratic signal.

Our two-photon QWIP structures were grown by molecular beam epitaxy on semi-insulating GaAs substrates and comprise 20 Si-doped quantum wells (4×10^{11} cm^{-2} electrons per well). Sample 1 contains 7.6 nm wide GaAs quantum wells between 47 nm $Al_{0.33}Ga_{0.67}As$ barriers, with a peak detection wavelength of 10.4 μm and sample 2 is based on 6.8 nm $In_{0.10}Ga_{0.90}As$ wells and 47 nm $Al_{0.38}Ga_{0.62}As$ barriers, resulting in a peak wavelength of 8 μm. The wafers were processed into mesa detectors of 120×120 and 240×240 μm^2 in area. The radiation is coupled into the structure via 45° facets. Further details are provided in Ref. 5. Since the two-photon response of sample 1 has been calibrated previously[5] using a CO_2 laser, we chose this device for measurements at 77 K, whereas sample 2 was preferred at 300 K due to its larger intersubband energy.

Autocorrelation measurements were performed using a Michelson interferometer setup and a rapid-scan delay stage operating at a typical frequency of 20 Hz. The photocurrent signal was fed into a current preamplifier (Femto DLPCA 200) and recorded with a digital oscilloscope. Since only a few percent of the radiation measured by our external power meter reached the active area of the two-photon QWIP device, the actual time-averaged power density was calibrated using the two-photon responsivity S determined previously,[5] which amounts to $S=4\times10^{-7}$ A cm^2/W^2 for continuous-wave radiation. Due to the quadratic response, this value translates into $S=0.01$ A cm^2/W^2 for the duty cycle of 4×10^{-5} for two time-delayed pulses (see below) of FEL radiation, valid for the low-intensity regime far from saturation.

Figure 1(a) shows a complete interferometric autocorrelation trace together with an intensity autocorrelation where the fringes have been filtered out numerically. The envelope of the interferometric autocorrelation, normalized to the photocurrent at large delay, corresponds to the theoretically expected value of 8 at zero delay (it actually appears slightly higher due to some high-frequency noise). Also the intensity autocorrelation yields a ratio of 2.9 between the value at zero

[a]Electronic mail: h.schneider@fz-rossendorf.de

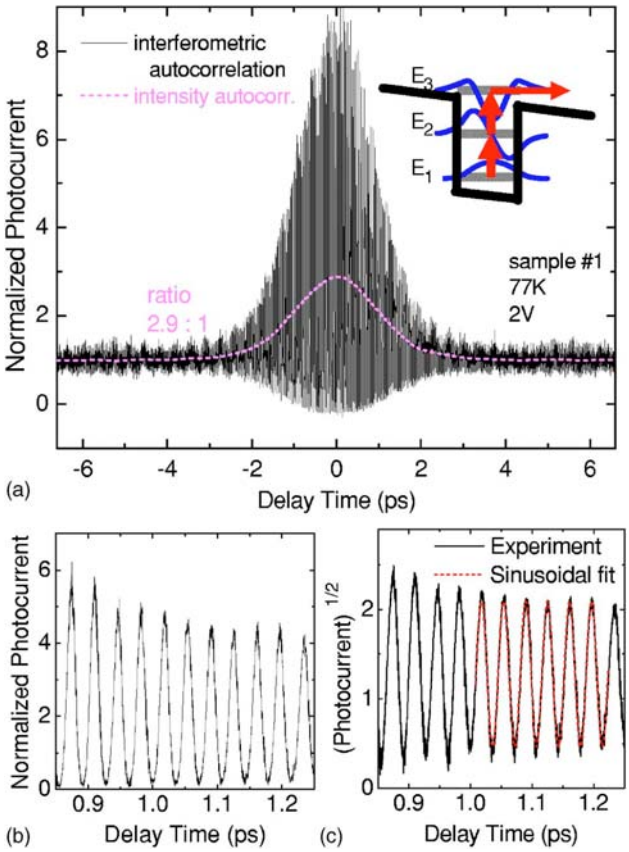

FIG. 1. (Color online) Interferometric and intensity autocorrelation of two-photon QWIP 1 at 1.3 kW/cm^2 (a) peak power density, (b) autocorrelation fringes, and square root of the signal with sinusoidal fit. The inset of (a) indicates the operation of the device.

delay and large delay, which is extremely close to the theoretical value of 3. Since Fig. 1(a) does not resolve the more than 100 fringes, a part of the autocorrelation trace is plotted in an expanded scale in Fig. 1(b). The asymmetric shape of the fringes becomes perfectly sinusoidal if the square root of the signal is plotted [Fig. 1(c)], which further demonstrates nicely the quadratic detection properties of the device. We point out that the complete autocorrelation trace has been obtained without any signal averaging in a single rapid scan, i.e., within 25 ms; thus this approach is useful for monitoring the pulse properties of the FEL. Figure 1(a) indicates an autocorrelation width of 2.3 ps, which yields a FEL pulse width of ~1.6 ps full width at half maximum and a FEL duty cycle of 2×10^{-5}.

Now turning to the intensity dependence of the photocurrent signal, we have plotted in Fig. 2 the photocurrent density as a function of power density. While the signal exhibits truly quadratic power dependence at low power, saturation occurs at around 100 kW/cm^2 peak power. In order to better understand the observed behavior, let us now consider different saturation mechanisms. First, we tentatively assume that the electric field inside the QWIP is screened by viewing the device as a capacitor that is discharged by the photocurrent. Taking the signal I (and the photoconductive gain) proportional to the electric field, we thus arrive at the equation

$$I = (1 - I/I_{\mathrm{sat}})(RP + SP^2), \tag{1}$$

with the (linear) responsivity R and the saturation current I_{sat}, yielding the expression $I=(1/I_{\mathrm{sat}}+1/(RP+SP^2))^{-1}$. The prediction of this linear saturation model (with $R=0$ for $T=77$ K) is plotted in Fig. 2. It can be seen that the behavior at intermediate power density is not well described.

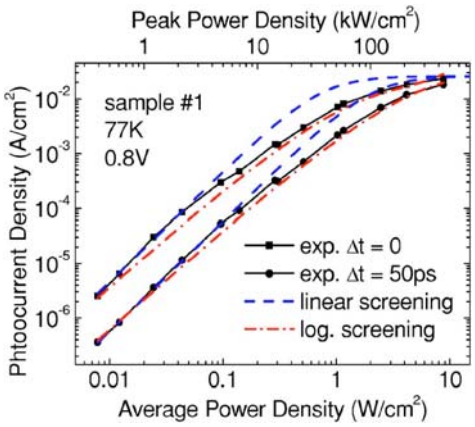

FIG. 2. (Color online) Photocurrent density vs power density of sample 1 at zero delay and large delay. Predictions of linear and logarithmic screening are also shown.

Our second approach is based on the low-power photocurrent nonlinearity[7,8] known from linear QWIPs. This nonlinearity essentially arises since the "first" barrier at the emitter side of the QWIP only carries a thermal current whereas also a photoexcited current is flowing across the remaining barriers. In order to keep the total current constant, the electric field thus has to be higher at the emitter barrier than in the rest of the active region. To obtain an analytical model, we now assume that the thermal current increases exponentially with the electric field F [i. e., $I\sim\exp(\alpha F)$ with a prefactor α] and that the photocurrent is proportional to F. This exponential behavior is a good approximation for the observed dark current of a QWIP if the voltage drop per QWIP period exceeds the thermal energy k_BT. For a two-photon QWIP with N quantum wells and $N+1$ barriers, this leads to the equation

$$I = (\ln I_{\mathrm{sat}} - \ln I)(\tilde{R}P + \tilde{S}P^2), \tag{2}$$

with $\tilde{R}=R/N\alpha F$ and $\tilde{S}=S/N\alpha F$. Equation (2), which we will refer to as logarithmic screening, has the solution $I=(\tilde{R}P+\tilde{S}P^2)W(I_{\mathrm{sat}}/(\tilde{R}P+\tilde{S}P^2))$, where W is Lambert's W function.[10] As can be seen from Fig. 2, this model describes the overall power dependence reasonably well. However, there is some deviation from the observed quadratic behavior since the W function behaves like the logarithm for very large arguments. We point out, however, that the underlying assumption that the field is constant except for the emitter barrier is only valid in the stationary case (and should be a reasonable approximation at very high power where charge redistribution can occur at short time scales). For weak laser pulses, however, the space charge is expected to be distributed over all quantum wells, which should lead to modifications in the intensity dependence but with similar functional behavior.

For linear QWIPs, photocurrent saturation has been studied previously by Duboz *et al.*[11] They observed saturation to set in only at very high threshold levels of several MW/cm^2, where absorption saturation is expected to occur.[1,11] In our present experiments, photocurrent saturation is already observed at about two orders of magnitude lower intensity, such

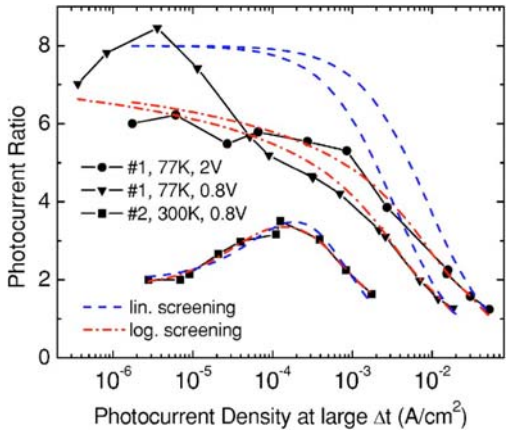

FIG. 3. (Color online) Photocurrent ratio at 77 K (sample 1) and 300 K (sample 2) between zero delay and large delay vs photocurrent density under different experimental conditions as indicated and fitting curves according to the linear and logarithmic screening models. For clarity, the data for 300 K are shifted to the left by a factor of 10.

that we can exclude absorption saturation as a possible cause. An independent estimate for space charge saturation thresholds is obtained from the geometric capacitance of our samples, which amounts to 10 nF/cm^2 for a depletion width of 1.1 μm. Complete discharging of such a capacitor for, say, 1 V bias gives rise to a charge density of $6\times10^{10}\ e/cm^2$. This value is more than two orders of magnitude below the $8\times10^{12}\ cm^{-2}$ electrons inside the quantum wells which would have to be excited to saturate the absorption. The expected threshold for space charge saturation thus agrees nicely with the photocurrent saturation threshold observed in the present experiments.

In order to see the influence of photocurrent saturation on the autocorrelation trace, we have plotted in Fig. 3 the ratio between the photocurrents measured at zero and large time delays as a function of the signal at large time delay. Surprisingly, a ratio of 8 was difficult to achieve experimentally, whereas the ratio approaches unity close to saturation as expected. Applying the models behind Eqs. (1) and (2), the ratio for $R=0$ is given by $8I_{sat}/(I_{sat}+7I)$ and $8W((I_{sat}/8I)\ln(I_{sat}/I))/\ln(I_{sat}/I)$, respectively. Both expressions are independent of the quadratic coefficient S, thus depending just on one single parameter I_{sat}. Taking this into account, the overall dependence is predicted reasonably well by the logarithmic screening model, whereas there are strong deviations for linear screening.

Nevertheless, it is experimentally possible to reach the desired ratio of 8 at low power where additional effects such as dark current and thermal background current might be of some influence. This regime is not completely understood and needs further investigations. Further parameters to be optimized include the bias voltage and temperature. Since the intrinsic quadratic behavior is still present in spite of some distorted intensity dependence, an appropriate numerical compensation of saturation-induced distortions of the autocorrelation traces should be possible.

Finally, we have also investigated whether our two-photon QWIPs allow quadratic detection at room temperature. As pointed out already in Refs. 5 and 6, thermal excitation into the intermediate subband causes a linear responsivity signal which exhibits a thermally activated behavior. Since the expected responsivity at room temperature is of the order of 1 mA/W, the linear signal will dominate at lower power. We have therefore investigated the intensity dependence of the ratio in the case of sample 2, which is also included in Fig. 3. In fact, the observed linear behavior manifests itself by a ratio of two at low power. Thus the linear regime merges with the saturation regime, such that the maximum observed ratio amounts to a value of only 3.5. However, two-photon QWIPs designed for shorter detection wavelengths are expected to make quadratic autocorrelation measurements possible also at room temperature.

In conclusion, two-photon QWIPs have been exploited for pulse monitoring of free-electron laser radiation by rapid-scan interferometric autocorrelation measurements. We have also investigated the saturation behavior of the two-photon QWIP signal, which is limited by the generation of internal space charges rather than capacitive discharging or absorption saturation. At 77 K, enhancement factors up to the theoretically expected value of 8:1 have been observed for interferometric autocorrelation, whereas only lower values were possible at room temperature where an additional linear contribution to the signal is present.

The authors are grateful to P. Michel and the whole ELBE team for their dedicated support. Part of this work has been supported by EuroMagNET under the EU Contract No. RII3-CT-2004-506239 of the sixth Framework "Structuring the European Research Area, Research Infrastructures Action."

[1]H. Schneider and H. C. Liu, *Quantum Well Infrared Photodetectors: Physics and Applications*, Springer Series in Optical Sciences (2006), Vol. 126.
[2]P. D. Grant, R. Dudek, L. Wolfson, M. Buchanan, and H. C. Liu, Electron. Lett. **41**, 214 (2005).
[3]S. Steinkogler, H. Schneider, M. Walther, and P. Koidl, Appl. Phys. Lett. **82**, 3925 (2003).
[4]A. Zavriyev, E. Dupont, P. B. Corkum, H. C. Liu, and Z. Biglov, Opt. Lett. **20**, 1885 (1995).
[5]H. Schneider, T. Maier, H. C. Liu, M. Walther, P. Koidl, Opt. Lett. **30**, 287 (2005).
[6]T. Maier, H. Schneider, M. Walther, P. Koidl, and H. C. Liu, Appl. Phys. Lett. **84**, 5162 (2004).
[7]C. Mermelstein, H. Schneider, A. Sa'ar, C. Schönbein, M. Walther, and G. Bihlmann, Appl. Phys. Lett. **71**, 2011 (1997).
[8]M. Ershov, H. C. Liu, M. Buchanan, Z. R. Wasilewski, and V. Ryzhii, Appl. Phys. Lett. **70**, 414 (1997).
[9]P. Michel, F. Gabriel, E. Grosse, P. Evtushenko, T. Dekorsy, M. Krenz, M. Helm, U. Lehnert, W. Seidel, R. Wünsch, D. Wohlfarth, and A. Wolf, Proceedings of the 26th International FEL Conference (Comitato Conference Elettra, Trieste, Italy, 2004; http://accelconf.web.cern.ch/AccelConf/f04/papers/MOAIS04/MOAIS04.pdf
[10]B. Hayes, Am. Sci. **93**, 104 (2005).
[11]J. Y. Duboz, E. Costard, J. Nagle, J. M. Berset, and J. M. Ortega, J. Appl. Phys. **78**, 1224 (1995).

APPLIED PHYSICS LETTERS **88**, 151108 (2006)

Pump-probe spectroscopy of interminiband relaxation and electron cooling in doped superlattices

D. Stehr,[a] S. Winnerl, and M. Helm
Institute of Ion Beam Physics and Materials Research, Forschungszentrum Rossendorf, P.O. Box 510119, 01314 Dresden, Germany

T. Dekorsy
Fachbereich Physik, Universität Konstanz, 78457 Konstanz, Germany

T. Roch and G. Strasser
Institut für Festkörperelektronik, TU Wien, Floragasse 7, 1040 Wien, Austria

(Received 11 January 2006; accepted 1 March 2006; published online 14 April 2006)

The picosecond dynamics of electrons in a doped GaAs/AlGaAs superlattice have been investigated by pump-probe experiments using an infrared free-electron laser. We observe a fast bleaching of the interminiband absorption followed by thermalization and a slower cooling component. The latter can lead to a positive or negative transmission change, resulting from the temperature dependence of the linear absorption spectrum at the respective wavelength. We show that the superlattice in contrast to quantum wells provides a unique picosecond thermometer for the electron temperature based on the dependence of the absorption on the electron distribution function. © *2006 American Institute of Physics*. [DOI: 10.1063/1.2194868]

The relaxation and cooling behavior of electrons in semiconductors and their heterostructures are of crucial importance for most optoelectronic devices.[1] As a prime example the intersubband relaxation dynamics in quantum wells have to be known and well understood for the design of quantum cascade lasers.[2–4] Many such investigations have been performed over the past two decades in quantum structures based on different materials systems, and an impressive level of insight has been obtained.[5] Yet semiconductor superlattices (SLs), while representing a key model system of an artificial semiconductor structure, have been much less investigated in this respect, although they provide the basis of SL cascade lasers[6] or Bloch oscillators.[7] Compagnone *et al.*[8] have calculated the interminiband relaxation rates and the stationary electron distribution function using a Monte Carlo technique, but no time resolved experiments have been performed to the best of our knowledge.

In this letter we present pump-probe transmission measurements on a doped GaAs/$Al_{0.3}Ga_{0.7}As$ superlattice using the infrared free-electron laser FELBE at the Forschungszentrum Rossendorf.[9] We observe transient bleaching followed by interminiband relaxation on a picosecond time scale as well as heating and subsequent cooling of the electron system.

The superlattice was grown by molecular beam epitaxy (MBE) on a semi-insulating GaAs substrate. It consists of 300 periods of 9.0 nm thick quantum wells and 2.5 nm thick barriers, resulting in a width of 12 and 50 meV for the first and second minibands, respectively. The wells are doped in the central 6 nm to $n=3\times10^{16}$ cm^{-3}, corresponding to a density of 1.5×10^{16} cm^{-3} averaged over one SL period and an areal density of 2×10^{10} cm^{-2} per period. The Fermi energy at low temperature lies 1 meV below the first miniband, when the impurity states are fully taken into account (see Ref. 10; neglecting impurity states it would lie 2.5 meV above the bottom miniband edge). The linear interminiband absorption spectrum, measured on a sample with 45° polished facets and one total internal reflection, is shown in Fig. 1 for different temperatures. At high temperature, the spectra reflect the van Hove singularities of the joint density of states at the center and edge of the mini-Brillouin zone, at low temperature they are dominated by impurity transitions (see inset of Fig. 1).[10] We would like to point out that the strong temperature dependence of the absorption spectrum provides a means for measuring the effective temperature of the electron system.[11]

For the time-resolved experiments the above sample was placed into a LHe flow cryostat equipped with KRS-5 windows and excited with the free-electron laser (FEL), which provided bandwidth limited Gaussian pulses[12] with a full width at half maximum (FWHM) between 1 and 2.5 ps (depending on the wavelength) at a 13 MHz repetition rate. This

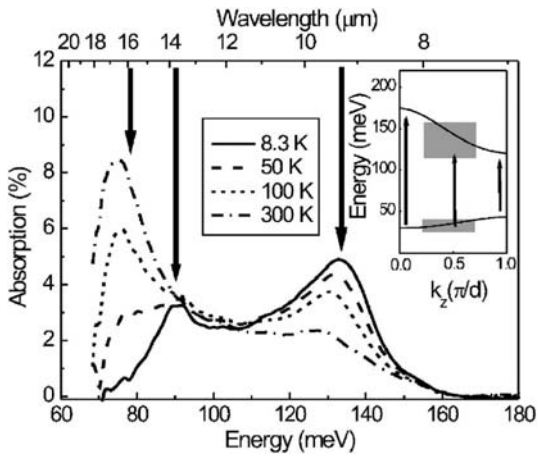

FIG. 1. Experimental infrared absorption spectrum of the sample at different temperatures. The arrows indicate the excitation wavelengths. The cutoff at 70 meV is due to the detector employed in the measurement. The inset illustrates the interminiband and impurity transitions.

[a]Electronic mail: d.stehr@fz-rossendorf.de

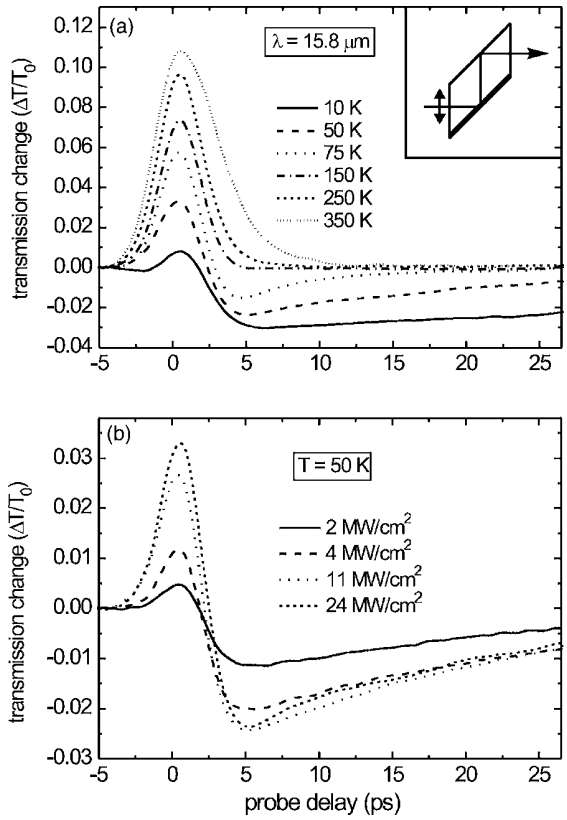

FIG. 2. Probe transmission as a function of pump-probe delay recorded at 15.8 μm for different temperatures (a) and different pump intensities at $T=50$ K (b). Note that the intensity values are only accurate up to a factor of 2 approximately, while their relative values are accurate within 10%. The inset illustrates the sample geometry.

high repetition rate results in a far superior signal-to-noise ratio compared to macropulsed FELs or kilohertz optical parametric amplifier systems. The maximum pulse energy used for excitation was 50 nJ, corresponding to 650 mW average power, taking the sample geometry and attenuation of the cryostat windows into account. Under these conditions the lattice temperature of the samples increases by a few Kelvins. A fraction of the laser beam was split off using a Mylar beam splitter and served as the probe beam. Both pump and probe were focused onto the sample using a 10 cm focal-length off-axis parabolic mirror, taking care that the focal spot of the pump was larger than that of the probe. Behind the sample the transmitted probe beam was detected with a LN_2 cooled mercury-cadmium telluride (MCT) detector. The signals were recorded by chopping the pump beam mechanically at 350 Hz and measuring the probe signal using a lock-in amplifier at this frequency. The pump-probe delay was achieved using a mechanical delay line.

Let us first analyze the pump-probe signals recorded at a wavelength of 15.8 μm shown in Fig. 2. The FEL spectrum exhibited a FWHM of $\Delta\lambda=0.16$ μm, which corresponds to a pulse duration of 2.2 ps for bandwidth limited Gaussian pulses. By varying the lattice temperature [Fig. 2(a)] and the pump power [Fig. 2(b)] we observe drastic changes of the transient behavior. At low temperatures the induced transmission first rises due to bleaching of the transition, then decreases again within a few picoseconds and even goes negative, corresponding to induced absorption. This latter component relaxes on a much longer time scale. The fast bleaching component recovers by interminiband relaxation as well as by thermalization due to electron-electron scattering, which leads to a carrier distribution thermalized at a temperature higher than the lattice temperature. Exactly this is the reason for the negative (i.e., induced absorption) signal: from the linear absorption spectrum in Fig. 1 we know that at a wavelength of 15.8 μm the absorption rises significantly with temperature. Thus an increase of the electron temperature leads to an increased absorption at this wavelength. The subsequent slower decay corresponds to the cooling of the electron distribution down to the lattice temperature. At higher temperature it is observed that (*i*) the bleaching component becomes stronger, which is simply due to the fact that the linear absorption is larger, and (*ii*) the thermalization/cooling component becomes weaker and faster. This is because at higher temperature the optical-phonon related energy loss rate of the electrons increases,[11] but also there is more energy absorbed according to the spectra in Fig. 1, leading to an even stronger energy loss. On the other hand the amplitude of the signal gets weaker, because at higher temperature the linear absorption does not change so much anymore (i.e., the intrinsic "thermometer" becomes less sensitive). The cooling time changes from 50 ± 5 ps at $T=10$ K to 6 ± 1 ps at $T=75$ K. At 250 K the fast relaxation and slower cooling component nearly cancel each other, and at $T=350$ K a single exponential interminiband relaxation of 2.2 ± 0.1 ps is observed.

The observations in Fig. 2(b), which show the intensity dependence of the signal at a constant lattice temperature of 50 K, are consistent with the above picture: at higher pump intensity both the positive bleaching and the negative thermalization/cooling signal get larger and the cooling speeds up due to the larger temperature increase. Note that the vertical scale in Fig. 2 is quantitative: the bleaching at the highest pump power reaches 3%, which corresponds to full saturation when compared with the vertical scale of the linear absorption spectrum (at 50 K and 15.8 μm). The negative heating signal reaches 2.4%, which corresponds to a rise from 50 K to approximately 100 K when again compared to Fig. 1. Fitting an exponential decay on the cooling curve (not shown) yields cooling times from 40 ± 4 ps for the lowest to 18 ± 2 ps for the highest pump intensity.

We performed similar pump-probe measurements at two other wavelengths: one at the high-energy peak of the absorption spectrum at $\lambda=9$ μm, which corresponds to transitions near the center of the mini-Brillouin zone, and at an intermediate wavelength of 13.75 μm. The used pump intensities were 40 MW/cm^2 at 9 μm and 20 MW/cm^2 at 13.75 μm, respectively. From the laser spectrum we could estimate the pulselength to 1.5 ps for 9 μm. These data are shown in Fig. 3. We clearly see the difference of the recorded signals: with shortening the wavelength, the induced absorption (at 15.8 μm) first becomes much smaller and finally turns into induced *transmission* in the case $\lambda=9.0$ μm. However, this behavior is again completely consistent with the temperature dependence of the linear absorption spectra (Fig. 1). At 13.75 μm, the temperature change of the absorption is very small, e.g., we see a very small negative (i.e., induced absorption) signal (in other words, the intrinsic thermometer is not sensitive at this wavelength). At $\lambda=9.0$ μm, it is obvious from Fig. 1 that the absorption decreases at higher temperatures. As a consequence now also the slow cooling transient is completely positive at all times. Due to the sim-

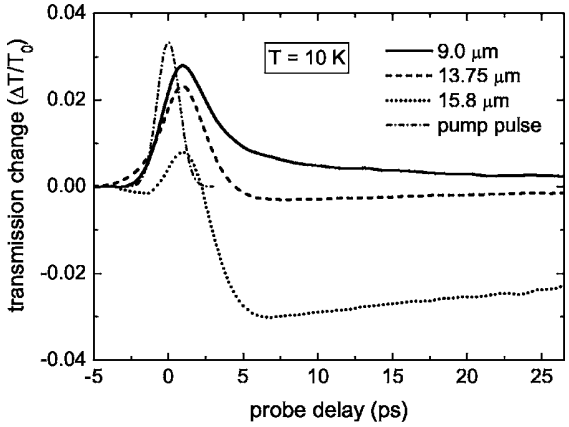

FIG. 3. Probe transmission as a function of pump-probe delay recorded at $T=10$ K for different wavelengths as indicated. Also shown is the temporal pulse shape used to extract the decay times.

pler shape of the decay curve, it can now be fitted using a biexponential decay, yielding $\tau_1 \approx 2.2 \pm 0.1$ ps and $\tau_2 \approx 23 \pm 4$ ps as the best fit. While τ_2 corresponds to the cooling time, τ_1 reflects a combination of the interminiband relaxation and thermalization times of the excited electrons. The value agrees reasonably well with calculations for optical-phonon induced interminiband relaxation[8] (these calculations were performed for InGaAs/InAlAs), indicating that electron-electron scattering cannot be much faster.

Due to the large spectral spreading of the interminiband absorption in a superlattice and its temperature dependence it is thus possible to clearly separate different contributions of the electron dynamics. In isolated quantum wells this is not possible due to the parallel dispersion of the subbands, or at least to a much lesser degree: Lutgen *et al.*[13] were actually able to observe similar though much weaker effects in quantum wells due to the finite nonparabolicity of the subbands.

A similar behavior—positive and negative pump-probe signals—has also been observed by Woerner *et al.*[14] for the inter-valence-band absorption in *p*-Ge. However, they ascribed both signal components to a change of carrier temperature (possible due to a nonmonotonic dependence of the absorption on the carrier temperature and a very fast hole-hole scattering) and excluded a real bleaching of the transition. Since in the present case the absorption depends monotonically on temperature for each wavelength, the fast signal must result from saturating the transition.

In summary, we have performed pump-probe measurements on interminiband transitions in GaAs/AlGaAs superlattices. We have observed a fast bleaching with subsequent relaxation and thermalization as well as a slower signal due to cooling of the hot electron distribution. The latter signal can be positive or negative, depending on the temperature dependence of the linear absorption at the respective wavelength, thus providing an internal thermometer for the electrons.

The authors are grateful to P. Michel and the whole ELBE team for their dedicated support, to W. Seidel for friendly collaboration, and to H. Schneider for critical discussions.

[1] J. Shah, *Ultrafast Spectroscopy of Semiconductors and Semiconductor Nanostructures* (Springer, Berlin, 1999).
[2] C. Gmachl, F. Capasso, D. L. Sivco, and A. Y. Cho, Rep. Prog. Phys. **64**, 1533 (2001).
[3] M. Troccoli, G. Scamarcio, V. Spagnolo, A. Tredicucci, C. Gmachl, F. Capasso, D. L. Sivco, A. Y. Cho, and M. Striccoli, Appl. Phys. Lett. **77**, 1088 (2000).
[4] M. S. Vitiello, G. Scamarcio, V. Spagnolo, B. S. Williams, S. Kumar, Q. Hu, and J. L. Reno, Appl. Phys. Lett. **86**, 111115 (2005).
[5] T. Elsaesser and M. Woerner, Phys. Rep. **321**, 253 (1999).
[6] G. Scamarcio, F. Capasso, C. Sirtori, J. Faist, A. L. Hutchinson, D. L. Sivco, and A. Y. Cho, Science **276**, 773 (1997).
[7] N. Sekine and K. Hirakawa, Phys. Rev. Lett. **94**, 057408 (2005); P. G. Savvidis, B. Kolasa, G. Lee, and S. J. Allen, Phys. Rev. Lett. **92**, 196802 (2004).
[8] F. Compagnone, A. DiCarlo, and P. Lugli, Appl. Phys. Lett. **80**, 920 (2002); S. Tortora, F. Compagnone, A. DiCarlo, and P. Lugli, Physica E (Amsterdam) **7**, 20 (2000).
[9] P. Michel, F. Gabriel, E. Grosse, P. Evtushenko, T. Dekorsy, M. Krenz, M. Helm, U. Lehnert, W. Seidel, R. Wünsch, D. Wohlfarth, and A. Wolf, *Proceedings of the 26th International FEL Conference*, Trieste, 2004. http://accelconf.web.cern.ch/AccelConf/f04/papers/MOAIS04/MOAIS04.pdf
[10] D. Stehr, C. Metzner, M. Helm, T. Roch, and G. Strasser, Phys. Rev. Lett. **95**, 257401 (2005). The impurity nature of the transition at low temperature is not expected to change the dynamics observed in this experiment, since the excited impurity band largely overlaps with the excited miniband.
[11] W. Hilber, M. Helm, K. Alavi, and R. Pathak, Appl. Phys. Lett. **69**, 2528 (1996).
[12] U. Lehnert, P. Michel, W. Seidel, D. Stehr, J. Teichert, D. Wohlfarth, and R. Wünsch, *Proceedings of the 27th International FEL Conference*, Stanford, 2005. http://accelconf.web.cern.ch/AccelConf/f05/papers/TUPP030.pdf
[13] S. Lutgen, R. A. Kaindl, M. Woerner, T. Elsaesser, A. Hase, and H. Künzel, Phys. Rev. B **54**, R17343 (1996).
[14] M. Woerner, T. Elsaesser, and W. Kaiser, Phys. Rev. B **41**, 5463 (1990).

APPLIED PHYSICS LETTERS **89**, 171104 (2006)

Femtosecond pump-probe spectroscopy of intersubband relaxation dynamics in narrow InGaAs/AlAsSb quantum well structures

C. V.-B. Tribuzy,[a] S. Ohser, S. Winnerl, J. Grenzer, H. Schneider, and M. Helm
Institute of Ion Beam Physics and Materials Research, Forschungszentrum Rossendorf, P.O. Box 510119, 01314 Dresden, Germany

J. Neuhaus and T. Dekorsy
Department of Physics, University of Konstanz, 78457 Konstanz, Germany and Center for Applied Photonics, University of Konstanz, 78457 Konstanz, Germany

K. Biermann and H. Künzel
Fraunhofer Institute for Telecommunications, Heinrich Hertz Institut, 10587 Berlin, Germany

(Received 10 May 2006; accepted 21 August 2006; published online 23 October 2006)

Intersubband relaxation dynamics in InGaAs/AlAsSb multiquantum wells (QWs) is studied by single-color femtosecond pump-probe measurements. At early delay times, all samples show an exponential decay of the transient transmission occurring with time constants of the order of a picosecond. The relaxation dynamics at later delay times strongly depend on both QW thickness and doping location. A non-single-exponential decay behavior indicates extra competing relaxation channels, as further confirmed by solving three-level rate equations. It is shown that slowly decaying components are due to electron transfer to states related to indirect valleys in the wells or in the barriers. © *2006 American Institute of Physics*. [DOI: 10.1063/1.2360242]

Intersubband transitions in semiconductor quantum wells (QWs) have been employed for midinfrared optoelectronic devices, in particular, lasers and detectors.[1] Also ultrafast all-optical switching[2,3] is an interesting application due to the short relaxation times of intersubband transitions,[4] which are several orders of magnitude faster than for interband transitions. Recently there have been attempts to extend the range of intersubband devices towards the near infrared, i.e., to wavelengths shorter than 3 μm (Ref. 5) and even towards the 1.55 μm telecommunication range.[2,3,6] This requires material systems with a large conduction band discontinuity, such as strained InGaAs/AlAs on GaAs (Ref. 7) or InP substrates,[8] $In_{0.53}Ga_{0.47}As/AlAs_{0.56}Sb_{0.44}$ lattice matched to InP,[9,10] InAs/AlSb on GaSb,[5] or nitrides such as InGaN/AlGaN (Refs. 11 and 12) and II-VI compounds such as ZnSe/BeTe.[13] While the latter two material systems exhibit ultrafast, subpicosecond intersubband relaxation due to their strong electron-phonon coupling, they may be less suited for quantum cascade emitters, which appear more promising in the InP (Refs. 14 and 15) or GaSb (Ref. 5) based systems.

A common feature of some of the above material combinations is the indirect character of the barrier material, i.e., an X or L valley represents the lowest-energy states. In narrow QWs (<3 nm), required to achieve short-wavelength intersubband absorption, the first excited subband state may be raised above such indirect state in the barrier or even in the QW, which would strongly influence the relaxation behavior and also the performance of quantum cascade lasers.[16] Indications for such an effect have been observed in some intersubband relaxation experiments for the InGaAs/AlAs (Ref. 7) and ZnSe/BeTe systems.[13]

In the present letter we investigate the intersubband relaxation dynamics in narrow InGaAs/AlAsSb QWs, which are the building block for short-wavelength quantum cascade lasers.[15] We employ femtosecond pump-probe spectroscopy and focus on the possible role of intervalley electron transfer in the relaxation dynamics. Though time resolved experiments on this material system have been reported before,[10] the role of indirect states has remained open. The shortest lasing wavelength in this material system to date is around 3.8 μm,[15] but electroluminescence down to 3.1 μm has been observed[17] despite the fact that at this wavelength the excited subband is supposed to lie already above the lowest X state in the InGaAs QW. By investigating QWs of different thicknesses and doping the present investigation shows that there is a distinct influence of indirect states on the relaxation behavior.

The InGaAs/AlAsSb multiple QWs with 50 periods were grown lattice matched to InP substrates by molecular beam epitaxy. We focus here on three samples, one with a nominal well thickness of 4.5 nm (sample A) and the other two with 3.0 nm thickness (samples B and C). Of the latter two, one (sample C) is doped (with Si) in the QW and the other (sample B) is modulation doped in the center of 20 nm of the 30 nm thick barriers, both yielding an areal electron concentration of $3\times10^{12}\,cm^{-2}/QW$. The thicker-QW sample (A) is also modulation doped in the barrier, but nominally three times higher. High-resolution x-ray diffraction and reflection measurements yielded actual QW thicknesses of 4.0 nm for sample A and 2.9 nm for both samples B and C. It was also found that the last two samples (B and C) show a better structural quality (interface roughness of ~0.5 nm) than sample A. For the optical measurements, we used short trapezoidal waveguides with 38° polished facets having only one internal reflection occurring at the epitaxial surface.

Figure 1 shows the ratios between p- and s-polarized transmission spectra of the three investigated samples obtained by Fourier transform infrared spectroscopy. For sample A, the absorption peak is observed at 0.39 eV and for

[a]Electronic mail: c.tribuzy@fz-rossendorf.de

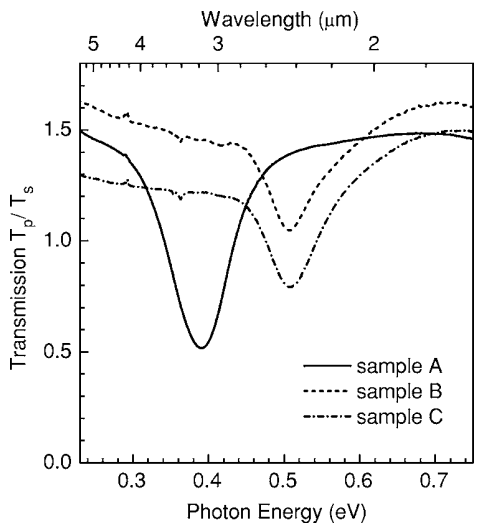

FIG. 1. Ratio between *p*- and *s*-polarized transmissions of the three investigated samples vs photon energy. The transmission curve for sample B has been shifted vertically by 0.1 for clarity.

samples B and C at 0.51 eV. Due to the higher doping, sample A exhibits a larger integrated absorption than samples B and C.

For the pump-probe measurements, femtosecond optical pulses with about 240 fs duration were generated at 78 MHz repetition rate by an optical parametric oscillator tunable from 1.3 to 3.2 μm. A small angle between the pump and probe beams, which were polarized parallel to the growth direction, was used in order to separate both beams. For the measurements a scanning delay generator (shaker) between pump and probe beams was operated at a frequency of 48 Hz and the signal was accumulated with a fast analog/digital converter (fast-scanning technique). All measurements were performed at room temperature. The pump-pulse energy was about 130 pJ at a wavelength of 2.4 μm and 70 pJ at 3.1 μm, exciting only about 1% of the electrons into the excited state. As discernible in Figs. 2(a)–2(c) below, the high pulse repetition rate together with the fast-scanning technique provides an unprecedented signal quality. Transmission changes of 1% are measured with a signal-to-noise ratio of up to 1000, making absorption changes of 10^{-5} detectable, several orders of magnitude better than reported in previous intersubband relaxation measurements.

Figure 2(a) shows the relative probe transmission change $\Delta T/T_0$ for sample A. At very early delay times we observe a coherent artifact[18] arising from self-diffraction of the pump into the direction of the probe beam, which will not be discussed here further. At later time delays, the decay of the signal can be accurately fitted by a single exponential, yielding a decay time constant of τ=1.5 ps.

The band structure of our samples was calculated by a self-consistent solution of the Schrödinger and Poisson equations, including nonparabolicity as described in Ref. 19 and using an InGaAs band edge mass of $0.0427m_0$ at the Γ point. m_0 is the free electron mass. Other parameters are taken from Ref. 20. Figure 2(d) shows the conduction band edge profile of sample A at the Γ and X minima (for simplicity, the L valley is not shown), as well as the square of the modulus of the lowest two subband wave functions at both minima. Even though the second Γ subband coincides approximately with the X levels for the chosen band parameters, the pump-probe data appear to be unaffected by intervalley scattering.

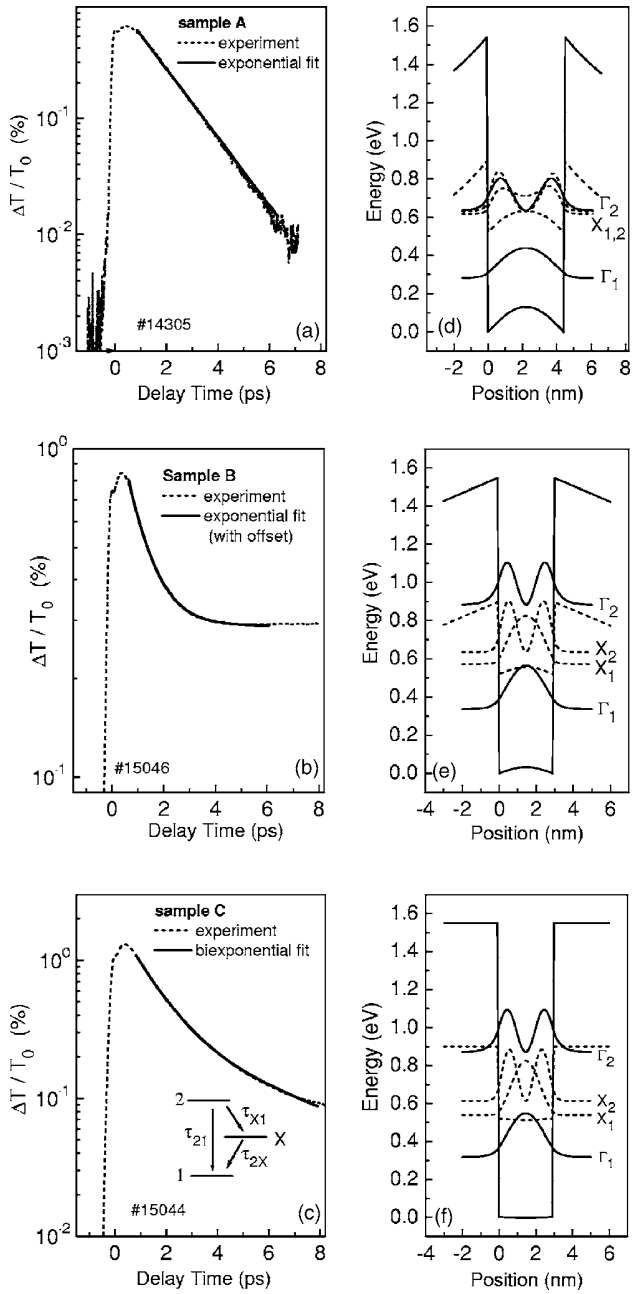

FIG. 2. Measured probe transmission of samples A (a), B (b), and C (c) vs delay time together with numerical fits of the decay curve. Self-consistent conduction band edge profiles at the Γ (solid lines) and X points (dashed lines) for the same samples [(d)–(f)]; probability densities of the subband states are also shown. The inset of (c) displays a three-level configuration as discussed in the text.

Studying the relaxation time of sample B, its pump-probe curve is best fitted by a single-exponential plus a constant offset, as shown in Fig. 2(b). The offset is necessary to describe the slow decay (nanosecond regime) observed at later delay times. For sample B a decay time constant of τ =0.8 ps was found. As plotted in Fig. 2(e), the excited Γ subband is raised significantly above the X levels due to the reduced well width. In addition, the excited carriers can now easily escape into the barriers, where metastable states at the X minimum exist due to the barrier doping. The extremely slow relaxation at large delays indicates the relevance of the

latter process. In fact, these barrier-confined metastable states exhibit negligible tunneling probabilities due to the large effective mass at the indirect minimum and a high barrier (about 0.4 eV) for thermionic emission back into the QW.

Comparing these decay time constants, sample B should exhibit a longer intersubband relaxation time than sample A due to its larger intersubband energy and the $1/q^2$ dependence of the optical phonon scattering, where q is the momentum transfer. The observed opposite behavior is therefore another signature for the additional relaxation channels present in this sample.

In order to eliminate long-lived states in the barrier, we now turn to sample C where the Si impurities are located inside the QWs and space charge effects are negligible [see Fig. 2(f)]. The resulting pump-probe data are shown in Fig. 2(c). Indeed the plateaulike component at later delay times is not present. Nevertheless a slow component is also observed. In fact, the pump-probe curve of this sample is best fitted by a biexponential decay without offset. The two characteristic decay time constants are 1.2 and 6.2 ps. According to Fig. 2(f), levels related to indirect valleys inside the InGaAs QW are the only possible origin of the long time constant.

We have also performed a rate equation analysis involving three levels [shown in the inset of Fig. 2(c)] to describe the two decay time constants. Assuming one effective level (X) for the X and L states, the longer decay time τ_{X1} then characterizes the return time from the X or L levels to level 1, the fundamental Γ subband. This return time is expected to be longer than the scattering time τ_{2X} from level 2 into the side valleys due to the higher effective masses of the latter.[21] The initial decay time τ_i is thus attributed to the combined scattering between the two Γ levels of the QW (τ_{21}) and the one related to Γ-X or Γ-L transfer (τ_{2X}), leading to the relation $1/\tau_i = 1/\tau_{21} + 1/\tau_{2X}$. Even though τ_{21} and τ_{2X} cannot be determined independently, both time constants have to exceed the observed value of τ_i (1.2 ps). In fact, this conclusion is further supported by the observation that this value of the "fast" decay time is shorter than for the configuration of Fig. 2(d) where intervalley scattering has only negligible influence and longer than for Fig. 2(e) where emission into the barrier provides an additional channel. Knowing that typical Γ-X scattering times for bulk III-V materials are of the order of 100 fs,[22] our observations indicate that intervalley scattering times in QWs should be significantly longer than for bulk material, as also suggested in Refs. 23 and 24, however, depending very strongly on the exact wave functions involved. Our observations are sustained by the fact that pronounced intersubband luminescence has been observed from states located somewhat above the side valleys,[17] which implies a reasonably long intervalley scattering time.

In conclusion, pump-probe measurements on InGaAs/AlAsSb QWs at low excitation densities were carried out in single-pass geometry with very high signal-to-noise ratios. At early delay times, all samples show an exponential decay of the transient transmission occurring with time constants of 0.8–1.5 ps. The relaxation dynamics at later time delays strongly depends on both QW thickness and doping location. For barrier-doped structures, very long time constants in the nanosecond regime can emerge if carriers escape into the barriers. In the case of well doping, intervalley scattering of high-energy electrons located above the indirect minima of the well material was found to occur with much longer time constants, in the picosecond regime, than for bulk material. In particular, the latter observation suggests that intersubband lasing involving states above indirect minima of the well material should be possible. This work additionally provides important details about the relaxation dynamics of short wavelength intersubband transitions relevant for all-optical intersubband modulators designed for telecommunication wavelengths and saturable absorbers for IR to mid-IR solid state or fiber lasers.

One of the authors (C.V.-B.T.) acknowledges support from the Alexander-von-Humboldt Foundation. The work of the two authors (J.N. and T.D.) is supported through the Ministry of Science, Research and the Arts of Baden-Württemberg.

[1] *Intersubband Transitions in Quantum Wells: Physics and Device Applications*, Semiconductors and Semimetals, Vols. 62 and 66, edited by H. C. Liu and F. Capasso (Academic, San Diego, 2000).
[2] T. Akiyama, N. Georgiev, T. Mozume, H. Yoshida, A. V. Gopal, and O. Wada, IEEE Photonics Technol. Lett. **14**, 495 (2002).
[3] R. Akimoto, B. S. Li, K. Akita, and T. Hasama, Appl. Phys. Lett. **87**, 181104 (2005).
[4] T. Elsaesser and M. Woerner, Phys. Rep. **321**, 254 (1999).
[5] D. Barate, R. Teissier, Y. Wang, and A. N. Baranov, Appl. Phys. Lett. **87**, 051103 (2005).
[6] D. Hofstetter, E. Baumann, F. R. Giorgetta, M. Graf, M. Maier, F. Guillot, E. Bellet-Amalric, and E. Monroy, Appl. Phys. Lett. **88**, 121112 (2006).
[7] G. Ghislotti, E. Riedo, D. Ielmini, and M. Martinelli, Appl. Phys. Lett. **75**, 3626 (1999).
[8] N. Georgiev, T. Dekorsy, F. Eichhorn, M. Helm, M. P. Semtsiv, and W. T. Masselink, Appl. Phys. Lett. **83**, 210 (2003).
[9] N. Georgiev and T. Mozume, J. Appl. Phys. **89**, 1064 (2001).
[10] T. Mozume, J. Kasai, N. Georgiev, T. Simoyama, A. V. Gopal, and H. Yoshida, Jpn. J. Appl. Phys., Part 1 **42**, 5500 (2003).
[11] J. D. Heber, C. Gmachl, H. M. Ng, and A. Y. Cho, Appl. Phys. Lett. **81**, 1237 (2002).
[12] J. Hamazaki, H. Kunugita, K. Ema, A. Kikuchi, and K. Kishino, Phys. Rev. B **71**, 165334 (2005).
[13] R. Akimoto, K. Akita, F. Sasaki, and T. Hasama, Appl. Phys. Lett. **81**, 2998 (2002).
[14] M. P. Semtsiv, M. Ziegler, S. Dressler, W. T. Masselink, N. Georgiev, T. Dekorsy, and M. Helm, Appl. Phys. Lett. **85**, 1478 (2004).
[15] Q. Yang, C. Manz, W. Bronner, K. Köhler, and J. Wagner, Appl. Phys. Lett. **88**, 121127 (2006).
[16] L. R. Wilson, D. A. Carder, J. W. Cockburn, R. P. Green, D. G. Revin, M. J. Steer, M. Hopkinson, G. Hill, and R. Airey, Appl. Phys. Lett. **81**, 1378 (2002).
[17] D. G. Revin, M. J. Steer, L. R. Wilson, R. J. Airey, J. W. Cockburn, E. A. Zibik, and R. P. Green, Electron. Lett. **40**, 874 (2004).
[18] P. Borri, F. Romstad, W. Langbein, A. Kelly, J. Mork, and J. Hvam, Opt. Express **7**, 107 (2000).
[19] P. Harrison, *Quantum Wells, Wires and Dots: Theoretical and Computational Physics of Semiconductor Nanostructures*, 2nd edition (Wiley-Interscience, Chichester, England, 2005), pp. 103ff.
[20] I. Vurgaftman, J. R. Meyer, and L. R. Ram-Mohan, J. Appl. Phys. **89**, 5815 (2001).
[21] C. J. Stanton and D. W. Bailey, Phys. Rev. B **45**, 8369 (1992).
[22] S. Zollner, S. Gopalan, and M. Cardona, Appl. Phys. Lett. **54**, 614 (1989).
[23] D. Indjin, P. Harrison, R. W. Kelsall, and Z. Ikonić, Appl. Phys. Lett. **81**, 400 (2002).
[24] J. W. Cockburn, J. J. Finley, M. S. Skolnick, P. Wisniewski, R. Grey, G. Hill, and M. A. Pate, Appl. Phys. Lett. **70**, 622 (1997).

Statistics

Monographs & Book Chapters

1. Gemming, S.; Enyashin, A.; Schreiber, M.
Amorphisation at Heterophase Interfaces
in: Karl Heinz Hoffmann, Arnd Meyer: Parallel Algorithms and Cluster Computing - Lecture Notes in Computational Science and Engineering, Berlin - Heidelberg - New York: Springer, 2006, ISBN: 3-540-33539-0, pp. 235-254

2. Schneider, H.; Liu, H. C.
Quantum Well Infrared Photodetector: Physics and Applications
Heidelberg: Springer-Verlag, 2006, ISBN: 3-540-36323-8

3. Schneider, H.; Liu, H. C.
Quantum Well Infrared Photodetector: High Absorption and High Speed Properties, and Two-Photon Response (Chapter 7)
in: Paiella, R.: Intersubband Transitions in Quantum Structures, New York: Mc. Graw-Hill, 2006, ISBN: 0-071-45792-5, pp. 285-313

Publications

Ion-Solid-Interaction

1. Abrasonis, G.; Möller, W.; Ma, X. X.
Anomalous ion accelerated bulk diffusion of interstitial nitrogen
Physical Review Letters ***96****, 065901 (2006).*

2. Ayache, R.; Bouabellou, A.; Eichhorn, F.; Richter, E.; Mücklich, A.
Surface modification of Si(111) substrate by iron ion implantation: growth of a thin beta-$FeSi_2$ layer
Review of Scientific Instruments ***77****, 03C108 (2006).*

3. Chen, S. H.; Schumacher, G.; Xu, Z. Y.; Richter, E.
Changes in hardness and elasticity of a Ti6Al4V alloy under helium irradiation
Journal of Nuclear Materials ***358****, 26 (2006).*

4. Foerster, C. E.; da, Silva S. L. R.; Fitz, T.; Dekorsy, T.; Prokert, F.; Kreissig, U.; Richter, E.; Möller, W.; Lepienski, C. M.; Siqueira, C. J. D.
Carbon ion implantation into aluminium: mechanical and tribological properties
Surface and Coatings Technology ***200****, 5210 (2006).*

5. Silva, M. M.; Ueda, M.; Otani, C.; Reuther, H.; Lepienski, C. M.; Soares Jr., P. C.; Otubo, J.
Hybrid processing of Ti6Al4V using plasma immersion ion implantation combined with plasma nitriding
Materials Research ***9****, 97 (2006).*

6. Turos, A.; Abdul-Kader, A. M.; Grambole, D.; Jagielski, J.; Piątkowska, A.; Madi, N. K.; Al-Maadeed, M.
The effects of ion bombardment of ultra-high molecular weight polyethylene
Nuclear Instruments and Methods in Physics Research B ***249****, 660 (2006).*

7. Donchev, A.; Richter, E.; Schütze, M.; Yankov, R. A.
Improvement of the oxidation behavior of TiAl alloys by treatment with halogens
Intermetallics ***14****, 1168 (2006).*

Thin Films

8. Abrasonis, G.; Gago, R.; Vinnichenko, M.; Kreissig, U.; Kolitsch, A.; Möller, W.
Sixfold ring clustering in sp^2-dominated carbon and carbon nitride thin films: a Raman spectroscopy study
Physical Review B ***73****, 125427 (2006).*

9. Andersson, J. M.; Wallin, E.; Helmersson, U.; Kreissig, U.; Münger, E. P.
Phase control of Al_2O_3 thin films grown at low temperatures
Thin Solid Films ***513****, 57(2006).*

10. Beckers, M.; Schell, N.; Martins, R. M. S.; Mücklich, A.; Möller, W.
Phase stability of epitaxially grown Ti_2AlN thin films
Applied Physics Letters ***89****, 074101 (2006).*

11. Beckers, M.; Schell, N.; Martins, R. M. S.; Mücklich, A.; Möller, W.; Hultman, L.
Microstructure and non-basal plane growth of epitaxial MAX phase Ti_2AlN thin films
Journal of Applied Physics ***99****, 34902 (2006).*

12. Cizek, J.; Melikhova, O.; Prochazka, I.; Brauer, G.; Anwand, W.; Mücklich, A.; Kirchheim, R.; Pundt, A.
Defects in nanocrystalline Nb films: effect of sputtering temperature
Applied Surface Science ***252****, 3245 (2006).*

13. Cizek, J.; Prochazka, I.; Brauer, G.; Anwand, W.; Mücklich, A.; Kirchheim, R.; Pundt, A.; Bähtz, C.; Knapp, M.
Defect studies of hydrogen-loaded thin Nb films
Applied Surface Science ***252****, 3237 (2006).*

14. Cizek, J.; Procházka, I.; Brauer, G.; Anwand, W.; Mücklich, A.; Kirchheim, R.; Pundt, A.; Bäthz, C.; Knapp, M.
Study of hydrogen-defect interaction in thin Nb film on Si substrate using positron annihilation
Materials Structure in Chemistry, Biology, Physics and Technology ***13****, 82 (2006).*

15. Gemming, S.; Seifert, G.
$SrTiO_3$(001) | $LaAlO_3$(001) multilayers: a density-functional investigation
Acta Materialia ***54****, 4299 (2006).*

16. Guerassimov, N.; Möller, W. (Editors)
Highlights from the 14th International Summer School on Vacuum, Electron and Ion Technologies (VEIT 2005)
Plasma Processing and Polymers ***3****, 87 (2006).*

17. Maitz, M.; Gago, R.; Abendroth, B.; Camero, M.; Caretti, I.; Kreissig, U.
Hemocompatibility of low-friction boron-carbon-nitrogen containing coatings
Journal of Biomedical Materials Research Part B ***77B****, 179 (2006).*

18. Maitz, M.; Shevchenko, N.
Plasma-immersion ion-implanted nitinol surface with depressed nickel concentration for implants in blood
Journal of Biomedical Materials Research Part A ***76A****, 356 (2006).*

19. Martin-Palma, R. J.; Gago, R.; Torres-Costa, V.; Fernandez-Hidalgo, P.; Kreissig, U.; Martinez Duart, J. M.
Optical and compositional analysis of functional SiO_xC_y:H coatings on polymers
Thin Solid Films ***515****, 2493 (2006).*

20. Martins, R. M. S.; Braz Fernandes, F. M.; Silva, R. J. C.; Beckers, M.; Schell, N.
In-situ observation of Ni-Ti thin film growth by synchrotron radiation scattering
Materials Science Forum ***514-516****, 1588 (2006).*

21. Martins, R. M. S.; Braz Fernandez, F. M.; Silva, R. J. C.; Pereira, R. J. C.; Gordo, P. R.; Maneira, M. J. P.; Beckers, M.; Mücklich, A.; Schell, N.
The influence of a poly-Si intermediate layer on the crystallization behaviour of Ni-Ti SMA magnetron sputtered thin films
Applied Physics A ***83****, 139 (2006).*

22. Martins, R. M. S.; Schell, N.; Beckers, M.; Mahesh, K. K.; Silva, R. J. C.; Braz Fernandes, F. M. B.
Growth of sputter-deposited Ni-Ti thin films: effect of a SiO_2 buffer layer
Applied Physics A ***84****, 285 (2006).*

23. Patra, A. K.; Neu, V.; Fähler, S.; Grötzschel, R.; Schultz, L.
Metastable, epitaxial $PrCo_7$ films with high energy product
Applied Physics Letters ***89****, 142512 (2006).*

24. Pereira, L.; Águas, H.; Beckers, M.; Martins, R. M. S.; Fortunato, E.; Martins, R.
Spectroscopic ellipsometry study of nickel induced crystallization of a-Si
Journal of Non-Crystalline Solids ***352****, 1204 (2006).*

25. Pereira, L.; Martins, R. M. S.; Schell, N.; Fortunato, E.; Martins, R.
Nickel-assisted metal-induced crystallization of silicon: effect of native silicon oxide layer
Thin Solid Films ***511-512****, 275 (2006).*

26. Rogozin, A.; Shevchenko, N.; Vinnichenko, M.; Seidel, M.; Kolitsch, A.; Möller, W.
Annealing of indium tin oxide films by electric current: properties and structure evolution
Applied Physics Letters ***89****, 061908 (2006).*

27. Rogozin, A.; Vinnichenko, M.; Shevchenko, N.; Kolitsch, A.; Möller, W.
Plasma influence on the properties and structure of indium tin oxide films produced by reactive middle frequency pulsed magnetron sputtering
Thin Solid Films ***496****, 197 (2006).*

28. Rosen, J.; Widenkvist, E.; Larsson, K.; Kreissig, U.; Mraz, S.; Martinez, C.; Music, D.; Schneider, J. M.
Reducing the impurity incorporation from residual gas by ion bombardment during high vacuum magnetron sputtering
Applied Physics Letters ***88****, 191905 (2006).*

29. Tinchev, S. S.; Dyulgerska, Y.; Nikolova, P.; Grambole, D.; Kreissig, U.; Babeva, Tz.
Optical properties of PECVD deposited DLC films prepared with air addition
Journal of Optoelectronics and Advanced Materials ***8****, 308 (2006).*

30. Ueda, M.; Reuther, H.; Beloto, A. F.; Kuranaga, C.; Abramof, E.
Annealing effects on silicon oxynitride layer synthesized by N plasma immersion ion implantation
IEEE Transactions on Plasma Science ***34****, 1080 (2006).*

31. Yang, P.; Huang, N.; Leng, Y.; Yao, Z.; Zhou, H.; Maitz, M.; Leng, Y.; Chu, P.
Wettability and biocompatibility of nitrogen-doped hydrogenated amorphous carbon films: Effect of nitrogen
Nuclear Instruments and Methods in Physics Research B ***242****, 22 (2006).*

Nanoscale Magnetism

32. Cantelli, V.; von Borany, J.; Grenzer, J.; Kaltofen, R.; Schumann, J.; Fassbender, J.
Influence of He-ion-irradiation on thin NiMn/NiFe exchange bias films
Journal of Applied Physics ***99****, 08C102 (2006).*

33. Dev, B. N.; Bera, S.; Satpati, B.; Goswami, D. K.; Bhattacharjee, K.; Satyam, P. V.; Yamashita, K.; Liedke, M. O.; Potzger, K.; Fassbender, J.; Eichhorn, F.; Grötzschel, R.
Nonmagnetic to magnetic nanostructures via ion irradiation
Microelectronic Engineering ***83****, 1721 (2006).*

34. Fassbender, J.; Bischoff, L.; Mattheis, R.; Fischer, P.
Magnetic domains and magnetization reversal of ion-induced magnetically patterned RKKY-coupled Ni81Fe19/Ru/Co90Fe10 films
Journal of Applied Physics ***99****, 08G301 (2006).*

35. Fassbender, J.; McCord, J.
Control of saturation magnetization, anisotropy and damping due to Ni implantation in thin Ni81Fe19 layers
Applied Physics Letters ***88****, 252501 (2006).*

36. Fassbender, J.; Mücklich, A.; Potzger, K.; Möller, W.
Mixing and subsequent amorphization of ultrathin Ni81Fe19/Ta bilayers by 30 keV Ni implantation
Nuclear Instruments and Methods in Physics Research B ***248****, 343 (2006).*

37. Fassbender, J.; von Borany, J.; Mücklich, A.; Potzger, K.; Möller, W.; McCord, J.; Schultz, L.; Mattheis, R.
Structural and magnetic modifications in Cr implanted Permalloy
Physical Review B ***73****, 184410 (2006).*

38. Galakhov, V. R.; Ovechkina, N. A.; Shkvarin, A. S.; Shamin, S. N.; Kurmaev, E. Z.; Küpper, K.; Takács, A. F.; Raekers, M.; Robin, S.; Neumann, M.; Gavrila, G.-N.; Semenova, A. S.; Kellerman, D. G.; Käämbre, T.; Nordgren, J.
Electronic structure and X-ray spectra of defect oxides Li_xCoO_2
Physical Review B ***74****, 045120 (2006).*

39. Ghosh, S.; Mäder, M.; Grötzschel, R.; Gupta, A.; Som, T.
Correlation between phase formation and magnetic properties of heavy ion irradiated Co/Pt bilayers
Applied Physics Letters ***89****, 104104 (2006).*

40. Küpper, K.; Klingeler, R.; Reutler, P.; Büchner, B.; Neumann, M.
Electronic structure of $LaSrMnO_4$: XPS and XES studies
Journal of Applied Physics ***99****, Q308 (2006)8.*

41. Küpper, K.; Klingeler, R.; Reutler, P.; Büchner, B.; Neumann, M.
Excited and ground state properties of $LaSrMnO_4$: A combined X-ray spectroscopic study
Physical Review B 74*, 115103 (2006).*

42. Liedke, M. O.; Potzger, K.; Bothmer, A.; Hillebrands, B.; Rickart, M.; Freitas, P. P.; Fassbender, J.
Domain structure during magnetization reversal of PtMn/CoFe exchange bias micro-patterned lines
Journal of Applied Physics ***100****, 043918 (2006).*

43. Mentes, T. O.; Bondino, F.; Magnano, E.; Zangrando, M.; Küpper, K.; Galakhov, V. R.; Mukovskii, Y. M.; Neumann, M.; Parmigiani, F.
Excitation dynamics in $La_{0.875}Sr_{0.125}MnO_3$ measured by resonant Auger electron and resonant X-ray

emission spectroscopies
Physical Review B ***74****, 205409 (2006).*

44. Potzger, K.; Reuther, H.; Zhou, S.; Mücklich, A.; Grötzschel, R.; Eichhorn, F.; Liedke, M. O.; Fassbender, J.
Ion beam synthesis of Fe nanoparticles in MgO and Y:ZrO_2
Journal of Applied Physics ***99****, 08N701 (2006).*

45. Potzger, K.; Zhou, S.; Eichhorn, F.; Helm, M.; Skorupa, W.; Mücklich, A.; Fassbender, J.; Herrmannsdörfer, T.; Bianchi, A.
Ferromagnetic Gd-implanted ZnO single crystals
Journal of Applied Physics ***99****, 063906 (2006).*

46. Potzger, K.; Zhou, S. Q.; Reuther, H.; Mücklich, A.; Eichhorn, F.; Schell, N.; Skorupa, W.; Fassbender, J.; Helm, M.; Herrmannsdörfer, T.; Papageorgiou, T. P.
Fe implanted ferromagnetic ZnO
Applied Physics Letters ***88****, 052508 (2006).*

47. Prinz, M.; Takács, A.; Schnack, J.; Balasz, I.; Burzo, E.; Kortz, U.; Küpper, K.; Neumann, M.
Magnetic and electronic properties of the iron-containing polyoxotungstate $[Fe_4(H_2O)_{10}(\beta\text{-}SbW_9O_{33})_2]_6$-
Journal of Applied Physics ***99****, 08J505 (2006).*

48. Radke De Cuba, M.; Emmerich, H.; Gemming, S.
Zwei-Skalen-Modellierung von Adsorptionsprozessen an strukturierten Oberflächen
Zeitschrift für Anorganische und Allgemeine Chemie ***632****, 2144 (2006).*

49. Raekers, M.; Küpper, K.; Hesse, H.; Balasz, I.; Deac, I. G.; Constantinescu, S.; Burzo, E.; Valeanu, M.; Neumann, M.
Investigation of chemical and grain boundary effects in highly ordered Sr_2FeMoO_6: XPS and Moessbauer studies
Journal of Optoelectronics and Advanced Materials ***8****, 455 (2006).*

50. Stromberg, F.; Keune, W.; Chen, X.; Bedanta, S.; Reuther, H.; Mücklich, A.
The origin of ferromagnetism in ^{57}Fe ion-implanted semiconducting 6H-polytype silicon carbide
Journal of Physics: Condensed Matter ***18****, 9881 (2006).*

51. Takács, A.; Neumann, M.; Postnikov, A. V.; Küpper, K.; Scheurer, A.; Sperner, S.; Prince, K. C.; Saalfrank, R. W.
Electronic structure study by means of X-ray spectroscopy and theoretical calculations of the "ferric star" single molecule magnet
The Journal of Chemical Physics ***124****, 044503 (2006).*

52. Talut, G.; Reuther, H.; Mücklich, A.; Eichhorn, F.; Potzger, K.
Nanocluster formation in Fe implanted GaN
Applied Physics Letters ***89****, 161909 (2006).*

53. Weber, M. C.; Nembach, H.; Carey, Matt J.; Hillebrands, B.; Fassbender, J.
Real time evidence of two-magnon scattering in exchange coupled bilayers
Journal of Applied Physics ***99****, 08J308 (2006).*

54. Zhou, S.; Potzger, K.; Zhang, G.; Eichhorn, F.; Skorupa, W.; Helm, M.; Fassbender, J.
Crystalline Ni nanoparticles as the origin of ferromagnetism in Ni implanted ZnO crystals
Journal of Applied Physics ***100****, 114304 (2006).*

Nanostructures

54. Akhmadaliev, Ch.; Schmidt, B.; Bischoff, L.
Defect induced formation of $CoSi_2$ nanowires by focused ion beam synthesis
Applied Physics Letters ***89****, 22312 (2006).*

55. Akhmadaliev, Ch.; Bischoff, L.; Schmidt, B.
$CoSi_2$ nanostructures by writing FIB ion beam synthesis
Materials Science and Engineering C ***26****, 818 (2006).*

56. Bar-Sadan, M.; Enyashin, A. N.; Gemming, S.; Popovits-Biro, R.; Hong, S. Y.; Prior, Y.; Tenne, R.; Seifert, G.
Structure and stability of molybdenum sulfide fullerenes
Journal of Physical Chemistry B ***110****, 25399 (2006).*

57. Beyer, V.; von Borany, J.; Klimenkov, M.
Determination and evolution of tunneling distances in Ge nanocrystal based memories
Applied Physics Letters ***89****, 193505 (2006).*

58. Bischoff, L.; Schmidt, B.; Akhmadaliev, Ch.; Mücklich, A.
Investigation of FIB assisted $CoSi_2$ nanowire growth
Microelectronic Engineering ***83****, 800 (2006).*

59. Enyashin, A.; Gemming, S.; Heine, T.; Seifert, G.; Zhechkov, L.
C28 fullerites - structure, electronic properties and intercalates
Physical Chemistry, Chemical Physics ***8****, 28 063AN (2006).*

60. Fan, H. J.; Knez, M.; Scholz, R.; Nielsch, K.; Pippel, E.; Hesse, D.; Zacharias, M.; Gösele, U.
Monocrystalline spinel nanotube fabrication based on the Kirkendall effect
Nature Materials ***5****, 627 (2006).*

61. Fan, H.; Knet, M.; Scholz, R.; Nielsch, K.; Pippel, E.; Hesse, D.; Gösele, U.; Zacharias, M.
Single-crystalline $MgAl_2O_4$ spinel nanotubes using a reactive and removable MgO nanowire template
Nanotechnology ***17****, 5157 (2006).*

62. Gemming, S.; Seifert, G.; Vilfan, I.
Li-doped Mo_6S_6 nanowires: elastic and electronic properties
Physica Status Solidi (B) ***243****, 3320 (2006).*

63. Grigorian, S.; Grenzer, J.; Datta, D. P.; Hazra, S.; Chini, T. K.; Sanyal, M. K.; Pietsch, U.
Micro-structural anisotropy at the ion-induced rippled amorphous – crystalline interface of silicon
Applied Physics Letters ***89****, 231915 (2006).*

64. Ivanovskaya, V. V.; Heine, T.; Gemming, S.; Seifert, G.
Structure, stability and electronic properties of composite $Mo_{1-x}Nb_xS_2$ nanotubes
Physica Status Solidi (B) ***243****, 1757 (2006).*

65. Kolb, F. M.; Berger, A.; Hofmeister, H.; Pippel, E.; Gösele, U.; Zacharias, M.
Periodic chains of gold nanoparticles and the role of oxygen during the growth of silicon nanowires
Applied Physics Letters ***89****, 173 111 (2006).*

66. Luchnikov, V.; Stamm, M.; Akhmadaliev, Ch.; Bischoff, L.; Schmidt, B.
Focused-ion-beam-assisted fabrication of polymer rolled-up microtubes
Journal of Micromechanics and Microengineering ***16****, 1602 (2006).*

67. Meijer, J.; Vogel, T.; Burchard, B.; Rangelow, I. W.; Bischoff, L.; Wrachtrup, J.; Domhan, M.; Jelezko, F.; Schnitzler, W.; Schulz, S. A.; Singer, K.; Schmidt-Kaler, F.
Concept of deterministic single ion doping with sub-nm spatial resolution
Applied Physics A ***83****, 321 (2006).*

68. Oates, T. W. H.
Real time observation of silver nanoparticle growth in ultrathin polymer films
Applied Physics Letters ***88****, 213115 (2006).*

69. Pelka, J. B.; Brust, M.; Gierlowski, P.; Paszkowicz, W.; Schell, N.
Structure and conductivity of self-assembled films of gold nanoparticles
Applied Physics Letters ***89****, 063110 (2006).*

70. Rangelow, I.; Ivanov, T.; Volland, B.; Dontsov, D.; Sarov, Y.; Ivanova, K.; Persaud, A.; Filenko, D.; Nikolov, N.; Schmidt, B.; Zier, M.; Gotszalk, T.; Sulzbach, T.
Scanning probe microscopy with cantilever arrays
Technisches Messen ***73****, 485 (2006).*

71. Röntzsch, L.; Heinig, K.-H.; Schmidt, B.; Mücklich, A.
Experimental evidence of Si nanocluster δ-layer formation in the vicinity of ion-irradiated SiO_2-Si interfaces
Nuclear Instruments and Methods in Physics Research B ***242****, 149 (2006).*

72. Schmidt, B.; Heinig, K.-H.; Röntzsch, L.; Müller, T.; Stegemann, K.-H.; Votintseva, E.
Ion irradiation through SiO_2/Si-interfaces: non-conventional fabrication of Si nanocrystals for memory applications
Nuclear Instruments and Methods in Physics Research B ***242****, 146 (2006).*

73. Som, T.; Satpati, B.; Prokert, F.; Cantelli, V.; Kabiraj, D.
Phase formation within Au and Ge nanoislands by room temperature ion irradiation
Nanotechnology ***17****, 5248 (2006).*

74. Yakimov, A. I.; Nikiforov, A. I.; Dvurechenskii, A. V.; Ulyanov, V. V.; Volodin, V. A.; Grötzschel, R.
Effect of the growth rate on the morphology and structural properties of hut-shaped Ge islands in Si(001)
Nanotechnology ***17****, 4743 (2006).*

Doping and Defects of Semiconductors

75. Beyer, R.; Beyreuther, E.; von Borany, J.; Weber, J.
Charge storage in silicon-implanted silicon dioxide layers examined by scanning probe microscopy
Thin Solid Films ***513****, 159 (2006).*

76. Borseth, T. M.; Tuomisto, F.; Cristensen, J. S.; Skorupa, W.; Monakhov, E.; Svensson, B. G.; Kuznetsov, A.
Deactivation of Li by vacancy clusters in ion-implanted and flash-annealed ZnO
Physical Review B ***74****, 161202(R) (2006).*

77. Brauer, G.; Anwand, W.; Eichhorn, F.; Skorupa, W.; Hofer, C.; Teichert, C.; Kuriplach, J.; Cizek, J.; Prochazka, I.; Coleman, Paul G.; Nozawa, T.; Kohyama, A.
Characterization of a SiC/SiC composite by X-ray diffraction, atomic force microscopy and positron spectroscopies
Applied Surface Science ***252****, 3342 (2006).*

78. Brauer, G.; Anwand, W.; Skorupa, W.
Characterization of 6H-SiC surfaces after ion implantation and annealing using positron annihilation spectroscopy and atomic force microscopy
Journal of Applied Physics ***99****, 023523 (2006).*

79. Brauer, G.; Becvar, F.; Anwand, W.; Skorupa, W.
Further indication of a low quartz structure at the SiO_2/Si interface from coincidence Doppler broadening spectroscopy
Applied Surface Science ***252****, 3368 (2006).*

80. Brauer, G.; Anwand, W.; Skorupa, W.; Kuriplach, J.; Melikhova, O.; Moisson, C.; von Wenckstern, H.; Schmidt, H.; Lorenz, M.; Grundmann, M.
Defects in virgin and N^+ ion-implanted ZnO single crystals studied by positron annihilation, Hall effect and deep level transient spectroscopy
Physical Review B ***74****, 045208 (2006).*

81. Brauer, G.; Anwand, W.; Skorupa, W.; Schmidt, H.; Diaconu, M.; Lorenz, M.; Grundmann, M.
Structure and ferromagnetism of Mn^+ ion implanted ZnO thin films on sapphire
Superlattices and Microstructures ***39****, 41 (2006).*

82. Gao, F.; Devanathan, R.; Zhang, Y.; Posselt, M.; Weber, W. J.
Atomic-level simulation of epitaxial recrystallization and phase transformation in SiC
Journal of Materials Research ***21****, 1420 (2006).*

83. Gao, F.; Zhang, Y.; Posselt, M.; Weber, W. J.
Atomic-level simulations of epitaxial recrystallization and amorphous-to-crystalline transition in 4H-SiC
Physical Review B ***74****, 104108 (2006).*

84. Heera, V.; Madhusoodanan, K. N.; Skorupa, W.; Dubois, C.; Romanus, H.
A comparative study of the electrical properties of heavily Al implanted, single crystalline and nanocrystalline SiC
Journal of Applied Physics ***99****, 123716 (2006).*

85. Kögler, R.; Mücklich, A.; Eichhorn, F.; Posselt, M.; Reuther, H.; Skorupa, W.
Solid-state nanocluster formation of praseodymium compounds in silicon and silicon dioxide
Journal of Applied Physics ***100****, 104314 (2006).*

86. Kögler, R.; Peeva, A.; Mücklich, A.; Eichhorn, F.; Skorupa, W.
Alternating layers of vacancy-type and interstitial-type defects in Ge ion implanted silicon
Applied Physics Letters ***88****, 1918 (2006).*

87. Kortov, V. S.; Zatsepin, A. F.; Biryukov, D. Yu.; Schmidt, B.
Optical stimulated electron emission from amorphous silicon dioxide implanted with iron ions
Poverkhnost (Surface) ***7****, 84 (2006).*

88. Kups, Th.; Weih, P.; Voelskow, M.; Skorupa, W.; Pezoldt, J.
High dose high temperature ion implantation of Ge into 4H-SiC
Materials Science Forum ***527****, 851 (2006).*

89. Posselt, M.; Bischoff, L.; Grambole, D.; Herrmann, F.
Competition between damage buildup and dynamic annealing in ion implantation into Ge
Applied Physics Letters ***89****, 151918 (2006).*

90. Posselt, M.; Gao, F.; Weber, W. J.
Atomistic simulations on the thermal stability of the antisite pair in 3C- and 4H-SiC
Physical Review B ***73****, 125206 (2006).*

91. Romanek, J.; Grambole, D.; Herrmann, F.; Voelskow, M.; Posselt, M.; Skorupa, W.; Zuk, J.
Ion implantation-induced damage depth profile determination in SiC by means of RBS/C and bevelling technique
Nuclear Instruments and Methods in Physics Research B ***251****, 148 (2006).*

92. Shiryaev, A. A.; Iakoubovskii, K.; Grambole, D.; Dubrovinskaia, N.
Spectroscopic study of defects and inclusions in bulk poly- and nanocrystalline diamond aggregates
Journal of Physics: Condensed Matter ***18****, L493 (2006).*

93. Smith, M. P.; Mcmahon, R. A.; Voelskow, M.; Skorupa, W.; Stoemenos, J.; Ferro, G.
Process control and melt depth homogenization for SiC-on-Si structures during flash lamp annealing by carbon implantation
Journal of Applied Physics ***100****, 094909 (2006).*

94. Smith, M.; Seffen, K.; Mc Mahon, R.; Voelskow, M.; Skorupa, W.
Analysis of wafer stresses during millisecond thermal processing
Journal of Applied Physics ***100****, 63515 (2006).*

95. Ulyashin, A.; Christensen, J. S.; Svensson, B. G.; Kögler, R.; Skorupa, W.
Hydrogen gettering at buried defect layers in ion-implanted silicon by plasma hydrogenation and annealing
Nuclear Instruments and Methods in Physics Research B ***253****, 126 (2006).*

96. von Wenckstern, H.; Pickenhain, R.; Schmidt, H.; Brandt, M.; Biehne, G.; Lorenz, M.; Grundmann, M.; Brauer, G.
Deep acceptor states in ZnO single crystals
Applied Physics Letters ***89****, 092122 (2006).*

97. Zhong, Z. Q.; Wu, D. X.; Gong, M.; Wang, O.; Shi, S. L.; Xu, S. J.; Chen, X. D.; Ling, C. C.; Fung, S.; Beling, C. D.; Brauer, G.; Anwand, W.; Skorupa, W.
Primary photoluminescence in as-neutron (electron)-irradiated n-type 6H-SiC
Journal of Applied Physics ***99****, 093511 (2006).*

Optoelectronics

98. Aronzon, B. A.; Drachenko, A. N.; Ryl'kov, V. V.; Leotin, J.
The effect of high magnetic field on the photoresponse of Si:B structures with blocked conductivity in the impurity band
Semiconductors ***40****, 798 (2006).*

99. Bartels, A.; Thoma, A.; Janke, C.; Dekorsy, T.; Dreyhaupt, A.; Winnerl, S.; Helm, M.
High-resolution THz spectrometer with kHz scan rates
Optics Express ***14****, 430 (2006).*

100. Dreyhaupt, A.; Winnerl, S.; Helm, M.; Dekorsy, T.
Optimum excitation conditions for the generation of high-electric-field THz radiation from an oscillator-driven photoconductive device
Optics Letters ***31****, 1546 (2006).*

101. Helm, M.; Michel, P.
FELBE: a new infrared free-electron-laser user facility
Notiziario Neutroni e Luce di Sincrotrone ***11****, 33 (2006).*

102. Nazarov, A.; Osiyuk, I.; Tyagulskii, I.; Lysenko, V.; Prucnal, S.; Sun, J.; Skorupa, W.; Yankov, R. A.
Charge trapping phenomena in high-efficiency metal-oxide-silicon light-emitting diodes with ion-implanted oxide
Journal of Luminescence ***121****, 213 (2006).*

103. Potfajova, J.; Sun, J. M.; Schmidt, B.; Dekorsy, T.; Skorupa, W.; Helm, M.
Silicon-on-insulator microcavity light emitting diodes with two Si/SiO_2 Bragg reflectors
Journal of Luminescence ***121****, 290 (2006).*

104. Schneider, H.; Drachenko, O.; Winnerl, S.; Helm, M.; Walther, M.
Quadratic autocorrelation of free-electron laser radiation and photocurrent saturation in two-photon quantum well infrared photodetectors
Applied Physics Letters ***89****, 133508 (2006).*

105. Semtsiv, M. P.; Müller, U.; Masselink, W. T.; Georgiev, N.; Dekorsy, T.; Helm, M.
Intersubband transitions in GaP–AlP heterostructures
Applied Physics Letters ***89****, 184102 (2006).*

106. Stehr, D.; Helm, M.; Metzner, C.; Wanke, M. C.
Microscopic theory of impurity states in coupled quantum wells and superlattices
Physical Review B ***74***, *085311 (2006).*

107. Stehr, D.; Winnerl, S.; Helm, M.; Dekorsy, T.; Roch, T.; Strasser, G.
Pump-probe spectroscopy of interminiband relaxation and electron cooling in doped superlattices
Applied Physics Letters ***88***, *51108 (2006).*

108. Sun, J. M.; Prucnal, S.; Skorupa, W.; Dekorsy, T.; Mücklich, A.; Helm, M.; Rebohle, L.; Gebel, T.
Electroluminescence properties of the Gd^{3+} ultraviolet luminescent centers in SiO_2 gate oxide layers
Journal of Applied Physics ***99***, *103102 (2006).*

109. Sun, J. M.; Prucnal, S.; Skorupa, W.; Helm, M.; Rebohle, L.; Gebel, T.
Increase of blue electroluminescence from Ce-doped SiO_2 layers through sensitization by Gd^{3+} ions
Applied Physics Letters ***89***, *091908 (2006).*

110. Tribuzy, C. V.-B.; Ohser, S.; Winnerl, S.; Grenzer, J.; Schneider, H.; Helm, M.; Neuhaus, J.; Dekorsy, T.; Biermann, K.; Künzel, H.
Femtosecond pump-probe spectroscopy of intersubband relaxation dynamics in narrow InGaAs/AlAsSb quantum well structures
Applied Physics Letters ***89***, *171104 (2006).*

111. Tyschenko, I. E.; Zhuravlev, K. S.; Cherkov, A. G.; Popov, V. P.; Misiuk, A.; Yankov, R. A.
Wavelength-selective enhancement of the intensity of visible photoluminescence in hydrogen-ion-implanted silicon-on-insulator structures annealed under high pressure
Applied Physics Letters ***89***, *013106 (2006).*

Others

112. Gomez, S.; Preoteasa, E. A.; Harangus, L.; Iordan, A.; Grambole, D.; Herrmann, F.
Micro-PIXE and histochemical studies of Zn and Ca distribution in normal bone
Nuclear Instruments and Methods in Physics Research B ***249***, *673 (2006).*

113. Grynszpan, R. I.; Baclet, N.; Darque, A.; Flament, J. L.; Zielinski, F.; Anwand, W.; Brauer, G.
Positron and deuteron depth profiling in He-3-implanted electrum-like alloy
Applied Surface Science ***252***, *3252 (2006).*

114. Ignatova, V. A.; van Dyck, S.; Grötzschel, R.; Möller, W.
XPS depth profiling of oxide scales of stainless steels formed in high-temperature aqueous conditions
Surface and Interface Analysis ***38***, *396 (2006).*

115. Krause-Rehberg, R.; Sachert, S.; Brauer, G.; Rogov, A.; Noack, K.
EPOS – an intense positron beam project at the Research Center Rossendorf
Applied Surface Science ***252***, *3106 (2006).*

116. Mackova, A.; Salavkova, L.; Spirkova, J.; Grötzschel, R.; Eichhorn, F.
RBS-channeling, ERDA and XRD study of lithium tantalate modified by annealed proton exchange (APE)
Nuclear Instruments and Methods in Physics Research B ***249***, *339 (2006).*

117. Markov, A. B.; Günzel, R.; Reuther, H.; Shevchenko, N.; Akhmadeev, Yu. Kh.; Schanin, P. M.; Koval, N. N.; Rotshtein, V. P.; Proskurovsky, D. I.
Pulsed electron-beam irradiation followed by nitriding of Ti-6Al-4V titanium alloy
Russian Physics Journal ***49***, *276 (2006).*

118. Markov, A. B.; Günzel, R.; Reuther, H.; Shevchenko, N.; Rotshtein, V. P.; Akhmadeev, Yu. Kh.; Schanin, P. M.
Effect of electron-beam treatment on subsequent titanium alloy nitriding
Electrotechnica & Elektronica ***5-6***, *230 (2006).*

119. Nebel, F.; Szerypo, J.; Zech, E.; Faestermann, T.; Grötzschel, R.; Gross, M.; Habs, D.; Krucken, R.; Maier-Komor, P.; Thirolf, P.; Yakushev, A.
Radioactivity distribution at MAFF
European Physical Journal A ***29***, *369 (2006).*

120. Nebel, F.; Zech, E.; Faestermann, T.; Krücken, R.; Maier-Komor, P.; Assmann, W.; Szerypo, J.; Gross, M.; Kester, O.; Thirolf, P. G.; Grötzschel, R.
Time-dependent radioactivity distribution in MAFF
Nuclear Instruments and Methods in Physics Research A ***561***, *83 (2006).*

121. Rother, A.; Reibold, M.; Lichte, H.; Leisegang, T.; Levin, A. A.; Paufler, P.; Meyer, D. C.; Gemming, S.; Chaplygin, I.; Seifert, G.; Ormeci, A. H.

X-ray investigation, high-resolution electron holography, and density functional calculations of single-crystalline BaTiO3
Physical Review B ***74****, 134116 (2006).*

122. Rotstein, V. P.; Günzel, R.; Markov, A. B.; Proskurovskij, D. I.; Pham, M. T.; Richter, E.; Shulov, V. A.
Surface modification of Ti-6Al-4V alloy with a low-energy, high-current electron beam at elevated initial temperatures
Fisika i Khimiya Obrabotki Materialov ***1****, 62 (2006).*

123. Rotshtein, V. P.; Markov, A. B.; Proskurovsky, D. I.; Günzel, R.; Pham, M. T.; Richter, E.; Shevchenko, N.; Shulov, V. A.; Rubshtein, A. P.
Surface modification of Ti-6Al-4V alloy with a low-energy, high-current electron beam at elevated initial temperatures
Russian Physics Journal ***49****, 337 (2006).*

124. Rotshtein, V. P.; Markov, A. B.; Proskurovsky, D. I.; Kagadei, V. A.; Günzel, R.; Shevchenko, N.; Reuther, H.; Shulov, V. A.
Surface alloying of Ti-6Al-4V with zirconium by pulsed electron-beam melting of film – substrate system
Russian Physics Journal ***49****, 262 (2006).*

125. Sass, J.; Mazur, K.; Surma, B.; Eichhorn, F.; Litwin, D.; Galas, J.; Sitarek, S.
X-ray studies of ultra-thin Si wafers for mirror application
Nuclear Instruments and Methods in Physics Research B ***253****, 236 (2006).*

126. Yang, S.; Troyanov, Sergey, I..; Popov, A.; Krause, M.; Dunsch, L.
Deviation from the planarity - a large Dy_3N cluster encapsulated in an I_h-C_{80} cage: an X-ray crystallographic and vibrational spectroscopic study
Journal of the American Chemical Society ***128****, 16733 (2006).*

127. Zen, A.; Bilge, A.; Galbrecht, F.; Alle, R.; Meerholz, K.; Grenzer, J.; Neher, D.; Scherf, U.; Farrell, T.
Solution processable organic field-effect transistors utilizing an alpha,alpha '-dihexylpentathiophene-based swivel cruciform
Journal of the American Chemical Society ***128****, 3914 (2006).*

128. Zen, A.; Saphiannikova, M.; Neher, D.; Grenzer, J.; Grigorian, S.; Pietsch, U.; Asawapirom, U.; Janietz, S.; Scherf, U.; Lieberwirth, I.; Wegner, G.
Effect of molecular weight on the structure and crystallinity of poly(3-hexylthiophene)
Macromolecules ***39****, 2162 (2006)*

Conference Proceedings

1. Dekorsy, T.; Sun, J. M.; Skorupa, W.; Helm, M.; Rebohle, L.; Gebel, T.
Traditional hot-electron MOS devices for novel optoelectronic applications
Springer Proceedings in Physics ***110****, 265 (2006).*

2. Gemming, S.
Modelling ferroic functional elements
Multiscale Materials Modeling, Stuttgart: Fraunhofer IRB Verlag 2006, ISBN 3-8167-7206-4, pp. 835-842

3. Gemming, T.; Nufer, S.; Gemming, S.; Kurtz, W.; Marinopoulos, A. G.; Fabris, S.; Elsässer, C.; Rühle, M.
Atomistic structure of grain boundaries determined by first-principles calculations and quantitative HRTEM
DFTEM 2006, Editio Amici/Physicae et chimicae solidorum amici, 3-902548-00-2, pp. 142-145

4. Kockelmann, W.; Kirfel, A.; Neelmeijer, C.; Walcha, H.-M.
The mineralogy of Böttger stoneware
in: A. Denker, A. Adriaens, M. Dowsett, A. Giumlia-Mair: COST Action G8: Non-destructive testing and analysis of museum objects, Stuttgart: Fraunhofer IRB Verlag, 2006, ISBN 3-8167-7178-5, pp. 120-127

5. Martins, R. M. S.; Braz Fernandes, F. M.; Silva, R. J. C.; Beckers, M.; Schell, N.
Structural in-situ studies of Ni-Ti thin films
Proceedings Shape Memory and Superelastic Technologies (SMST-2004), ASM International 2006, pp. 421-426

6. Napolitani, E.; Kuznetsov, A.; Skorupa, W.; Foad, M. (Editors)
Si-based materials for advanced microelectronic devices: synthesis, defects and diffusion
European Materials Research Society (E-MRS) Symp. Proceedings ***210****, Elsevier Science Ltd, UK (2006).*

7. Pereira, L.; Águas, H.; Beckers, M.; Martins, R. M. S.; Fortunato, E.; Martins, R.
Characterization of nickel induced crystallized silicon by spectroscopic ellipsometry
Material Research Society Symposium Proceedings ***910****, 0910-A21 (2006).*

8. Pecz, B.; Barna, Á.; Heera, V.; Skorupa, W.
Magic matching in semiconductor heterojunctions
Springer Proceedings in Physics ***107****, 159 (2006).*

9. Semtsiv, M. P.; Masselink, W. T.; Georgiev, N.; Dekorsy, T.; Helm, M.
Intersubband transitions in GaP-AlP heterostructures for infrared applications
Institute of Physics Conference Series ***187****, 209 (2006).*

10. Winnerl, S.; Dreyhaupt, A.; Peter, F.; Stehr, D.; Helm, M.; Dekorsy, T.
High-intensity THz radiation from a large-aperture photoconductive emitter
Springer Proceedings in Physics ***110****, 73 (2006).*

Invited Conference Talks

1. Bischoff, L.; Akhmadaliev, Ch.; Pilz, W.
The application of alloy liquid metal ion sources in mass separated focused ion beams
1st Workshop on Ion Beams from LMIS and Applications, 03.12.2006, Lamia, Greece

2. Brauer, G.; Kuriplach, J.; Cizek, J.; Anwand, W.; Melikhova, O.; Prochazka, I.; Skorupa, W.
Positron lifetimes in ZnO single crystals
VIth International Conference on Ion Implantation and Other Applications of Ions and Electrons, 26.-29.06.2006, Kazimierz Dolny, Poland

3. Fassbender, J.
Ion beam modifications of magnetic films
23rd Summer School and International Symposium on the Physics of Ionized Gases, 28.08.-01.09.2006, Kopaonik, Serbia

4. Fassbender, J.
Ion beam modifications of magnetic films
Workshop on Ion Beam Applications for Materials Modification and Analysis,,02.09.2006, Belgrade, Serbia

5. Fassbender, J.
Magnetic properties of thin magnetic films on rippled and smooth substrates
Workshop on Properties of Ultrathin Magnetic films, EU-Network Nanomag-ToK, 07.-09.09.2006, Bialowieza, Poland

6. Gebel, T.; Rebohle, L.; Fendler, R.; Hentsch, W.; Skorupa, W.; Voelskow, M.; Anwand, W.; Yankov, R.
Millisecond annealing with flash lamps: tool and process challenges
14th Int. Conf. on Advanced Thermal Processing of Semiconductors, 10.10.2006, Kyoto, Japan

7. Gemming, S.
Modelling ferroic functional elements
MMM 2006 - International Conference on Multiscale Materials Modelling, Fraunhofer Institute for Mechanics of Materials IWM, 17.-22.09.2006, Freiburg, Brsg., Germany

8. Grambole, D.; Herrmann, F.
Ion beam analysis by nuclear microprobes
VIth International Conference on Ion Implantation and Other Applications of Ions and Electrons, 26.-29.06.2006, Kazimierz Dolny, Poland

9. Grambole, D.; Herrmann, F.; Heera, V.; Meijer, J.
Study of crystal damage by ion implantation using micro RBS/Channeling
10th International Conference on Nuclear Microprobe Technology and Applications, 10.-14.07.2006, Singapore, Singapore

10. Heinig, K.-H.
Growth and modification of nanostructures with ion beams
International Workshop on Nanostructured Materials (Nanomat 2006), 21.-23.06.2006, Antalya, Turkey

11. Heinig, K.-H.
Synthesis of nanostructures with ion beams
Nanotechnology Research Forum, Middle East Technical University, 16.-20.10.2006, Ankara, Turkey

12. Helm, M.
Infrared pump-probe spectroscopy of carrier dynamics in semiconductor quantum structures
Int. Conf. on Engineering Physics and 9th Vietnamese-German Seminar, 09.-11.10.2006, Hanoi, Vietnam

13. Kögler, R.; Mücklich, A.; Eichhorn, F.; Schell, N.; Skorupa, W.; Christensen, J. S.
Praseodymium compound formation in silicon by ion beam synthesis

VIth International Conference on Ion Implantation and Other Applications of Ions and Electrons, 26.-29.06.2006, Kazimierz Dolny, Poland

14. Michel, P.; Buettig, H.; Gabriel, F. G.; Helm, M.; Lehnert, U.; Schneider, Ch.; Schurig, R.; Seidel, W.; Stehr, D.; Teichert, J.; Winnerl, S.; Wuensch, R.
The Rossendorf IR-FEL ELBE
28th Free Electron Laser Conference 2006, 27.08.-01.09.2006, Berlin, Germany

15. Möller, W.
Mechanisms of target poisoning during reactive sputtering of TiN
BELVAC Symposium on Reactive Sputter Deposition, 30.11.2006, Ghent, Belgium

16. Pilz, W.; Lange, H.; Akhmadaliev, Ch.; Zimmermann, L.; Bischoff, L.
PC driven etching system for emitter needle tips
1st Workshop on Ion Beams from LMIS and Applications, 03.12.06, Lamia, Greece

17. Posselt, M.
Atomistic simulation of interstitial cluster migration in silicon
European Materials Research Society (E-MRS) Spring Meeting 2006, 29.05.-02.06.2006, Nice, France

18. Reuther, H.
Contribution of Mössbauer spectroscopy to the exploration of diluted magnetic semiconductors
6th Workshop on Mössbauer Spectroscopy, 07.-11.06.2006, Seeheim, Germany

19. Röntzsch, L.; Heinig, K.-H.; Akhmadaliev, Ch.; Bischoff, L.; Schmidt, B.
Synthesis of nanowire structures using focused ion beams
17th Symposium of the MRS-J, The Materials Research Society of Japan, 08.-10.12.2006, Tokyo, Japan

20. Schmidt, B.
Nanostructures by ion beams
Workshop on Ion Beam Studies of Nanomaterials: Synthesis, Modification and Characterization, 26.06.-01.07.2006, Trieste, Italy

21. Schneider, H.
QWIP camera development and applications
International Workshop on Quantum Well Infrared Photodetectors (QWIP2006),, 18.-24.06.2006, Kandy, Sri Lanka

22. Skorupa, W.
Silicon MOS light emitters by rare earth doping
1st Optence Workshop on Silicon Photonics, 10.11.2006, Mainz, Germany

23. Skorupa, W.; Prucnal, S.; Sun, J. M.; Helm, M.; Rebohle, L.; Gebel, T.; Nazarov, A.; Osiyuk, I.; Tjagulski, I.; Zuk, J.
Efficiency and stability issues of MOSLEDs made by RE ion implantation
Materials Research Society (MRS) Spring Meeting 2006, 17.-21.04.2006, San Francisco, USA

24. Sun, J. M.; Prucnal, S.; Potfajova, J.; Skorupa, W.; Schmidt, B.; Mücklich, A.; Helm, M.; Rebohle, L.; Gebel, T.
Recent progress in efficient electroluminescence from silicon-based light emitting devices made by ion beam processing
European Materials Research Society (E-MRS) Spring Meeting 2006, 29.05.-02.06.2006, Nice, France

25. Vredenberg, A.; Dawi, E.; Mink, M.; Heinig, K.-H.; Toulemonde, M.; Nordlund, K.; Kuronen, A.
Shaping of nanometals by high energy ion beams
Materials Research Society (MRS) Fall Meeting 2006, 27.11.-01.12.2006, Boston/MA, USA

26. Winnerl, S.; Stehr, D.; Drachenko, O.; Schneider, H.; Helm, M.; Seidel, W.; Michel, P.; Schneider, S.; Seidel, J.; Grafström, S.; Eng, L.-M.; Roch, T.; Strasser, G.; Maier, T.; Walther, M.
FELBE Free-Electron Laser: Status and Application for Time Resolved Spectroscopy Experiments
Joint 31st International Conference on Infrared and Millimter Waves and 14th International Conference on Terahertz Electronics, 18.-22.09.2006, Shanghai, China

27. Zacharias, M.; Gösele, U.
Si Nanocrystals for nanoelectronic applications
European Materials Research Society (E-MRS) Spring Meeting 2006, 29.05.-02.06.2006, Nice, France

Conference Contributions

1. Abendroth, B.; Abrasonis, G.; Möller, W.; Ma, X. X.
Low energy Ar ion accelerated diffusion of interstitial nitrogen
13. Workshop "Oberflächentechnologie mit Plasma- und Ionenstrahlprozessen", 14.-16.03.2006, Mühlleithen, Germany

2. Abrasonis, G.; Krause, M.; Gago, R.; Kolitsch, A.; Möller, W.
Probing six-fold ring clusters in alloyed sp^2 dominated carbon thin films by the means of Raman spectroscopy
4th International Workshop on Nanoscale Spectroscopy and Nanotechnology, 17.-21.09.2006, Rathen, Germany

3. Abrasonis, G.; Möller, W.; Ma, X. X.; Keller, A.; Facsko, S.
Low energy ion accelerated diffusion of interstitial nitrogen in austenitic stainless steel
10th International Conference on Plasma Surface Engineering, 10.-15.09.2006, Garmisch-Partenkirchen, Germany

4. Akhmadaliev, Ch.; Bischoff, L.; Schmidt, B.; Mücklich, A.
Formation of $CoSi_2$ nanowires and nanochains in silicon by direct FIB writing
DPG-Frühjahrstagung 2006, 27.-31.03.2006, Dresden, Germany

5. Akhmadaliev, Ch.; Pilz, W.; Bischoff, L.
Mn containing alloy LMIS for spintronics
The European Focused Ion Beam Users Group Meeting(EFUG), 02.10.2006, Wuppertal, Germany

6. Akhmadaliev, Ch.; Pilz, W.; Bischoff, L.
Characterization of Ga-Bi liquid metal alloy ion source
The European Focused Ion Beam Users Group Meeting(EFUG), 02.10.2006, Wuppertal, Germany

7. Akhmadaliev, Ch.; Bischoff, L.; Schmidt, B.
FIB assisted silicide nanowires formation in silicon
European Materials Research Society (E-MRS) Spring Meeting 2006, 29.05.-02.06.2006, Nice, France

8. Andreev, A.; Hou, Y.; Teichert, C.; Brauer, G.; Djurisic, A.
Characterization of semi-conducting nanorods by AFM and conducting AFM
56. Jahrestagung der Österreichischen Physikalischen Gesellschaft, 18.-21.09.2006, Graz, Austria

9. Bartels, A.; Thoma, A.; Janke, C.; Dekorsy, T.; Dreyhaupt, A.; Winnerl, S.; Helm, M.
High-Resolution THz Spectrometer with kHz scan rates
Conference on Lasers and Opto-Electronics, 21.-26.05.2006, Long Beach, USA

10. Berndt, M.; Vinnichenko, M.; Kreissig, U.; Abrasonis, G.; Kolitsch, A.; Möller, W.
Growth of carbon and carbon nitride thin films by low energy (~150 eV) N_2/Ar ion assisted evaporation of C60
10th International Conference on Plasma Surface Engineering(PSE 2006), 10.-15.09.2006, Garmisch-Partenkirchen, Germany

11. Beyer, R.; Schmidt, B.; Beyreuther , E.; Weber, J.; von Borany, J.
Scanning capacitance microscopy and the role of localized charges in dielectric films: infering or challenging ?
European Materials Research Society (E-MRS) Spring Meeting 2006, 29.05.-02.06.2006, Nice, France

12. Bischoff, L.; Akhmadaliev, Ch.; Pilz, W.; Schmidt, B.
Application of a mass separated focused ion beam
1st FIB Workshop, Focused Ion Beams In Research, Science and Technology, 22.-23.05.2006, Dresden, Germany

13. Bischoff, L.; Akhmadaliev, Ch.; Schmidt, B.
Defect induced nanowire growth by FIB implantation
32nd International Conference on Micro- and Nano-Engineering (MNE), 17.-21.09.2006, Barcelona, Spain

14. Bischoff, L.; Pilz, W.; Ganetsos, Th.; Forbes, R.; Akhmadaliev, Ch.
GaBi liquid metal alloy ion source for the production of ions of interest in microelectronics research
The Joint 19th International Vacuum Nanoelectronics Conference and 50th International Field Emission Symposium, 17.-20.07.2006, Guilin, China

15. Børseth, T. M.; Christensen, J. S.; Anwand, W.; Skorupa, W.; Svensson, B. G.; Kuznetsov, A. Yu.
Electrical activation of implantation-induced defects in ZnO by flash-annealing
15th International Conference on Ion Beam Modification of Materials, 18.-22.09.2006, Taormina, Italy

16. Borseth, T. M.; Cristensen, J. S.; Monakhov, E.; Svensson, B. G.; Kuznetsov, A.; Tuomisto, F.; Skorupa, W.
Engineering of radiation defects and Li by flash anneals in ion-implanted ZnO
4th International Workshop on ZnO and Related Materials, 03.-06.10.2006, Giessen, Germany

17. Brandt, M.; von Wenckstern, H.; Benndorf, G.; Lenzner, J.; Schmidt, H.; Lorenz, M.; Grundmann, M.; Braunstein, G.; Brauer, G.
Optical and microelectrical characterization of ZnO single crystals implanted with group V elements
DPG-Frühjahrstagung 2006, 27.-31.03.2006, Dresden, Germany

18. Brauer, G.; Anwand, W.; Skorupa, W.; Kuriplach, J.; Melikhova, O.; Cizek, J.; Prochazka, I.; Moisson, C.; von Wenckstern, H.; Schmidt, H.; Lorenz, M.; Grundmann, M.
Comparative characterization of differently grown ZnO single crystals by positron annihilation and Hall effect
European Materials Research Society (E-MRS) Spring Meeting 2006, 29.05.-02.06.2006, Nice, France

19. Brauer, G.; Anwand, W.; Skorupa, W.; Kuriplach, J.; Melikhova, O.; Cizek, J.; Prochazka, I.; von Wenckstern, H.; Brandt, M.; Lorenz, M.; Grundmann, M.
Defects in N^+ ion-implanted ZnO single crystals studied by positron annihilation and Hall effect
14th International Conference on Positron Annihilation (ICPA-14), 23.-28.07.2006, Hamilton/Ontario, Canada

20. *4th International Wokshop on ZnO and Related Materials, 03.-06.10.2006, Giessen, Germany*

21. *19th International Conference on the Application of Accelerators in Research and Industry (CAARI2006), 20.-25.08.2006, Ft. Worth/Texas, USA*

22. Candeloro, P.; Blomeier, S.; Beck, A.; Schultheiss, H.; Nembach, H.; Hillebrands, B.; Liedke, M. O.; Fassbender, J.; Reuscher, B.
Magnetization reversal in NiFe/FeMn ion irradiated patterns
21st General Conference of the EPS Condensed Matter Division, 27.-31.03.2006, Dresden, Germany

23. Cantelli, V.; von Borany, J.; Grenzer, J.; Fassbender, J.
Influence of energetic ions on the $L1_0$ ordering of FePt films fabricated by magnetron sputtering
DPG-Frühjahrstagung 2006, 27.-31.03.2006, Dresden, Germany

24. *15th International Conference on Ion Beam Modification of Materials, 18.-22.09.2006, Taormina, Italy*

25. Chen, X. D.; Ling, C. C.; Djurisic, A. B.; Brauer, G.; Anwand, W.; Skorupa, W.; Reuther, H.
Influence of hydrogen peroxide treatment on Au/n-ZnO contact
14th International Conference on Positron Annihilation (ICPA-14), 23.-28.07.2006, Hamilton/Ontario, Canada

26. Cieslak, J.; Dubiel, S. M.; Eichhorn, F.; Menzel, M.; Reuther, H.
Investigation of single-crystals of chromium implanted with ^{119}Sn – ions of various energies
15th International Conference on Ion Beam Modification of Materials, 18.-22.09.2006, Taormina, Italy

27. *15th International Conference on Solid Compounds of Transition Elements, 15.-20.07.2006, Krakow, Poland*

28. Cizek, J.; Prochazka, I.; Danis, S.; Vlach, M.; Zaludova, N.; Brauer, G.; Anwand, W.; Mücklich, A.; Gemma, R.; Nikitin, E.; Kirchheim, R.; Pundt, A.
Defect studies of hydrogen loaded Nb: bulk metals and thin films
14th International Conference on Positron Annihilation (ICPA-14), 23.-28.07.2006, Hamilton/Ontario, Canada

29. Claverie, A.; Bonafos, C.; Ben Assayag, G.; Schamm, S.; Cherkashin, N.; Paillard, V.; Dimitrakis, P.; Kapetenakis, E.; Tsoukalas, D.; Muller, T.; Schmidt, B.; Heinig, K.-H.; Perego, M.; Fanciulli, M.; Mathiot, D.; Carrada, M.; Normand, P.
Materials science issues for the fabrication of nanocrystal memory devices by ultra low energy ion implantation
2nd International Conference on Diffusion in Solids and Liquids, 26.-28.07.2006, Aveiro, Portugal

30. Dawi, E.; Mink, M.; Heinig, K.-H.; Toulemonde, M.; Nordlund, K.; Vredenberg, A.
Shaping of nanometals by swift heavy ions
15th International Conference on Ion Beam Modification of Materials, 18.-22.09.2006, Taormina, Italy

31. Donchev, A.; Richter, E.; Schuetze, M.; Yankow, R. A.
Improving the oxidation resistance of TiAl-alloys with fluorine
12th International IUPAC-Conference on High Temperature Materials Chemistry HTMC, 17.-22.09.2006, Vienna, Austria

32. Drachenko, O.; Leotin, J.; Schneider, H.; Helm, M.
Portable THz cyclotron resonance spectrometer
Semiconductor sources and detectors of THz frequencies, 06.-07.12.2006, Montpellier, France

33. Drachenko, O.; Winnerl, S.; Schneider, H.; Helm, M.
Fast THz time-domain spectrometer
Semiconductor Sources and Detectors of THz Frequencies, 06.-07.12.2006, Montpellier, France

34. Drachenko, O.; Winnerl, S.; Schneider, H.; Helm, M.; Wosnitza, J.
Fast THz time-domain spectrometer for pulsed magnets
17th International Conference on High Magnetic Fields in Semiconductor Physics (HMF), 20.07.-04.08.2006, Würzburg, Germany

35. Dreyhaupt, A.; Winnerl, S.; Dekorsy, T.; Helm, M.
Efficient terahertz radiation of a large-area photoconductive device
DPG-Frühjahrstagung 2006, 27.-31.03.2006, Dresden, Germany

36. Dreyhaupt, A.; Winnerl, S.; Dekorsy, T.; Helm, M.
Intense terahertz radiation from a large-area photoconductive device.
2006 MRS Spring Meeting, 17.-21.04.2006, San Francisco, USA

37. Dreyhaupt, A.; Winnerl, S.; Schneider, H.; Helm, M.; Bartels, A.; Thoma, A.; Janke, C.; Dekorsy, T.
High-resolution rapid-scan THz spectrometer using a large-area photoconductive emitter in combination with asynchronous optical sampling
2nd Workshop on Terahertz Technology, 01.-02.03.2006, Kaiserslautern, Germany

38. Facsko, S.
Kontinuumsgleichungen zur Beschreibung ionenstrahlinduzierter Nanostrukturen
Workshop "Ionenstrahlphysik und Nanotechnologie", 16.05.2006, Berlin, Germany

39. Facsko, S.; Som, T.; Wilhelm, R.; Heller, R.; Möller, W.
Changing carbon films by highly charged ions
International Workshop on Inelastic Ion-Surface Collisions (IISC-16), 17.-22.09.2006, Hernstein, Austria

40. Fan, H. J.; Alexe, M.; Hauschild, R.; Kalt, H.; Zacharias, M.
Ordered arrays of ZnO nanowires: piezoelectric properties and stimulated emission from single wires
European Materials Research Society (E-MRS) Spring Meeting 2006, 29.05.-02.06.2006, Nice, France

41. Fassbender, J.
Ion beam induced magnetic property modifications
Workshop "Ionenstrahlphysik und Nanotechnologie", 16.-17.05.2006, Berlin, Germany

42. Fassbender, J.; McCord, J.
Control of saturation magnetization, anisotropy and damping due to Ni implantation in thin $Ni_{81}Fe_{19}$ layers
International Colloquium on Magnetic Films and Surfaces, 14.-18.08.2006, Sendai, Japan

43. Fassbender, J.; McCord, J.
Control of magnetic damping by means of Ni implantation in thin Ni81Fe19 layers
Joint European Magnetics Symposium, 26.-30.06.2006, San Sebastian, Spain

44. Fassbender, J.; von Borany, J.; Mücklich, A.; Potzger, K.; Möller, W.; McCord, J.; Schultz, L.; Mattheis, R.
Tailoring magnetic properties by implantation doping of thin Ni81Fe19 layers
15th International Conference on Ion Beam Modification of Materials, 18.-22.09.2006, Taormina, Italy

45. Friedrich, M.; Akhmadaliev, Ch.; Bürger, W.; Weise, A.; Vetter, A.
Investigations at alkali vapor charge exchange canals and installation of an additional injector for negative helium ions at the Rossendorf 3 MV Tandetron
5th Accelerator Technical Forum and the 40th Symposium of North Eastern Accelerator Personnel, 15.-20.10.2006, Sydney/Canberra, Australia

46. Gao, F.; Zhang, Y.; Devanathan, R.; Posselt, M.; Weber, W. J.
Computer simulations of epitaxial recrystallization and amorphous-to-crystalline transition in 4H-SiC
8th Int. Conf. on Computer Simulation of Radiation Effects in Solids (COSIRES 2006), 18.-23.06.2006, Richland, WA, USA

47. Gemming, S.; Olbrich, C.; Morawetz, K.; Schreiber, M.; Loppacher, C.; Seifert, G.; Eng, L. M.
Simulation and AFM-measurement of PTCDA on Ag-supported KBr films
16th Int. Microscopy Congress (IMC16)*, 02.-07.09.2006, Sapporo, Japan*

48. Gemming, T.; Nufer, S.; Gemming, S.; Kurtz, W.; Marinopoulos, A. G.; Fabris, S.; Elsässer, C.; Rühle, M.
Atomistic structure of grain boundaries determined by first-principles calculations and quantitative HRTEM
DFTEM 2006 - bringing together two communities International Conference on Density Functional Theory and Transmission Electron Microscopy, 21.-23.04.2006, Wien, Austria

49. Gessner, H.; Posselt, M.
Atomistic study of bulk properties and point defects in Ge
DPG-Frühjahrstagung 2006, 27.-31.03.2006, Dresden, Germany

50. Gessner, H.; Posselt, M.
An improved interatomic potential for Ge
8th Int. Conf. on Computer Simulation of Radiation Effects in Solids (COSIRES 2006), 18.-23.06.2006, Richland, WA, USA

51. Gessner, H.; Posselt, M.
Equilibrium concentration and diffusivity of vacancies in Ge: An atomistic study with an improved interatomic potential
European Materials Research Society (E-MRS) Spring Meeting 2006, 29.05.-02.06.2006, Nice, France

52. Grenzer, J.; Bischoff, L.; Posselt, M.; Pietsch, U.
X-ray grazing incidence investigations of focused ion beam interactions with a Si and GaAs surfaces
DPG-Frühjahrstagung 2006, 27.-31.03.2006, Dresden, Germany

53. *8th Biennial Conference on High Resolution X-ray Diffraction and Imaging, 19.-22.09.2006, Karlsruhe, Germany*

54. *Deutsche Tagung für Forschung mit Synchrotronstrahlung, Neutronen und Ionenstrahlen an Grossgeräten (SNI-2006), 04.-06.10.2006, Hamburg, Germany*

55. Grenzer, J.; Bischoff, L.; Posselt, M.; Pietsch, U.
X-ray studies of semiconductor surfaces modified by focused ion beam implantation
8th Biennial Conference on High Resolution X-ray Diffraction and Imaging, 19.-22.09.2006, Karlsruhe, Germany

56. *Deutsche Tagung für Forschung mit Synchrotronstrahlung, Neutronen und Ionenstrahlen an Grossgeräten (SNI-2006), 04.-06.10.2006, Hamburg, Germany*

57. Grenzer, J.; Bischoff, L.; Posselt, M.; Pietsch, U.
High resolution grazing incidence diffraction on lateral nanostructures created by focused ion beam implantation on semiconductor surfaces
Deutsche Tagung für Forschung mit Synchrotronstrahlung, Neutronen und Ionenstrahlen an Grossgeräten (SNI-2006), 04.-06.10.2006, Hamburg, Germany

58. Grigorian, S.; Grenzer, J.; Pietsch, U.
Ripple morphology versus Ar^+ implantation dose in silicon
DPG-Frühjahrstagung 2006, 27.-31.03.2006, Dresden, Germany

59. Grynszpan, R. I.; Anwand, W.; Brauer, G.
Radiation damage in zirconia investigated by positively charged particles
19th International Conference on the Application of Accelerators in Research and Industry (CAARI2006), 20.-25.08.2006, Ft. Worth/Texas, USA

60. Grynszpan, R. I.; Brauer, G.; Anwand, W.
Positron annihilation investigation in ion-implanted Yttria-stabilized zirconia
Materials Research Society (MRS), 2005 Fall Meeting, 28.11.-02.12.2005, Boston/MA, USA

61. Güttler, D.; Abendroth, B.; Grötzschel, R.; Möller, W.
Real-time in-situ analysis of target poisoning during reactive magnetron sputtering by nuclear reaction analysis and energy resolved mass spectroscopy
10th International Conference on Plasma Surface Engineering, 11.-15.09.2006, Garmisch, Germany

62. Güttler, D.; Abendroth, B.; Möller, W.
An investigation of target poisoning during reactive magnetron sputtering using ion beam analysis and energy resolved mass spectroscopy
Workshop "Oberflächentechnologie mit Plasma- und Ionenstrahlprozessen", 14.-16.03.2006, Mühlleithen, Germany

63. Heera, V.; Madhusoodanan, K. N.; Skorupa, W.; Dubois, C.; Romanus, H.
The electrical properties of heavily Al-implanted, nanocrystalline and single crystalline SiC layers
SiC Rundgespräch 2006, 17.-18.07.2006, Kloster Banz, Staffelstein, Germany

64. Heinig, K.-H.; Müller, T.; Schmidt, B.
Predictive process simulation of Si nanocluster layer formation by low-energy ion implantation
MRS Spring Meeting 2006, 17.-21.04.2006, San Francisco, USA

65. Heinig, K.-H.; Röntzsch, L.
Self-aligned doubly-stacked Si dots fabrication for improved data retention of nanocrystal memories
European Materials Research Society (E-MRS) Spring Meeting 2006, 29.05.-02.06.2006, Nice, France

66. Heinig, K.-H.; Röntzsch, L.
Doubly-stacked Si dots in SiO_2 formed by ion beam mixing – a way to improve retention of nanocrystal memories
15th International Conference on Ion Beam Modification of Materials, 18.-22.09.2006, Taormina, Italy

67. Heinig, K.-H.; Schmidt, B.; Müller, T.; Röntzsch, L.; Stegemann, K.-H.
CMOS compatible bottom-up approach of multi-dot floating-gate nonvolatile memory fabrication.
MRS Spring Meeting 2006, 17.-21.04.2006, San Francisco, USA

68. Heinig, K.-H.; Schmidt, B.; Müller, T.; Röntzsch, L.
Nucleation and nanostructure formation at mixed interfaces
Int. Workshop on Polymorphism in Condensed Matter, 13.-17.11.2006, Dresden, Germany

69. Heinig, K.-H.; Vredenberg, A.; Toulemonde, M.; Nordlund, K.
Ion beam shaping of nanometals: process modeling and atomistic simulations of extreme conditions
MRS Spring Meeting 2006, 20.-21.04.2006, San Francisco, USA

70. Heinig, K.-H.; Vredenberg, A.; Toulemonde, M.; Nordlund, K.
Synthesis of aligned nanowire arrays by shaping of nanometals with swift heavy ions – modelling and atomistic simulations
European Materials Research Society (E-MRS) Spring Meeting 2006, 29.05.-02.06.2006, Nice, France

71. Heinig, K.-H.; Vredenberg, A.; Toulemonde, M.; Nordlund, K.
Mechanisms of swift-heavy-ion-assisted shaping of Au nanospheres into wires and their subsequent "Ostwald ripening"
15th International Conference on Ion Beam Modification of Materials, 18.-22.09.2006, Taormina, Italy

72. Heller, R.; Facsko, S.; Kost, D.; Zschornack, G.
The Rossendorf two-source facility – a device for the observation of the interaction of slow highly charged ions with surfaces
International PhD Seminar 2006, Faculty of Materials Science and Technology SUT Trnava, 23.04.2006, Smolenice, Slowakia

73. Heller, R.; Facsko, S.; Kost, D.; Zschornack, G.
Modification of solid surfaces by slow highly charged ions: effects of highly confined excitation
13th International Conference on the Physics of Highly Charged Ions (HCI), 28.08.2006, Belfast, Northern Ireland, U.K.

74. Heller, R.; Zschornack, G.
Extraktion hochgeladener Ionen aus der Dresden EBIT im Überlaufregime
Workshop, Energiereiche Atomare Stösse, 02.05.2006, Riezlern, Austria

75. Hui, C. W.; Zhang, Z. D.; Taojun, Z.; Ling, C. C.; Beling, C. D.; Fung, S.; Brauer, G.; Anwand, W.; Skorupa, W.
Positron annihilation spectroscopic study of hydrothermal grown n-type zinc oxide single crystal
14th International Conference on Positron Annihilation (ICPA-14), 23.-28.07.2006, Hamilton/Ontario, Canada

76. Keller, A.; Facsko, S.; Plantevin, O.; Carbone, D.; Metzger, T. H.; Gago, R.
In-situ X-ray diffraction of GaSb nanopatterned by normal incidence sputter erosion
DPG-Frühjahrstagung 2006, 27.-31.03.2006, Dresden, Germany

77. Keller, A.; Rossbach, S.; Facsko, S.; Möller, W.
Off-normal ion erosion of silicon – simultaneous observation of two ripple modes
22nd International Conference on Atomic Collisions in Solids, 21.-26.07.2006, Berlin, Germany

78. Keller, A.; Rossbach, S.; Facsko, S.; Möller, W.
Ion induced nanopatterns on semiconductors: formation and application
16th International Workshop on Inelastic Ion-Surface Collisions, 17.-22.09.2006, Hernstein, Austria

79. Kögler, R.
Ion beam engineering in the initial stage of SIMOX processing
Workshop "Ionenstrahlphysik und Nanotechnologie", 16.-17.05.2006, Berlin, Germany

80. Kögler, R.
Excess vacancy generation in SiGe
European Materials Research Society (E-MRS) Spring Meeting 2006, 29.05.-02.06.2006, Nice, France

81. Kögler, R.; Mücklich, A.; Vines, L.; Krecar, D.; Kuznetsov, A.; Skorupa, W.
Defect engineering in the initial stage of SIMOX processing
15th International Conference on Ion Beam Modification of Materials, 18.-22.09.2006, Taormina, Italy

82. Kögler, R.; Peeva, A.; Mücklich, A.; Kutznetsov, A.; Christensen, J. S.; Svensson, B. G.; Skorupa, W.
Excess vacancies in high energy ion implanted SiGe
15th International Conference on Ion Beam Modification of Materials, 18.-22.09.2006, Taormina, Italy

83. Kost, D.; Facsko, S.
Relaxation of slow highly charged ions penetrating a solid surface - energy deposition and reemission

DPG-Frühjahrstagung 2006 and 21st General Conference of the EPS Condensed Matter Division, 27.-31.03.2006, Dresden, Germany

84. Kost, D.; Facsko, S.; Heller, R.; Schlenk, R.; Wustmann, B.; Zschornack, G.
Die Zweiquellenanlage des Forschungszentrum Rossendorf - Neue Möglichkeiten für Experimente mit hochgeladenen Ionen
Workshop Energiereiche Atomare Stösse, 06.-10.02.2006, Riezlern, Östereich

85. Kost, D.; Röder, F.; Möller, W.
Deposition and re-emission of potential energy - extended dynamical COB simulation -
13th International Conference on the Physics of Highly Charged Ions, 27.08.-01.09.2006, Belfast, Northern Ireland, UK

86. Krause-Rehberg, R.; Brauer, G.; Krille, A.; Jungmann, M.; Sachert, S.; Rogov, A.; Noack, K.
The pulsed high-brightness positron source EPOS
14th International Conference on Positron Annihilation (ICPA-14), 23.-28.07.2006, Hamilton/Ontario, Canada

87. *19th International Conference on the Application of Accelerators in Research and Industry (CAARI2006), 20.-25.08.2006, Ft. Worth/Texas, USA*

88. Küpper, K.; Bondino, F.; Prince, K. C.; Zangrando, M.; Zacchigna, M.; Takacs, A. F.; Matteucci, M.; Parmigiani, F.; Winiarski, A.; Galakhov, V. R.; Mukovskii, Ya. M.; Neumann, M.
Investigation of orbital ordering in $La_{7/8}Sr_{1/8}MnO_3$ by means of X-ray linear dichroism at the Mn L edge
DPG-Frühjahrstagung 2006, 27.-31.03.2006, Dresden, Germany

89. Küpper, K.; Buess, M.; Raabe, J.; Quitmann, C.; Fassbender, J.
Dynamic vortex − antivortex interaction and magnetization dynamics of a single cross-tie wall
4th International Workshop on Nanoscale Spectroscopy and Nanotechnology, 17.-21.09.2006, Rathen, Germany

90. Küpper, K.; Fassbender, J.; Bischoff, L.; Mattheis, R.; Fischer, P.
Magnetic domains and magnetization reversal of ion-induced magnetically patterned RKKY-coupled $Ni_{81}Fe_{19}/Ru/Co_{90}Fe_{10}$ films
364. WE-Heraeus-Seminar Nanoscale Magnets - Top-down meets Bottom-up, 04.-06.01.2006, Bad Honnef, Germany

91. *DPG-Frühjahrstagung 2006, Deutsche Physikalische Gesellschaft, 27.-31.03.2006, Dresden, Germany*

92. Küpper, K.; Kadiroglu, M.; Postnikov, A. V.; Prince, K. C.; Matteucci, M.; Galakhov, V. R.; Hesse, H.; Borstel, G.; Neumann, M.
Electronic structure of highly ordered Sr_2FeMoO_6: XPS and XES studies
DPG-Frühjahrstagung 2006, 27.-31.03.2006, Dresden, Germany

93. Küpper, K.; Klingeler, R.; Reutler, P.; Büchner, B.; Neumann, M.
Electronic structure of $LaSrMnO_4$: XPS and XES studies
Magnetism and Magnetic Materials Conference, 30.10.-03.11.2005, San Jose, USA

94. Küpper, K.; Bischoff, L.; Mattheis, R.; Fischer, P.; Kim, D.-H.; Fassbender, J.
Investigation of element specific hysteresis loops of ion-induced magnetically patterned Ni81Fe19/Ru/Co90Fe10 films with magnetic soft X-ray microscopy.
MRS Fall Meeting 2006, 27.11.-01.12.2006, Boston, USA

95. Lebelt, P.; Gehrke, J.; Schütz, A.; Reuther, H.
Flammenpyrolytische Oberflächenvorbehandlung von beschichteten Halbzeugen vor dem Kleben
Thüringer Grenz- und Oberflächentage, 13.09.2006, Oberhof, Germany

96. Liedke, M. O.; Keller, A.; Facsko, S.; Fassbender, J.
Ripple induced modifications of magnetic properties
Int. Workshop on Nanomagnets by Self-Organization, 08.-11.10.2006, Eisenerz, Austria

97. *MRS Fall Meeting 2006, 27.11.-01.12.2006, Boston, USA*

98. Liedke, M. O.; Liedke, B.; Keller, A.; Rossbach, S.; Facsko, S.; Fassbender, J.
Ion erosion induced ripples as templates for ultrathin magnetic films – ripple-induced anisotropies
15th International Conference on Ion Beam Modification of Materials, 18.-22.09.2006, Taormina, Italy

99. Liedke, M. O.; Potzger, K.; Bothmer, A.; Hillebrands, B.; Rickart, M.; Freitas, P. P.; Fassbender, J.
Domain structure during magnetization reversal of PtMn/CoFe exchange bias micro-patterned lines
DPG-Frühjahrstagung 2006, 27.-31.03.2006, Dresden, Germany

100. Liedke, M. O.; Rossbach, S.; Facsko, S.; Hillebrands, B.; Fassbender, J.
Exchange bias on rippled substrates – step induced uniaxial versus unidirectional anisotropy
International Magnetics Conference (Intermag 2006), 08.-12.05.2006, San Diego, USA

101. Liedke, M. O.; Rossbach, S.; Facsko, S.; Hillebrands, B.; Fassbender, J.
Exchange bias on rippled substrates
3rd Joint European Magnetic Symposia, 26.-30.06.2006, San Sebastian, Spain

102. *International Colloquium on Magnetic Films and Surfaces, 14.-18.08.2006, Sendai, Japan*
103. *Workshop on Properties of Ultrathin Magnetic Films, EU-Network Nanomag-ToK, 06.-09.09.2006, Bialowieza, Poland*
104. Markov, A. B.; Günzel, R.; Reuther, H.; Shevchenko, N.; Akhmadeev, Yu. Kh.; Schanin, P. M.; Koval, N. N.; Rotshtein, V. P.; Proskurovsky, D. I.
Pulsed electron-beam irradiation followed by nitriding of Ti-6Al-4V titanium alloy
8th International Conference on Modification of Materials with Particle Beams and Plasma Flows, 10.-15.09.2006, Tomsk, Russia
105. Markov, A. B.; Günzel, R.; Reuther, H.; Shevchenko, N.; Rotshtein, V. P.; Akhmadeev, Yu. Kh.; Schanin, P. M.
Effect of electron-beam treatment on subsequent titanium alloy nitriding
8th International Conference on Electron Beam Technologies, 05.-10.06.2006, Varna, Bulgaria
106. Martins, R. M. S.; Schell, N.; Beckers, M.; Mücklich, A.; Reuther, H.; Silva, R. J. C.; Mahesh, K. K.; Braz Fernandes, F. M.
In-situ study of the preferential orientation of magnetron sputtered Ni-Ti thin films as a function of bias and substrate type
Conference on Shape Memory and Superelastic Technology 2006, 07.-11.05.2006, Asilomar, USA
107. Martins, R. M. S.; Schell, N.; Beckers, M.; Silva, R. J. C.; Braz Fernandes, F. M.
Characterization of Ni-Ti SMA thin films: from annealing to in-situ sputtering
ESRF Science Days 2006, 07.-08.06.2006, Autrans, France
108. Martins, R. M. S.; Schell, N.; Beckers, M.; Silva, R. J. C.; Mahesh, K. K.; Braz Fernandes, F. M.
Role of the substrate on the growth of Ni-Ti sputtered thin films
ESOMAT 2006 - European Symposium on Martensitic Transformations and Shape Memory Alloys, 10.-15.09.2006, Bochum, Germany
109. Martins, R. M. S.; Schell, N.; Beckers, M.; Silva, R. J. C.; Mahesh, K. K.; Braz Fernandes, F. M.
The role of a TiN buffer layer on the growth of Ni-Ti sputtered thin films
ESRF Science Days 2006, 07.-08.06.2006, Autrans, France
110. Martins, R. M. S.; Schell, N.; Beckers, M.; Silva, R. J. C.; Mahesh, K. K.; Braz Fernandes, F. M.
In-situ XRD during sputtering deposition of Ni-Ti shape memory alloys on TiN/SiO_2/Si(100)
ESRF User's Meeting 2006, 07.-08.02.2006, Grenoble, France
111. Martins, R. M. S.; Schell, N.; Silva, R. J. C.; Mahesh, K. K.; Braz Fernandes, F. M.
In-situ study of Ni-Ti film growth by synchrotron radiation scattering
MICRODIFF'06 - Local Mechanical Stresses and Microdiffraction, 28.-29.09.2006, Grenoble, France
112. Martins, R. M. S.; Schell, N.; Silva, R. J. C.; Pereira, L.; Mahesh, K. K.; Braz Fernandes, F. M.
In-situ study of Ni-Ti thin film growth on a TiN intermediate layer by X-ray diffraction
European Materials Research Society (E-MRS) Spring Meeting 2006, 29.05.-02.06.2006, Nice, France
113. Melikhova, O.; Kuriplach, J.; Cizek, J.; Prochazka, I.; Anwand, W.; Brauer, G.; Konstantinova, T. E.; Danilenko, I. A.
Positron annihilation in three zirconia polymorphs
14th International Conference on Positron Annihilation (ICPA-14), 23.-28.07.2006, Hamilton/Ontario, Canada
114. Menzel, S.; Zibik, E. A.; Aivaliotis, P.; Carpenter, B. A.; Stehr, D.; Winnerl, S.; Helm, M.; Steer, M. J.; Hopkinson, M.; Cockburn, J. W.; Wilson, L. R.
Electron intraband capture and relaxation in self-assembled InAs/GaAsquantum dots
Int. Conf. on Superlattices, Nanostructures and Nanodevices 2006, 30.07.-04.08.2006, Istanbul, Turkey
115. Möller, W.
Ion induced stress release – by thermal or collisional spikes?
Thin Film Workshop, 17.06.2006, Linköping, Sweden
116. Mukherjee, S.; Nadesalingam, M.; Davis, B.; Brauer, G.; Kohyama, A.; Nozawa, T.; Weiss, A.
Positron annihilation-induced Auger electron emission from 6H-SiC surfaces
14th International Conference on Positron Annihilation (ICPA-14), 23.-28.07.2006, Hamilton/Ontario, Canada
117. Nazarov, A.; Osiyuk, I.; Tyagulskii, I.; Lysenko, V.; Prucnal, S.; Sun, J. M.; Skorupa, W.
Charge trapping phenomena in high efficiency Metal-Oxide-Silicon light-emitting diodes with ion-implanted oxide
European Materials Research Society (E-MRS) Spring Meeting 2006, 29.05.-02.06.2006, Nice, France
118. Oliveira, R. M.; Ueda, M.; Rossi, J. O.; Reuther, H.; Lepienski, C. M.; Beloto, A. F.
Nitrogen plasma ion implantation of Al alloy in the high-voltage glow discharge mode
International Conference on Íon Implantation Technology, 11.-16.06.2006, Marseille, France

119. Peter, F.; Winnerl, S.; Dreyhaupt, A.; Schneider, H.; Helm, M.
Profile of a photoconductive THz Emitter excited by an amplified laser system
DPG-Frühjahrstagung 2006, 27.-31.03.2006, Dresden, Germany

120. Pezoldt, J.; Kups, Th.; Voelskow, M.; Skorupa, W.
Ion beam synthesis of 4H-($Si_{1-x}C_{1-y}$)Ge_{x+y} solid solutions
EXMATEC 06, Universität Cadiz Spain, 15.-17.05.2006, Cadiz, Spain

121. Popov, V. P.; Tyschenko, I.; Cherkov, A.; Voelskow, M.
Silicon-germanium heterostructure-on-insulator formed by Ge^+ ion implantation and hydrogen transfer
210th ECS Meeting, 29.10.-03.11.2006, Cancun, Mexico

122. Popov, V. P.; Tyschenko, I.; Cherkov, A.; Voelskow, M.
Nanoscaled semiconductor heterostructures for CMOS transistors formed by ion implantation and hydrogen transfer
NATO ARW Conference "Nanoscaled SOI Structures and Devices", 15.-19.10.2006, Sudak/Krim, Ukraine

123. Posselt, M.
Interstitial contribution to self-diffusion in Si: dependence of the correlation factor on the migration mechanism
8th Int. Conf. on Computer Simulation of Radiation Effects in Solids (COSIRES 2006), 18.-23.06.2006, Richland, WA, USA

124. Posselt, M.; Bischoff, L.; Grambole, D.; Herrmann, F.; Grötzschel, R.
Dose rate and temperature dependence of ion-beam-induced defect evolution in germanium
European Materials Research Society (E-MRS) Spring Meeting 2006, 29.05.-02.06.2006, Nice, France

125. Posselt, M.; Gao, F.; Weber, W. J.
Antisite pair recombination in SiC by a modified concerted exchange mechanism
44. Arbeitskreis "Punktdefekte", TU Dresden, 23.-25.03.2006, Dresden, Germany

126. Potfajova, J.; Sun, J. M.; Schmidt, B.; Dekorsy, T.; Skorupa, W.; Helm, M.
Silicon-on-insulator microcavity light emitting diodes with two Si/SiO_2 Bragg reflectors
European Materials Research Society (E-MRS) Spring Meeting 2006, 29.05.-02.06.2006, Nice, France

127. Potzger, K.; Reuther, H.; Zhou, S.; Mücklich, A.; Grötzschel, R.; Eichhorn, F.; Liedke, M.; Fassbender, J.; Lichte, H.; Lenk, A.
Ion beam synthesis of Fe nanoparticles in MgO and YSZ
DPG-Frühjahrstagung 2006, 27.-31.03.2006, Dresden, Germany

128. Potzger, K.; Zhou, S.; Reuther, H.; Mücklich, A.; Eichhorn, F.; Talut, G.; Herrmannsdörfer, T.; Bianchi, A.; Fassbender, J.
Fe doped ZnO – a diluted magnetic semiconductor?
364. Heraeus Workshop on Nanoscale Magnets - Top-Down meets Bottom-Up, 04.-06.01.2006, Bad Honnef, Germany

129. Potzger, K.; Zhou, S.; Zhang, G.; Reuther, H.; Talut, G.; Mücklich, A.; Eichhorn, F.; Schell, N.; Grötzschel, R.; Skorupa, W.; Helm, M.; Anwand, W.; Brauer, G.; Fassbender, J.
Diluted magnetic semiconductors created by non-equilibrium processing - new challenges for ion beams
15th International Conference on Ion Beam Modification of Materials, 18.-22.09.2006, Taormina, Italy

130. *European Materials Research Society (E-MRS) Fall Meeting 2006, 04.-08.9.2006, Warszawa, Poland*

131. Prinz, M.; Takács, A.; Schnack, J.; Balasz, I.; Burzo, E.; Kortz, U.; Küpper, K.; Neumann, M.
Magnetic and electronic properties of the iron-containing polyoxotungstate $[Fe_4(H_2O)_{10}(\beta\text{-}SbW_9O_{33})_2]_6$-
Magnetism and Magnetic Materials Conference, 30.10.-03.11.2005, San Jose, USA

132. Prucnal, S.; Sun, J. M.; Mücklich, A.; Skorupa, W.
Flash lamp processing in the millisecond-range for metal-oxide-silicon-based light emitting diodes
Materials Research Society (MRS) Spring Meeting 2006, 17.-21.04.2006, San Francisco, USA

133. Prucnal, S.; Sun, J. M.; Reuther, H.; Skorupa, W.
Optical activation and electrical stabilization of the EL from SiO_2:Gd gate oxide layers by fluorine and potassium co-implantations
Materials Research Society (MRS) Spring Meeting 2006, 17.-21.04.2006, San Francisco, USA

134. Prucnal, S.; Sun, J. M.; Reuther, H.; Skorupa, W.
The effect of potassium and fluorine implantation on the electroluminescence stability in Gd and Tb implanted SiO_2 layers
European Materials Research Society (E-MRS) Spring Meeting 2006, 29.05.-02.06.2006, Nice, France

135. Prucnal, S.; Sun, J. M.; Reuther, H.; Skorupa, W.
Energy transfer by Gd to ion implanted Ce and Er atoms in metal-oxide-silicon-based light emitting

diodes
Materials Research Society (MRS) Spring Meeting, 17.-21.04.2006, San Francisco, USA

136. Prucnal, S.; Sun, J. M.; Reuther, H.; Skorupa, W.; Buchal, C.
Electronegativity and point defect formation in ion implanted SiO_2 layers
VIth International Conference on Ion Implantation and other Applications of Ions and Electrons (ION2006), 26.-29.06.2006, Kazimierz Dolny, Poland

137. Rogozin, A.; Shevchenko, N.; Vinnichenko, M.; Kolitsch, A.; Möller, W.
New annealing methods of indium tin oxide films by electric current
International Conference on Coatings on Glass and Plastics, FEP, 18.-22.06.2006, Dresden, Germany

138. Rogozin, A.; Vinnichenko, M.; Shevchenko, N.; Kolitsch, A.; Möller, W.
Optimization of reactive pulsed magnetron sputtering for epitaxial growth of undoped ZnO films
10th International Conference on Plasma Surface Engineering, 10.-15.09.2006, Garmisch-Partenkirchen, Germany

139. Röntzsch, L.; Heinig, K.-H.
Reaction pathways of a regular disintegration of nanowires by thermocapillarity
DPG-Frühjahrstagung 2006, 27.-31.03.2006, Dresden, Germany

140. Röntzsch, L.; Heinig, K.-H.
Search for reaction pathways of a CMOS-compatible fabrication of nanofluidic channels by means of atomistic computer simulations
Materials Research Society (MRS) Spring Meeting, 17.-21.04.2006, San Francisco, USA

141. Röntzsch, L.; Heinig, K.-H.
Size and position control of chains or arrays of nanoparticles by surface-plasmon-polariton-induced thermocapillarity
Materials Research Society (MRS) Spring Meeting, 17.-21.04.2006, San Francisco, USA

142. Röntzsch, L.; Heinig, K.-H.
Nanowire synthesis with focused ion beams: predictive atomistic simulations on the fabrication of functional nanowire structures
European Materials Research Society (E-MRS) Spring Meeting 2006, 29.05.-02.06.2006, Nice, France

143. Röntzsch, L.; Heinig, K.-H.
Nanowire transformation into long-range-ordered nanocluster chains controlled by thermocapillarity
European Materials Research Society (E-MRS) Spring Meeting 2006, 29.05.-02.06.2006, Nice, France

144. Röntzsch, L.; Heinig, K.-H.
Predictive process simulation of the FIB-based fabrication of metallic nanoparticle waveguides
Materials Research Society (MRS) Spring Meeting, 17.-21.04.2006, San Francisco, USA

145. Röntzsch, L.; Heinig, K.-H.
Focused-ion-beam-based synthesis of semiconductor nanowires and functional structures – an atomistic computer simulation study
Materials Research Society (MRS) Spring Meeting, 17.-21.04.2006, San Francisco, USA

146. Röntzsch, L.; Heinig, K.-H.
Modeling of focused-ion-beam-based synthesis of nanowire structures
15th International Conference on Ion Beam Modification of Materials, 18.-22.09.2006, Taormina, Italy

147. Rotshtein, V. P.; Markov, A. B.; Proskurovsky, D. I.; Günzel, R.; Pham, M. T.; Richter, E.; Shevchenko, N.; Shulov, V. A.; Rubshtein, A. P.
Surface modification of Ti-6Al-4V alloy with a low-energy, high-current electron beam at elevated initial temperatures
8th International Conference on Modification of Materials with Particle Beams and Plasma Flows, 10.-15.09.2006, Tomsk, Russia

148. Rotshtein, V. P.; Markov, A. B.; Proskurovsky, D. I.; Kagadei, V. A.; Günzel, R.; Shevchenko, N.; Reuther, H.; Shulov, V. A.
Surface alloying of Ti-6Al-4V with zirconium by pulsed electron-beam melting of film – substrate system
8th International Conference on Modification of Materials with Particle Beams and Plasma Flows, 10.-15.09.2006, Tomsk, Russia

149. Satta, A.; D'Amore, A.; Simoen, E.; Janssens, T.; Clarysse, T.; Anwand, W.; Skorupa, W.
Germanium shallow junction formation by flash annealing
15th International Conference on Ion Beam Modification of Materials, 18.-22.09.2006, Taormina, Italy

150. Scheerschmidt, K.; Kuhlmann, V.; Rother, A.; Gemming, S.
Electron imaging based on charge density potentials and frozen lattices
16th Int. Microscopy Congress (IMC 16), 02.-07.09.2006, Sapporo, Japan

151. Schmidt, B.; Akhmadaliev, Ch.; Bischoff, L.
FIB induced cobalt disilicide nanowire growth in silicon
15th International Conference on Ion Beam Modification of Materials, 18.-22.09.2006, Taormina, Italy

152. Schmidt, B.; Mücklich, A.; Röntzsch, L.; Heinig, K.-H.
How do high energy heavy ions shape Ge nanoparticles embedded in SiO_2?
15th International Conference on Ion Beam Modification of Materials, 18.-22.09.2006, Taormina, Italy

153. Schneider, H.; Drachenko, O.; Winnerl, S.; Helm, M.; Walther, T.; Maier, M.
Autocorrelation measurements of free-electron laser radiation using a two-photon QWIP
International Workshop on Quantum Well Infrared Photodetectors (QWIP2006), 18.-24.06.2006, Kandy, Sri Lanka

154. Schneider, S.; Seidel, J.; Grafström, S.; Loppacher, C.; Cebula, M.; Eng, L. M.; Winnerl, S.; Stehr, D.; Helm, M.
Scattering scanning near-field optical microscopy on anisotropic dielectrics using a free-electron laser light source
DPG-Frühjahrstagung 2006, 27.-31.03.2006, Dresden, Germany

155. Shevchenko, N.; Maitz, M. F.; Richter, E.
Modification of NiTi surface by plasma immersion ion implantation
International Conference on Shape Memory and Superelastic Technologies (SMST 2006), 07.-11.05.2006, Pacific Grove, California, USA

156. Shevchenko, N.; Reuther, H.; Kreissig, U.; Richter, E.
Plasma immersion ion implantation for NiTi surface modification
15th International Conference on Ion Beam Modification of Materials, 18.-22.09.2006, Taormina, Italy

157. Silva, G.; Ueda, M.; Rossi, J. O.; Reuther, H.
Implantação Iônica por Imersão em Plasma de Nitrogênio Usando Baixa Energia
XII Encontro e Exposição Brasileira de Tratamentos de Superfície & II INTERFINISH Latino-Americano, 09.-11.05.2006, Sao Paulo, Brasil

158. Skorupa, W.; Anwand, W.; Schumann, T.; Voelskow, M.; Luethge, Th.; Adam, D.
Flash lamp processing for conductive ITO layers
Summer School Nanotronics 2006, Creavis-Degussa AG, 11.-13.09.2006, Marl, Germany

159. Smith, M. P.; Mcmahon, R. A.; Seffen, K. A.; Panknin, D.; Voelskow, M.; Skorupa, W.
Thermal and stress modeling for the flash lamp crystallization of amorphous silicon films
Materials Research Society (MRS) Spring Meeting 2006, 17.-21.04.2006, San Francisco, USA

160. Smith, M. P.; Seffen, K. A.; Mcmahon, R. A.; Anwand, W.; Skorupa, W.
Thermally induced deformation and stresses during millisecond flash lamp annealing
Materials Research Society (MRS) Spring Meeting 2006, 17.-21.04.2006, San Francisco, USA

161. Smith, M. P.; Voelskow, M.; Mcmahon, R. A.; Mücklich, A.; Anwand, W.; Skorupa, W.
Process control during liquid phase regrowth of 3C-SiC on Si substrates
Materials Research Society (MRS) Spring Meeting 2006, 17.-21.04.2006, San Francisco, USA

162. Stehr, D.; Helm, M.; Metzner, C.; Wanke, M. C.
Theory of impurity states in coupled quantum wells and superlattices and their infrared absorption spectra
28th International Conference on the Physics of Semiconductors, 24.-28.07.2006, Wien, Austria

163. Stehr, D.; Metzner, C.; Helm, M.
Resonant impurity states in quantum wells and superlattices
DPG-Frühjahrstagung 2006, 27.-31.03.2006, Dresden, Germany

164. Stehr, D.; Winnerl, S.; Helm, M.; Andrews, A. M.; Roch, T.; Strasser, G.
Picosecond dynamics of interminiband transitions in doped GaAs/AlGaAs superlattices
POISE Summer School, 25.-30.06.2006, Cortona, Italia

165. Stehr, D.; Winnerl, S.; Helm, M.; Andrews, A. M.; Roch, T.; Strasser, G.
Relaxation dynamics of interminiband transitions and electron cooling in doped GaAs/AlGaAs superlattices
28th International Conference on the Physics of Semiconductors, 24.-28.07.2006, Vienna, Austria

166. Talut, G.; Reuther, H.; Eichhorn, F.; Mücklich, A.; Potzger, K.
Magnetic, structural and electronic properties of Fe implanted GaN
DPG-Frühjahrstagung 2006, 27.-31.03.2006, Dresden, Germany

167. Talut, G.; Reuther, H.; Eichhorn, F.; Mücklich, A.; Potzger, K.; Stromberg, F.; Zhou, S.
Magnetic and structural properties of Fe implanted GaN
6th Workshop on Mössbauer Spectroscopy, 07.-11.06.2006, Seeheim, Germany

168. Toimil-Molares, M. E.; Karim, S.; Sigle, W.; Heinig, K.-H.; Röntzsch, L.; Trautmann, C.; Cornelius, T. W.; Neumann, R.
Thermal instability of copper nanowires
Gordon Research Conference "Electrodeposition", 30.07.-04.08.2006, New London, NH, USA

169. Tribuzy, C. V.-B.; Ohser, S.; Neuhaus, J.; Dekorsy, T.; Winnerl, S.; Schneider, H.; Helm, M.; Biermann, K.; Künzel, H.; Semtsiv, M. P.; Masselink, W. T.
Intersubband relaxation dynamics in narrow InGaAs/AlAsSb and InGaAs/AlAs quantum well structures using pump-probe spectroscopy
DPG-Frühjahrstagung 2006, 27.-31.03.2006, Dresden, Germany

170. Tsyganov, I. A.; Mashina, A. I.; Richter, E., Maitz, M. F.; Rustichelli, F.
Use of metal plasma immersion ion implantation and deposition for preparation of hemocompatible titanium-based coatings
International Conference on Advanced Technologies and Equipment in Mechanical Engineering and Metallurgy, 11.-12.05.2006, Lipetsk, Russia

171. Tsyganov, I. A.; Maitz, M. F.; Richter, E.; Reuther, H.; Mashina, A. I.
Correlation between physical surface properties and blood compatibility of titanium-based coatings prepared by metal plasma immersion ion implantation and deposition
15th International Conference on Ion Beam Modification of Materials, 18.-22.09.2006, Taormina, Italy

172. Ueda, M.; Oliveira, R. M.; Rossi, J. O.; Reuther, H.; Silva, G.
Plasma immersion ion implantation with a 4 kV/10 kHz Compact high-voltage pulser
6th International Conference on Íon Implantation Technology, 11.-16.06.2006, Marseille, France

173. Ulrich, K.-U.; Rossberg, A.; Scheinost, A.; Reuther, H.; Zaenker, H.
Structural investigation on uranium mine water colloids and their interaction with UO^{22+}
232nd ASC National Meeting, 10.-14.09.2006, San Francisco, USA

174. Ulyashin, A. G.; Bentzen, A.; Diplas, S.; Suphellen, A.; Gunnaes, A. E.; Olsen, A.; Svensson, B. G.; Marstein, E. S.; Holt, A.; Grambole, D.; Sauar, E.
Hydrogen release and defect formation during heat treatments of SiNx:H/a-Si:H double passivation layer on c-Si substrate
2006 IEEE 4th World Conference on Photovoltaic Energy Conversion, 05.-12.05.2006, Hawaii, USA

175. Vinnichenko, M.; Rogozin, A.; Shevchenko, N.; Kolitsch, A.; Möller, W.
Epitaxial thin films of undoped ZnO grown by reactive pulsed magnetron sputtering
European Materials Research Society (E-MRS) Spring Meeting 2006, 29.05.-02.06.2006, Nice, France

176. Vinnichenko, M.; Rogozin, A.; Shevchenko, N.; Ozerov, M.; Kolitsch, A.; Möller, W.
Spectroscopic ellipsometry of ZnO thin films grown by pulsed reactive magnetron sputtering at elevated temperatures
DPG-Frühjahrstagung 2006, Deutsche Physikalische Gesellschaft, 27.-31.03.2006, Dresden, Germany

177. von Wenckstern, H.; Schmidt, H.; Pickenhain, R.; Biehne, G.; Brandt, M.; Brauer, G.; Lorenz, M.
Electrical spectroscopy of acceptor states in N+ implanted ZnO single crystals
DPG-Frühjahrstagung 2006, 27.-31.03.2006, Dresden, Germany

178. von Wenckstern, H.; Schmidt, H.; Pickenhain, R.; Biehne, G.; Brandt, M.; Brauer, G.; Lorenz, M.; Dadgar, A.; Krost, A.; Grundmann, M.
Electrical characterization of deep acceptor states in ZnO
Materials Research Society (MRS) Fall Meeting 2006, 27.11.-01.12.2006, Boston/MA, USA

179. von Wenckstern, H.; Schmidt, H.; Pickenhain, R.; Biehne, G.; Brandt, M.; Brauer, G.; Lorenz, M.; Grundmann, M.
Electrical characterization of deep acceptor states in nitrogen implanted ZnO single crystals
European Materials Research Society (E-MRS) Spring Meeting 2006, 29.05.-02.06.2006, Nice, France

180. Weber, M.; Blomeier, S.; Hillebrands, B.; Fassbender, J.
Laser induced precessional switching in exchange biased NiFe/FeMn bilayers
21st General Conference of the EPS Condensed Matter Division, 27.-31.03.2006, Dresden, Germany

181. Weishart, H.; Heera, V.; Skorupa, W.
Electrical conductivity of nitrogen doped SiC nanocrystals in diamond
5. Siliziumkarbid-Rundgespräch, 17.-18.07.2006, Kloster Banz, Staffelstein, Germany

182. Yankov, R. A.; Donchev, A.; Schuetze, M.; Richter, E.
Ion implantation of halogens: a promising technique for enhancing the high-temperature oxidation resistance of TiAl alloys
21st General Conference EPS and Meeting of the German Physical Society, 27.-31.03.2006, Dresden, Germany

183. Yankov, R. A.; Richter, E.; Donchev, A.; Schütze, M.
Efficient oxidation protection of gamma-TiAl alloys by ion implantation of halogens
15th International Conference on Ion Beam Modification of Materials, 18.-22.09.2006, Taormina, Italy

184. Zen, A.; Pingel, P.; Neher, D.; Grenzer, J.; Zhuang, W.; Rabe, J. P.; Bilge, A.; Galbrecht, F.; Nehls, B.; Farrell, T.; Scherf, U.; Abellons, R. D.; Grozema, F. C.; Siebbeles, L. D. A.
Organic field-effect transistors utilising oligothiophene based swivel cruciform
DPG-Frühjahrstagung 2006, 27.-31.03.2006, Dresden, Germany

185. Zhang, G.; Potzger, K.; Zhou, S.; Mücklich, A.; Ma, Y.; Fassbender, J.
Memory effects in interacting and non-interacting ion beam synthesized nanoparticle systems
15th International Conference on Ion Beam Modification of Materials, 18.-22.09.2006, Taormina, Italy

186. Zhou, S.; Potzger, K.; Eichhorn, F.; Helm, M.; Skorupa, W.; Mücklich, A.; Fassbender, J.; Herrmannsdörfer, T.; Bianchi, A.
Ferromagnetic Gd-implanted ZnO single crystals
DPG-Frühjahrstagung 2006, 27.-31.03.2006, Dresden, Germany

187. Zhou, S.; Potzger, K.; Mücklich, A.; Reuther, H.; Eichhorn, F.; Schell, N.; Skorupa, W.; Helm, M.; Fassbender, J.
Magnetic nanoparticle formation in Fe implanted ZnO
European Materials Research Society (E-MRS) Spring Meeting 2006, 29.05.-02.06.2006, Nice, France

188. Zhou, S.; Potzger, K.; Reuther, H.; Mücklich, A.; Eichhorn, F.; Schell, N.; Skorupa, W.; Helm, M.; Fassbender, J.
Ferromagnetic $ZnFe_2O_4$ synthesized by Fe implantation into ZnO
4th International Conference on Physics and Applications of Spin Related Phenomena in Semiconductors, 15.-18.08.2006, Sendai, Japan

189. Zhou, S.; Potzger, K.; Zhang, G.; Mücklich, A.; Eichhorn, F.; Grötzschel, R.; Schmidt, B.; Skorupa, W.; Helm, M.; Fassbender, J.
Mn-silicide nanoparticles formed inside Si using ion implantation
DPG-Frühjahrstagung 2006, 27.-31.03.2006, Dresden, Germany

190. Zhou, S.; Potzger, K.; Zhang, G.; Mücklich, A.; Eichhorn, F.; Grötzschel, R.; Schmidt, B.; Skorupa, W.; Helm, M.; Fassbender, J.
Mn-silicide nanoparticles: the origin of ferromagnetism in Mn-implanted Si?
15th International Conference on Ion Beam Modification of Materials, 18.-22.09.2006, Taormina, Italy

191. Zier, M.; Schmidt, B.; Rangelow, I.; Ivanov, T.; Sarov, Y.; Dontsov, D.; Schott, W.
Fabrication of ultra-shallow p-n junctions as piezoresistive sensors for AFM deflection sensing
Micro- and Nanoengineering 2006, 17.-20.09.2006, Barcelona, Spain

Lectures

1. Bischoff, L.; Akhmadaliev, Ch.
Mass separated FIB applications from alloy liquid metal ion sources
FIB User Meeting 2006, Orsay Physics, 18.-19.05.2006, Fufeau, France

2. Brauer, G.
Recent results of slow positron implantation spectroscopy to characterize vacancy-type damage in ion-implanted 6H-SiC
Seminar held at
University of Hong Kong, Physics Department, 13.01.2006, Hong Kong, China
Chinese University of Hong Kong, Department of Electronic Engineering, 17.01.2006, Hong Kong, China

3. Brauer, G.
Characterization of ZnO single crystals by positron annihilation
Seminar held at
University of Western Ontario, Department of Physics and Astronomy, 31.07.2006, London/Ontario, Canada
McMaster University, Brockhouse Institute for Materials Research, 3.08.2006, Hamilton/Ontario, CanadaUniversity of North Texas, Department of Materials Science and, 28.08.2006, Denton/Texas, USA
University of Texas at Austin, Department of Physics, 30.08.2006, Austin/TX, USA
University of Texas at Arlington, Physics Department, 31.08.2006, Arlington/Texas, USA
Texas Christian University, Department of Physics and Astronomy, 1.09.2006, Ft. Worth/Texas, USA

4. Facsko, S.; Keller, A.; Liedke, M. O.; Fassbender, J.; Möller, W.
Properties of thin films grown on periodically corrugated surfaces
Seminar, Fachbereich Physik, Universität Konstanz, 30.05.2006, Konstanz, Germany

5. Facsko, S.; Keller, A.; Rossbach, S.; Möller, W.
Periodic surface patterns induced by low energy ion erosion
Seminar, II. Physikalische Institut, Universität Göttingen, 15.12.2006, Göttingen, Germany

6. Fassbender, J.
Ion beam induced magnetic property modifications
Seminar, Max Planck Institut für Mikrostrukturforschung, 6.06.2006, Halle, Germany

7. Fassbender, J.
Ion beam induced magnetic property modifications
Seminar, Universität Goettingen, 8.12.2006, Goettingen, Germany

8. Gemming, S.
Scale-hopping modelling of ferroic functional elements
Seminar, ITF, IFW Dresden, 7.11.2006, Dresden, Germany

9. Grambole, D.
Zerstörungsfreie, quantitative Wasserstoff-Analytik mittels Ionenstrahlen
Seminar, Universität Karlsruhe, SFB 551, 4.04.2006, Karlsruhe, Germany

10. Heinig, K.-H.
Nanostructure growth and modification with ion beams
Physikalisches Kolloquium, I. Physikalisches Institut der RWTH Aachen, 25.01.2006, Aachen, Germany

11. Heinig, K.-H.
Growth and Taming of Nanostructures with Ion Beams
Seminar, RWTH Aachen, 26.01.2006, Aachen, Germany

12. Kreissig, U.
Heavy Ion ERDA at the 5 MV Tandem Accelerator in Rossendorf
Seminar, Nuclear Physics Institute Rez, 25.07.2006, Rez, Czech Republic

13. Möller, W.
Ion irradiation for generation and control of nanostructures
Seminar, Dept. of Macromolecular Physics, Charles University, 10.01.06, Prag, Czech Republic

14. Möller, W.
Ioneninduzierte Nanostrukturen
Festkolloquium, Fakultät für Mathematik, Naturwissensch. & Informatik, BTU Cottbus, 6.12.2006, Cottbus, Germany

15. Möller, W.
Tutorial "Fundamentals and Trends of Plasma Surface Processing"
connected with 10th Int. Conference on Plasma Surface Engineering, 9.-10.09.2006 Garmisch-Partenkirchen, Germany

16. Posselt, M.
Atomic-level simulations of ion implantation, defect formation and defect migration
Seminar, Institut für Integrierte Systeme der ETH Zürich, 5.04.2006, Zürich, Schwitzerland

17. Potzger, K.; Zhou, S.; Zhang, G.; Reuther, H.; Talut, G.; Mücklich, A.; Eichhorn, F.; Schell, N.; Grötzschel, R.; Skorupa, W.; Helm, M.; Anwand, W.; Brauer, G.; Fassbender, J.
Diluted magnetic semiconductors created by non-equilibrium processing -new challenges for ion beams
Institutsseminar, Physikalisches Instituts der Universität Karlsruhe, 6.11.2006, Karlsruhe, Germany

18. Schmidt, B.
Erzeugung von Nano-Strukturen mit Ionenstrahlen
Seminar, AMD Dresden, 27.03.2006, Dresden, Germany

19. Schneider, H.
Quantum well infrared photodetectors: Physics and applications
Seminarvortrag, 12.01.2006, TU Dresden, Germany

20. Schneider, H.
Halbleiterspektroskopie mit ultrakurzen Laserpulsen
Physikalisches Kolloquium, Bergakademie Freiberg, 5.07.2006, Freiberg, Germany

21. Shevchenko, N.
Plasma immersion ion implantation for surface modification
Seminar, Boston Scientific, 3.05.2006, Maple Grove, Minnesota, USA

22. Skorupa, W.
Mikro-Nano-Piko: Elektronik und Photonik erobern das Nichts
Technologietag der FDP-Fraktion am Sächsischen Landtag, FDP-Fraktion am Sächsischen Landtag, 18.05.2006, Dresden, Germany

23. Skorupa, W.
Advanced thermal processing of semiconductor materials in the msec-range
Seminar, Institut für Experimentelle Physik der Bergakademie Freiberg, 7.06.2006, Freiberg, Germany

24. Skorupa, W.
Ausgründung einer GmbH aus dem FZD aus der Perspektive eines Wissenschaftlers
Treffen mit Mittelstandsvereinigung Saxonia der sächsischen FDP, nanoparc GmbH und FZD, 9.06.2006, Dresden-Rossendorf, Germany

25. Skorupa, W.
Advanced thermal processing of semiconductor materials in the msec-range
Projekttreffen OSTEC Advanced Quantum Beam Project, FZD-FWI, 27.09.2006, FZ Dresden-Rossendorf, Germany

26. Skorupa, W.
Thermische Prozesse im msec-Bereich für Elektronik und Photonik
Seminar am Institut für Bio- und Nanosysteme des Forschungszentrums Jülich, Institut für Bio- und Nanosysteme des Forschungszentrums Jülich, 16.10.2006, Jülich, Germany

27. Skorupa, W.
Blitzlampen-Prozessieren: Stress und Oberflächen-Schmelzen bei Silizium
Deutsches Nutzertreffen Kurzzeitausheilung, Fraunhofer Gesellschaft, IISB, 23.11.2006, Villach, Austria

28. Vinnichenko, M.; Ozerov, M.; Rogozin, A.; Shevchenko, N.; Kolitsch, A.
Spectroscopic ellipsometry of ZnO thin films: choice of optimum parameterization of dielectric function
Woollam-Ellipsometrie-Seminar, L.O.T.-Oriel GmbH & Co. KG, 25.10.2006, Darmstadt, Germany

PhD Theses

1. Mrotchek, I.
Oberflächenmodifikation des Hartmetalls Wolframkarbid-Kobalt durch Bor-Ionenimplantation
TU Dresden, Oct 17, 2006
Wissenschaftlich-Technische Berichte, FZD-462, 2007

2. Sinning, S.
Ultraschnelle optelektronische und Materialeigenschaften von stickstoffhaltigem GaAs
TU Dresden, Jan 04, 2006
Wissenschaftlich-Technische Berichte, FZR-450, 2006

3. Ullmann, F.
Untersuchung der Erzeugung hochgeladener Ionen in einer Raumtemperatur-Elektronenstrahl-Ionenfalle
TU Dresden, Jan 18, 2006

Master & Diploma Theses

1. Berendt, M.
Herstellung von Hartstoffschichten aus AlMgB14 mittels Ionenimplantation
HTW Dresden, 15.12.2006

2. Ohser, S.
Ultrafast dynamics of electrons in semiconductor quantum wells
Universität Jena, 22.6.2006

3. Peter, F.
Untersuchung der räumlichen Strahlcharakteristik von fotoleitenden Terahertz-Strahlungsquellen
TU Dresden, 6.11.2006

4. Petr, V.
Prädiktive Kompensation von Schwankungen der Beschleunigungsspannung von Van-de-Graaff-Ionenbeschleunigern
HTW Dresden, 25.10.2006

5. Wagner, M.
Erzeugung, Charakterisierung, und Anwendung ultrakurzer THz-Pulse
Universität Konstanz, 3.7.2006

Organization of Conferences

1. Möller, W.
   10th Int. Conference on Plasma Surface Engineering (Scientific Program Coordination)
   Garmisch-Partenkirchen, Sept 10-15, 2006

Laboratory Visits

1. Beckers, M.
   Linköping University, Sweden; Jan 18 - 22, 2006
2. Borany, J. von
   ESRF Grenoble, France; July 19 - 21 / Oct 30 - Nov 6 / Nov 27 - Dec 5, 2006
3. Brauer, G.
   City University of Hongkong, China; Jan 5 - 19, 2006
4. Cantelli, V.
   ESRF Grenoble, France; Nov 27 - Dec 5, 2006
5. Drachenko, O.
   Toulouse High Magnetic Field Lab, France; Feb 10 - 20 / Dec 1 - 15, 2006
6. Eichhorn, F.
   ESRF Grenoble, France; Feb 8 - 15 / Oct 3 - 10 / Nov 7 - 14, 2006
7. Grenzer, J.
   ESRF Grenoble, France; Feb 21 - 28 / July 4 - 11 / Nov 7 - 14, 2006
8. Heinig, K.-H.
   Stanford University, USA; April 21 - 26, 2006
9. Küpper, K.
   Lawrence Berkeley National Lab, USA; April 21 - May 3 / Oct 5 - 27, 2006
10. Küpper, K.
    Swiss Light Source, PSI Villigen, CH; March 10 - 17 / July 10 - 19
11. Martins, R.
    Linköping University, Sweden; Jan 18 - 22, 2006
12. Rogozin, A.
    ESRF Grenoble, France; May 15 - 23 / Oct 3 - 10, 2006
13. Röntzsch, L.
    Stanford University, USA; April 21 - 26, 2006
14. Schell, N.
    University Aarhus, Denmark, March 30 - April 3, 2006
    CENIMAT, Lisboa, Portugal, Aug 24 - 28, 2006
    HASYLAB, Hamburg, June, 27 - July, 3, 2006
    ANKA, Karlsruhe, Sept 9 - 11, 2006
    University and Academy of Science, Lanzhou, China, Oct 16 - 21, 2006
15. Scholz, A.
    ESRF Grenoble, France; Nov 30 - Dec 5, 2006
16. Shevchenko, N.
    ESRF Grenoble, France, May 15 - 23 / Oct 3 - 10, 2006
    Siberian Physical and Technical Institute, Tomsk, Russia, July 3 - 7, 2006
    Boston Scientific, Maple Grove, Minnesota, USA, May, 3 - 5, 2006
17. Winnerl, S.
    THALES, Paris, France; Feb 12 - 18, 2006
18. Zhang, G.
    ESRF Grenoble, France; July 14 - 18, 2006
19. Zhou, S.
    ESRF Grenoble, France; July 14 - 18, 2006

Guests

1. Al-Weheibi, A.
   Sultan Qaboos University, Oman, April 1 – Aug 1, 2006
2. Asgekar, V.
   University of Pune, India, June 9 – July 14, 2006
3. Bera, S.
   Institute of Physics Bhubaneswar, India, March 13 – 31, 2006
4. Beshkova, M.
   Institute of Electronics Sofia, Bulgaria, Oct 5 – Dec 15, 2006
5. Cheng, R.
   Lanzhou University, China, Oct 1 – Dec 25, 2006
6. Cizek, J.
   Charles Unviversity Prague, Czech Republic, May 25 – June 16, 2006
7. Dev, B.N.
   Institute of Physics, Bhubaneswar, India, Jan 1 - March 31, 2006
8. Dvurechenskii, A.
   AdW Novolibirsk, Russia, March 31 – April 08, 2006
9. Glotov, A.
   IPPE Obninsk, Russia, Aug 13 – 19, 2006
10. Gooda, P.
    Imperial College London, Great Britain, July 31 – Oct 20, 2006
11. Hreben, S.
    Westböhmische Universität Plzen, Czech Republic, June 6 – Sept 8, 2006
12. Kabiraj, D.
    Inter-University New Delhi, India, May 29 – June 17, 2006
13. Krok, F.
    Jagiellonian University of Krakow, Poland, Sept 24 – 29, 2006
14. Kuriplach, J.
    Charles University Prague, Czech Republic, Nov 1 – 15/ Nov 28 – Dec 12, 2006
15. Markov, A.
    Institut für Hochstromelektronik Tomsk, Russia, Oct 8 – Dec 16, 2006
16. Martins, R. M. S
    University of Lisboa, Portugal, March 1, 2006 – Feb 28, 2007
17. Mashina, A.
    Universität Lipezk, Russia, April 17 – May 15, 2006
18. Mukesh, R.
    Institute for Plasma Research Gandhingar, India, Sept 15 – Dec 15, 2006
19. Nazarov, A.
    Institut of Semiconductor Physics Kyiv, Ukraine, April 23 – June 9, 2006
20. Oates, T.
    University of Sydney, Australia, Aug 1 – 31/ Oct 1 – 31, 2006
21. Odor, G.
    KFKI Budapest, Hungary, July 2 – 14/ Sept 3 – 15/ Oct 9 – 21, 2006/ Nov 12 – 24, 2006
22. Osiuk, I.
    Institut of Semiconductor Physics Kyiv, Ukraine, April 23 – June 9, 2006
23. Ozerov, M.
    National Kyiv Taras Shevchenko University, Ukraine, June 5 – Sept 5, 2006

24. Pagowska, K.
Institute of Electronic Materials Technology, Poland, March 5 – 11, 2006

25. Peng, H.
Lanzhou University, China, Oct 1 – Dec 25, 2006

26. Rudolphi, M.
Institute of Geological and Nuclear Science Lower Hutt, New Zealand, June 26 – July 7, 2006

27. Sass, J.
Institute of Electronic Materials Technology, Poland, May 21 – 25,2006

28. Satpati, B.
Paul-Drude-Institut Berlin, Germany, Feb 8 – 11, 2006

29. Smith, M.
Cambridge University, Great Britain, May 1 – Dec 15, 2006

30. Som, T.
Institute of Physics Bhubaneswar, India, March 1 – June 2, 2006

31. Stonert, A.
Institute of Electronic Materials Technology, Poland, March 5 – 11/ June 4 – 10, 2006

32. Tsyganov, I.
Universität Lipezk, Russia, April 17 – May 10 / July 24 – Sept 14/ Sept 23 – 27/ Dec 29, 2006 – Feb. 28, 2007

33. Turos, A.
Institute of Electronic Materials Technology, Poland, March 5 – 11/ May 28 – June 8, 2006

34. Tyagulski, I.
Institut of Semiconductor Physics Kyiv, Ukraine, April 23 – June 9, 2006

35. Wang, T.
Lanzhou University, China, May 23 – June 31, 2006

36. Windl, W.
Ohio State University, USA, July 26 – 27, 2006

37. Yankov, R.
Universität Almaty, Kazakhstan, July 5 – Sept 8, 2006

AIM Visitors

1. Barlak, M.
Soltan Institute, Warschau, Poland; Sept 2 - 8 / Dec 4 - 14, 2006

2. Beckers, M.
Uni Linköping, Sweden; July 9 - 17 / Sept 3 - 9, 2006

3. Gago, R
Uni Madrid, Spain; Sept 16 - 22, 2006

4. Gordillo, N.
Uni Madrid, Spain; Oct 30 - Nov 23, 2006

5. Krickl, R.
Uni Wien, Austria; Nov 6 - 11, 2006

6. Menendez, E.
Uni Barcelona, Spain; Sept 20 - Oct 7 / Dec 12 - 22, 2006

7. Misjak, F.
KFKI Budapest, Hungary; Nov 9 - 18, 2006

8. Müller, D. C.
ETH Zürich, Switzerland; July 24 - 27, 2006

9. Nasdala, L.
Uni Wien, Austria; Nov 6 - 8, 2006

10. Poberaj, G.
ETH Zürich, Switzerland; June 25 - 30 / Oct 22 - 27, 2006

11. Piekoszewski, J.
Soltan Institute, Warschau, Poland; Sept 2 - 8 / Dec 4-14, 2006

12. Radnoczi, G.
KFKI Budapest, Hungary; Nov 9 - 18, 2006

13. Redondo, A.
Uni Madrid, Spain; Sept 16 - 22, 2006

14. Sort, J.
Uni Barcelona, Spain; Sept 20 - Oct 7, 2006

IA-SFS Visitors

1. Carpenter, B.
University of Sheffield, U.K.; Dec 5 - 9, 2006

2. Ceponkus, J.
Vilnius University, Lithuania; May 9 - 13 / Sept 10-16 / Nov 5 - 11, 2006

3. Jobson, K.
University of Sheffield, U.K.; Sept 4 - 13, 2006

4. Khalil, G. E.
University of Sheffield, U.K.; Sept 4 - 13, 2006

5. Sablinskas, V.
Vilnius University, Lithuania; Feb 27 - March 3 /April 10 - 14 / May 9 - 13 / Sept 10 - 16 / Nov 5 - 11, 2006

6. Wilson, L.E.
University of Sheffield, U.K.; Nov 3 - Dec 2, 2006

7. Zibik, E.
University of Sheffield, U.K.; Nov 30 - Dec 9, 2006

ROBL-MRH Visitors

1. Beckers, M.
Linköping University, Linköping, Sweden; March 1 - 7 / Oct 31 - Nov 7, 2006

2. Braz Fernandes, F. M.
CENIMAT F.C.T./Universidade Nova de Lisboa, Lisbon, Portugal,
Feb 15 - 21 / April 19 - 25 / April 26 - May 2 / July 5 - 10, 2006

3. Cordeiro Silva, R. J.
CENIMAT F.C.T./Universidade Nova de Lisboa, Lisbon, Portugal, Feb 15 - 21 / July 5 - 10, 2006

4. Fuhrmann, N.
AMD Saxony, Dresden, Germany; Aug 30 - Sept 5, 2006

5. Gaca, J.
ITME Warsaw, Poland; Feb 9 - 14, 2006

6. Höglund, C.
Linköping University, Linköping, Sweden; March 1 - 7, Oct 31 - Nov 7, 2006

7. Kräusslich, J.
Institut für Optik und Quantenelektronik, FSU Jena, Jena, Germany; July 12 - 15, 2006

8. Mahesh, K.
CENIMAT F.C.T./Universidade Nova de Lisboa, Lisbon, Portugal; Feb 15 - 21 / July 5 - 10, 2006

9. Pinto, H. C.
Institut für Werkstoffkunde, TU Wien, Vienna, Austria; June 21 - 27, 2006

10. Prinz, H.
AMD Saxony, Dresden, Germany; March 8 - 13, 2006

11. Rinderknecht, J.
AMD Saxony, Dresden, Germany; March 8 - 13 / Aug 30 - Sept 5, 2006

12. da Silva, P.
Institut für Werkstoffkunde, TU Wien, Vienna; Austria; June 21 - 27, 2006

13. Sket, F.
Institut für Werkstoffkunde, TU Wien, Vienna, Austria; June 21 - 27, 2006

14. Teichert, S.
Qimonda Dresden, Germany; Sept 23 - 26, 2006

15. Wehrhan, O.
Institut für Optik und Quantenelektronik, FSU Jena, Jena, Germany; July 12 - 15, 2006

16. Zastrau, U.
Institut für Optik und Quantenelektronik, FSU Jena, Jena, Germany; July 12 - 15, 2006

17. Wojcik, M.
ITME Warsaw, Poland; Feb 9 - 14, 2006

18. Zienert, I.
AMD Saxony, Dresden, Germany; March 8 - 13 / Aug 30 - Sept 5, 2006

Colloquium

1. Back, C.- Universität Regensburg, Institut für Experimentelle Physik, Germany
Magnetisierungsdynamik: Als die magnetischen Bilder laufen lernten
Feb 2, 2006

2. Ratzinger, U. - Universität Frankfurt, Institut für Angewandte Physik, Germany
Kompakte Ionen - Linearbeschleuniger für gepulsten sowie für Dauerstrichbetrieb
May 4, 2006

3. Aziz, M. - Harvard University, Cambridge, MA, USA
Nanoscale morphology control using ion beams
Sept 13, 2006

4. Helmersson, U. - Linköping University, Sweden
Ionized deposition using high power pulsed sputtering
Oct 19, 2006

5. Price, K. - EOS Development, U.K.
EU funded research: how to be successful
Oct 25, 2006

6. Straede, C. - CemeCon Scandinavia A/S, Denmark
Industrial implementation of ion implantation in the tooling industry
Nov 2, 2006

7. Huber, B. - Centre Interdisciplinaire de Recherche Ions Lasers CIRIL - GANIL, France
Stability and fragmentation of charged finite-size systems: From molecules to micro droplets
Nov 16, 2006

8. Wegener, M. – Universität Karlsruhe, Germany
Photonic crystals: Tailored optical materials for the 21st century
Dec 8, 2006

9. Nylandsted Larsen, A. - University of Aarhus, Denmark
The never ending story of the E-center in silicon
Dec 14, 2006

10. von Blanckenburg, F. - Institut für Mineralogie, Universität Hannover, Germany
Kosmogene Nuklide in den Erd- und Umweltwissenschaften
Dec 21, 2006

Seminars

1. Arps, J. H. – Southwest Research Institute San Antonio TX, USA
   Surface engineering experiments at the Southwest Research Institute
   July 3, 2006

2. Bersani, M. – ITC-irst Trento, Italy
   Aspects and examples of dopant depth profiling in semiconductors by SIMS-ITC-irst structure, projects and capabilities
   Oct 19, 2006

3. Buatier de Mongeot, F. – University of Genova, Italy
   Nanoscale pattern formation on metal surfaces inducted by growth and erosion instabilities
   Sept 28, 2006

4. Chini, T. K. - Saha Institute, India
   Medium-keV Ar-ion-induced surface repples in silicon: experiment vs theory
   Jan 25, 2006

5. Falke, M. – Technische Universität Chemnitz, Germany
   Different disilicide thin films and aberration corrected scanning transmission electron microscopy: Composition, defects, interfaces and texture
   Nov 13, 2006

6. Gupta, R. – School of Instrumentation, D.A. University Indore, India
   Influence of preparation conditions and ion irradiations on the microstructure and magnetic properties of thin magnetic films
   July 4, 2006

7. Kalish, R. – Technion Haifa, Israel
   Nanoscale modification of diamond – Interesting science and promising
   May 8, 2006

8. Kishino, K. – Sophia University Tokyo, Japan
   GaN-based nanostructure devices – blue to red InGaN nanocolumn LEDs and 1.55 µm GaN/AIN QWIP
   March 6, 2006

9. Krok, F. – Jagellonian University Krakau, Poland
   Principles of non-contact AFM
   Sept 9, 2006

10. Meissl, W. – Technische Universität Wien, Austria
    Surface modifications on and electron emission from insulator surfaces induced by impact of slow highly charged ions
    Nov 14, 2006

11. Morawetz, K. – Technische Universität Chemnitz, Germany
    Kinetic theory for strong correlation effects
    Dec 18, 2006

12. Müller, D. C. – ETH Zürich, Switzerland
    Dopant interactions in highly doped silicon junctions: Ab initio simulations
    July 25, 2006

13. Mukherjee, S. – IPP Ghandinagar, India
    Effect of hydrogen and charge exchange on plasma diffusion treatments
    June 22, 2006

14. Odor, G. – KFKI Budapest, Hungary
    The role of diffusion in reaction-diffusion systems
    Oct 10, 2006

15. Sahli, B. – ETH Zürich, Switzerland
    Ab-initio molecular dynamics simulation of diffusion in silicon
    Dec 12, 2006

16. Satpati, B. – Paul-Drude-Institut for Solid State Electronics Berlin, Germany
    Ion irradiation effects in metal nanostructures grown on semiconductor surfaces
    Feb 9, 2006

17. Sort, J. – Universität Barcelona, Spain
Exchange biased magnetic vortex structures
Sept 29, 2006

18. Windl, W. - Ohio State University Columbus, USA
Silicon technology and the predictive power of ab-initio calculations
July 26, 2006

19. Linz, S. – Universität Münster, Germany
Generalized Kuramoto-sivashinsky equations as models for ion-beam erosion
May 9, 2006

Projects

1. 10/2002 – 09/2006 European Union EU
New Fullerene - Synthesis, structure and properties of new fullerene like materials
Dr. A. Kolitsch Tel.: 0351 260 3348 a.kolitsch@fzd.de

2. 11/2002 – 01/2006 Deutsche Forschungsgemeinschaft DFG
Phasen- und Strukturdesign von Ti-Al-N-Schichten durch Echtzeit-in-situ-Röntgendiffraktion
Dr. N. Schell Tel.: +33 (0)4.76.88.23.67 schell@esrf.fr

3. 03/2004 – 02/2009 European Union EU
IA-SFS - Integrating activity on synchrotron and free electron laser science
Prof. M. Helm Tel.: 0351 260-2260 m.helm@fzd.de

4. 07/2004 – 06/2006 Deutsche Forschungsgemeinschaft DFG
Theoretische Untersuchungen zu Wachstum, Stabilität und Funktionalität von Nanodrähten
Dr. K.-H. Heinig Tel.: 0351 260-3288 k.h.heinig@fzd.de

5. 07/2004 – 06/2006 Deutsche Forschungsgemeinschaft DFG
Synthese von Nanodrähten und Nanoketten mit feinfokussierten Ionenstrahlen
Dr. B. Schmidt Tel.: 0351 260 2726 bernd.schmidt@fzd.de

6. 08/2004 – 07/2006 European Union, Marie-Curie-Program EU
POLYION - Polymer surface modification by ion implantation
Dr. E. Richter Tel.: 0351 260-3326 e.richter@fzd.de

7. 09/2004 – 06/2006 Bundesministerium für Bildung und Forschung BMBF
Funktionalisierung der Oberflächen von Polyurethan als Basiswerkstoff für flexible und im Blutkontakt stehende medizinische Implantate und Devices
Dr. E. Richter Tel.: 0351 260 3326 e.richter@fzd.de

8. 09/2004 – 08/2007 WTZ with Russia WTZ
Titan im Blutkontakt
Dr. E. Richter Tel.: 0351 260 3326 e.richter@fzd.de

9. 01/2005 – 12/2006 DAAD-Poland DAAD
Ionenstrahlmodifizierung mit Polymeren
Dr. D. Grambole Tel.: 0351 260 3050 d.grambole@fzd.de

10. 01/2005 – 12/2008 European Union EU
EuroMagNET – A coordinated approach to access, experimental development and scientific exploitation of European large infrastructures for high magnetic fields
Prof. M. Helm Tel.: 0351 260 2260 m.helm@fzd.de

11. 02/2005 – 03/2006 European Union EU
NANOMULTI – Nanostructured nonmagnetic and magnetic multilayers
Dr. R. Grötzschel Tel.: 0351 260 3294 r.groetzschel@fzd.de

12. 04/2005 – 12/2007 DEGUSSA AG Industry
Untersuchungen zur Blitzlampentemperung beschichteter Substrate
Dr. W. Skorupa Tel.: 0351 260 3612 w.skorupa@fzd.de

13. 04/2005 – 06/2007 Arbeitsgemeinschaft industrieller Forschungsvereinigungen AiF
Oxidationsschutz für neuartige Hochtemperatur-Leichtbauwerkstoffe durch Ionenimplantation (III)
Dr. A. Kolitsch Tel.: 0351 260 3348 a.kolitsch@fzd.de

14. 04/2005 – 03/2010 European Union EU
PRONANO – Technology for the production of massively parallel intelligent cantilever-probe platforms for nanoscale analysis and synthesis
Dr. B. Schmidt Tel.: 0351 260 2726 bernd.schmidt@fzd.de

15. 06/2005 – 12/2006 AMD Saxony Industry
Röntgen-Mikrofokus an ROBL
Dr. N. Schell Tel.: +33 (0)4.76.88.23.67 schell@esrf.fr

16. 06/2005 – 11/2007 Deutsche Forschungsgemeinschaft DFG
Mössbauerspektroskopie an ionenimplantierten magnetischen Halbleitern
Dr. H. Reuther Tel.: 0351 260 2898 h.reuther@fzd.de

17. 07/2005 – 06/2007 Robert Bosch GmbH Industry
NanoHoch - Nanostrukturierte Hochtemperatur-Halbleiter für integrierte Abgassensoren in Dieselmotor- und Magermotorapplikationen
Dr. V. Heera Tel.: 0351 260 3343 v.heera@fzd.de

18. 09/2005 – 02/2010 European Union EU
FOREMOST – Fullerene-based opportunities for robust engineering: Making optimised surfaces for tribology
Dr. A. Kolitsch Tel.: 0351 260 3348 a.kolitsch@fzd.de

19. 11/2005 – 10/2007 Eifeler GmbH Industry
Technologietransfer c- BN
Dr. A. Kolitsch Tel.: 0351 260 3348 a.kolitsch@fzd.de

20. 01/2006 – 03/2007 Boston Scientific Scimed Industry
Nitinol II
Dr. A. Kolitsch Tel.: 0351 260 3348 a.kolitsch@fzd.de

21. 01/2006 - 12/2009 European Union EU
ITS-LEIF - Ion Technology and Spectroscopy at Low Energy Ion Beam Facilities
Dr. S. Facsko Tel.: 0351 260 2987 s.facsko@fzd.de

22. 02/2006 - 01/2010 European Union EU
AIM - Center for Application of Ion Beams to Materials Research
Dr. A. Kolitsch Tel.: 0351 260 3348 a.kolitsch@fzd.de

23. 07/2006 - 09/2007 Deutsche Forschungsgemeinschaft DFG
Hybrid-Modell
Dr. S. Gemming Tel.: 0351 260 2470 s.gemming@fzd.de

24. 07/2006 - 10/2009 Deutsche Forschungsgemeinschaft DFG
Magnetschicht (FOR520)
Dr. S. Gemming Tel.: 0351 260 2470 s.gemming@fzd.de

25. 08/2006 - 11/2007 Sächsisches Staatsministerium für Wirtschaft und Arbeit SMWA
Solarmetall - Entwicklung und Optimierung der optisch transparenten und elektrisch leitfähigen Deckschicht
Dr. A. Kolitsch Tel.: 0351 260 3348 a.kolitsch@fzd.de

26. 12/2006 - 11/2008 Qimonda Dresden Industry
Ionenstreu-Analysen an Halbleiter-Materialien
Dr. R. Grötzschel Tel.: 0351 260 3294 r.groetzschel@fzd.de

27. 11/2006 - 10/2007 Qimonda Dresden Industry
Röntgenbeugungs-Analysen an Halbleiter-Materialien
Dr. J. von Borany Tel.: 0351 260 3378 j.v.borany@fzd.de

28. 12/2006 - 11/2007 Sächsisches Staatsministerium für Wirtschaft und Arbeit SMWA
Materialcharakterisierung MUSIGUSS
Dr. W. Skorupa Tel.: 0351 260 3612 w.skorupa@fzd.de

29. 12/2006 - 11/2008 Arbeitsgemeinschaft industrieller Forschungsvereinigungen AiF
Nanomorph - Amorphe Nanostrukturen
Dr. A. Kolitsch Tel.: 0351 260 3348 a.kolitsch@fzd.de

30. 01/2006 – 12/2007 DAAD-Portugal DAAD
Erzeugung und Charakterisierung von Ni-Ti Shape Memory Dünnschicht-Legierungen
Dr. N. Schell Tel.: +33 (0)4.76.88.23.67 schell@esrf.fr

31. 06/2006 – 11/2006 Sächsisches Staatsministerium für Wissenschaft und Kunst SMWK
Gastaufenthalt von Herrn Dr. Odor aus Ungarn
Dr. K.-H. Heinig Tel.: 0351 260-3288 k.h.heinig@fzd.de

32. 07/2006 – 09/2006 Sächsisches Staatsministerium für Wissenschaft und Kunst SMWK
Gastaufenthalt von Herrn Dr. Zyganov aus Russland
Dr. E. Richter Tel.: 0351 260-3326 e.richter@fzd.de

33. 07/2006 – 09/2006 ICT GmbH Industry
Fertigung von PrSi-LAMS Emittern
Dr. B. Schmidt Tel.: 0351 260 2726 bernd.schmidt@fzd.de

34. 11/2006 – 06/2008 SARAD GmbH Industry
Entwicklung und Herstellung von ionenimplantierten Si-Strahlungsdetektoren
Dr. B. Schmidt Tel.: 0351 260 2726 bernd.schmidt@fzd.de

35. 11/2006 – 01/2007 ETH Zürich Industry
Herstellung und Untersuchung von co-implantierten Schichtstrukturen
Dr. B. Schmidt Tel.: 0351 260 2726 bernd.schmidt@fzd.de

36. 12/2006 – 12/2009 VKTA e.V. Dresden Bilateral
Durchführung von REM- bzw. EDX- sowie Mössbauer-spektroskopischen Untersuchungen an Metallproben
Dr. H. Reuther Tel.: 0351 260 2898 h.reuther@fzd.de

Experimental Equipment

1. Accelerators, Ion Implanters and Ion-Assisted-Deposition

⇒	Van de Graaff Accelerator	(VdG)	1,8 MV	*TuR Dresden, D*
⇒	Tandem Accelerator	(Td)	5 MV	*NIIEFA, RU*
⇒	Tandetron Accelerator	(Tdtr)	3 MV	*HVEE, NL*
⇒	Low-energy Ion Implanter		0.5 - 50 kV	*Danfysik, DK*
⇒	High-current Ion Implanter		20 - 200 kV	*Danfysik, DK*
⇒	High-energy Ion Implanter		40 - 500 kV	*HVEE, NL*
⇒	Plasma Immersion Ion Implantation		5 - 60 keV	*GBR, D/Home-built*
⇒	Focused Ion Beam (15 nm)		30 keV, 10 A/cm²	*Orsay Physics, F*
⇒	Dual-beam Magnetron Sputter Deposition			*Roth & Rau; D*
⇒	Ion-beam-assisted Deposition			
⇒	UHV Ion Irradiation (Ar, He, etc.)		0 - 5 keV, Scan 10 ×10mm²	*VG, USA*

2. Ion Beam Analysis (IBA)

A wide variety of advanced IBA techniques are available at the MeV accelerators.

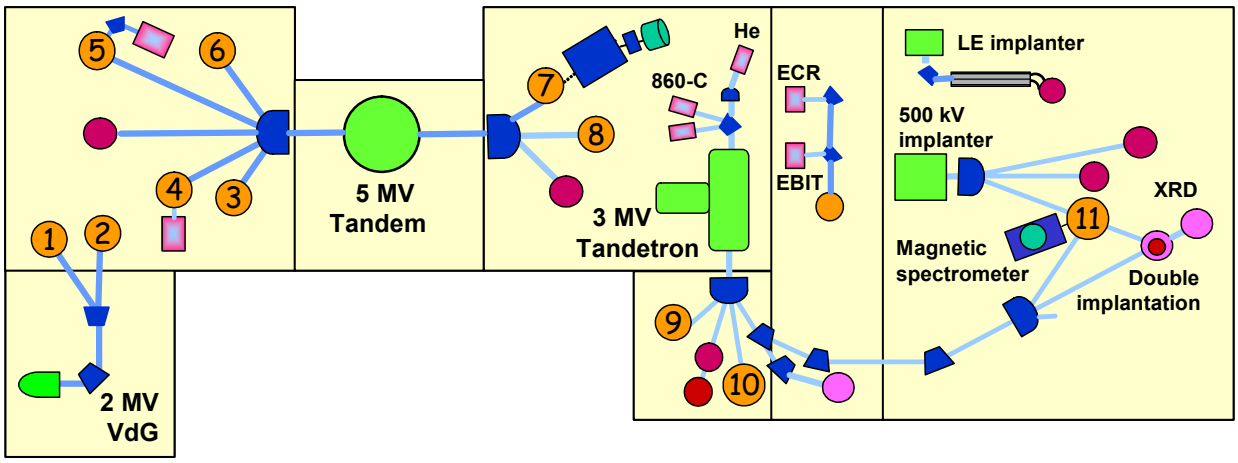

⇒	RBS	Rutherford Backscattering	(1), (2), (3), (9)	VdG, Td, Tdtr
⇒	RBS/C	RBS + Channelling	(1), (2), (3), (9)	VdG, Td, Tdtr
		High-resolution RBS/C	(11)	Tdtr
⇒	ERDA	Elastic Recoil Detection Analysis	(2), (4), (5)	VdG, Td
⇒		High-resolution ERDA	(7), (8)	Td
⇒	PIXE	Proton-induced x-ray Emission	(3)	Td
⇒	PIGE	Proton-induced γ Emission	(3)	Td
⇒	NRA	Nuclear Reaction Analysis	(4)	Td
⇒	NRRA	Nuclear Resonance Reaction Anal.	(6)	Td
⇒		Nuclear Microprobe	(10)	Tdtr

Some stations are equipped with additional process facilities which enable *in-situ* IBA investigations during ion irradiation, sputtering, deposition, annealing etc.

3. Other Particle Based Analytical Techniques

⇒	SEM	Scanning Electron Microscope	1 - 30 keV + EDX	*Hitachi, Jp*
⇒	TEM	Transmission Electron Microscope (Titan 80-300 with Image Corrector)	80 - 300 keV + EDX, +GIF	*FEI, NL*
⇒	AES	Auger Electron Spectroscopy	+ XPS	*Fisions, GB*
⇒	CEMS	Mössbauer Spectroscopy	^{57}Fe source	*Home-built*
⇒	PAS	Positron Annihilation Spectroscopy	^{22}Na source 30 V - 36 kV	*Home-built*

4. Photon Based Analytical Techniques

⇒	XRD/XRR	X-Ray Diffraction and Reflection	Cu-K_α	*Bruker axs, D*
	HR-XRD	High-Resolution XRD	Cu-K_α	*GE Inspection, D*
	XRD/XRR	with Synchrotron Radiation	5 – 35 keV	*ROBL-CRG at ESRF, F*
⇒	SE	Spectroscopic Ellipsometry	250 - 1700 nm	*Woolam, USA*
⇒	FTIR	Fourier-Transform Infrared Spectr.	600 - 7000 cm^{-1}	*Nicolet, USA*
⇒	FTIR	Fourier-Transform Infrared Spectr.	50 - 15000 cm^{-1}	*Bruker, D*
⇒		Ti:Sapphire Femtosecond Laser		*Spectra Physics, USA*
⇒		Femtosecond Optical Parametric Oscillator		*APE, D*
⇒		Ti:Sapphire Femtosecond Amplifier		*Femtolasers, A*
⇒		Femtosecond Optical Parametric Amplifier		*Light Conversion, LT*
⇒	Raman	Raman Spectroscopy	> 45 cm^{-1} shift	*Jobin-Yvon-Horiba, F*
⇒	PL	Photoluminescence	300 - 1500 nm	*Jobin-Yvon-Horiba, F*
⇒	EL	Electroluminescence (10-300 K)	300 - 1500 nm	*Jobin-Yvon-Horiba, F*
		Opt. Split-Coil Supercond. Magnet	7 T	*Oxford Instrum.., UK*
⇒	PR	Photomodulated Reflectivity	300 - 1500 nm	*Jobin-Yvon-Horiba, F*
⇒	PLE	Photoluminescence Excitation	300 - 1500 nm	*Jobin-Yvon-Horiba, F*
⇒	TRPL	Time-Resolved PL	τ > 5 ns	*Stanford Research, USA*

5. Magnetic Thin Film Deposition and Properties Analysis

⇒	MBE	Molecular Beam Epitaxy with in-situ FIB		*CreaTec,D*
⇒	MBE	Molecular Beam Epitaxy		*Home-built*
⇒	MFM	Magnetic Force Microscope	~ 50 nm resol.	*Veeco/DI, USA*
⇒	SQUID	Supercond. Quantum Interf. Device	± 7 T	*Quantum Design, USA*
⇒	MOKE	Magneto-Optic Kerr Effect (in-plane)	± 0.35 T	*Home-built*
⇒	MOKE	Magneto-Optic Kerr Effect (perp.)	± 2 T	*Home-built*
⇒	SKM	Scanning Kerr Microscope		*Home-built*
⇒	TR-MOKE	Time-Resolved MOKE (pump-probe)		*Home-built*
⇒	VNA-FMR	Vector Network Analyzer Ferromagnetic Resonance		*Agilent/Home-built*

6. Other Analytical and Measuring Techniques

⇒	Scanning Tunneling Microscope (with AFM-option)	*DME, DK*
⇒	In-situ Scanning Tunneling Microscope (variable-Temp.)	*Omicron, D*
⇒	Dektak Surface Profilometer	*Veeco, USA*
⇒	Micro Indenter / Scratch Tester	*Shimatsu, Jp*
⇒	Wear Tester (pin-on disc)	*Home-built*
⇒	Spreading Resistance Profiling	*Sentech, D*
⇒	Hall Effect Equipment (2 - 400 K, ≤ 9 T)	*LakeShore, USA*
⇒	I-V and C-V Analyzer	*Keithley, USA*

7. Processing and Preparation Techniques

⇒	Etching / Cleaning	incl. Anisotropic Selective KOH-Etching	
⇒	Photolithography	2 µm-level	*Süss, D*
⇒	Thermal Treatment	Room Temperature - 2000°C	
		• Furnace	*InnoTherm, D*
		• Rapid Thermal Annealing	*ADDAX, F*
		• Flash-lamp Unit (0.5 – 20 ms)	*Home-built*
		• RF-Heating (Vacuum)	*JIP.ELEC, F*
⇒	Physical Deposition	Sputtering DC / RF, Evaporation	*Nordiko, GB*
		Electron Beam Evaporation System	*Leybold Optics, D*
⇒	Dry Etching	Plasma and RIE Mode	*Sentech, D*
⇒	Bonding Techniques	Anodic, Si-Si and Wire Bonding	
⇒	Cutting, Grinding, Polishing		*Bühler, D*
⇒	TEM Sample Preparation	Plan View and Cross Section	
		incl. Ion Milling Equipment	*Gatan, USA*

Services

The institute serves as a user center and technology transfer point in connection with its many years of experience in the application of ion beams for modification and analysis of solid surfaces and thin films of arbitrary materials.
Ion beam treatment of metallic materials (e.g. light metals like Al, Ti; stainless steel) can be advantageously applied for the improvement of the tribological properties (hardness, wear, corrosion resistance etc.). Using ion beam assisted deposition, hard coatings with special properties are obtained, such as a high adhesive strength and low internal stress. New technologies of high energy ion implantation or focused ion beam techniques result in new applications of electronic devices or microintegrated circuits.
Ion beams are an excellent instrument for the analysis of solid state surfaces. The interaction of the incident ion beam with the surface layer of a material leads to a specific radiation response, which yields information on the elemental composition as function of depth in a quantitative and essentially non-destructive way.
Additional means of preparation and diagnostics are available to fulfill the needs of users from different industrial branches. Do not hesitate to contact our experienced team.

Main Areas of Competence:

- Development and fabrication of sensors and detectors for charged particle spectroscopy
- Deposition of functional coatings using ion-assisted physical vapor deposition
- Fabrication of wear protection layers on metallic materials or alloys
- Deposition of blood compatible layers (i.e. TiO_x) on different materials
- Ion implantation in a broad range of ion energy (~ 200 eV to ~ 50 MeV) and substrate temperature
- Advanced ion beam technologies (high energy ion implantation, focused ion beam) for microelectronic applications
- Application of high energy ion implantation for power devices and laser structures
- Doping of semiconductors, in particular wide bandgap semiconductors
- Surface analysis of solid materials with high energy ion beams
- Computer simulation of ion beam interaction with materials
- Optical characterization of materials (luminescence, FTIR, Raman)

Offers:

- Consultation and problem evaluation for ion beam applications
- Process development for ion beam treatment of different materials (metals, ceramics, semiconductors)
- Process development in ion-assisted deposition of thin films
- Preparation and treatment of material samples, tools or complex parts of devices
- Ion implantation and ion beam analysis services
- Ion implantation into semiconductor materials for applications in microsystems and micro- and power electronics,
- Preparation / fabrication of semiconductors or silicon radiation sensors under clean room conditions
- Structural diagnostics of materials surfaces including e-beam- (SEM, TEM, AES) and X-ray techniques (XRD, XRR with both Cu-K and Synchrotron (5-35 keV) radiation).

Examples:

- Improvement of wear resistance of austenitic stainless steels using plasma immersion ion implantation
- High energy ion implantation for power semiconductor devices,
- Micro- and nanoengineering with focused ion beams
- Non-destructive quantitative hydrogen analysis in materials
- Non-destructive ion beam analysis of art objects
- Doping of wide-bandgap-semiconductors (SiC, diamond)
- Nuclear microprobe for ion beam analysis with high spatial resolution
- Synchrotron radiation analysis of materials at the ROBL Beamline in Grenoble.

Contact:

Please direct your inquiry about the application of ion beams for modification and analysis of materials to one of the following experts:

Field of application	Name	Phone / Fax	E-mail
Ion implantation (metals, ceramics, polymers, biomaterials)	Dr. Andreas Kolitsch	3348 / 2703	a.kolitsch@fzd.de
Ion implantation (semiconductors, in particular high energy)	Dr. Johannes von Borany	3378 / 3438	j.v.borany@fzd.de
Thin film deposition	Dr. Andreas Kolitsch	3348 / 2703	a.kolitsch@fzd.de
High energy ion beam analysis	Dr. Rainer Grötzschel	3294 / 2870	r.groetzschel@fzd.de
Semiconductor preparation Detector / Sensor fabrication	Dr. Bernd Schmidt	2726 / 3285	bernd.schmidt@fzd.de
Focused ion beams	Dr. Lothar Bischoff	2963 / 3285	l.bischoff@fzd.de
Structural diagnostics	Dr. Johannes von Borany	3378 / 3438	j.v.borany@fzd.de
Materials research with synchrotron radiation at ROBL (ESRF)	Dr. Carsten Bähtz	2372	c.baehtz@esrf.fr
Optical materials characterization	Dr. Harald Schneider	2880 / 3285	h.schneider@fzd.de

For all phone/ fax-numbers choose the country / local code: + 49 351 260 - xxxx (for FZD)
+ 33 47 688 - xxxx (for ROBL)

The institute also recommends the homepages of its spin-off companies

- "GeSiM mbH" www.gesim.de
- "APT Dresden" www.apt-dresden.de

Forschungszentrum Dresden - Rossendorf e.V.

Institute of Ion Beam Physics
and Materials Research (IIM)

Postfach 51 01 19
D-01314 Dresden

Tel.: 0351 260 2345
Fax: 0351 260 3285
http://www.fzd.de/FWI

DIRECTORS

Prof. Dr. Wolfhard Möller
2245

Prof. Dr. Manfred Helm
2260

DIVISIONS

ION TECHNOLOGY
(FWII)
Dr. Andreas Kolitsch / 3326

- MeV accelerators
- Ion Implanter / PIII operation
- Ion Beam and Plasma Assisted Deposition
- Biotechnological Materials
- Industrial Services and Projects

SEMICONDUCTOR MATERIALS
(FWIM)
Dr. Wolfgang Skorupa / 3612

- Semiconductors
- Optoelectronic Applications
- Rapid Thermal Annealing Processes
- Defect Engineering
- Positron Annihilation Spectroscopy

NANOFUNCTIONAL FILMS
(FWIN)
Dr. Jürgen Fassbender / 3096

- Modification of Magnetic Materials
- High Anisotropy Nanoparticles
- Magnetic Semiconductors / Spintronics
- Magnetization Dynamics
- Fullerene-like Materials

SEMICONDUCTOR SPECTROSCOPY
(FWIH)
Dr. Harald Schneider / 2880

- Semiconductor Quantum Structures
- Terahertz Spectroscopy
- Femtosecond Spectroscopy
- Free Electron Laser at ELBE
- Optical Characterization (PL, FTIR, Raman)

ION BEAM ANALYSIS
(FWIA)
Dr. Rainer Grötzschel / 3294

- Ion-Solid-Interaction
- High-Energy Ion Beam Analysis
- Channeling Studies of Crystal Defects
- Non-destructive Analysis of Art Objects
- Composition / Modification of Materials

STRUCTURAL DIAGNOSTICS
(FWIS)
Dr. Johannes von Borany / 3378

- Electron Microscopy (TEM, SEM)
- Electron Spectroscopy (AES, XPS)
- Mössbauer Spectroscopy
- X-ray Analysis
- Materials Research with Synchrotr. Radiation

THEORY
(FWIT)
Dr. Matthias Posselt / 3279

- Ion-Beam Synthesis of Nanostructures
- Formation and Evolution of Defects
- Atomistic Simulation of Ion implantation and Ion-Assisted Deposition
- Interatomic Potentials for Solids
- Reaction-Diffusion-Models

PROCESS TECHNOLOGY
(FWIP)
Dr. Bernd Schmidt / 2726

- Semiconductor Technology
- Focused Ion Beam Technology
- Thin Film Deposition
- Computer Aided Structure Design
- Electrical Characterization
- Clean Room Operation

List of Personnel

Directors:

Prof. M. Helm
Prof. W. Möller

Office:

I. Heidel
S. Kirch
L. Post

Scientific Staff:

Permanent:

Dr. G. Abrasonis
Dr. L. Bischoff
Dr. J. von Borany
Dr. W. Bürger
Dr. F. Eichhorn
Dr. S. Facsko
Dr. J. Faßbender
Dr. M. Friedrich
Dr. S. Gemming
Dr. D. Grambole
Dr. J. Grenzer
Dr. R. Grötzschel
Dr. V. Heera
F. Herrmann
Dr. K.-H. Heinig
Dr. R. Kögler
Dr. A. Kolitsch
Dr. U. Kreißig
Dr. A. Mücklich
Dr. C. Neelmeijer
Dr. M. Posselt
Dr. K. Potzger
Dr. H. Reuther
Dr. E. Richter
Dr. N. Schell
Dr. B. Schmidt
Dr. H. Schneider
Dr. W. Skorupa
Dr. M. Voelskow
Dr. S. Winnerl
Dr. M. Zacharias

Post Docs:

Dr. K. Küpper
Dr. J. Sun
Dr. M. Vinnichenko

Projects:

Dr. B. Abendroth
Dr. C. Akhmadaliev
W. Anwand
Dr. G. Brauer
Dr. O. Drachenko
Dr. M. Krause
R.S.M. Martins
Dr. F. Munnik
Dr. T. Oates
Dr. W. Pilz
Dr. A. Rogozin
Dr. N. Shevchenko
Dr. C. V.-B. Tribuzy
Dr. H. Weishart
Dr. R. Yankov
Dr. M. Zier

PhD Students:

M. Beckers
M. Berndt
V. Cantelli
A. Dreyhaupt
H. Geßner
D. Güttler
R. Heller
A. Keller
D. Kost
B. Liedke
M. O. Liedke
D. Markó
A. Martinavicius
F. Peter
J. Potfajova
S. Prucnal
L. Röntzsch
D. Stehr
G. Talut
M. Thieme
M. Wagner
S. Zhou

Diploma Students:

M. Berendt
T. Kunze
D. Nauert
S. Ohser
F. Peter
V. Petr
A. Silze
T. Strache
M. Wagner

Technical Staff:

Permanent:

R. Aniol
R. Aniol
G. Anwand
E. Christalle
H. Felsmann
K. Fukarek
B. Gebauer
H.-J. Grahl
P. Hartmann
J. Haufe
G. Hofmann
S. Klare
J. Kreher
A. Kunz
H. Lange
U. Lucchesi
F. Ludewig
M. Mißbach
C. Neisser
E. Quaritsch
A. Reichel
B. Richter
M. Roch
B. Scheumann
G. Schnabel
A. Schneider
J. Schneider
A. Scholz
T. Schumann
K. Thiemig
A. Vetter
R. Weidauer
A. Weise
J. Winkelmann
G. Winkler
I. Winkler
L. Zimmermann

Projects:

S. Eisenwinder
M. Steinert
I. Skorupa
J. Zscharschuch